Aerodynamic Interaction Effects in Boundary Layer Ingestion
An Experimental Study of a Propulsive Fuselage Concept Aircraft

Della Corte, B.

DOI
10.4233/uuid:d62dd009-cf40-4736-9271-aea4fe37a095

Publication date
2026

Document Version
Final published version

Citation (APA)
Della Corte, B. (2026). *Aerodynamic Interaction Effects in Boundary Layer Ingestion: An Experimental Study of a Propulsive Fuselage Concept Aircraft*. [Dissertation (TU Delft), Delft University of Technology]. https://doi.org/10.4233/uuid:d62dd009-cf40-4736-9271-aea4fe37a095

Aerodynamic Interaction Effects in Boundary Layer Ingestion

An Experimental Study of a Propulsive Fuselage Concept Aircraft

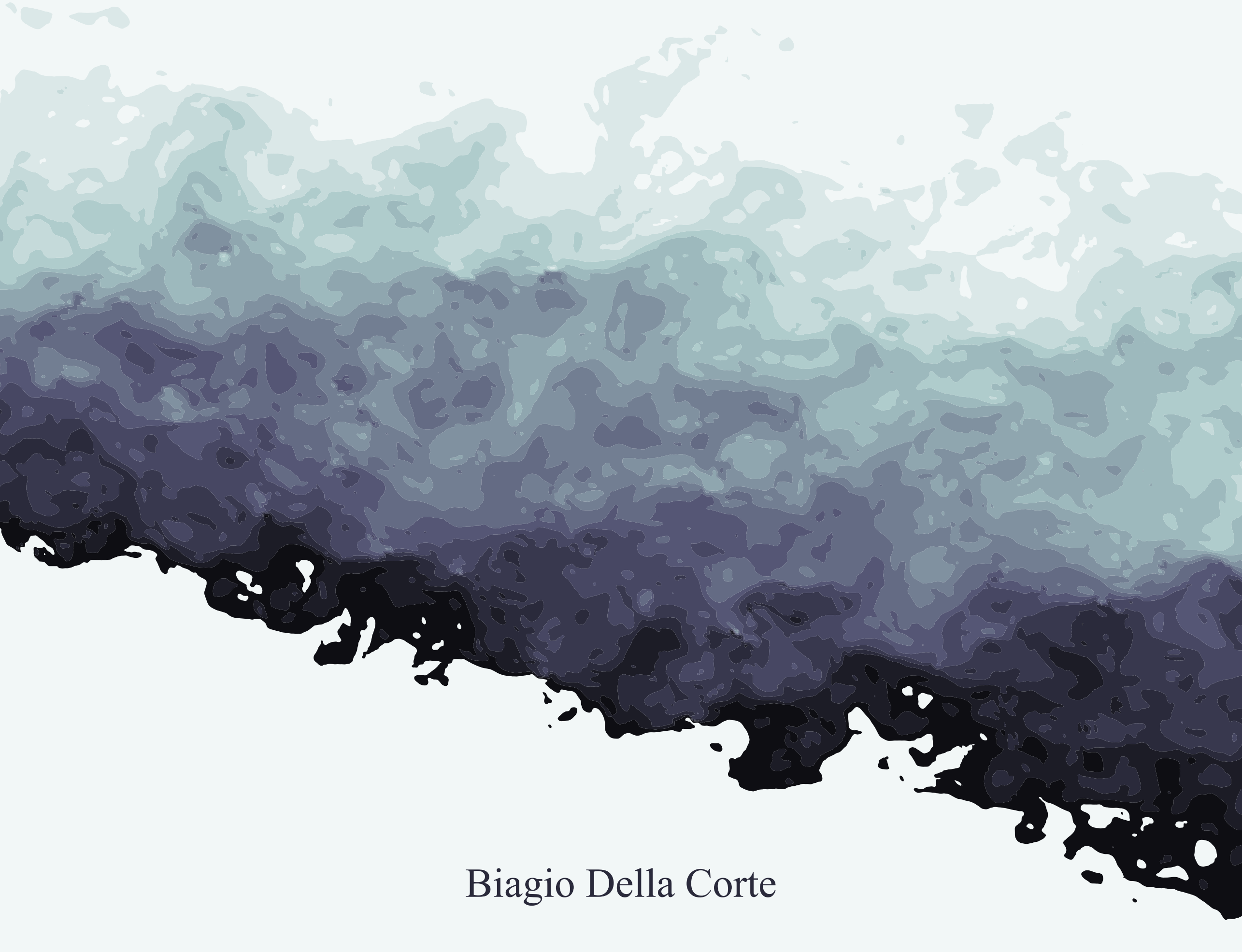

Biagio Della Corte

AERODYNAMIC INTERACTION EFFECTS IN BOUNDARY LAYER INGESTION

AN EXPERIMENTAL STUDY OF A PROPULSIVE FUSELAGE CONCEPT AIRCRAFT

AERODYNAMIC INTERACTION EFFECTS IN BOUNDARY LAYER INGESTION

AN EXPERIMENTAL STUDY OF A PROPULSIVE FUSELAGE CONCEPT AIRCRAFT

Dissertation

for the purpose of obtaining the degree of doctor
at Delft University of Technology,
by the authority of the Rector Magnificus, prof. dr. ir. T.H.J.J. van der Hagen,
chair of the Board for Doctorates,
to be defended publicly on *Tuesday 13 January 2026 at 17:30*

by

Biagio DELLA CORTE

Master of Science in Aerospace Engineering,
Università degli Studi di Napoli "Federico II", Italia,
born in Napoli, Italia.

This dissertation has been approved by the promotors.

Composition of the doctoral committee:

Rector Magnificus,	chairperson
prof. dr. A. Gangoli Rao,	Delft University of Technology, *promotor*
prof. dr. ir. L. L. M. Veldhuis,	Delft University of Technology, *promotor*

Independent members:

Prof. dr. ir. B.J. Boersma,	Delft University of Technology
Prof. dr. C. Hall,	University of Cambridge, United Kingdom
Prof. dr. A.I.K. Kalfas	Aristotle University of Thessaloniki, Greece
Dr. A. Seitz	Bauhaus Luftfahrt, Germany
Prof. Dr.-Ing. G. Eitelberg,	Delft University of Technology, reserve member

This work was conducted within the CENTRELINE project, which has received funding from the European Union's Horizon 2020 research and innovation programme under Grant Agreement No. 723242.

Keywords: Boundary layer ingestion, propulsion integration, aero-propulsive interactions, wind-tunnel testing.
Printed by: Gildeprint – www.gildeprint.nl
Front & Back: Experimental visualization of a turbulent boundary layer.

ISBN 978-94-6518-197-4

An electronic version of this dissertation is available at
`http://repository.tudelft.nl/`

Caminante, son tus huellas
el camino y nada más.

SUMMARY

Sustainability of civil aviation in the future must be achieved through a drastic reduction of aircraft emissions. To accomplish this, new generation aircraft must be employed that exploit innovative technologies, architectures and energy sources. Unconventional aircraft–propulsion integration promises a leap in aircraft efficiency by leveraging synergistic aerodynamic interactions. In particular, Boundary Layer Ingestion (BLI) has raised interest due to the expected benefits on the aircraft power consumption. Unlike in conventional aircraft, in BLI the propulsive system (consisting of one or more distributed propulsors) is tightly coupled and integrated with the aircraft. In particular, the BLI propulsor operates within the low-momentum, low-energy fluid in close proximity to the aircraft surface. By transferring energy to this flow region, viscous dissipation that would otherwise occur in the aircraft wake is avoided, reducing the amount of power needed to sustain flight. In recent years, different BLI configurations have been proposed, of which one of the most promising designs is the so-called propulsive fuselage, featuring a BLI propulsor at the aft-fuselage section. This particular design is the focus of the work presented in this thesis.

One characteristics of these unconventional aircraft configurations with integrated propulsors is that the system performance is driven by the aerodynamic interactions occurring between the aircraft and the propulsive system. Alike conventional aircraft, the design of these new aircraft accounts for the integration interactions at an early stage and, when possible, leverages these interactions to maximize the system performance. In order to obtain a successful design, it is paramount to have a thorough understanding of the fundamental interaction mechanisms taking place in such configurations.

The research work discussed in this thesis has investigated the aerodynamic interactions occurring between the propulsor and the aircraft in a propulsive fuselage concept. The objective of the research was to identify and quantify the main physical mechanisms characterizing the aero-propulsive interactions and their effects on the system performance. For this purpose, extensive experimental simulations were carried out in low-speed wind-tunnel campaigns featuring a scaled-down powered model. A bottom-up approach was used for the experiments, utilizing a setup with increasing complexity in geometry and flow conditions. These experiments were complemented by numerical simulations for relevant high-speed flight conditions.

The results of this work have highlighted the main effects of the mutual aerodynamic interactions. Specifically, the effects of the propulsor on the upstream fuselage boundary layer were quantified for various thrust settings and flight conditions. Through the analysis of the measured flowfields, a significant decrease (up to 15%) of the boundary layer thickness was observed, due to the increased momentum in the inner regions of the boundary layer. Moreover, downstream of the propulsor, a strong hub vortex, characterized by high axial vorticity and low pressure, increases the pressure drag on the fuselage body, hence reducing the achievable performance benefit. Similarly, the influence of the aircraft on the propulsor inflow and performance was analysed at a wide range of operating conditions. The overall system performance were quantified through the application of advanced flow analysis techniques (power balance). In particular, a methodology was developed for the application of the power balance on experimental data. The data shows that, for the analysed setup, a power benefit of around 4% could be achieved with an ideal BLI propulsor. Finally, the effects of the aerodynamic scaling (i.e. the effects of the Reynolds and Mach numbers) were assessed through numerical simulations to expand the experimental results to flight conditions typical of a full-scale aircraft. This study confirmed that the main interaction mechanisms observed in the low-speed experiments had the same relevance at high-speed conditions.

In conclusion, this thesis summarizes extensive research efforts on the aerodynamics of a novel aircraft configuration. It presents high quality and well-documented experimental data obtained through a unique experimental setup, and employing state-of-the-art measurement and analysis techniques. This work expands the body of knowledge concerning Boundary Layer Ingestion, serving as a support for aerodynamicists and aircraft designers in this field and thereby contributing to a greener aviation.

SAMENVATTING

De duurzaamheid van de civiele luchtvaart in de toekomst moet worden bereikt door een drastische vermindering van de emissies van vliegtuigen. Om dit mogelijk te maken, moet een nieuwe generatie vliegtuigen worden ontwikkeld die gebruik maakt van innovatieve technologieën, architecturen en energiebronnen. Van onconventionele integraties van vliegtuig en voortstuwingsysteem wordt verwacht zij een significante sprong maken in efficiëntie door gebruik te maken van synergetische aerodynamische interacties. In het bijzonder heeft Boundary Layer Ingestion (BLI) interesse gewekt vanwege de verwachte voordelen voor het energieverbruik van het vliegtuig. In tegenstelling tot conventionele vliegtuigen is bij BLI het voortstuwingssysteem (bestaande uit één of meerdere gedistribueerde propellers) sterk gekoppeld en geïntegreerd met het vliegtuig. De BLI-voorstuwingssysteem opereert namelijk in het traagstromende, energiearme deel van de stroming, vlakbij het oppervlak van het toestel. Door energie toe te voegen aan dit stromingsveld, wordt viskeuze dissipatie in het zog van het vliegtuig verminderd, waardoor minder vermogen nodig is tijdens de vlucht.

In de afgelopen jaren zijn verschillende BLI-configuraties voorgesteld, waarvan het zogenoemde propulsive fuselage concept — met een BLI-systeem aan de achterzijde van de romp — als één van de meest veelbelovende ontwerpen wordt beschouwd. Dit specifieke ontwerp staat centraal in dit proefschrift.

Een kenmerk van deze vliegtuigconfiguraties met geïntegreerde propulsoren is dat de systeemprestaties worden bepaald door de aerodynamische interacties tussen het vliegtuig en het voortstuwingssysteem. Net als bij conventionele vliegtuigen wordt bij het ontwerp van deze nieuwe vliegtuigen reeds in een vroeg stadium rekening gehouden met integratie-effecten, en wordt, waar mogelijk, getracht deze interacties te benutten om de systeemprestaties te maximaliseren. Voor een succesvol ontwerp is het dan ook essentieel om een grondig inzicht te hebben in de fundamentele interactiemechanismen die bij deze configuraties optreden.

Het onderzoekswerk in dit proefschrift analyseert de aerodynamische interacties tussen de propulsor en het vliegtuig voor het propulsive fuselage concept. Het doel van het onderzoek is het identificeren en kwantificeren van de belangrijkste fysische mechanismen die de aero-propulsieve interacties kenmerken, en hun effect op de systeemprestaties. Hiertoe zijn uitgebreide experimentele simulaties uitgevoerd in windtunnelcampagnes in het laag-subsone snelheidsbegeid met een geschaald aangedreven model. Voor deze experimenten werd een bottom-up benadering toegepast, met een opstelling van toenemende geometrische en stromingscomplexiteit. Deze experimenten zijn aangevuld met numerieke simulaties voor relevante vluchtcondities bij representatieve hogere vliegsnelheid.

De resultaten van dit werk tonen de belangrijkste effecten van de wederzijdse aerodynamische interacties. Specifiek werd het effect van de voortstuwer op de grenslaag van de voorliggende romp gekwantificeerd voor verschillende stuwkrachtinstellingen en vluchtcondities. Uit analyse van de gemeten stromingsvelden bleek een significante afname (tot 15%) van de grenslaagdikte, veroorzaakt door de toegenomen impuls in de binnenste lagen van de grenslaag. Verder werd stroomafwaarts van de propulsor een sterke hub-vortex waargenomen, gekenmerkt door hoge axiale wervelsterkte en lage druk, die de drukweerstand op de romp verhoogt en daarmee het haalbare prestatievoordeel vermindert. Evenzo werd de invloed van het vliegtuig op de instroom en prestaties van de propulsor geanalyseerd over een breed bereik aan bedrijfscondities. De algehele systeemprestaties zijn gekwantificeerd via geavanceerde stromingsanalysetechnieken. Hiervoor de zgn. Power-balance-method toegepast op experimentele data. De data tonen aan dat voor de geanalyseerde opstelling een bij behoud van de vliegsnelheid een vermogensafname van circa 4% mogelijk is met een ideale BLI-propulsor.

Ten slotte werd het effect van aerodynamische schaling (d.w.z. de invloed van Reynoldsgetal en Machgetal) beoordeeld via numerieke simulaties, om de experimentele resultaten te kunnen extrapoleren naar vluchtcondities representatief voor een vliegtuig op ware grootte. Deze studie bevestigde dat de belangrijkste interactiemechanismen waargenomen in de lagesnelheidsexperimenten ook relevant blijven onder kruiscondities van het volle Schaal vliegtuig.

CONTENTS

NOMENCLATURE

Acronyms

CDI	Circumferential distortion index
DC(60)	Distortion index based on a 60° sector
RDI	Radial distortion index
BF	Bare Fuselage
BL	Boundary Layer
BLI	Boundary Layer Ingestion
LTT	Low Turbulence Tunnel
PF	Powered Fuselage
PFC	Propulsive Fuselage Concept
PIV	Particle Image Velocimetry
SP-FoV	Symmetry-Plane Field of View
VTP	Vertical Tail Plane
WP-FoV	Wake-Plane Field of View

Greek Symbols

α	Angle of attack
β	Angle of sideslip
δ^*	Displacement thickness, m
δ_{99}	Boundary layer physical thickness, m
ϵ	Uncertainty
Γ	Circulation, $\mathrm{m^2/s}$
κ	Turbulence kinetic energy, $\mathrm{m^2/s^2}$
μ	Dynamic viscosity, Pa s
Ω	Fan angular velocity, rad/s

ω	Vorticity, s^{-1}
ϕ	Azimuthal angle (Chapter 5)
ϕ	Flow coefficient, $\dot{m}/\rho S_d U_{\mathrm{mid}}$ (Appendix C)
Π	Pressure rise coefficient, $\Delta p_t/\rho U_{\mathrm{mid}}^2$
ψ	Load coefficient, $\Delta h_0/U_{\mathrm{mid}}^2$
ρ	Density, $\mathrm{kg/m^3}$
σ	Blade solidity, $2\pi r/n_b c$ (Appendix C)
σ	Standard deviation (Chapter 3, 4)
θ	Swirl angle
θ^*	Momentum thickness, m
ζ	Radial angle

Latin Symbols

$\bar{c}$	Wing mean aerodynamic chord, m
$\dot{E}_a$	Axial kinetic energy flow rate, W
$\dot{E}_p$	Pressure work rate, W
$\dot{E}_v$	Transverse kinetic energy flow rate, W
$\mathscr{L}$	Roll moment, N m
$\mathscr{M}$	Pitch moment, N m
$\mathscr{N}$	Yaw moment, N m
A	Myring body parameter
c	Airfoil chord, m
$C_{\mathscr{L}}$	Roll moment coefficient, $\mathscr{L}/(q_\infty S c)$
$C_{\mathscr{M}}$	Pitch moment coefficient, $\mathscr{M}/(q_\infty S c)$
$C_{\mathscr{N}}$	Yaw moment coefficient, $\mathscr{N}/(q_\infty S c)$
c_{f}	Fan mid-span chord, m
C_S	Surface area coefficient, $S/(\pi D l)$
C_V	Volume coefficient, $4V/(\pi D^2 l)$
$C_{\dot{\mathcal{E}}}$	Total mechanical power outflow coefficient

$C_{\dot{E}_a}$	Axial kinetic energy deposition rate coefficient
$C_{\dot{E}_p}$	Pressure work rate coefficient
$C_{\dot{E}_r}$	Radial kinetic energy deposition rate coefficient
$C_{\dot{E}_t}$	Tangential kinetic energy deposition rate coefficient
$C_{\dot{E}_\kappa}$	Turbulence kinetic energy deposition rate coefficient
$C_{\dot{E}}$	Kinetic energy deposition rate coefficient
C_ϕ	Viscous dissipation rate coefficient
C_{D_0}	Drag coefficient at zero-incidence (Chapter 3)
C_{D_0}	Drag coefficient of the bare fuselage (Chapter 4-6)
C_D	Drag coefficient, $D/(q_\infty S)$
C_{F_x}	Axial momentum flux coefficient
C_L	Lift coefficient, $L/(q_\infty S)$
C_N	Net axial force coefficient
C_{P_k}	Propulsor mechanical power input coefficient
C_{p_t}	Total pressure coefficient, $(p_t - p_{t\infty})/q_\infty$
C_Y	Lateral force coefficient, $Y/(q_\infty S)$
D	Drag force, N
$d\dot{E}_a$	Axial kinetic energy flux density, W/m^2
$d\dot{E}_p$	Pressure work density, W/m^2
$d\dot{E}_v$	Transverse kinetic energy flux density, W/m^2
D_0	Reference drag force, N
D_f	Fan diameter, m
dF_a	Axial momentum flux density, $dF_a = -dF_x$ N/m^2
dF_x	Axial momentum flux density, N/m^2
dt	Pulse separation, s
f	Fineness ratio, L/D
F_a	Axial momentum flow rate, $F_a = -F_x$ N

F_x	Axial momentum flow rate, N
H	Boundary layer shape factor
h	Non-dimensional blade span
h_0	Specific stagnation enthalpy, J/kg
k	Induced drag coefficient
L	Lift force, N
l	Body section length, m
L_b	Fuselage length, m
M	Mach number, V/a
n	Boundary-normal direction (Chapter 4)
n	Ellipsoid body parameter (Chapter 3)
n_b	Number of blades
p	Static pressure, Pa
p_t	Total pressure, Pa
q	Dynamic pressure, Pa
R_b	Fuselage radius, m
R_f	Fan radius, m
Re	Reynolds number, $\rho_\infty V_\infty L_b/\mu$
S	Wetted area (Chapter 3), m^2
S	Wing planform area (Chapter 5), m^2
s	Wall-normal distance, m
S_ref	Reference area, m^2
S_TS	Test-section cross area, m^2
S_d	Disk area, m^2
S_p	Planform area, m^2
u, v, w	Cartesian velocity components, m/s
u, v_r, v_t	Cylindrical velocity components, m/s
U_mid	Blade mid-section speed, m/s

U_{tip}	Fan tip speed, m/s
u_t, u_n	Wall-tangential and wall-normal velocity components, m/s
V	Velocity magnitude, m/s
x, r, ϕ	Cylindrical reference system
x, y, z	Cartesian coordinates
X_{tr}	Axial position of turbulent transition, m
Y	Side force, N
y^+	Dimensionless wall distance

Sub-scripts

∞	Freestream conditions

1

INTRODUCTION

1.1. BACKGROUND

Aviation has undergone a tremendous growth in the last decades. The economic and societal developments, combined with the technical advancements, have resulted in a significant rise of commercial air transport. Consequently, the number of passengers flying in a year has increased exponentially [1, 2]. Recent forecasts confirm this trend for the next years, predicting almost 8 billion passengers to travel in 2036 [3–5]. The global COVID-19 pandemic (ongoing at the time of writing) has obviously altered the trends [6]. Nevertheless, predictions show that once the effects of the pandemic fade, the growth trend of the aviation industry will relatively quickly fall back on the predictions done before the pandemic [7, 8].

Even though technological improvements have reduced the amount of emissions per passenger compared to the year 2000, the overall emissions due to commercial flights have continuously increased together with the number of flights. To give an example, in year 2017, aviation accounted for nearly 4% of the total CO_2 emissions in Europe [9, 10]. Before the COVID-19 outbreak, these emissions were expected to triple by the year 2050 [1, 11].

To ensure sustainability in the long-term future of civil aviation, the Advisory Council for Aeronautics Research in Europe (ACARE) has set ambitious goals through the Flight-Path 2050 [12] and within the Strategic Research and Innovation Agenda (SRIA) [13]. One of the main challenges is the reduction of CO_2 emissions and hence of the carbon footprint that aviation produces globally. In particular, the SRIA has set the goal of achieving a reduction of 60% of the CO_2 emissions by year 2035 compared to the year 2000. According to recent studies on the CO_2 emissions of commercial aviation, narrow-body and wide-body passenger flights account for around 90% of the overall aviation emissions [11, 14]. Consequently, reducing the fuel burn and emissions of large passenger aircraft would have the strongest effect on the aviation environmental impact.

Large passenger aircraft propulsion rely on turbofan engines. During the last decades, fuel-efficiency and emissions of such propulsive systems have been substantially improved through evolutionary development (e.g. through a continuous increase of the by-pass ratio and sub-system efficiency). Meanwhile, aircraft performance has been enhanced through a continuous improvement of the airframe structures, aerodynamics and flight systems, resulting in an higher aircraft efficiency. However, the overall aircraft and propulsion architecture remained essentially unaltered. Despite these great improvements, projections to the next decades show that the evolutionary development of conventional aircraft configurations will not suffice to achieve the goals set by ACARE [15].

In order to meet the sustainability targets, innovative aircraft architectures must be considered. Several technological solutions are being investigated: from unconventional aircraft architectures to natural laminar flow, to new energy sources like hydrogen and bio-fuels. In particular, electric propulsion systems can be an enabling technology for novel aircraft configurations. In fact, it allows deviating from the conventional tube-and-wing architecture towards more unconventional propulsion-airframe integration technologies, such as distributed propulsion. In aircraft featuring distributed propulsion, the propulsor-airframe integration becomes a key design challenge. In fact, the aerodynamic interaction occurring between the airframe and the propulsive systems can have a substantial impact on the overall aircraft aero-propulsive performance [16].

One of the technologies that exploits the synergistic integration of the propulsive system and the airframe is *Boundary Layer Ingestion* or *BLI*. In this configuration, the propulsor is placed in close proximity of the airframe such that it operates on the low-momentum fluid in the boundary layer. By accelerating the boundary layer to produce the required thrust, less kinetic energy is left in the wake and dissipated by viscous diffusion. As a consequence, the thrust-drag equilibrium can be achieved with an higher propulsive efficiency compared to a conventional configuration, where the propulsor operates on fluid at freestream conditions.

The benefit of operating a propeller in the boundary layer of a body has been long known in naval engineering, as testified by the theoretical and experimental work of Froude in 1883 [17]. Already at the beginning of the twentieth century, Durand and Betz theorized the application of pusher propellers ingesting the wake of upstream bodies for application in the aviation field [18, 19]. Since then, many studies have been performed on similar pusher-propeller configurations for submerged bodies [20], airships [21] and helicopter applications [22, 23] confirming the power consumption benefit. Smith carried out a theoretical study on a propeller operating in the wake of a body for aircraft application [24]. By relating the boundary layer integral properties to the propulsor properties, a maximum propulsive benefit of 20% was estimated for the ideal wake ingestion case (for which the wake of the body is fully recovered).

The design and analysis of paradigm-altering aircraft configuration poses many challenges. In fact, due to the close coupling of the airframe and of the propulsor systems, conventional performance analysis based on the definitions of forces (i.e. *drag* and *thrust*) are not well suited to study BLI configurations [24]. Other analysis methods, based on the study of the energy sources and sinks within the flowfield have been proven more effective in analyzing and understanding BLI configurations. In particular, the mechanisms responsible for the expected power-consumption benefit of BLI configurations have been theoretically discussed with the introduction of the power balance method (PBM) [25]. This method is a control volume analysis which is based on the equilibrium between the mechanical power input of the propulsors, the power dissipation occurring within the volume (e.g. due to viscous effects) and the kinetic energy flow rate across the volume boundaries (e.g. in the wake). The introduction of the PBM allowed for a better understanding of the flow mechanisms associated with BLI. In particular, it clearly showed that the BLI power-consumption benefit stems from the reduction of the kinetic energy which is normally dissipated in the wake of the vehicle [25, 26]. Since a BLI propulsor re-energizes the low-momentum boundary layer flow (the so-called "wake-filling" effect), less energy is dissipated in the aircraft wake and hence less power is required to sustain the flight.

In the last decade, a large variety of concepts of future aircraft featuring boundary layer ingestion has been proposed. Some of these designs are shown in Figure 1.1. Trade-off conceptual studies have shown that the integration of a BLI propulsor at the fuselage aft-section promises the highest fuel consumption benefit [16, 27] when compared to other integrated configurations (e.g. wing-based BLI). This configuration is generally known as Propulsive Fuselage Concept (PFC). The PFC has numerous advantages over other BLI concepts. First, the fuselage geometry is well-suited for a BLI propulsor which can possibly ingest the entire fuselage boundary layer. As a consequence, viscous losses in the wake can be minimized as a large portion of the airframe boundary layer can be energized [27]. In addition, the inflow distortion associated with the fuselage boundary layer could be axisymmetric. Therefore, this distortion would not induce large unsteady fan blade loading and the fan design can be adapted to minimize the fan installation penalty [28]. Finally, the PFC is a relatively conventional design which can ease the design and analysis while still providing a first step toward unconventional aircraft configurations. For these reasons, the PFC has attracted a broad interest in recent years. The DisPURSAL project studied a PFC aircraft with the fuselage fan powered through a gas turbine. A block fuel burn reduction of around 10% was estimated compared to an equivalent conventional design [16]. More recently, the EU-funded CENTRELINE project proposed a turbo-electric PFC design for a long-range passenger aircraft [29]. In cruise conditions, the electric-driven BLI fan has a power share equal to approximately 30% of the total propulsive power, leading to a power saving of around 5% over a conventional aircraft [29]. NASA investigated a similar PFC configuration named the STARC-ABL estimating similar power benefits.[30]

1.2. THESIS MOTIVATION

In BLI aircraft configurations, the aerodynamic interaction taking place between the airframe and the propulsor plays a key role in determining the overall-system performance. Fig. 1.2 schematically shows the expected interaction mechanisms in a Boundary Layer Ingestion aircraft. In such configurations, the airframe and propulsor systems must be designed and analysed in a close-coupled manner. Moreover, due to the influence of the ingested boundary layer and to the flow around other airframe elements, the BLI rotor operates in non-uniform inflow. As a consequence of the inlet distortions, the propulsor is subject to unsteady blade loadings which lead to aeroacoustic and aeroelastic limitations (see for example Ref. [38]). For these reasons, the aerodynamics of BLI needs to be understood in detail.

Thorough investigation of the physical mechanisms that control the main aerodynamic interactions is paramount in order to be able to advance the readiness of the BLI

(a) TU Delft AHEAD. Credits: TU Delft.

(b) MIT D8 [31–33]. Credits: NASA/MIT/Aurora.

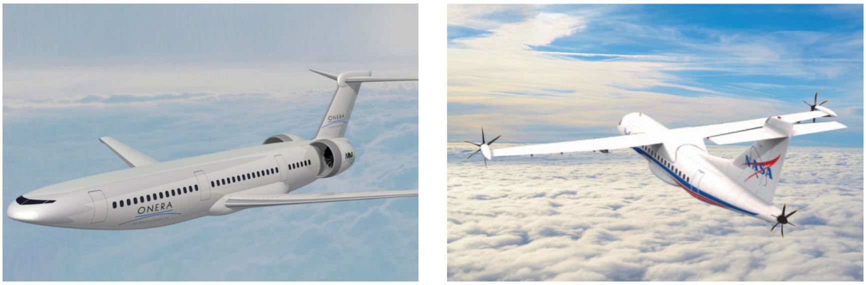

(c) ONERA Nova [34]. Credits: Onera.

(d) NASA PEGASUS [35]. Credits: NASA Langley SACD.

(e) NASA STARC-ABL [30]. Credits: NASA Langley.

(f) CENTRELINE PFC [29]. Credits: Bauhaus Luftfahrt.

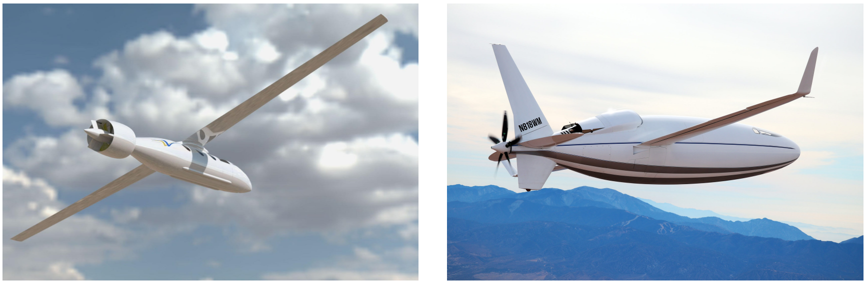

(g) Ampaire TailWind [36, 37]. Credits: Ampaire.

(h) Otto Aviation Celera 500l. Credits: Otto Aviation.

Figure 1.1: Aircraft concepts featuring Boundary Layer Ingestion proposed by recent studies.

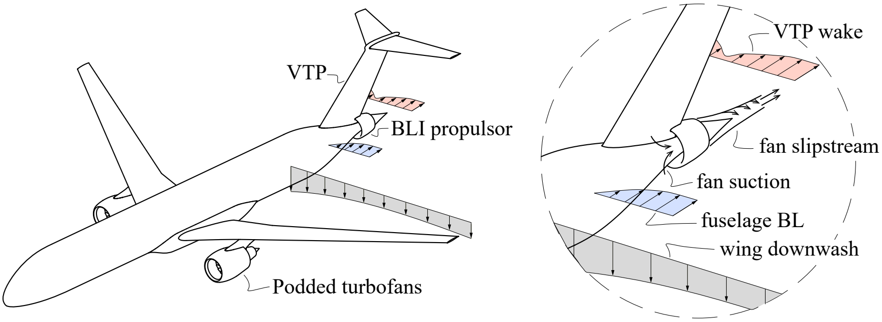

Figure 1.2: Schematic of the CENTRELINE Propulsive Fuselage Concept. Based on [29, 42].

technology. Currently, only few examples of experimental works focusing on the flow physics of BLI are available in literature (see Refs. [23, 33, 39–41]). Some of these works analyzed de-coupled configurations, where the propulsor is placed far downstream of the body to avoid the potential flowfield interaction (Refs. [23, 40, 41]), hence failing in representing a fundamental mechanisms of the aerodynamic interactions. On the other hand, dedicated research was carried out on the design and analysis of propellers and fans in BLI conditions (see Refs. [38, 42–44]). These works focus on the propulsor system, artificially introducing the BLI distortions and ignoring the upstream interaction effects.

In the open literature currently available, the interaction mechanisms that drive the aerodynamics performance of BLI are still not completely understood. Moreover, there is limited knowledge of the aerodynamic interactions that can take place at off-design conditions (i.e. in presence of an angle of attack or sideslip). As a consequence, further studies are needed to study the aerodynamics of an integrated BLI configuration under various inflow and operating conditions.

Additionally, the viscous flowfield around an axisymmetric body of revolution poses an interesting problem, which gains a stronger relevance when looking at the PFC aerodynamics. Previous studies demonstrate that the behaviour of the boundary layer around axisymmetric objects behaves differently than in a planar flowfield. Moreover, when the body is placed at incidence, strong separations and vortical structures arising on the suction side have been discussed in numerical and experimental investigations [45–48]. These structures produce recirculation and crossflow which can affect the performance of a propulsor placed at the aft-fuselage in a BLI configuration. Further investigations are needed on the aerodynamics of axisymmetric bodies under zero and non-zero incidence angles.

1.3. OBJECTIVES

Previous studies on Boundary Layer Ingestion have highlighted the potential fuel consumption benefit of this technology towards a greener future aviation. However, as discussed in the previous section, the aerodynamic interactions occurring between the aircraft and the BLI propulsor have not yet been completely explored. A thorough understanding of the physical mechanisms that drive the aerodynamic interactions in BLI is necessary to maximize the achievable benefit and to facilitate the transition of the technology to the industry. However, only few examples of experimental studies of BLI are available in the open literature so far. Experimental evidence of the main flow mechanisms in BLI is required to enhance the body of knowledge currently available. Furthermore, experimental data on a representative BLI configuration could contribute to the validation of numerical analysis tools, further aiding to the maturity of the technology. This thesis aims at filling these gaps in the scientific literature.

In order to clearly define the research objective, the following research question has been formulated:

> *What are the key aerodynamic interaction effects in boundary layer ingestion and how do they impact the overall system aerodynamic performance?*

The research question is then divided in the following sub-questions:

1. *What are the fundamental flow mechanisms that drive the aerodynamic interaction occurring between the propulsive system and the airframe?*

2. *What are the effects of the operating conditions (i.e. thrust setting and aircraft incidence) on the local flow phenomena and overall aerodynamic performance?*

3. *What is the effect of Reynolds number and Mach number scaling on the main flow phenomena highlighted in this work'?*

The rationale at the basis of the decomposition of the research question follows a bottom-up approach, with a focus that goes from the understanding of fundamental physics to more practical engineering aspects. First, the fundamental aerodynamic interaction mechanisms are identified and investigated. Subsequently, the effects of these mechanisms on the system performance is assessed. Finally, the effect of other key variables is studied.

The following section discusses in more details the focus and methods used in this thesis.

1.4. FOCUS AND METHOD

Boundary layer ingestion has been studied in a number of different aircraft architectures in literature. This research focuses on the Propulsive Fuselage Concept (PFC), a tube-and-wing aircraft equipped with a BLI engine at the aft-section of the fuselage body. The reasons for this are:

1. The PFC promises the highest reduction in power consumption (in the order of 5 to 10%, as detailed in Refs. [16, 27] and in Chapter 2) because it maximizes the amount of low-momentum flow that can be ingested. It is therefore the most attractive BLI configuration for future commercial aviation.

2. The application of BLI on an axisymmetric fuselage body offers significant advantages at the design and analysis phases. The simplification related by the symmetry of the configuration provides an attractive test case for the analysis of the main physical effects of BLI in a baseline case.

3. This thesis work was carried out within the scope of the CENTRELINE project [29, 49]. The aim of this EU-funded Horizon 2020 program was to propose a turbo-electric PFC design based on the Airbus A330 class for entry into service in 2035. Therefore, the aerodynamic studies carried out in this thesis directly contributed to the design and analysis activities performed on the CENTRELINE PFC during the project.

The proposed research question can, in principle, be tackled through theoretical, numerical and experimental analyses. Given the complexity of the studied topic, in which the viscous boundary layer developing over a three-dimensional surface interacts with a rotating propulsive device, the experimental approach was preferred as main investigation method over numerical analysis for two reasons:

1. Numerical simulations are inherently affected by different sources of errors and in particular by modeling errors. Namely, in RANS simulations, the modeling of turbulence can have a strong influence on the simulation result. This is especially relevant in the study of boundary layer ingestion, where accurate predictions of the boundary layer properties are crucial. More advanced numerical simulations like LES or hybrid RANS-LES can partially overcome the problem of turbulence modeling but at the cost of a prohibitive computational cost. Obviously, experimental simulations are inherently not affected by these modeling errors.

2. Experimental simulations allow the investigation of the effect of different parameters in an effective manner. This can include: operating parameters (e.g. test speed, incidence angles, thrust settings) as well as geometrical configurations (e.g. effect of shroud installation, wing installation, tail installation).

The chosen experimental approach suffers from limitations due to e.g. measurement errors, geometrical simplifications and, particularly, related to the aerodynamic scaling with respect to a full-scale flight case. These limitations and their effects on the research results are discussed in more details in the following section. Nevertheless, to partially overcome the scaling limitations, a simplified numerical study was performed to understand the effects of Reynolds number and Mach number scaling effects on the aerodynamics of a PFC aircraft configuration.

The thesis objectives were tackled with a set of different wind-tunnel experiments. Each experimental campaign was designed to answer a key aspect of the research question. Moreover, the experiments were approached with an increasing level of complexity. Fig. 1.3 schematically represents the three main setups which were tested in the wind-tunnel experiments.

First, an isolated axisymmetric body representative of a fuselage body was tested (see Setup I, Fig. 1.3a). This experiment consolidated the understanding of the aerodynamics of axisymmetric bodies in different conditions (i.e. zero and non-zero angle of incidence). Furthermore, this experiment provides a dataset publicly available for validation of numerical simulations (already employed within the CENTRELINE project).

Subsequently, an axisymmetric body with an integrated BLI propulsor was investigated at zero incidence angle (Setup II, Fig. 1.3b). The focus of this setup was to study

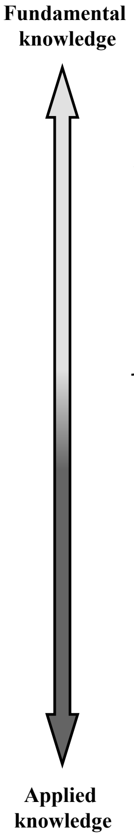

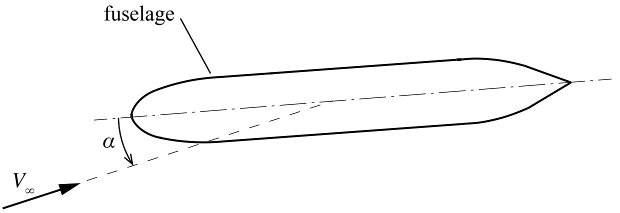

a) Setup I: axisymmetric fuselage in symmetric and asymmetric flow conditions

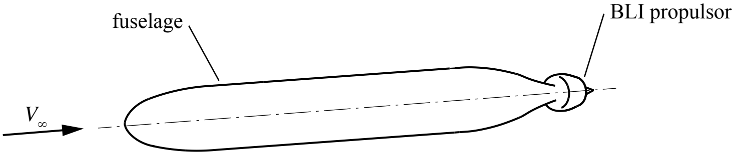

b) Setup II: axisymmetric BLI-fuselage in symmetric flow conditions

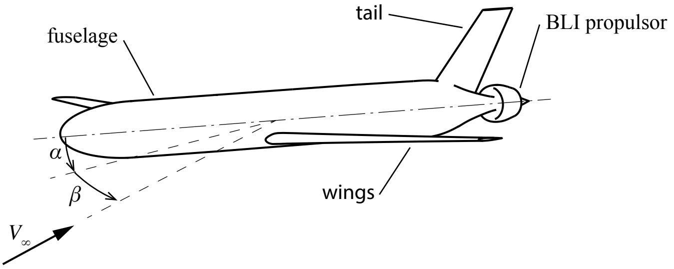

c) Setup III: aircraft with BLI-fuselage in asymmetric flow conditions

Figure 1.3: Overview of the three main setups tested in the wind-tunnel experiments.

the main aerodynamic interactions occurring between the fuselage and the BLI propulsor in axial inflow conditions and without the influence of secondary elements such as wings and tail surfaces.

Finally, an aircraft model equipped with a BLI propulsor integrated at the aft-section of the fuselage body was tested (Setup III, Fig. 1.3c). The goal of this experiment was to study the aerodynamics of a fuselage with BLI propulsion in a more realistic configuration (e.g. including the presence of the wing downwash and empennage wake) both in axial inflow and at non-zero incidence.

1.5. LIMITATIONS

As mentioned in the previous Section, wind-tunnel experiments are affected by different sources of errors. The main sources and their effects on the outcome of this research are discussed here.

First, as for all experimental activities, results from wind-tunnel experiments are affected by errors and uncertainty, due to the measurement instrumentation, techniques and other random factors. The quantification of these errors and their propagation in the measurements and analysis chains is often not trivial. During this work, experimental errors and measurements uncertainty have been estimated and reported in the effort to enhance the confidence in the results and mitigate this limitation.

Moreover, wind-tunnel experiments obviously introduce complexity due to the need of a scaled model that needs to be manufactured and instrumented. Also for the experiments carried out in this work, the model, albeit representative of a commercial aircraft, featured generic and simplified shapes. This undoubtedly has consequences on the extrapolation of the results found here to other, more realistic, shapes. However, this limitation was considered acceptable since validating a specific aircraft design lies out of the focus of this thesis. In fact, the main notions discussed in this work concerning the physical phenomena of the aerodynamic flow, are not expected to change dramatically if small geometrical modifications are introduced.

More importantly, wind-tunnel experiments introduce limitations associated with the aerodynamic scaling. In particular, the wind-tunnel experiments described in this thesis were carried out in atmospheric low-speed facilities. Consequently, the aerodynamic scaling parameters (namely Reynolds and Mach numbers) could not be matched to the values that are typical of a commercial aircraft during the cruise phase.

The Reynolds number governs the relative weight of convective and viscous phenomena. A low Reynolds number at the laboratory scale can induce significant differences in the flowfield when compared to the full-scale case. In practice, this could be mainly due to the delayed laminar-turbulent transition and to the thicker boundary layer relative to the geometry. Some aspects of the wind-tunnel setups were designed to mitigate these effects. First, the laminar-turbulent transition locations was fixed on all the fixed aerodynamic surfaces. Even though this procedure does not simulate the natural transition occurring at the full-scale flight conditions, it eliminates the uncertainty of the transition location and the possibility of laminar flow separation. Second, for the BLI experiments, the BLI propulsor size was scaled accordingly to the fuselage boundary layer size at wind-tunnel scale. In this way, even though the fuselage boundary layer was relatively larger, relative scale with the BLI propulsor was kept similar to what was predicted for the full-scale design.

The compressibility effects, governed by the Mach number, could not be replicated in the low-speed wind-tunnel facilities used for this study. In general, compressibility affects both the potential and viscous flowfield regions. In particular, for a commercial aircraft, compressibility effects are strongest on lifting surfaces (e.g. wings) and on transonic fan blades, where supersonic conditions may occur. For a non-lifting body, such as a fuselage body, compressibility effects are of less importance and are mostly related to the thermal effects in the boundary layer. The focus of the numerical study presented in this thesis was set on the scaling effects on the fuselage aerodynamics. Dedicated studies within the CENTRELINE project captured the compressibility effects on the fuselage fan of a PFC aircraft [28, 42]. Therefore, the numerical simulations employed to aid the experimental dataset from this research featured a simplified propulsor model to simulate the propulsive effects on the surrounding flowfield with limited computational costs.

In general, the Reynolds and Mach number scaling had a substantial effect on the quantitative results of the experimental investigations carried out during this thesis. However, the fundamental interaction mechanisms between the BLI propulsor and the airframe were effectively simulated in the wind-tunnel experiments in a qualitative sense. As a consequence, the same mechanisms are expected to occur in the full-scale flight conditions, possibly with different magnitudes. Since the focus of the experiments was to investigate the fundamental flow physics rather than accurately estimate performance benefits of a particular design, no direct scaling corrections were applied to the wind-tunnel data. Therefore, when discussing aero-propulsive performance, it should be kept in mind that for a full-scale aircraft the results drawn here could be quantitatively different. Other studies, of which some within the CENTRELINE project, were focused on the validation of the PFC aircraft (and in general of aircraft featuring BLI) with the goal of integrating the aero-propulsive benefit in an overall (full-scale) aircraft design process [16, 29].

1.6. OUTLINE

This thesis is divided into seven chapters. The thesis structure is schematically represented in the flow diagram in Fig. 1.4.

Chapter 1 contextualizes the research, discusses the objectives and the chosen general approach to the objectives.

Chapter 2 gives an overview of the main topics related to propulsion integration. After introducing the aerodynamic performance of uninstalled propulsive devices, the main aero-propulsive interactions are discussed. The concept of boundary layer ingestion is introduced together with the main analysis tools available to analyse such unconventional configurations.

Chapters 3, 4 and 5 represent the main body of the experimental results obtained. The results are organized for increasing configuration complexity, reflecting the increasing complexity of the test results (see again Fig. 1.3). As a result, each chapter builds on the previous ones.

Chapter 3 discusses the aerodynamic flowfield around an axisymmetric body under symmetric and non-symmetric flow conditions. The aerodynamics of an axisymmetric body with a BLI propulsor under symmetric flow conditions are investigated in Chapter 4. Finally, Chapter 5 provides a broad analysis of the aerodynamic performance of an aircraft equipped with a BLI propulsor on the fuselage in on- and off-design conditions.

Chapter 6 presents the results of a numerical study on an axisymmetric fuselage with a boundary-layer ingestion propulsor at the aft-section. The goal of this chapter is to highlight the main effects of the aerodynamic scaling parameters on the airframe-propulsion interaction mechanisms. This study complements the experimental data reported in the previous chapters which are taken at low-speed conditions.

Chapter 7 concludes the thesis summarizing the results and proposing some recommendations for future work.

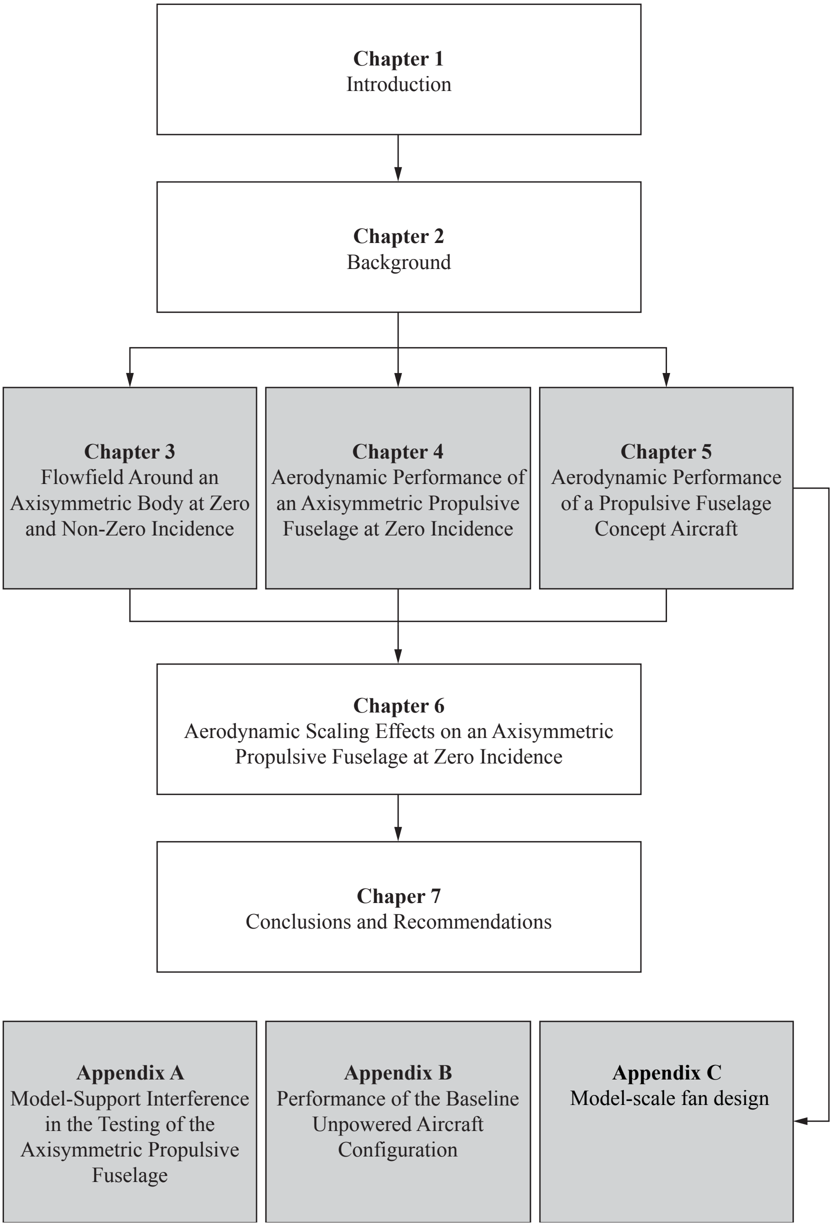

Figure 1.4: Flow diagram of the dissertation.

2

BACKGROUND

2.1. PRINCIPLES OF BOUNDARY LAYER INGESTION

In very general terms, a propulsor is a device that is used to produce a forward force (i.e. thrust) and sustain the motion of a vehicle. In a flying vehicle, a propulsor introduces momentum and energy into the surrounding air, modifying the speed and direction of the air stream that travels through it. This is done at the cost of mechanical power (i.e. shaft power) required by the propulsor. The thrust force, T, is obtained as the reaction force that the fluid exerts on the propulsor and it is associated with “useful” work, equal to (TV_∞), where V_∞ is the flight speed. The change in kinetic energy that is imposed on the fluid represents the power required by the propulsor to generate the thrust. The ratio between the useful work and the change in kinetic energy across the propulsor is the so-called Froude efficiency.

The simplest way to model a propulsor is to represent it in a two-dimensional form and express its performance through the momentum and energy integral equations. The propulsor is modeled as a infinitely thin actuator disk representing a discontinuity in the flowfield. The simplest form of the actuator disk model is obtained for a steady, incompressible, inviscid flow, and in the assumption that disk load is uniform and no tangential momentum is induced in the flow. In these conditions, the actuator disk produces the required thrust through a pressure jump, Δp, across the disk location, which induces a higher velocity to the flow that travels through the disk (see Fig. 2.1). The flow velocity inside the streamtube captured by the propeller can be expressed as the sum of the freestream velocity, V_∞, and the induced velocity, u, as: $V(x) = V_\infty + u(x)$. Due to mass continuity, as the velocity continuously increases along the streamwise direction, the streamtube contracts and its cross-section area, $S(x)$, decreases such that $\rho VS = \text{constant}$.

The thrust produced by the propeller can be expressed as the change in axial momentum induced by the disk:

$$T = \rho(V_\infty + u_d)S_d u_j \tag{2.1}$$

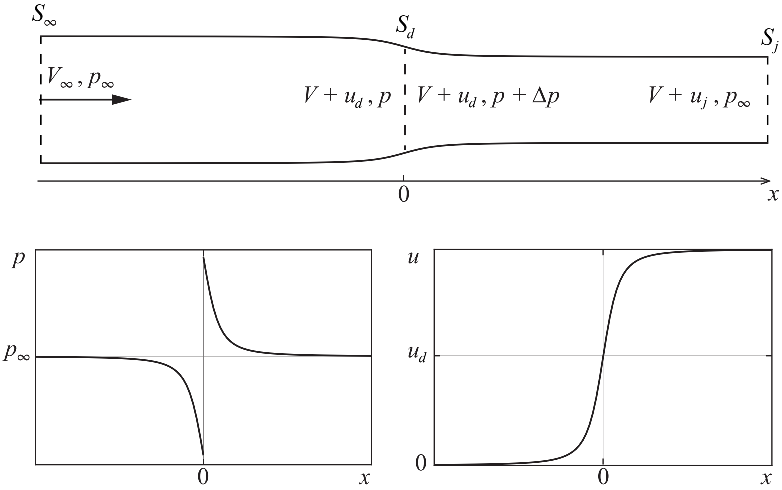

Figure 2.1: Schematics of the actuator disk model.

where ρ is the air density, V_∞ is the freestream flow velocity, S_d is the disk area, and u_d, u_j are the induced velocities at the actuator disk location and far downstream, respectively. Applying Bernoulli's theorem to the upstream and downstream flow tubes of the disk, we have:

$$p_\infty + \frac{1}{2}\rho V_\infty^2 = p + \frac{1}{2}\rho(V_\infty + u_d)^2 \tag{2.2}$$

$$p + \Delta p + \frac{1}{2}\rho(V_\infty + u_d)^2 = p_\infty + \frac{1}{2}\rho(V_\infty + u_j)^2 \tag{2.3}$$

Subtracting member by member the two Bernoulli's equations we obtain the pressure jump:

$$\Delta p = \rho\left(V_\infty + \frac{u_j}{2}\right)u_j \tag{2.4}$$

and we can re-write the thrust as:

$$T = S_d \Delta p = \rho\left(V_\infty + \frac{u_j}{2}\right)u_j S_d \tag{2.5}$$

Comparing Eq. 2.1 and 2.5, we can conclude that:

$$u_d = \frac{u_j}{2} \tag{2.6}$$

which implies that the total flow acceleration is equally split between the upstream and downstream regions of the actuator disk. This can be also understood intuitively since the model is symmetric and there is no preferred direction for the propagation of the disk effects.

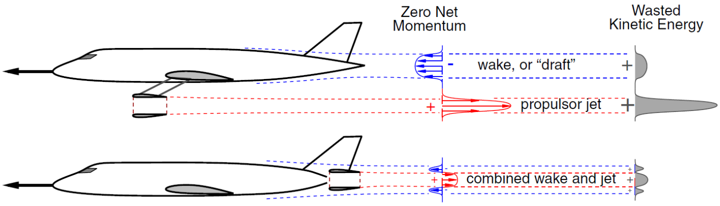

Figure 2.2: Schematics of the "wake-filling" principle of boundary layer ingestion (adapted from Ref. [33]).

With this notation, the thrust, T, can be written as:

$$T = \Delta p S_d = 2\rho S_d (V_\infty + u_d) u_d \tag{2.7}$$

and the required shaft power, P_K, is obtained as the change of mechanical energy flux across the actuator disk:

$$P_K = 2\rho S_d (V_\infty + u_d)^2 u_d = T(V_\infty + u_d) \tag{2.8}$$

The propulsive efficiency (or Froude efficiency) is the ratio between the work exerted by the thrust force and the power imparted to the fluid by the disk:

$$\eta = \frac{T V_\infty}{P_K} = \frac{V_\infty}{V_\infty + u_d} \tag{2.9}$$

which shows that part of the power supplied by the propulsor is "lost" in kinetic energy in the slipstream and not converted in "useful" work.

Fig. 2.2 sketches a conventional aircraft configuration featuring a podded propulsor (top) and an integrated aircraft with a BLI propulsor (bottom). In conventional aircraft design, the propulsor is installed such that it operates on freestream flow. In such configuration, the propulsor has a uniform inflow and the slipstream of the propulsor is separate from the viscous wake of the airframe.

On the contrary, in boundary layer ingestion, the propulsor operates on the boundary layer of the airframe. Two fundamental differences can be identified compared to the conventional configuration: first, the inflow to the propulsor coincides with the boundary layer developing along the airframe and has a lower momentum (i.e. velocity) than the freestream; second, the propulsor slipstream directly mixes with the wake of the airframe. These phenomena are at the base of the performance benefit associated with boundary layer ingestion.

To understand the effect of a decreased inflow velocity on the propulsor, we can use Eq. 2.7-2.9 to obtain the performance of an actuator disk as a function of V_∞. The required power, P_K, and the thrust-to-power ratio, T/P_K, are plotted against V_∞ for various thrust values in Fig. 2.3. Given a required thrust value, T, decreasing V_∞ results in a decrease of the power necessary to generate that thrust (Fig 2.3a). Similarly, the thrust-to-power ratio increases (Fig 2.3b). This means that if we fix the thrust requirements, a BLI propulsor will require less power to generate the required thrust compared to a freestream-ingesting propulsor, since it will perceive an inflow velocity that is lower than

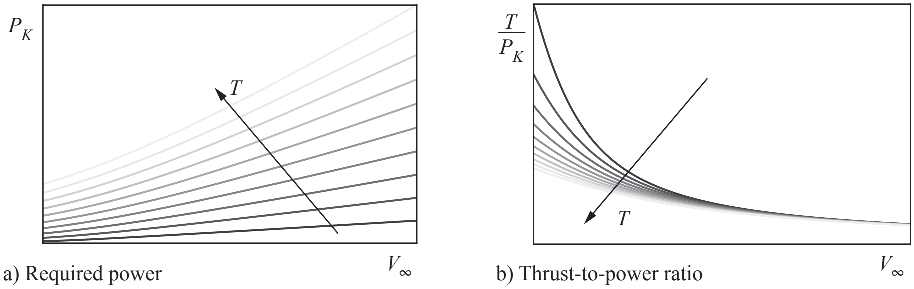

a) Required power b) Thrust-to-power ratio

Figure 2.3: Actuator disk performance as a function of the freestream velocity.

V_∞. It is interesting to notice that the sensitivity of T/P_K to V_∞ increases as T decreases. In other words, the benefit of operating the propulsor at a lower V_∞ (like for a BLI propulsor) becomes larger as the thrust decreases, relatively to a conventional propulsor with the same thrust requirements.

The second mechanism can be explained intuitively here and will be expanded in Sec. 2.4. In a viscous flow, both the wake and slipstream flows will be subjected to viscous dissipation until, far downstream of the aircraft, the velocity distribution is uniform and equal to V_∞ (freestream conditions). As a consequence, the kinetic energy contained in both wake and slipstream flows represent a loss for the aircraft performance. In a conventional configuration (Fig. 2.2 top), the wake and slipstream flows are separate and hence both subject to viscous effects. On the contrary, in a BLI configuration, the slipstream mixes (or partially coincides) with the wake flow. In this case, the net kinetic energy downstream of the aircraft is lower than a conventional configuration thanks to the "wake-filling" effect of the BLI propulsor. In fact, for a fixed net force, i.e. net momentum downstream of the aircraft, a lower velocity excess is seen in the wake of the aircraft as the low and high velocity regions are super-imposed (see again Fig. 2.2 bottom).

2.2. AIRCRAFT ARCHITECTURES

Different aircraft architectures have been proposed exploiting the potential propulsive efficiency benefits of BLI. Some of these configurations are shown in Fig. 2.4.

The MIT D8 aircraft (Fig 2.4a) features a lifting fuselage equipped with two BLI fans at the aft section. Similarly, many blended-wing-body aircraft, such as the Airbus ZERO-e (Fig. 2.4b), feature an array of boundary-layer-ingesting propulsors at the trailing edge of the fuselage section. Both these aircraft architectures utilize the relatively large boundary layer developing on the fuselage section to enhance the energy savings without compromising the efficiency of the lifting surfaces. In particular, for the MIT D8 a fuel saving of around 8% due to BLI was predicted [33].

Another popular configuration is the so-called "Propulsive Fuselage Concept" (PFC), already discussed in Chapter 1 and shown in Fig 2.4c. The PFC is a tube-and-wing aircraft with a BLI propulsor at the fuselage aft section. This configuration uses BLI without a complete paradigm change of the aircraft architecture, with expected benefits in the order of 5-10% [16, 27, 29].

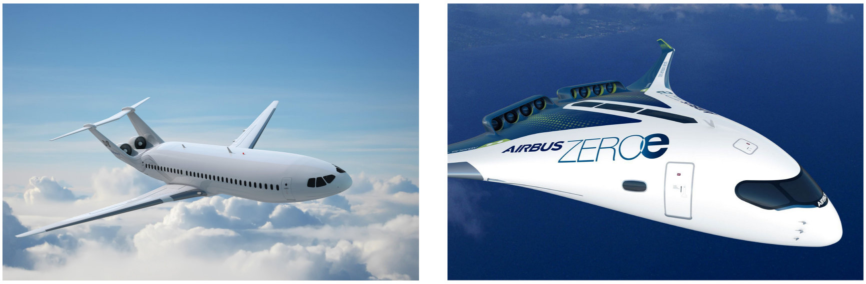

(a) MIT D8 [31–33]. Credits: NASA/MIT/Aurora.

(b) Airbus ZERO-e aircraft. Credits: Airbus.

(c) CENTRELINE aircraft. Credits: Bauhaus Lufthart.

(d) Lilium Jet. Credits: Lilium.

Figure 2.4: Aircraft configurations employing different forms of BLI.

Finally, examples of BLI technology are also found in general aviation and in particular in the fast-growing urban air mobility sector, where distributed propulsion and BLI are vastly used. For example, the Lilium Jet (Fig. 2.4d) featured an array of BLI fans integrated on the suction side of its lifting and control surfaces, also used for thrust vectoring.

All these different architectures successfully make use of the BLI principles with a large difference in the operating and boundary conditions. In order to predict the BLI power-consumption benefit in a preliminary design stage where, potentially, even largely different aircraft architectures are considered, aircraft designers have to rely on simple, top-level models. Such a model was pioneered in the aviation sector by a milestone theoretical and analytical study [24]. In this work, the actuator disk model was used to relate propulsive parameters (thrust and power coefficient, propulsive efficiency) to the boundary layer and wake parameters (displacement and momentum thickness, form factor) to deduce a model for the performance benefit of BLI. Understanding that using a momentum-based approach (i.e. based on the definition of thrust and drag) fails in a configuration where the aircraft is tightly coupled to the propulsor, this study had the intuition to define a simple, top-level, performance metric to compare BLI and non-BLI configurations based on power consumption, the Power Saving Coefficient (PSC). The PSC is simply the normalized difference between the power required to sustain the flight in a non-BLI and BLI configuration:

$$\text{PSC} = \frac{P'_p - P_p}{P'_p} = \frac{P'_p - P_p}{T' V_\infty / \eta'_p} \tag{2.10}$$

where P_p, T and η_p are respectively the propulsive power, thrust and Froude efficiency of the propulsor and the superscript refers to the non-BLI configuration. With this simplified model, it was possible to relate the PSC to parameters describing the flight conditions, the propulsor operation, the boundary layer characteristics and the overall-aircraft design, such as:

- V_j / V_∞, ratio between the jet and freestream velocity. A measure of the disk loading;
- δ^*, θ^*, H, the integral properties of the boundary layer;
- D^{ing} / T, a measure of the "ingested drag" relative to the installed propulsor thrust; D^{ing} represents the momentum deficit associated with the streamtube captured by the propulsor.
- R, the recovery factor. A measure of the propulsor effectiveness in "flattening" the wake profile (i.e. of "wake-filling").

Based on these model, the following top-level conclusions were drawn:

- The power saving increases with the boundary layer shape factor (H). This means that the propulsor should be placed as close as possible to the trailing edge.
- The BLI benefit increases with D^{ing} / T. This means that the amount of momentum deficit (i.e. the amount of boundary layer flow) ingested by the propulsor should be maximized.
- Increasing the propulsor size has a benefit until the entire boundary layer is ingested. This is due to the decreasing disk loading and hence increasing propulsor efficiency, combined with the increased ingested momentum deficit. Further increasing the propulsor size does not result in an increased BLI benefit.
- The power saving is highest for the perfect wake-filling condition (i.e. jet profile constant and equal to V_∞). However, when moving away from this ideal conditions, the kinetic energy left in the wake plays a second-order role on the overall power saving. This means that optimizing the propulsor shape (and disk loading distribution) to obtain a wake shape that is as uniform as possible is not essential to achieve a power-consumption benefit.

This analytical model was used in a multi-disciplinary assessment of transport aircraft featuring distributed propulsion architectures to estimate the potential BLI benefits for different configurations (Ref. [27]). The model was adapted for typical cruise conditions of a commercial transport aircraft. In particular, the correlation between the power saving coefficient (PSC) and the relative momentum deficit ingested by the BLI propulsor was obtained (shown in Fig. 2.5). These results were achieved by observing that:

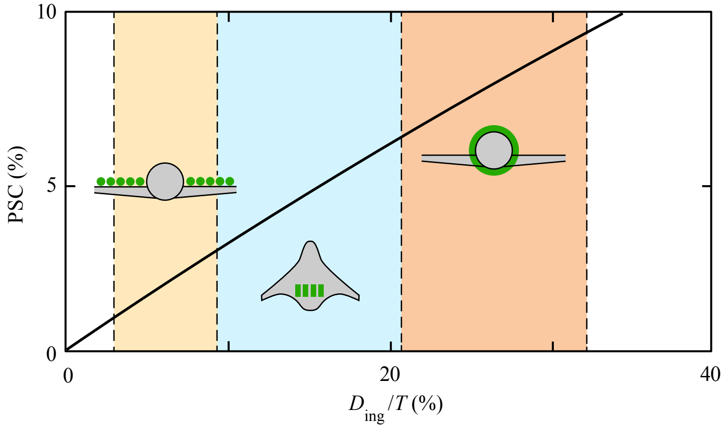

Figure 2.5: Expected BLI power benefit as a function of the ratio between ingested momentum deficit and required propulsive thrust. Results from Smith's analytical model (Ref. [24]), adapted by Ref. [27] for typical commercial aviation cruise conditions.

$$\frac{D^{\text{ing}}}{T} = \frac{D_p^{\text{ing}}}{D} = \frac{C_{D_p}^{\text{ing}}}{C_D} = \frac{C_{D_p}}{C_D}\frac{C_{D_p}^{\text{ing}}}{C_{D_p}} \tag{2.11}$$

where D_p is the *parasite* or *profile* drag of the aircraft. Consequently, the estimation of D^{ing}/T resulted in the evaluation of the two ratios on the right-hand side of Eq. 2.11. The first ratio is simply the ratio between parasite and total drag of the aircraft. The second ratio is the ratio between the "ingested" parasite drag in BLI conditions and the total parasite drag.

Fig. 2.5 shows that the propulsive fuselage concept is the configuration for which the maximum BLI benefits can be expected. In particular, PSC values of up to 10% were estimated. This is a consequence of the fact that the propulsive fuselage architecture allows to maximize the ratio $C_{D_p}^{\text{ing}}/C_{D_p}$ when compared to the other architectures considered in the study. In fact, the fuselage contributes to a considerable share of the total aircraft drag (up to around 30% according to Refs. [27, 29]). Moreover, the entire fuselage boundary layer can be ingested with a single BLI propulsor resulting in the highest ratio $C_{D_p}^{\text{ing}}/C_{D_p}$ and hence the highest PSC values.

Finally, the propulsive fuselage configuration allows to minimize other interaction effects that could potentially affect the aircraft performance and hence the overall power consumption benefit. These mechanisms and their effects will be described in the next section.

2.3. MAIN AERODYNAMIC INTERACTIONS IN BLI

When the propulsion system is placed in close proximity of (or integrated with) the aircraft elements (i.e. wing, tail, fuselage), mutual aerodynamic interactions occur. While these interactions are at the base of the aero-propulsive benefit, some of these mechanisms can have detrimental effects on the aircraft and propulsion performance, limiting the achievable advantages. The interactions effects can be evaluated by understanding how the flowfields induced by the aircraft and the propulsor affect each other performances. In particular, a distinction can be made between the *potential* and *viscous* effects. This helps separating and modeling the effects of different features (or regions) of the flowfield.

2.3.1. PROPULSOR EFFECTS ON THE AIRCRAFT

The flowfield around the propulsor is modified by the pressure and velocity induced by the propulsor itself (see again Fig. 2.1). In a BLI configuration, the propulsor-induced flowfield directly affects the aerodynamics of the aircraft. In particular, it is known that in a propulsive fuselage configuration the fuselage drag is increased as a result of the interaction with the propulsor (Ref. [26]). This is due to two interlinked mechanisms.

First, the pressure distribution around the aft-body is altered by the pressure field induced by the propulsor. In particular, the propulsor produces a suction effect (lower pressure upstream) and a negative pressure gradient. This reflects in the surface pressure distribution on the part of the body closer to the propulsor, as depicted in Fig. 2.6a. The reduced pressure recovery towards the trailing edge of the fuselage body results in an increased pressure drag component in the BLI configuration.

Moreover, the increased velocity due to the propulsor upstream effect results in an increased velocity outside and across the boundary layer around the fuselage aftbody (Fig 2.6b). This results in an increased velocity gradient in the wall-normal direction and hence in an increased wall-shear stress. As a consequence, the friction drag of the fuselage is increased. For a streamlined axisymmetric body at zero incidence, the viscous drag share is the biggest contribution to the total body drag. However, the body drag increase due to the upstream effect of the BLI propulsor is mainly related to the pressure drag increase (around 95% according to the numerical simulations reported in Ref. [26]).

2.3.2. AIRCRAFT EFFECTS ON THE PROPULSOR

The (downstream) effect of the aircraft on the propulsor system is a consequence of the distortions induced on the propulsor inflow by the presence of the aircraft. In fact, while a conventional propulsor operates in an (undisturbed) uniform flow, a BLI propulsor is subjected to a non-uniform inflow.

In general, the inflow distortions associated to BLI can be three-dimensional and asymmetric. Consequently, the propulsor blades will perceive an inflow varying along its span (i.e. radial distortion) and across its rotation (i.e. azimuthal distortion).

For typical BLI architectures, we can make a distinction between *axisymmetric* and *non-axisymmetric inflows*, as sketched in Fig. 2.7.

For the axisymmetric inflow case (Fig. 2.7a), representative of an ideal fuselage-BLI configuration, the inflow distortion at the propulsor is *radial*. This means that, the different sections across the blade perceive a changing inflow velocity (and hence inflow angle). However, their inflow conditions would stay constant through an entire rotation around the propulsor axis. Consequently, this inflow condition has an effect on the time-averaged propulsor performance (e.g. thrust, power, efficiency, stability margin, etc.), but it does not introduce unsteady phenomena. The BLI benefits are not asso-

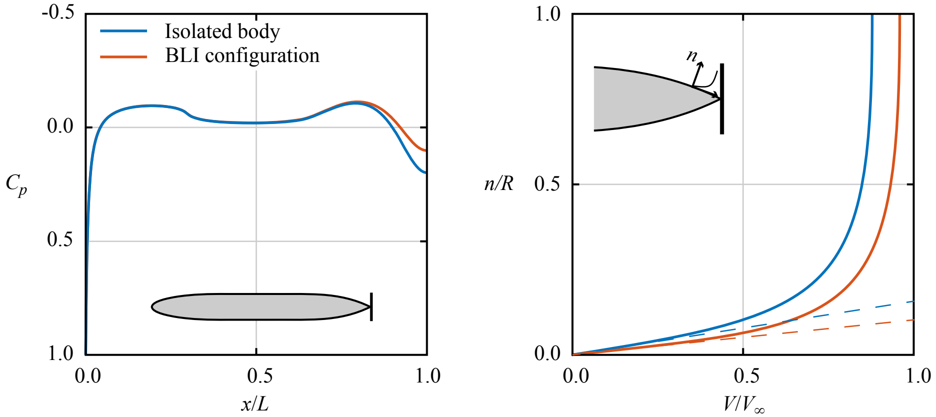

a) surface pressure distribution

b) boundary layer velocity profile

Figure 2.6: Qualitative propulsor effects on the upstream fuselage body in a BLI configuration. Adapted from Ref [26].

ciated with enhanced propulsion performance (e.g. enhanced propulsive efficiency). However, a sub-optimal propulsor design reduces the achievable BLI benefit, due to low propulsive efficiency, flow separations and other viscous losses.

In case of a non-axisymmetric inflow (sketched in Fig. 2.7c), typical for example of an over-the-wing BLI configuration (see Fig. 2.4b and 2.4d), the induced distortions are, at the same time, in the *radial* and *circumferential* direction. This means that, in addition to the spanwise inflow variations, the propulsor blade will encounter regions of high and low inflow velocity (i.e. momentum) and hence perceive a different inflow conditions during a complete rotation. As a consequence, the inflow angle of the blade elements will vary periodically depending on the azimuthal position of the blade leading to the onset of unsteady phenomena (e.g. time-dependant blade loadings, increased rotor noise etc.).

In addition to the local variation of the inflow conditions, the inlet distortions typically found in BLI configurations lead to a three-dimensional flow redistribution occurring upstream of the propulsor plane [38, 50], as sketched in Fig. 2.8. This pattern is due to the non-uniform disk loading distribution due to the inflow distortions. In regions of low momentum flow (i.e. low inlet velocity and total pressure), the local disk loading is enhanced due to the increased inflow angles perceived by the blade sections. As a consequence, an increased suction is produced and higher axial velocities are induced upstream of the rotor, resulting in a higher local mass flow. This leads to a migration of flow from the high momentum to the low momentum regions in proximity of the rotor plane resulting in an asymmetric swirl component that affects the blade inflow.

In case of axisymmetric inflow distortions, design studies suggest that it is possible to adapt the blades geometry (planform, sections shape and pitch distributions) to optimize the blade load distribution. When compared to a conventional design optimized for equivalent undistorted conditions, performance penalties associated to BLI could be

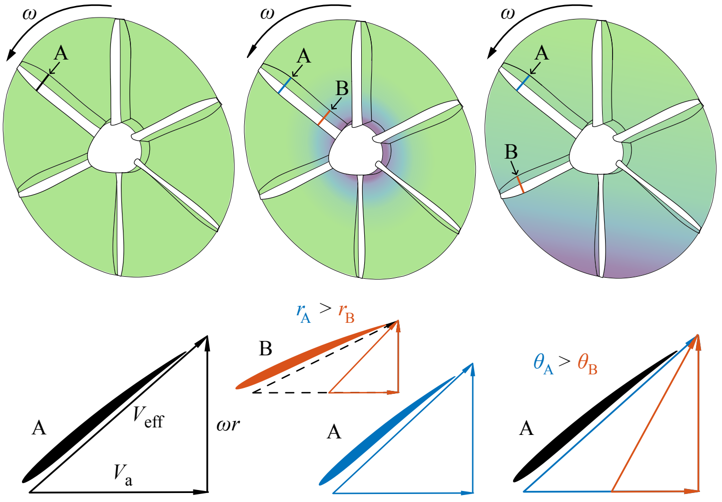

a) uniform inflow b) axisymmetric inflow c) non-axisymmetric inflow

Figure 2.7: Schematics of typical inflow conditions in a BLI proplsor.

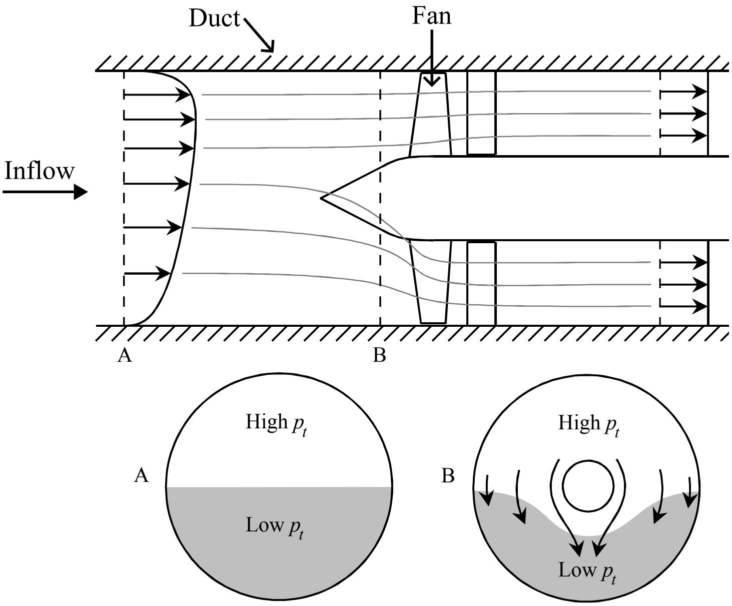

Figure 2.8: Three-dimensional flow pattern in BLI configurations (adapted from Ref. [38]).

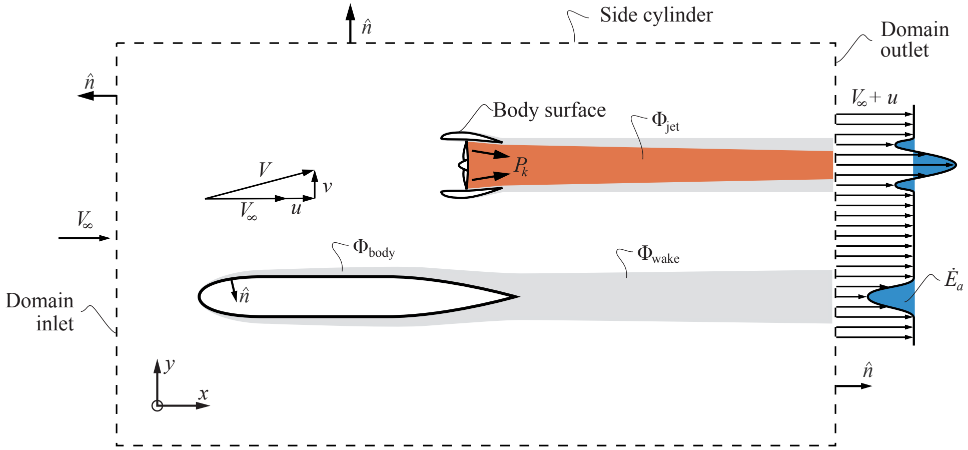

Figure 2.9: Control volume for the power balance method.

minimized (to less 1%), as demonstrated by Ref. [42, 51].

However, in presence of a three-dimensional inflow distortion, the design of the propulsive system must take into account the structural (aeroelasticity, vibrations, fatigue) and aeroacoustic drawbacks introduced by BLI.

2.4. POWER-BASED FLOW ANALYSIS

For a conventional aircraft configuration where the propulsor is separate, it is possible to unambiguously define the aerodynamic forces acting separately on the aircraft and propulsor. As a consequence, the analysis of these configurations can be based on classical thrust–drag bookkeeping methods based on the *momentum* balance in the flow (see for example Ref. [52]). However, when the propulsor is integrated with the aircraft in a BLI configuration, it is impossible to formally define the concepts of thrust and drag. This is due to the fact that the streamtube captured by the propulsor (associated to the thrust definition) is not physically distinct with the streamtube around the airframe (associated to the drag definition). As a consequence, the definition of "useful work" provided by the propulsor (i.e. $T V_\infty$) is inadequate for the definition of propulsive efficiency. Previous studies have highlighted this by showing values of propulsive efficiency exceeding unity (see Refs. [26, 53, 54]).

To overcome this limitation, analysis methods based on the *energy* or *power balance* have been proposed. These methods evaluate system performance using mechanical energy instead of forces. This allows a clear identification of power *sources* and *sinks* in the flow as opposed to concepts like thrust and drag. In this section, a brief summary of the power balance method and the main conclusions relevant to BLI are given, which are largely based on Ref. [25].

Fig. 2.9 provides an example control volume for the application of the power balance. The power balance method consists in equating the power sources inside the control volume to the power sinks, energy flow rates across the boundaries and the work exerted by the net forces. The integral mechanical power balance equation is:

$$P_S + P_K + P_V = \dot{E} + \Phi - \dot{W} \tag{2.12}$$

where:

$P_S = \iint \left[-(p - p_\infty)\hat{n} + \overline{\overline{\tau}} \cdot \hat{n} \right] \cdot \overline{V}\, dS$	is the net propulsor shaft power. Relevant for propulsors of which the surfaces (i.e. blades) are included in the volume boundaries.
$P_K = \iint -\left[(p - p_\infty) + \frac{1}{2}\rho\left(V^2 - V_\infty^2\right) \right] \overline{V} \cdot \hat{n}\, dS$	is the net propulsor mechanical power flow. Relevant for propulsors of which the surfaces (i.e. blades) are not included in the volume boundaries, i.e. when propulsor inlet and outlet surfaces are included in the boundaries.
$P_V = \iiint (p - p_\infty) \nabla \cdot \overline{V}\, d\mathcal{V}$	is the net pressure-volume power. Relevant for energy sources where the fluid is expanded against the atmospheric pressure (e.g. in a combustor).
$\Phi = \iiint \left(\overline{\overline{\tau}} \cdot \nabla\right) \cdot \overline{V}\, d\mathcal{V}$	is the viscous dissipation rate. Rate at which mechanical energy is converted into heat by the viscous stresses.
$\dot{E} = \iiint \left[\frac{1}{2}\rho\left(u^2 + v^2 + w^2\right)(V_\infty + u) + (p - p_\infty)u \right] dS$	is the mechanical energy outflow rate. Term representing the rate at which kinetic energy is transported outside the control volume and the net pressure work exerted at the volume boundaries. Here $(u, v, w) = \overline{V} - \overline{V}_\infty$ is the perturbation velocity.
$\dot{W} = -\overline{F}_{\text{net}} \cdot \overline{V}_\infty$	is the work exerted by the net force acting on the vehicle.

The left-hand side of Eq. 2.12 represents the rate of energy addition inside the control volume by all energy sources. These energy sources can be internal to the control volume (e.g. if rotating propulsor blades are part of the volume boundaries) or external (e.g. if the propulsor rotating elements are kept outside of the boundaries). The right-hand side of Eq. 2.12 consists of the sum of the rates at which energy is transported outside of the volume ($\dot{E}$), dissipated into heat by viscous stresses (Φ) and transformed into "useful" work by the net force ($\dot{W}$).

The general equation is valid for any type of flow or vehicle configuration. The last term, $\dot{W}$, is equal to zero in equilibrium flight conditions (i.e. zero net force on the vehicle) or, for example, $-F_x V_\infty$ in case of a non-zero net axial force (e.g. excess thrust).

The viscous dissipation, Φ, describes the amount of mechanical energy that is turned into heat through the viscous forces in the flowfield. This term is the highest, for example, in boundary layers, viscous wakes and jets. The relation between the energy outflow rate, $\dot{E}$, and the viscous dissipation, Φ, is very strict and depends on the position of the domain outlet surface.

To better understand the origin and interpretation of these various terms and their relations we can look at basic cases such as 2D airfoil and an ideal propulsor (sketched in Fig. 2.10).

In the case of an isolated 2D airfoil in incompressible flow (Fig. 2.10a), no energy sources are present and the only force acting on the body is the aerodynamic drag. Eq. 2.12 simplifies in:

$$DV_\infty = \dot{E} + \Phi \tag{2.13}$$

which intuitively states that the power required to sustain the motion is equal to the sum of the energy dissipated in the flow and the energy that exits the control volume. Downstream of the trailing edge, in the airfoil wake, viscous shears result in the diffusion of velocity gradients, irreversibly converting $\dot{E}$ into Φ. If the domain outlet plane is moved infinitely downstream, such that the flow conditions have returned to those of the freestream, the term $\dot{E}$ reduces to zero:

$$DV_\infty = \Phi_{\text{total}} = \Phi_{\text{body}} + \Phi_{\text{wake}} \tag{2.14}$$

where the terms Φ_{body} and Φ_{wake} represent the dissipation occurring, respectively, in the boundary layer near the body surface and in the wake of the body.

Moreover, if we consider an ideal propulsor operating in inviscid and incompressible conditions (Fig. 2.10b), the power balance reduces to:

$$P_K = TV_\infty + \dot{E} \tag{2.15}$$

where P_K is the mechanical power input by the propulsor and T is the generated thrust force. If we move the domain outlet plane far downstream so that we can consider the axial gradients equal to zero ($p = p_\infty$) and we assume the flow to be uniform in the radial direction, the mechanical energy flow rate is equal to:

$$\dot{E}_{\text{jet}} = \frac{1}{2}\rho u_{\text{jet}}^2 (V_\infty + u_{\text{jet}}) S_{\text{jet}} \tag{2.16}$$

Considering that the thrust provided by the propulsor is equal to the momentum flow rate at the domain outlet plane:

$$T = \rho u_{\text{jet}} (V_\infty + u_{\text{jet}}) S_{\text{jet}} \tag{2.17}$$

we can rewrite Eq. 2.16 as:

$$\dot{E}_{\text{jet}} = \frac{1}{2} T u_{\text{jet}} \tag{2.18}$$

that combined with Eq. 2.15 results in:

$$P_K = TV_\infty + \frac{1}{2} T u_{\text{jet}} \tag{2.19}$$

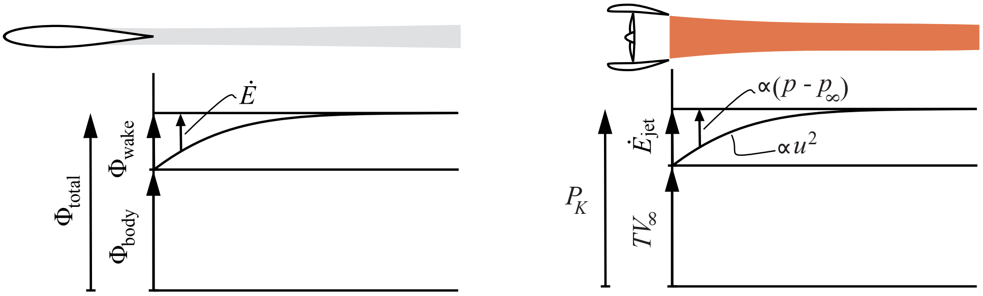

a) Isolated 2D airfoil

b) Ideal propulsor

Figure 2.10: Main power balance terms in simplified study cases.

which is equivalent to the known actuator disk results of Eq. 2.8 when considering that $u_{\text{jet}} = 2u_{\text{disk}}$.

These basic examples also help in understanding one of the fundamental principles behind the BLI benefit. In fact, as explained above, a fraction of the power required to sustain the flight of a body (i.e. DV_∞) is due to the energy dissipation occurring in the viscous wake (Φ_{wake}). Moreover, a fraction of the power (P_K) transmitted to the flow by the propulsor is not converted in useful work (TV_∞), but left in the slipstream ($\dot{E}_{\text{jet}}$), representing a loss. For an aircraft with conventional propulsion both these losses mechanisms would be present, as sketched in Fig. 2.11a.

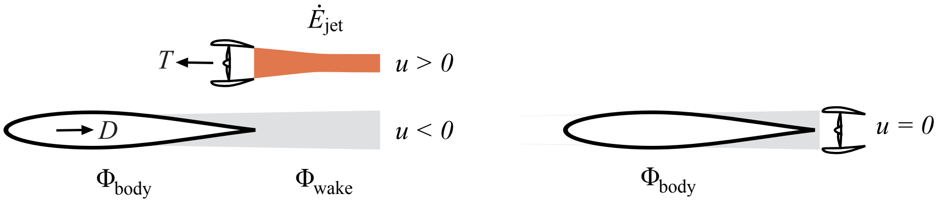

a) Non-BLI configuration

b) BLI configuration

Figure 2.11: Comparison of a conventional and a BLI configuration.

However, in an ideal BLI configuration, a BLI propulsor placed at the body trailing edge would *re-energize* the body wake to produce a jet velocity equal to V_∞. As a consequence, all the energy dissipation occurring in the body wake and propulsor slipstream would be avoided (see Fig. 2.11b).

In particular, for the conventional configuration without BLI, Eq. 2.12 reduces to:

$$\text{Body:} \qquad DV_\infty = \Phi_{\text{total}} = \Phi_{\text{body}} + \Phi_{\text{wake}} \tag{2.20}$$

$$\text{Propulsor:} \qquad P_K^{\text{non-BLI}} = TV_\infty + \dot{E}_{\text{jet}} = \Phi_{\text{body}} + \Phi_{\text{wake}} + \dot{E}_{\text{jet}} \tag{2.21}$$

where it is considered $T = D$. However, in the BLI configuration no dissipation occurs in the wake and slipstream regions, and Eq. 2.12 simplifies in:

$$P_K^{\text{BLI}} = \Phi_{\text{body}} \tag{2.22}$$

which confirms that one of the underlying saving mechanisms of BLI is related to the reduced wake and slipstream dissipation.

It must be noted that this analysis is simplified and aimed at highlighting the physical mechanisms of the BLI benefit. In particular:

- The reciprocal influence between the body and the propulsor is neglected. As detailed in Sec. 2.3, in a real BLI configuration the upstream effect of the propulsor increases the body drag (i.e. Φ_{body}), while the presence of the body reduces the efficiency of the propulsor.
- It is assumed that downstream of the BLI propulsor the jet velocity profile is uniform and equal to V_∞, such that no expansion and dissipation occur in the slipstream. In practice, it is not possible to achieve this and some dissipation will occur downstream of the propulsor.

From this discussion it can be deducted that the achievable BLI benefit is limited to the amount of power dissipated in the wake. In particular, as shown in Ref. [25], for a laminar flat plate around 20% of the total dissipation occurs in the wake. However, for a turbulent flat plate, this ratio drops to around 10-15% (see Ref. [55]). Similar values are estimated for an axisymmetric body in flow conditions representative of those of a high-subsonic commercial flight [55].

This chapter has provided the fundamental knowledge and tools to understand and analyse a BLI configuration. The chapter has explained the basic principles that drive the performance gain expected from BLI and how (and how much) different aircraft architectures exploit those principles. The fundamental aerodynamic interactions were outlined from previous studies, together with novel theoretical tools introduced to analyse non-conventional aircraft configuration, such as BLI concepts. The fundamental notions and ideas introduced in this chapters will hopefully aid the subsequent discussions.

In the next chapters, the core of the technical work of this research will be presented. As detailed in the chapter 1, the work will start with a focus on the aerodynamics of an isolated fuselage and subsequently move to the more complex case of a BLI fuselage with an integrated propulsor.

3

FLOWFIELD AROUND AN AXISYMMETRIC BODY AT ZERO AND NON-ZERO INCIDENCE

3.1. INTRODUCTION

As discussed in Chapters 1 and 2, BLI potentially provides the maximum benefit when applied to the aircraft fuselage body. In such configurations, the aerodynamics of the fuselage body is of key importance due to its influence on the BLI propulsive system. In particular, the flowfield around the fuselage body aft section represents the inflow of the BLI propulsor and hence has a strong impact on the overall system performance. Consequently, understanding how the flow evolves around a fuselage-like body at zero and non-zero incidence is a fundamental step to subsequently study the aerodynamics of fuselage-BLI integrated systems.

Extensive theoretical and numerical work on the prediction of the boundary layer at the tail of axisymmetric bodies at zero incidence was carried out during the 1970s by Patel *et al.* [56] The results of this work, corroborated by experimental data by the same authors [45], show the development of an axisymmetric boundary layer in an adverse pressure gradient and how it differs from a two-dimensional planar boundary layer. In fact, in the axisymmetric case the thickness of the boundary layer is of the same order of magnitude of the body thickness (radius) and significant variations in the static pressure across the boundary layer height exist. This is due to non-negligible normal velocity component and streamlines divergence. As a result of the relatively high boundary layer thickness and normal velocity component, the interaction between the potential flowfield region and the viscous flowfield region is strong. Finally, in turbulent conditions,

---

Contents of this chapter have been published in:
Della Corte, B., Orsini, L., van Sluis, M., Gangoli Rao, A., and Veldhuis, L. L. M., "Experimental Investigation of the Flow Past and Axisymmetric Body at Low Speed", *24th International Society of Air Breathing Engines Conference*, ISABE Paper 2019-24151, 2019.

Reynolds stresses are lower than as expected in thin planar boundary layers. Previous numerical work has already shown that turbulence models available in most commercial CFD packages over-predict the turbulence energy at the tail of axisymmetric bodies [46].

The Engineering Sciences Data Unit (ESDU) provides an useful reference for axisymmetric body shapes described by analytical equations [57]. For selected body shapes, the ESDU 79020 [58] presents a detailed boundary layer analysis based on the theoretical method developed by Myring [59]. This method leads to a prediction of the drag at sub-critical Mach numbers which is reported in the ESDU 78019 [60].

At non-zero incidence, most of the available literature is focused on the study of the flowfield around a prolate spheroid geometry. Chesnakas *et al.* performed Laser Doppler Velocimetry measurements around a 6:1 prolate spheroid at high incidences [48]. This work investigated the onset of cross-flow separation which generates primary and secondary vortical structures on the leeward side of the body. Numerical work on similar geometry and flow conditions was carried out by Xiao *et al.* [47]

Even though the available open literature on the low-speed aerodynamics of axisymmetric bodies is vast, a consistent and complete experimental data set is missing. Such data set should ideally be comprehensive of forces and flowfield data on a single geometry in well-defined flow conditions that could be used as benchmark for a thorough CFD validation.

In this chapter, the aerodynamic performance of an axisymmetric body representative of a conventional aircraft fuselage are further investigated through numerical and experimental analysis. This study set as a foundation for the subsequent investigation of the aft-fuselage BLI configuration. During the experiments, carried out in the Open-Jet wind-tunnel facility of Delft University Technology, aerodynamic forces and moments, surface pressure distributions and velocity fields were measured for a wide range of incidence angles. At zero incidence the integral boundary layer properties were inferred from Particle-Image Velocimetry measurements at the tail and near-wake regions of the model. The experimental dataset was used to validate a numerical simulation of the isolated fuselage body. The results of the validation of the RANS-based CFD simulation is also discussed hereafter. Particular attention is given to the capability of the simulation setup to represent the development of the turbulent boundary layer around the aft section of the fuselage.

3.2. METHODOLOGY

3.2.1. EXPERIMENTAL SETUP

WIND TUNNEL FACILITY AND MODEL

The experiments were performed in the Open Jet Facility (OJF) of Delft University of Technology. The OJF is a closed-circuit open-jet wind tunnel capable of a maximum test velocity of 30 m/s. It features an octagonal outlet which measures 2.85 m in width and height. The test hall measures 13.5 m in length, with a height of 6.5 m and a width of 6.0 m. In a vertical plane at two meters from the outlet, the freestream turbulence intensity level is lower than 0.24% and the velocity deviations are smaller than 0.5%. The model consisted of an axisymmetric body representative of a conventional aircraft fuselage, as shown in Figs 3.1 and 3.2.

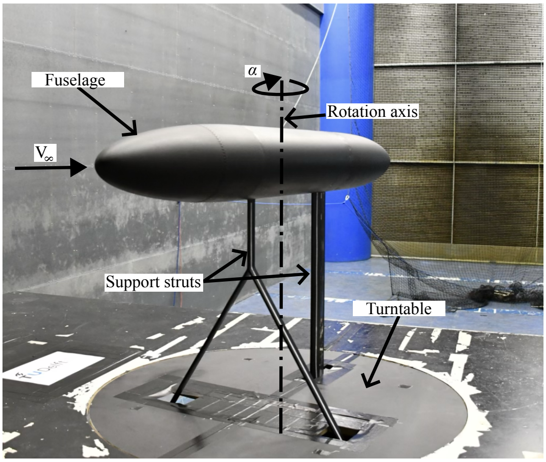

Figure 3.1: Overview of the experimental setup.

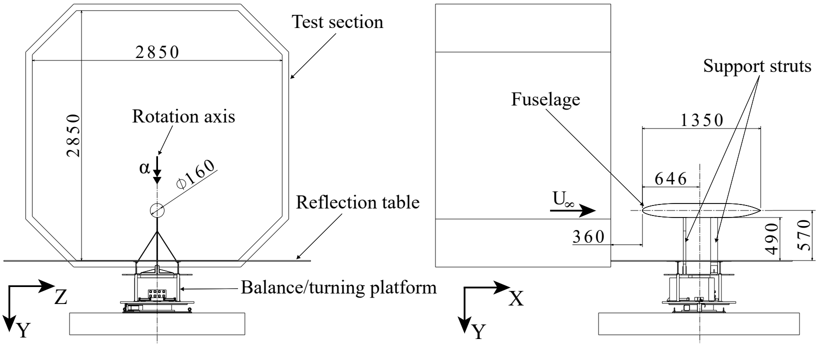

Figure 3.2: Details of the experimental setup. Dimensions in millimetres.

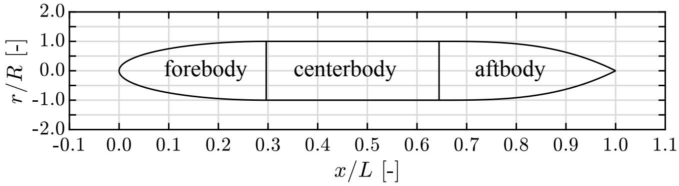

Figure 3.3: Body geometry.

Table 3.1: ESDU body parameters

	l/L	C_S	C_V
Forebody	0.296	0.799	0.667
Afterbody	0.356	0.759	0.643

The axisymmetric fuselage model featured a length $L = 1350$ mm and a maximum diameter $D = 160$ mm, with a resultant overall fineness ratio $f = L/D = 8.44$. The body geometry was obtained by combining together with a central cylindrical section two forebody and aftbody sections from the ESDU data [57].

The forebody section had a length $l_f = 400$ mm and was shaped as an ellipsoid (Body no. 6 with $n = 1/2$), while the aftbody section had a length $l_a = 480$ mm and shaped as Myring cubic (Body no. 9 with $A = 3/2$) [57]. Turbulent transition was fixed at 20 % of the fuselage length from the nose through the application of a 60° zig-zag turbolator tape with a thickness of 0.32 mm and a width of 12 mm. A detailed view of the body is presented in Figure 3.3 while Table 3.1 summarizes the main geometrical parameters. In the table, C_S is the surface area coefficient, $C_S = S/(\pi D l)$, and C_V is the volume coefficient, $C_V = 4V/(\pi D^2 L)$, where S and V are, respectively, the wetted surface area and internal volume of each body section.

The model was connected to the external six-axis balance through two separated struts connected to the cylindrical body. The front strut consisted of a reversed Y-beam with an angle of approximately 60°. The section featured an elliptical leading edge and a sharp trailing edge to reduce the aerodynamic interference with the model. The chord was 30 mm with a maximum thickness of 6 mm. The rear strut featured a NACA 0015 section with a chord of 80 mm and an exposed span of 490 mm. The flow on the struts was also tripped with a 60° zig-zag turbolator tape, with a thickness of 0.405 mm and a width of 6 mm at 20 % of the respective chords.

The model and the balance were then mounted on a rotating platform, which allowed angular movement of the entire setup to simulate an incidence angle. A reflection plane was used to confine the jet expansion and to avoid flow impinging on the balance and on the lower part of the struts. The reflection plane was aligned with the lower edge of the outlet.

MEASUREMENT TECHNIQUES

The flowfield around an fuselage body was investigated with mainly three different measurement techniques to characterize the fowfield with different level of detail.

The three components of the resultant aerodynamic force and moment acting on the entire fuselage were measured with the external balance at different incidence angles. As shown in Figure 3.2, the balance readings contained the effect of the aerodynamic forces and moments acting on both the fuselage surface and on the exposed support struts. The net values of the forces and moments acting on the fuselage were obtained by performing balance measurements with the fuselage body removed from the setup. No sting-interference measurements (e.g. with the use of a dummy sting) were done, therefore the above-mentioned tare procedure did not take into account the interference drag contri-

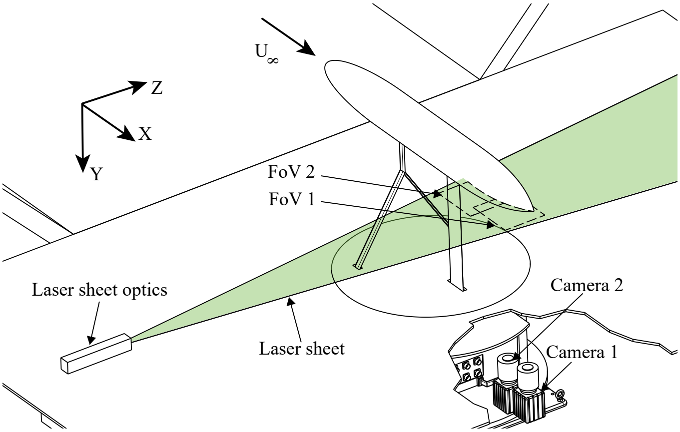

Figure 3.4: Particle Image Velocimetry setup.

bution. The measured struts-only forces and moments were subsequently subtracted from the overall readings. For each measurement point, the raw signal was sampled at 2 kHz for a period of 30 s, after which measurements were obtained by time-averaging the raw signal. In order to minimize the effect of any time-dependent drift in the readings, the angles of attack sequence was randomized to a different sequence for each run. Furthermore, the measurements were repeated in different times and conditions to estimate the random error and repeatability of the procedures. The results of the different runs were consequently averaged and the uncertainty was estimated as 95%-confidence level based on a Student's T distribution.

Any residual misalignment in the imposed geometric angle of attack α_{geom} were corrected by using the fuselage lift and drag polars. The bias was obtained by finding the value of the geometric angle for which zero lift and minimum drag were measured. This bias, $\Delta\alpha_{geom} = 0.15°$, was then applied to the geometric angle to obtain the aerodynamic angle of attack α.

The aftbody section was instrumented with pressure taps with which the surface static pressure distribution was measured for various angles of attack. The pressure taps were placed at a single azimuthal position ranging in the axial direction from 67.0 % to 99.3 % of the fuselage length. The aft-cone was rotated around the fuselage axis in steps of 15° to obtain the complete surface pressure distribution at each measured angle of attack. The symmetry of the distribution was confirmed for selected cases, after which the measurements were only carried out for a limited angular sector of 90° and subsequently mirrored to ease visualization. All the pressure readings were measured simultaneously at 2 kHz for 30 s using an electronic pressure scanner, and averaged over time to obtain each data point.

Planar Particle Image Velocimetry (PIV) was used to measure the boundary-layer and near-wake flow around the aftbody of the model. The PIV setup is shown in Figure 3.4.

Two LaVision Imager sCMOS cameras were used in a parallel planar setup. These cameras feature a 16-bit 2560 px × 2160 px sensor and are capable of acquiring images at a maximum frequency of 50 Hz at full resolution. Two Nikon AF Micro Nikkor 60 mm f/2.8D lenses were used at an aperture of f/5.6. Particle images were acquired and processed independently with the two cameras after which the resulting flowfields were stitched in a unique field. Illumination was provided by a Quantel Evergreen laser. This double-pulse Nd:YAG laser provides 532 nm beams with a repetition rate of 15 Hz at the pulse energy of 200 mJ. Standard coated cylindrical and spherical lenses were used to convey illumination in the desired laser sheet. In order to maximize the pixel displacement in the low-velocity boundary layer, the pulse separation dt was set equal to 45 µs leading to a freestream pixel displacement of 16 px. Image acquisition was done at 10 Hz and synchronized through a LaVision USB Programmable Time Unit. Hardware management, acquisition and processing were done with LaVision DaVis 8.40 software. An iterative multi-pass correlation algorithm with decreasing interrogation window size was used [61]. In the final pass an adaptive window weighting function was used [62]. The uncertainty ϵ' of the correlation for each image sample was estimated with the method developed by Wieneke [63]. The uncertainty values for the ensemble-average flowfields were obtained by averaging out the instantaneous uncertainty fields. Additionally, the standard deviation σ of the average flowfields was computed during the average operation. The maximum standard deviation in the field was used to estimate the two-sided 95%-confidence interval ϵ assuming Student's T distribution. The maximum values of ϵ' and ϵ obtained for each velocity components and the velocity magnitude are reported in the Table 3.2 for the zero-incidence case. It must be noted that the confidence interval ϵ is higher than the uncertainty ϵ' due to the fact that the standard deviation of the velocity is not entirely linked to measurement errors. In fact also natural velocity fluctuations due to turbulence are contributing to the standard deviation and, therefore, indirectly taken into account in the confidence interval estimation.

TEST CASES

Forces and pressure measurements were taken at a freestream velocity of 30 m/s with an incidence angle ranging from $-15°$ to $15°$. PIV measurements were only taken at the selected incidences of $0°$, $3°$, $6°$, $9°$ and $12°$. For each of these cases, measurements were also carried out at the respective negative angles and subsequently combined together to obtain a complete field of view around the fuselage aftbody.

3.2.2. NUMERICAL SETUP

The experimental dataset was used to validate a numerical simulation of the model at zero-incidence conditions. Reynolds Averaged Navier-Stokes (RANS) equations were solved with ANSYS Fluent R19.1 commercial fluid-dynamics package.

The flow was simulated in a computational domain consisting of a C-shaped volume around the body. Exploiting the symmetry of the setup, only half volume was considered to reduce computational power. The domain extended 15 body lengths upstream and in the lateral direction from the center of the fuselage body, while the downstream extension was increased to 20 body lengths. The domain was split into a laminar and turbulent zone, to mimic the transition point of the wind-tunnel model. The mesh was refined locally at the transition location to assure numerical transition to turbulent flow. A sketch of the computational domain is presented in Figure 3.5.

A structured hexahedral mesh was constructed with ANSYS ICEM. The mesh on the

Table 3.2: Summary of the main parameters of the Particle Image Velocimetry setup.

Parameter	Camera 1	Camera 2
Imaging		
Focal length [mm]	60	60
Aperture	f/5.6	f/5.6
Digital resolution [px/mm]	12.08	12.20
Field of view [mm x mm]	213.1 × 180.0	210.5 × 176.0
Acquisition		
Pulse delay [µs]	45	
Freestream pixel shift [px]	16	
Number of image pairs	1000	
Acquisition rate [Hz]	10	
Processing		
Starting interrogation window [px x px]	64 x 64	
Starting overlap factor [%]	50	
Starting window shape	2:1 ellipse	
Final interrogation window [px x px]	12 x 12	
Final overlap factor [%]	75	
Final window shape	Adaptive	
Spatial resolution [mm]	0.246	
Uncertainty		
X-component uncertainty ϵ'_u / V_∞ [%]	0.17	
Y-component uncertainty ϵ'_v / V_∞ [%]	0.12	
Velocity uncertainty ϵ'_V / V_∞ [%]	0.21	
X-component confidence interval ϵ_u / V_∞ [%]	0.34	
Y-component confidence interval ϵ_v / V_∞ [%]	0.24	
Velocity confidence interval ϵ_V / V_∞ [%]	0.33	

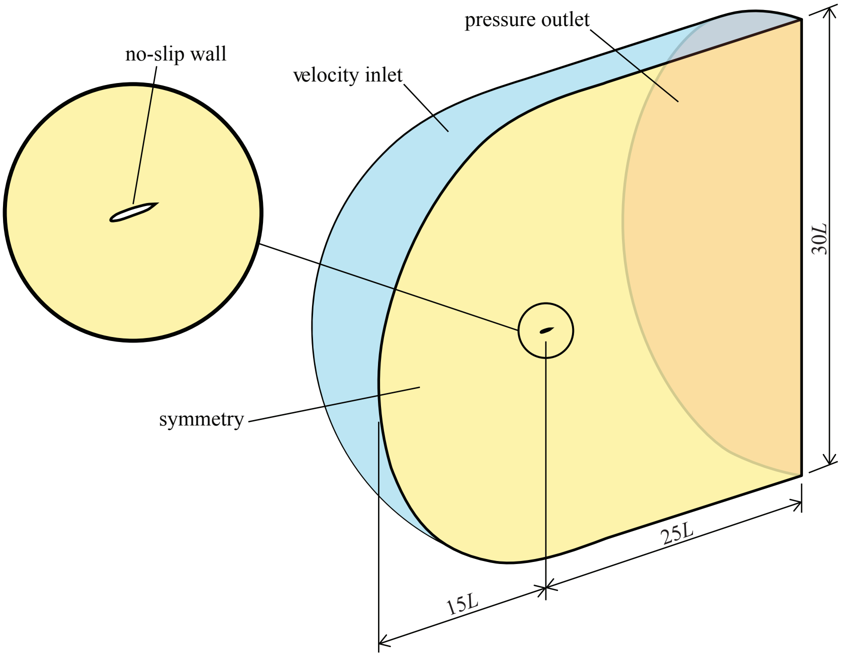

Figure 3.5: Computational domain and boundary conditions of the CFD setup.

body counted 450 divisions non-uniformly distributed along the axis with an angular resolution of 2.25°. The final 3D mesh used for the simulations counted 880,000 cells.

A pressure-based, coupled, pseudo-transient RANS solver scheme was used. Different discretization schemes were used for the governing equations: the second-order upwind scheme was used for the pressure, the third-order MUSCL scheme was selected for the momentum equations and, finally, the QUICK scheme was used for the turbulence equations.

The fluid was modeled as ideal-gas air while the three-coefficients Sutherland's law was used to model the dynamic viscosity. Turbulence was modeled with two Linear Eddy Viscosity Models, namely the one-equation model developed by Spalart and Allmaras (SA) [64] and the Shear Stress Transport model by Menter (SST) [65]. The mesh was tailored to obtain a $y^+ < 1$ over the whole fuselage surface. As a consequence, the boundary-layer flow was directly resolved up to the wall. Moreover, the y^+ was optimized for the respective turbulence model. Operating conditions were set as ISA+10 at sea level to match the experiments conditions. Inlet turbulence intensity was set to 0.1% with a turbulent viscosity ratio of 3. Velocity inlet and pressure outlet boundary conditions were used on the domain boundaries together with a symmetry condition on the symmetry plane, as sketched in Figure 3.5.

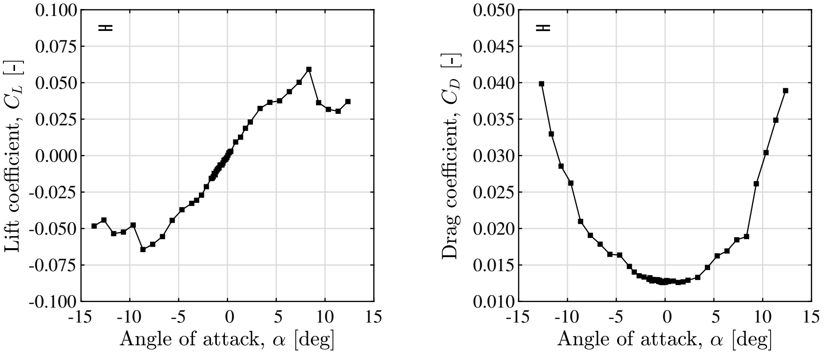

(a) Lift coefficient.

(b) Drag coefficient.

Figure 3.6: Fuselage lift and drag coefficients against the incidence angle. Measurements performed at a freestream velocity of 30 m/s and a Reynolds number of 2.5×10^6.

3.3. RESULTS

3.3.1. AERODYNAMIC CHARACTERISTICS

The raw aerodynamic forces measured through the external balance were scaled on the free-stream dynamic pressure $q_\infty = \frac{1}{2}\rho_\infty {V_\infty}^2$ and the fuselage planform area S_p to obtain the corresponding force coefficients. No corrections were applied to account for the model blockage and streamline curvature. This was justified by the consideration that the blockage effects in open test sections are small and the ratio between the model and tunnel cross-section is very low (around 0.2%) [66]. Moreover, the effect of the lower wall is neglected since the distance between the body surface and the wall is around $3D$.

Figure 3.6 presents the variation of fuselage lift and drag coefficients against the angle of attack for a fixed freestream velocity $V_\infty = 30\,\text{m/s}$ and a corresponding Reynolds number $Re_L = 2.5 \times 10^6$. The average two-sided Student's T 95%-confidence intervals are $\epsilon_{C_L} = 0.0014$ and $\epsilon_{C_D} = 0.0003$ for the lift and drag coefficient respectively. The confidence levels are also reported as error bars in the top-right corner of the respective plots.

The fuselage lift coefficient C_L, shown in Figure 3.6a, features a behaviour that can be divided in four parts: 1) a linear part for small incidence angles ($0° \leq \alpha < 4°$) where the lift coefficient C_L increases linearly with the angle of attack α. In this range the flow is predominantly attached to the body surface; 2) a non-linear region for $4° \leq \alpha < 8°$. In this range, an increased (closed) flow separation region is expected around the aftbody section in agreement with the flow topology study of Refs. [45, 67, 68]. 3) for incidences higher than 8° a steep drop in the C_L is found. This is likely due to the transition to an "open" flow separation and the detachment of a free-vortex layer from the body surface (see again Refs. [45, 67, 68]). It must be noted that the drop in lift found in the current experiment was not predicted by the CFD calculations of Ref. [67].

Given the symmetry in the geometry and flow conditions, the lift curve shows a symmetry about the origin. However, in the region across the stall, the positive and negative parts of the curve show some quantitative differences even though the qualitative trend is maintained. In particular a difference of around 8% is found in the maximum C_L.

Table 3.3: Comparison of the measured and predicted values for C_{D_0}.

Method X_{tr}/L	Experiment 0.20	CFD (SA) 0.20	CFD (SST) 0.20	CFD (SST) 0.00	ESDU 0.15	ESDU 0.01
C_{D_0}	0.0126 ± 0.0003	0.0119	0.0112	0.0124	0.0119	0.0126

Moreover, in the post-stall region the right-handed part of the lift curve shows a trend with a monotonic curvature which is not replicated by the left-handed part of the curve, which features a change in curvature at around $\alpha = 10°$. This difference is thought to be due to a slight asymmetry in the setup (geometry and flow alignment) which may have had critical effects on the separated flow. Furthermore, for $\alpha = -11.5°$, the estimated uncertainty was equal to 0.0155, one order of magnitude higher than the average ϵ_{C_L}, indicating unsatisfactory repeatability at this particular incidence.

The fuselage drag coefficient C_D is plotted against the angle of attack in Figure 3.6b. As for the lift coefficient, the drag curve shows an overall symmetry around the zero-incidence condition. For $-3.5° \leq \alpha \leq 3.5°$ the C_D behaves as a quadratic function of the lift coefficient (and incidence angle) with a minimum drag coefficient C_{D_0} equal to 0.0126. Outside this incidence range the curve moves away form the quadratic model due to the non-linear behaviour of the lift curve and continuously increases in the stall and post-stall regions of the polars.

Table 3.3 also reports the value of C_{D_0} obtained from the measurements and the values obtained with the CFD simulations and ESDU method [60]. The table shows that the drag coefficient estimated with the CFD simulations using the SA and the SST turbulence models differ from the measured drag coefficient of, respectively, 5.5% and 11% when transition was fixed at the same position as in the experiments (20% of the fuselage body). A fully turbulent CFD simulation with the SST turbulence model led to a drag estimation differing 1.5% from the experimental value. The ESDU method leads to similar results. It must be noted that, due to applicable boundaries of the ESDU method, transition location X_{tr} could not be fixed after 15% of the body length. This constraint most probably had an influence on the comparison. In fact, for higher extensions of laminar flow (higher values of X_{tr}) the estimated drag coefficient is lower. C_D values were computed for different transition positions X_{tr} up to $X_{\mathrm{tr}}/L = 0.15$ and used to extrapolate the C_D at the required transition position $X_{\mathrm{tr}}/L = 0.20$. The average between spline and linear extrapolations gives $C_D = 0.0112$, which increases the discrepancy against experimental data to more than 10%. On the contrary, simulating a fully turbulent condition with the ESDU method ($X_{\mathrm{tr}}/L = 1\%$) leads to $C_D = 0.0126$, indicating that the ESDU method is underestimating the drag value for this geometry and flow conditions.

3.3.2. SURFACE PRESSURE FIELD

In order to explain the behavior of the lift and drag force coefficients discussed in the previous Section, the surface pressure distribution contour is plotted for the most relevant measured incidences in Figure 3.7. As described in Section 3.2.1, the surface distribution of the pressure coefficient, $C_p = (p - p_\infty)/q_\infty$, was only measured for an azimuthal angular sector of 90° and the measurements were mirrored about the symmetry plane

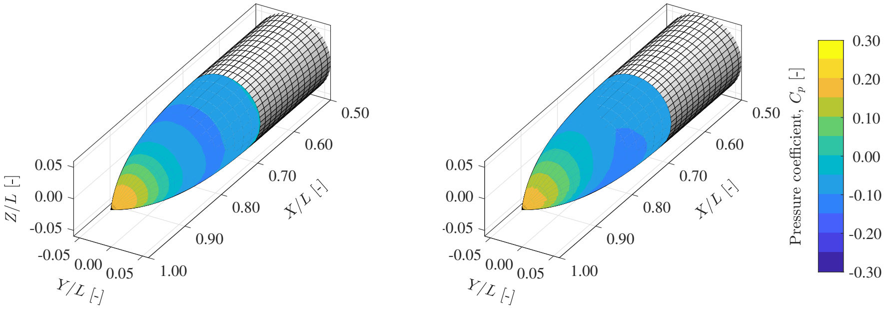

(a) $\alpha = -0.15°$, leeward side (b) $\alpha = 3.85°$, leeward side

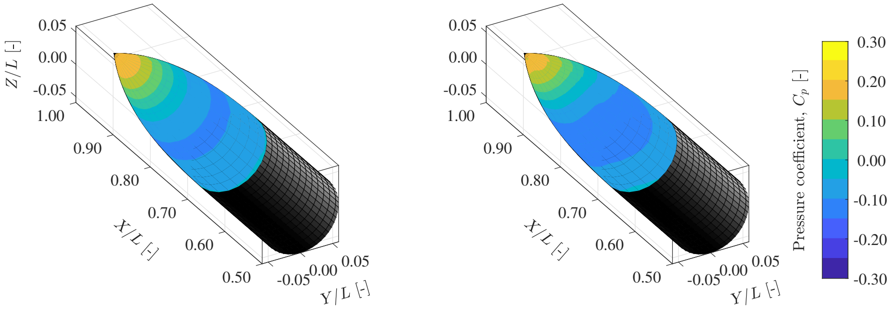

(c) $\alpha = -0.15°$, windward side] (d) $\alpha = 3.85°$, windward side

Figure 3.7: Surface pressure coefficient at various incidence angles. Measurements performed at a freestream velocity of 30 m/s and a Reynolds number of 2.5×10^6. (continued)

to ease visualization.

Figures 3.7a to 3.7d present the surface pressure distribution on the leeward and windward side of the fuselage aftbody for $\alpha = -0.15°$ and $\alpha = 3.85°$. These angles are the closest measured points to, respectively, the axisymmetric inflow condition and the upper edge of the linear region identified in the lift curve of Figure 3.6a. By comparing the zero-incidence case (Fig. 3.7a to 3.7c) to the moderate incidence case (Fig. 3.7b to 3.7d), it can be seen that due to the incidence angle the surface pressure is increased on the leeward side and decreased on the windward side. However, at this moderate incidence no strong changes in the flowfield are observed.

At slightly higher incidences, the pressure distribution strongly deviates from the axisymmetric case as shown in Figures 3.7e and 3.7g for $\alpha = 5.85°$. This is due to the onset of a relatively strong low pressure regions on the windward side of the fuselage centred at around $\phi = 60°$ and $X/L = 0.81$. These low pressure regions are created by the acceleration around the body contour of the crossflow component which is also found in the previous work by Chesnakas *et al.* [48] Further increasing the incidence angle to $\alpha = 8.85°$ (Fig. 3.7f to 3.7h) produces an enlarged low pressure region on the windward side.

At post-stall angles ($\alpha = 11.85°$ and 13.85° of Figures 3.7i to 3.7l) the surface pressure contour shows the appearance of a relatively low pressure bubble on the leeward side at an azimuthal position of around $\phi = 165°$. These low pressure peaks are linked to the onset of two counter-rotating vortical structures on the leeward side of the fuselage. Similar

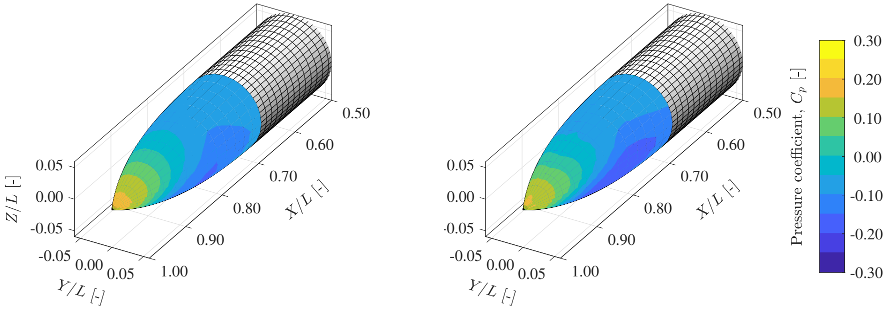

(e) $\alpha = 5.85°$, leeward side

(f) $\alpha = 8.85°$, leeward side

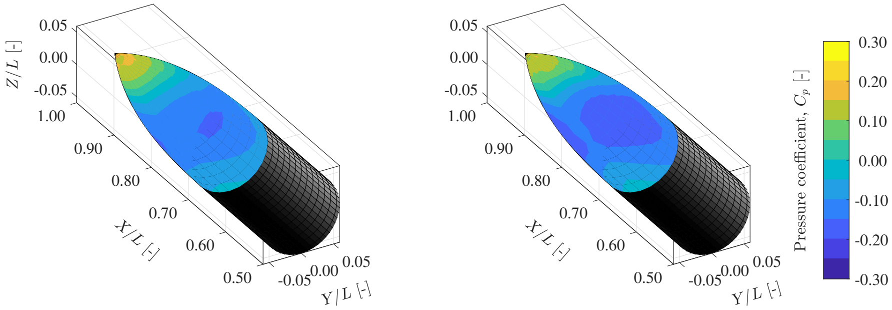

(g) $\alpha = 5.85°$, windward side

(h) $\alpha = 8.85°$, windward side

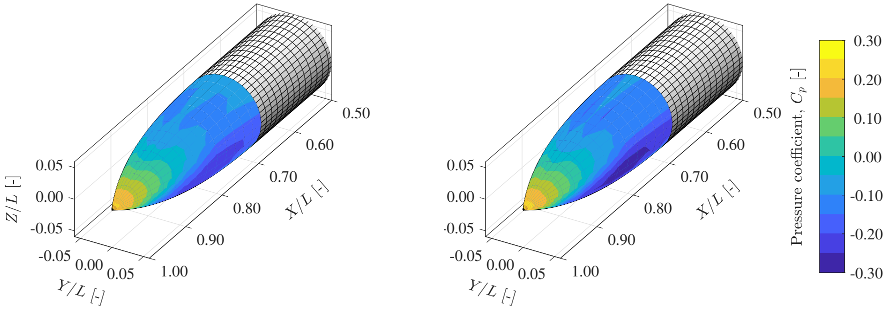

(i) $\alpha = 11.85°$, leeward side

(j) $\alpha = 13.85°$, leeward side

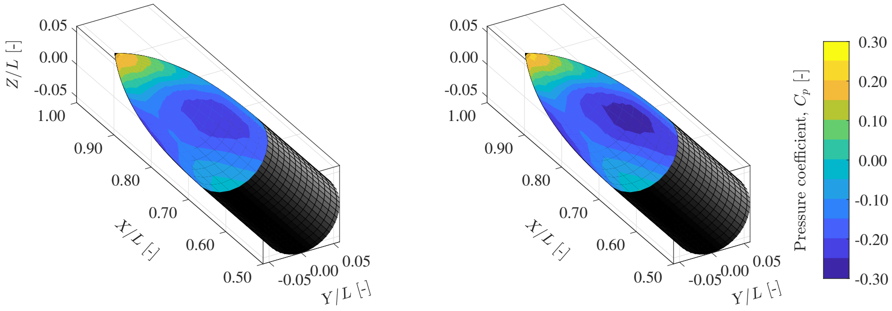

(k) $\alpha = 11.85°$, windward side

(l) $\alpha = 13.85°$, windward side

Figure 3.7: (continued) Surface pressure coefficient at various incidence angles. Measurements performed at a freestream velocity of 30 m/s and a Reynolds number of 2.5×10^6.

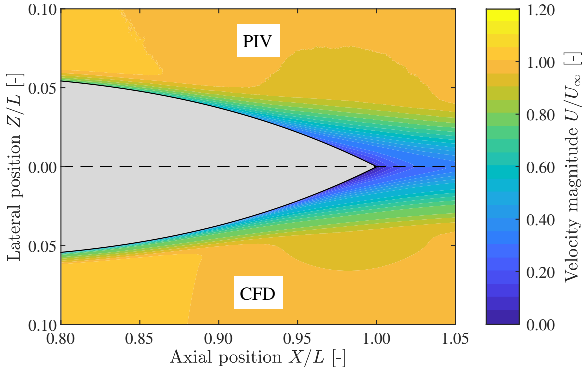

(a) Mean velocity magnitude

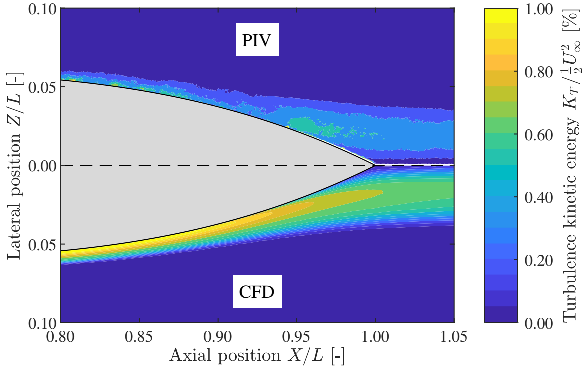

(b) Turbulence kinetic energy

Figure 3.8: Ensemble-average flowfields at $\alpha = -0.15°$. Particle-image velocimetry measurements performed at a freestream velocity of 30 m/s and a Reynolds number of 2.5×10^6. CFD simulation based on the SST turbulence model.

structures were associated with cross-flow separation at the aftbody of the fuselage and experimentally measured on a prolate spheroid at high incidence angles [48]. Consequently to the development of these flow structures, a non-linear behaviour is observed in the lift curve of Figure 3.6a.

3.3.3. BOUNDARY-LAYER FLOW AND ANALYSIS AT ZERO INCIDENCE

Planar Particle Image Velocimetry (PIV) measurements were carried out in the symmetry plane of the fuselage to measure the velocity in the boundary-layer and near-wake flow around the fuselage tail. The ensemble-average velocity and turbulence kinetic energy fields for the axisymmetric flow condition are presented in Figure 3.8. Results obtained with numerical simulations (CFD) based on the SST turbulence model are reported in the same figure.

The PIV velocity field shown on the upper side of Figure 3.8a shows the axial development of the viscous boundary layer on the aftbody surface. At $X/L = 0.8$, where the pressure gradient is still favourable (see Fig. 3.7a and 3.7c), the boundary layer physi-

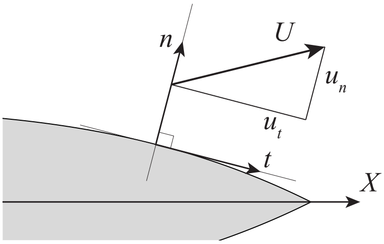

Figure 3.9: Coordinate system based on the local wall-normal direction used for the definition of the boundary layer profiles.

cal thickness δ_{99} is thin compared to the radius of the body. Downstream of this position, as the pressure gradient becomes unfavourable, the boundary layer experiences a substantial and abrupt thickening. The CFD velocity field reported on the lower side of Figure 3.8a shows the same features, confirming that the numerical setup is capable of capturing the main features of the mean flow. In particular, the boundary layer growth in the adverse pressure gradient region is reproduced in the CFD with good agreement with the experimental results.

The turbulence kinetic energy fields obtained from PIV and CFD data are reported in Figure 3.8b as percentage of the freestream kinetic energy. Since the PIV velocity measurements were done with a planar PIV setup, only the two in-plane components of the velocity field were captured. The estimation of the turbulence kinetic energy is corrected for the missing out-of-plane component in the assumption of isotropic turbulence, leading to $K_T = \frac{3}{2}\frac{1}{N}\sum_{i=1}^{N}\frac{1}{2}({u'_X}^2+{u'_Y}^2)$, where u' is the turbulence fluctuation component and N the number of PIV image pairs acquired. Moreover, the estimation of K_T was corrected by subtracting the uncertainty of the measurements ϵ' from the instantaneous PIV fields. As a consequence, the variance of the flow due to the correlation uncertainty and not to turbulence was removed.

The PIV results on the upper side of Figure 3.8b clearly show that turbulence kinetic energy is mainly confined in the viscous, rotational boundary layer flow while the energy level in the outer irrotational flow is negligible. Moreover, the average turbulence kinetic energy in the boundary layer remains constant when moving streamwise along the fuselage. In particular, the peak in the K_T shown by the PIV at $X/L = 0.95$ is thought to be caused by the presence of an irregularity on the surface due to the assembly of two separate pieces. Differently than with the the mean velocity, for the K_T there is a strong mismatch between the experimental and numerical results, which are shown in the bottom part of Figure 3.8b. The CFD simulation based on the SST turbulence model produces a higher turbulence kinetic energy than what was measured in the experiment.

To better evaluate the boundary layer growth and development, boundary layer velocity profiles were extracted from the flowfield and projected into a reference system locally tangent to the body contour, as sketched in Figure 3.9. The wall-tangential and wall-normal boundary layer profiles, u_t and u_n, obtained from experimental and numerical data are presented in Figure 3.10 for different axial stations.

The velocity profiles of Figure 3.10 are representative of a turbulent attached boundary layer. Up to the trailing edge, the tangential velocity u_t features an always positive second order derivative $\partial^2 u_t/\partial s^2$, which indicates that the boundary layer is not close to trailing edge separation. It should be noted that due to the laser reflection onto the fuse-

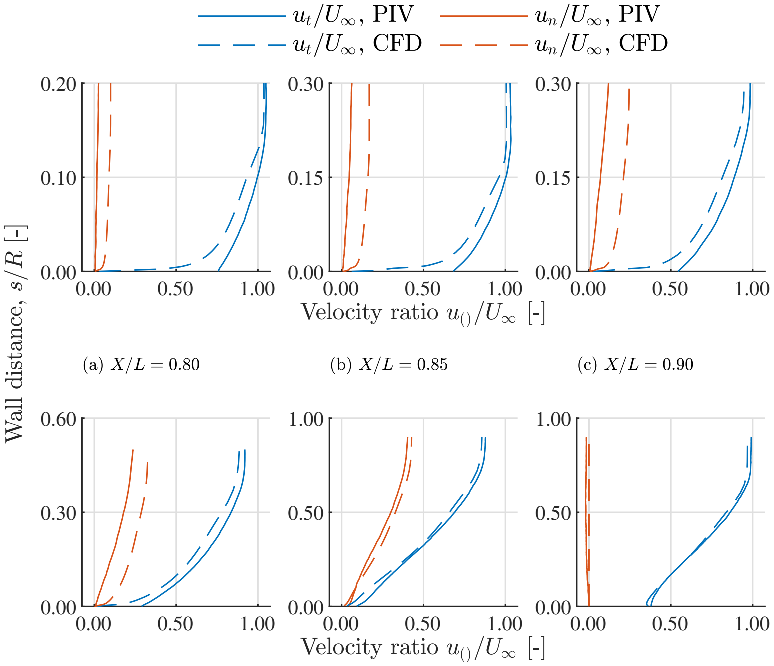

(a) $X/L = 0.80$ (b) $X/L = 0.85$ (c) $X/L = 0.90$

(d) $X/L = 0.95$ (e) $X/L = 1.00$ (f) $X/L = 1.05$

Figure 3.10: Boundary-layer velocity profiles at $\alpha = -0.15°$. Particle-image velocimetry measurements performed at a freestream velocity of 30 m/s and a Reynolds number of 2.5×10^6. CFD simulation based on the SST turbulence model.

lage surface and to the finite resolution of the PIV vector field, velocity data are missing in the immediate proximity of the wall. This is the reason why in the plots of Figure 3.10, the tangential velocity u_t does not reach 0 at the wall.

Figure 3.10a shows again in a quantitative manner that when the pressure gradient is favourable, the boundary layer thickness δ_{99} remains small ($\delta_{99}/R \approx 0.13$), whereas it increases rapidly under the adverse pressure gradient (for $X/L > 0.80$, Figures 3.10b to 3.10e). The thickening of the boundary layer is accompanied by the onset of the wall-normal component u_n. It can be seen in Figure 3.10e that the u_n velocity component is negligible for $X/L < 0.80$. In the contracting part of the aftbody the wall-normal component gradually increases and peaks at the trailing edge (Figure 3.10e), where, at the boundary layer edge, $u_n/u_t = 0.46$.

The velocity profiles of Figure 3.10 also provide the opportunity for a deeper quantitative comparison of numerical and experimental results. Overall, good agreement between the PIV and CFD results is found. However, a non-negligible difference in the numerical and experimental velocity profiles is found in the region where the boundary layer is thin and starts growing under the action of the pressure gradient (Figure 3.10a to 3.10c). In fact, for $X/L < 0.95$, the CFD predicts a higher tangential momentum deficit in the part of the boundary layer closer to the fuselage surface. This produces an higher normal component, as a consequence of mass continuity. On the other hand, close to the trailing edge and in the near wake, the agreement between the measurements and the numerical predictions is satisfactory.

Additionally, turbulence kinetic energy profiles were also extracted from the experimental and numerical fields (Fig. 3.8b) and plotted against the wall distance in Figure 3.11.

The measured turbulence kinetic energy profiles show that in the region where the boundary layer is relatively thin ($X/L \leq 0.90$, Fig. 3.11a to 3.11c) K_T reaches its maximum value very close to the wall and rapidly decreases moving away from the wall. On the other hand, as the boundary layer rapidly thickens ($X/L \geq 0.95$, Fig. 3.11d to 3.11e) the peak in K_T displaces toward the center of the boundary layer and the maximum value continuously decreases moving downstream. This might be caused by the onset of the normal-wall velocity component (see Figure 3.10) which leads to the convection of flow from the wall to the center of the boundary layer. Turbulence kinetic energy profiles obtained with the CFD simulation based on the SST turbulence model are also reported in Figure 3.11. Comparing these profiles to the measured data highlights again the critical difference in the prediction of turbulence quantities of the CFD simulation. However, qualitative trends are captured consistently with the CFD.

Finally, the velocity profiles presented in Figure 3.10 were used to estimate the integral boundary-layer properties along the fuselage axis. The boundary layer properties were defined as for classic planar boundary layer analysis [69], also in accordance with the method reported by ESDU [58]. In particular, the displacement thickness δ^*, momentum thickness θ^*, kinetic energy thickness κ^* and the shape factor H were estimated. Figure 3.12 shows the variation of the boundary layer integral parameters against the axial position. Results obtained from experimental PIV data and numerical CFD data are compared.

At a fixed axial station X, defining the boundary layer edge $\delta_{99}(X)$ was necessary to

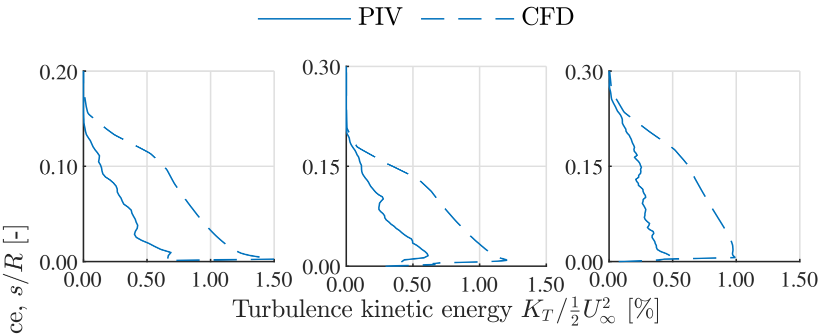

(a) $X/L = 0.80$

(b) $X/L = 0.85$

(c) $X/L = 0.90$

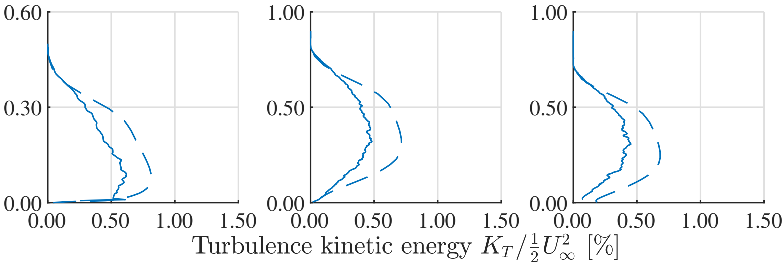

(d) $X/L = 0.95$

(e) $X/L = 1.00$

(f) $X/L = 1.05$

Figure 3.11: Boundary-layer turbulence kinetic-energy profiles at $\alpha = -0.15°$. Particle-image velocimetry measurements performed at a freestream velocity of 30 m/s and a Reynolds number of 2.5×10^6. CFD simulation based on the SST turbulence model.

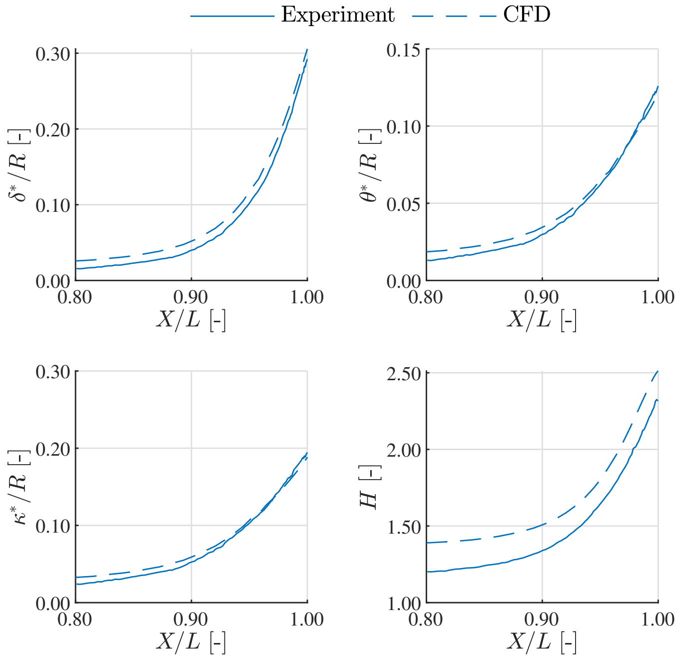

Figure 3.12: Integral boundary-layer properties at $\alpha = -0.15°$.

calculate the integral parameters at that station. Due to the potential flowfield generated by the presence of the body, the boundary-layer edge velocity $U_e(X)$ was in general different from the freestream velocity V_∞ and not known *a priori*. As a consequence, the conventional definition of the boundary-layer edge $\delta_{99}(X)$ for which $u_t(X, n = \delta_{99}) = 0.99U_e(X)$ was not applicable for the PIV experimental data. Therefore, the boundary-layer edge was defined as the wall-distance value at which the first-order derivative of the tangential velocity profile was two orders of magnitude higher than the measured slope at the wall. In other words, the boundary layer edge δ_{99} was located at the point where $\left.\frac{\partial u_t}{\partial n}\right|_{n=\delta} = 10^2 \cdot \left.\frac{\partial u_t}{\partial n}\right|_{n=0}$. Changing the value of the proportionality factor above 10^2 did not influence noticeably the final results. For the post-processing of CFD data, a different approach was used instead. Since total-pressure data were also available, at a given station the boundary-layer edge δ_{99} was defined as the wall-distance at which $\frac{p_t - p_\infty}{p_{t,\infty} - p_\infty} = 0.99$. The two approaches lead to a difference in the estimation of the boundary-layer edge of less than 2% at the fuselage trailing edge. As it can be seen from Figure 3.12, all reported quantities (δ^*, θ^*, κ^* and H) show similar trends, continuously increasing along the aftbody toward the trailing edge ($X/L = 1$). Moreover, the qualitative trends captured by the CFD simulation are in good agreement with the experimental results. However, from a quantitative point of view, important differences between the numerical and experimental curves exist. The displacement, momentum and kinetic-energy thicknesses (respectively δ^*, θ and κ^*) show similar behaviour when comparing numerical and experimental results. In fact, the difference between the two methods is non-negligible in the adverse pressure gradient region (from $X/L = 0.80$ to $X/L = 0.95$) while good agreement is obtained at the trailing edge region (toward $X/L = 1$). The fact that CFD predictions of displacement, momentum and kinetic energy thicknesses are higher than what measured is consistent with the velocity profiles reported in Figure 3.10 as CFD predicts profiles with higher momentum deficit close to the wall. Similar conclusions are drawn for the shape factor H, for which the maximum difference is found at $X/L = 0.8$ and decreases toward the trailing edge.

3.4. CONCLUSIONS

This Chapter presented the results of an experimental investigation of the low-speed flow around a conventional axisymmetric body shape representative of an aircraft fuselage. The results of the experiment represent a valuable data set on the low-speed aerodynamics of axisymmetric bodies at an incidence. The data set is comprehensive and consists of overall forces measurements, surface pressure measurements and flowfield (PIV) data. It therefore offers an interesting benchmark case for validation of numerical analysis tools.

Forces and surface-pressure measurements were taken at a wide range of incidence angles. Lift and drag polars of the fuselage show a non-linear behavior already at moderate angles ($3.5° < \alpha < 5.5°$). Surface static-pressure measurements indicate that at these angles the non-linearity in the forces was induced by the cross-flow component that created a relatively low-pressure region on the leeward side of the fuselage tail. Moreover, forces measurements show an abrupt stall behavior at around $\alpha = 9°$, after which lift coefficient features a non-linear post-stall. This is linked to the onset of cross-flow separation which causes counter-rotating vortical structures on the windward side of the aftbody, as demonstrated by surface pressure measurements.

Particle Image Velocimetry measurements were performed to capture the in-plane velocity components in the symmetry plane around the aftbody and in the near wake of the fuselage. PIV results at zero-incidence show the development of the boundary layer that thickens substantially in the adverse pressure-gradient region, deviating from a comparable planar boundary layer. This is confirmed by the results of a PIV-based boundary-layer analysis.

Finally, numerical results obtained from a RANS CFD simulation were compared to the experimental data. Numerical and experimental results show good agreement for the drag estimation. However, some discrepancy is found in the prediction of the boundary layer characteristics and especially in the turbulence kinetic energy.

As illustrated in chapter 2, the investigations presented in this thesis started off with the baseline case of an isolated axisymmetric body. The study presented in this chapter provided insight into the flow development around the aft-section of an axisymmetric body in isolated conditions (i.e. without an integrated BLI propulsor) and at different incidence angles. This chapter provides fundamental understanding of the baseline flowfield on which the effect of a BLI propulsor will be super-imposed. The aerodynamics of a fuselage body with an integrated BLI propulsor will be discussed in the next chapters.

4

AERODYNAMICS OF AN AXISYMMETRIC PROPULSIVE FUSELAGE AT ZERO INCIDENCE

4.1. INTRODUCTION

As explained in Chapter 1, the experimental analysis of a fuselage-BLI aircraft configuration was approached with an increasing level of complexity. After having analysed the fundamental aerodynamics of an isolated axisymmetric body in Chapter 3, this chapter discusses the aerodynamic performance of an axisymmetric body with an integrated boundary-layer-ingesting propulsor.

In the last decade, BLI has been utilized in numerous aircraft design studies to the aim of reducing the fuel consumption of future aircraft vehicles. Experimental and numerical studies estimated a power benefit of the order of 5-10% due to BLI [31, 33, 34, 70]. However, as already discussed in Chapter 1, different trade-off studies indicate the Propulsive Fuselage Concept (PFC) as possibly the most promising BLI design [16, 27].

Despite the great attention that BLI and the PFC in particular have had in the recent scientific research, the aerodynamic mechanisms playing a key role in the aerodynamic performance of such configurations requires more detailed studies. In fact, the predicted aero-propulsive benefit of the PFC vastly relies on Computational Fluid Dynamics (CFD) simulations where the BLI propulsor is often implemented through an actuator disk model [16, 29, 71–74]. This model does not capture the effects of the boundary layer inflow on the fan performance, non-uniform blade and disk loading and of the swirl in the propulsor slipstream. Previous experimental studies on the interaction between an axisymmetric fuselage and a downstream propeller focused on the wake-ingestion case,

---

Contents of this chapter have been published in:
Della Corte, B., van Sluis, M., Gangoli Rao, A., and Veldhuis, L. L. M., "Power Balance Analysis Experiments on an Axisymmetric Fuselage with an Integrated Boundary-Layer-Ingesting Fan", *AIAA Journal*, Vol. 59, No. 12, 2021. doi:10.2514/1.C036596.

where the propulsor is placed far downstream of the body to avoid any pressure field interactions [40, 41]. Recently, an experimental work on an axisymmetric-body with BLI proposed a benchmark for numerical modeling but did not investigate the aerodynamic field in great details [75]. Moreover, no examples of experimental implementation of the power balance method on an axisymmetric BLI configuration are present in literature.

In this chapter, wind-tunnel experiments of a simplified PFC configuration featuring an axisymmetric fuselage with a BLI propulsor integrated with the fuselage aft section are discussed. The geometry of the aft fuselage section of the model is based on the PFC configuration proposed within the CENTRELINE project [29]. The shrouded fan was designed to match the aerodynamic performance of the CENTRELINE full-scale fan and the inflow boundary layer properties [28]. The study presented in this chapter separated the main distortion component (i.e. fuselage boundary layer) from the secondary ones (wing and tail wakes), in an effort to obtain a direct measurement of the interaction between the fuselage boundary layer and the BLI fan. The Power Balance Method (see again section 2.4) was applied on flowfield data measured with Particle Image Velocimetry to understand how momentum and mechanical energy were distributed in the boundary layer of the fuselage and how they were affected by the BLI fan setting.

4.2. METHODS

The aim of the work presented is to investigate the fundamental aerodynamics of an axisymmetric BLI-fuselage configuration in symmetric flow conditions. To this end, low-speed wind-tunnel tests were employed to provide the relevant data. Given the scaling limitations, the Reynolds number and Mach number characterizing the wind-tunnel test did not match the expected full-flight scale conditions (corresponding to a Reynolds number based on the fuselage length, Re_{L_b}, of 400×10^6 and a Mach number, M_∞, of 0.82). However, the obtained data are considered relevant for the understanding of the aerodynamics of fuselage-BLI for various reasons. First, the BLI propulsor model was scaled to match the fuselage boundary layer, which is relatively thicker because of the Reynolds number effects (see Sec. 4.2.1). Second, previous work, for example Ref. [76–78], shows that the critical Mach number of axisymmetric bodies at zero incidence angles is higher than the typical commercial aviation cruise Mach number. As a consequence, compressibility effects are not expected to substantially affect the fuselage boundary layer.

4.2.1. WIND-TUNNEL FACILITY AND MODEL

FACILITY

The experiments were carried out at the Low Turbulence Tunnel (LTT) of Delft University of Technology. This facility is an atmospheric, closed-circuit wind tunnel with a closed test section. The freestream turbulence intensity level is about 0.02 % for a freestream velocity within 10 m/s and 40 m/s [79]. The test section features an octagonal cross-section with a width of 1.8 m and a height of 1.25 m.

MODEL SETUP

The tested model features an axisymmetric fuselage equipped with a shrouded fan integrated with the fuselage aft section. Photographs and technical drawings of the setup

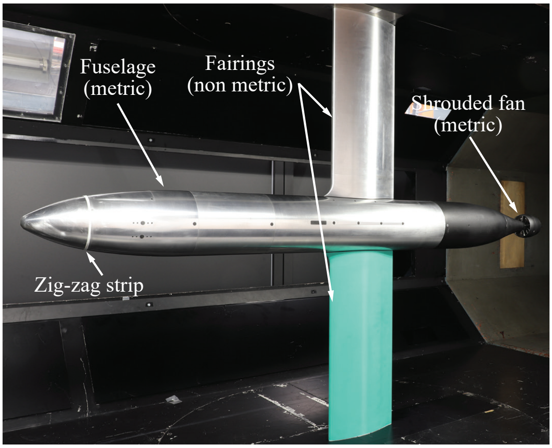

(a) Isometric assembly view.

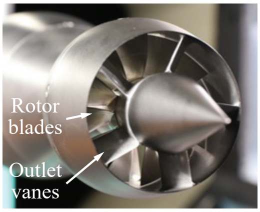

(b) Shrouded fan.

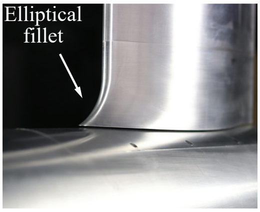

(c) Fairing-fuselage interface.

Figure 4.1: Wind-tunnel model setup used during the experiments in the Low Turbulence Tunnel of Delft University of Technology.

are presented in Fig. 4.1 and Fig. 4.2.

This setup has three main advantages: first, the effects of the fuselage boundary layer could be isolated from those of other inlet distortions sources, such as wing and tail surfaces; second, the fuselage boundary layer would produce, ideally, a purely radial distortion and an uniform blade loading, hence minimizing unsteady phenomena; finally, the forces acting on the fuselage-fan assembly could be directly measured by means of an external 6-component balance. The fuselage and the shrouded fan were connected to the external balance through a support beam, housed inside the fairing on the upper side of the fuselage. A second fairing was mounted at the bottom of the setup to enhance the setup symmetries. The fairings were directly bolted to the test-section walls and a gap of 1 mm ensured no contact with the fuselage model. Hence, only the fuselage and fan assembly were sensed by the external balance. This rendered unnecessary any tare procedure to remove the forces acting on the support structure from the total balance readings.

FUSELAGE MODEL

The axisymmetric fuselage body featured a radius, R_b, of 80 mm (at the central, cylindrical part) and a length, L_b, equal to 1776 mm. A turbulent boundary layer was ensured through zig-zag turbolator tape with a slope of 60°, a thickness of 0.4 mm and width of 12 mm installed at $x/L_b = 5\%$. The effectiveness of the transition strips and the uniformity of the transition behaviour around the entire fuselage contour were checked through the use of a stethoscope. The fuselage aft section could be arranged in two geometrical configurations, the Bare Fuselage (BF) and the Powered Fuselage (PF), sketched in Fig. 4.3. The bare fuselage configuration consisted of the baseline fuselage contour without the shrouded fan, while the powered fuselage configuration was obtained by mounting the shrouded fan onto the bare fuselage. The aft-cone geometry was adapted from the design of the CENTRELINE Propulsive Fuselage Concept (see for example [29]).

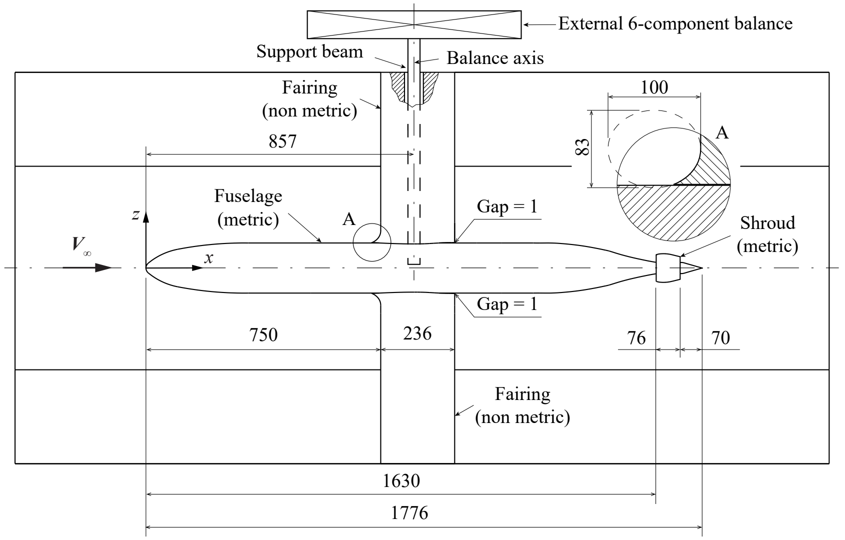

(a) Lateral view.

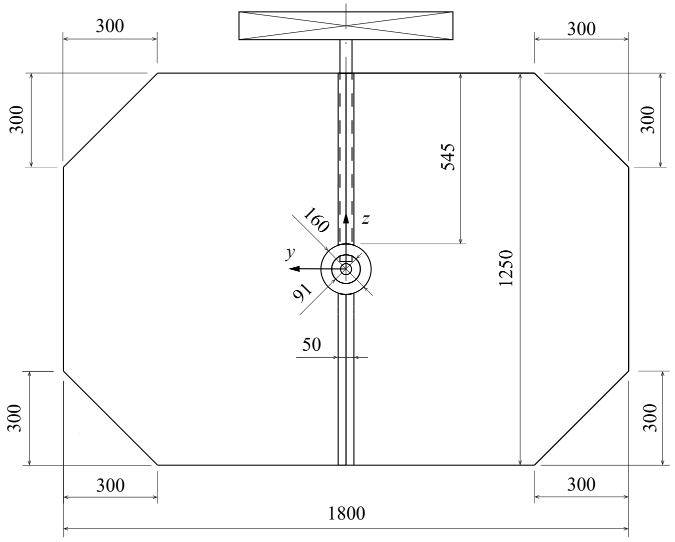

(b) Back view.

Figure 4.2: Technical drawing of the wind-tunnel setup used during the experiments in the Low Turbulence Tunnel of Delft University of Technology. (Dimensions are in mm.)

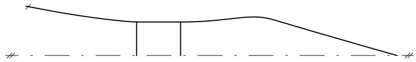

(a) Bare Fuselage (BF).

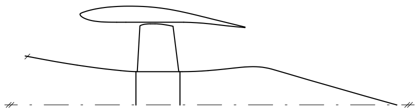

(b) Powered Fuselage (PF).

Figure 4.3: Fuselage aft section geometrical configurations as tested in the wind-tunnel experiments.

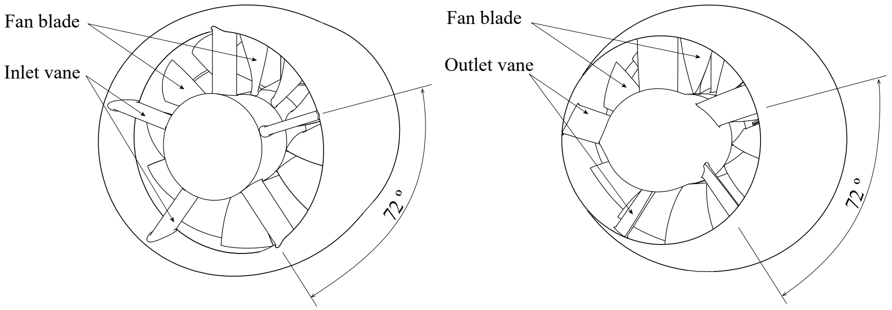

(a) Isometric front view.

(b) Isometric back view.

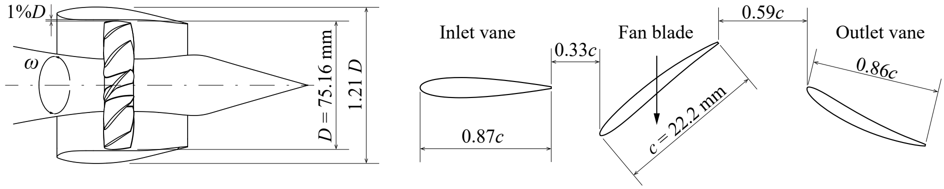

(c) Section view.

(d) Cross-section at 50% span.

Figure 4.4: Detail drawings of the fuselage-mounted shrouded fan.

FAN AND SHROUD MODEL

The powered fuselage aft-cone was equipped with a shrouded fan, of which detail drawings are presented in Fig. 4.4. The fan was driven by a three-phase electric motor, housed inside the fuselage aft section. During the measurements, the fan angular velocity, Ω, was measured through an US Digital© optical encoder mounted on the motor shaft. The fan model featured a 12-bladed rotor with a tip diameter, R_f, of 37.6 mm ($R_f/R_b = 0.47$). The hub radius was equal to 15.4 mm, resulting in a hub-to-tip-radii ratio of 0.41 and a blade height of 22 mm.

The fan was sized to ensure aerodynamic similarity with the full-scale CENTRELINE PFC. Due to the differences in Reynolds and Mach numbers between the wind-tunnel scale and full scale conditions, the boundary layer is expected to be larger relatively to the fuselage in the wind-tunnel test. Therefore, the fan diameter was adapted to the scaled boundary layer thickness to achieve the same ratio of momentum thickness to fan blade height as the full-scale CENTRELINE configuration. The blade geometry was optimized at the same design point of the full-scale fuselage-fan which is installed on the full-scale CENTRELINE PFC [28]. At the wind-tunnel scale, the design point was characterized by a $U_{\text{tip}}/V_\infty = 1.64$, where V_∞ is the freestream velocity and $U_{\text{tip}} = \Omega R_f$ is the fan tip speed. A more detailed discussion of the design procedure can be found in Appendix C.

The shroud contour was adapted from the CENTRELINE design. The tip gap was equal to 0.75 mm (approximately 1 % of the fan tip diameter). The shroud inlet featured five inlet vanes, as shown in Fig. 4.4a. The inlet vanes featured a symmetric airfoil section with a rectangular planform. The vanes had a structural function and were not optimized to de-swirl the flow. Two shroud outlet configurations were tested: 1) one featuring five outlet vanes to which the nozzle plug was mounted (showed in Fig. 4.4b); 2) one without the outlet vanes, in which the nozzle plug was rotating integrally with the fan. The outlet vanes design (airfoil shape and blade geometry) was adapted to the measured swirl angle in the fan slipstream to avoid detrimental effects on the flowfield (e.g. flow separation on the outlet vanes). However, the outlet vanes were not optimized to completely recover the swirl in the fan slipstream.

FAIRING CONFIGURATION

The fairings featured a NACA 66_4-021 airfoil section and a rectangular planform with a chord length of 236 mm. The inboard tip of the fairings featured a curved surface following the fuselage contour. A radial gap of 1 mm was ensured from the fuselage contour to avoid material contact. The inboard tips also featured an elliptical leading edge fillet (see Fig. 4.1) to reduce the distortions introduced in the flow by the fairing. The bottom fairing did not have any structural function and was employed to reduce the effects of the fairings on the flowfield around the fuselage aft section. More details of the fairing design were presented in a previous related work [80].

4.2.2. MEASUREMENT TECHNIQUES

BALANCE MEASUREMENTS

The external six-component balance was used to measure the aerodynamic forces and moments acting on the model. Since the fairings were directly bolted to the wind-tunnel walls and no material contact was allowed between the fairing and the fuselage, only the fuselage model was sensed by the balance. Therefore, the balance readings directly provided the net force acting on the fuselage-fan assembly. The measurements were averaged out over a time of at least 10 s to filter out fluctuations due to turbulence or vibrations. Force coefficients are computed using the freestream dynamic pressure, q_∞, and the fuselage surface frontal area, $S_{\text{ref}} = \pi R_b^2$, as reference values.

To assess the data uncertainty due to various error sources (e.g. random error, variations in ambient and freestream conditions, model surface contamination, turbulence fluctuations etc.) the same measurements were replicated in various runs. A maximum deviation of 0.006 was found for the axial force coefficient C_N, approximately equal to 4% of the bare fuselage drag coefficient C_{D_0}.

Since the focus of the balance measurements was to asses the effect of the BLI propulsor relatively to the bare configuration, wind-tunnel wall and model blockage correc-

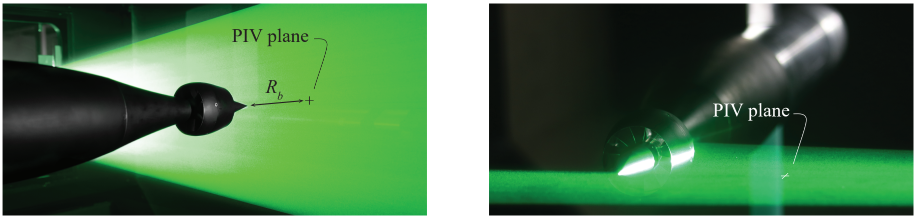

(a) Wake-Plane Field of View (WP-FoV).

(b) Symmetry-Plane Field of View (SP-FoV).

Figure 4.5: Stereoscopic Particle Image Velocimetry measurement setup.

tions were not employed.

PARTICLE IMAGE VELOCIMETRY MEASUREMENTS

Stereoscopic Particle Image Velocimetry (PIV) was used to measure the three velocity components in two different planes, which are shown in Fig. 4.5. Tab. 4.1 summarizes the main parameters of the two PIV setups. The Wake-Plane Field of View (WP-FoV) shown in Fig. 4.5a, was orthogonal to the freestream velocity direction and placed at a distance of $1R_b$ from the fuselage trailing edge (corresponding to $x/L_b = 1.05$). The velocity data measured in this plane were used to obtain a 3-D wake analysis. In addition, the Symmetry-Plane Field of View (SP-FoV) shown in Fig. 4.5b allowed a more detailed analysis of the flow around the fuselage propulsor. The velocity data obtained in the SP-FoV plane were used to analyze the momentum and mechanical energy distribution in the fuselage boundary layer and around the BLI propulsor.

For both planes, two LaVision Imager sCMOS© cameras were used in a stereoscopic setup. These cameras feature a 16-bit 2560 px × 2160 px sensor and have a maximum acquisition frequency of 50 Hz. The cameras were equipped with Nikon 105 mm f/2.8 AF-D Micro Nikkor© lenses and with LaVision Scheimpflug Adapters©. During all the measurements, the aperture was set to f/8. The airflow was seeded with Safex Inside Nebelfluid© and via a Safex Twin Fog© smoke generator. Illumination was provided by a Quantel Evergreen© double-pulse Nd:YAG laser. A laser sheet with a thickness of around 2.5 mm was obtained through standard laser optics.

Images acquisition was controlled via LaVision DaVis 8.4© software and synchronized via a LaVision USB Programmable Time Unit©. The pulse separation was set in order to achieve a freestream particle displacement of around 10 px. For each case, sets of 1000 to 1500 image pairs were recorded at around 10 Hz. In cases with powered fan, the acquisition frequency was set to avoid phase-locking with the fan blades. Post-processing of particle images was also performed in LaVision DaVis 8.4© with an iterative multi-pass correlation algorithm with a decreasing window size [61]. For each case, the instantaneous vector fields were averaged to obtain the ensemble-average velocity measurement. For the SP-FoV case, the PIV setup (laser optics and cameras) was automatically translated in the axial direction thanks to an electronic traversing system. To obtain a sufficient spatial resolution in a large domain, the SP-FOV field was obtained by measuring the velocity in two co-planar domains. The two vector fields were subsequently stitched together.

Table 4.1: Summary of the main parameters of the Particle Image Velocimetry setups.

Parameter	WP-FoV	SP-FoV
Imaging		
Focal length [mm]	105	105
Aperture	f/8	f/8
Digital resolution [px/mm]	12.08	12.20
Acquisition		
Pulse delay [µs]	20	10
Number of image pairs	>1000	1500
Processing		
Interrogation window [px x px]	32 x 32	24 x 24
Overlap factor [%]	50	75
Spatial resolution [mm]	0.25	0.40
Uncertainty		
u component uncertainty ϵ_u/V_∞ [%]	0.5	0.6
v component uncertainty ϵ_v/V_∞ [%]	0.6	0.8
w component uncertainty ϵ_w/V_∞ [%]	0.6	0.9
Velocity magnitude uncertainty ϵ_V/V_∞ [%]	0.9	1.1

The uncertainty of the PIV measurements was estimated for each measured vector during the correlation operation, using a statistical analysis of the image pair correlation results [63]. The uncertainty values for the average flowfield were obtained by averaging out the uncertainty fields of each instantaneous field. The maximum value of the uncertainty on the velocity magnitude and on each of the velocity components is reported in Tab. 3.2. The uncertainty was subtracted from the computation of turbulence statistics like the turbulence kinetic energy.

TOTAL PRESSURE MEASUREMENTS

Total pressure measurements were carried out in the wake of the model using a rake consisting of 44 total-pressure probes. The scanned plane coincided with the WP-FoV PIV plane of Fig. 4.5. The probes were non-evenly distributed with a minimum lateral spacing of 3 mm (equal to 3.75 % of R_b) at the center of the rake. The rake was traversed in the vertical direction with a minimum step size of 0.5 mm (0.625 % of R_b) at the fuselage center and gradually increasing at larger z positions (see Fig. 4.2). At each scanned position, total pressure measurements were acquired with an electronic pressure scanner for a period of 10 s and time-averaged to obtain each single data point. During each measurement, the freestream conditions were measured through a static Pitot probe positioned at the test-section inlet and recorded simultaneously using the same pressure scanner. Each wake-rake measurement was non-dimensionalized with the corresponding freestream values to obtain the total pressure coefficient $C_{p_t} = (p_t - p_{t,\infty})/q_\infty$.

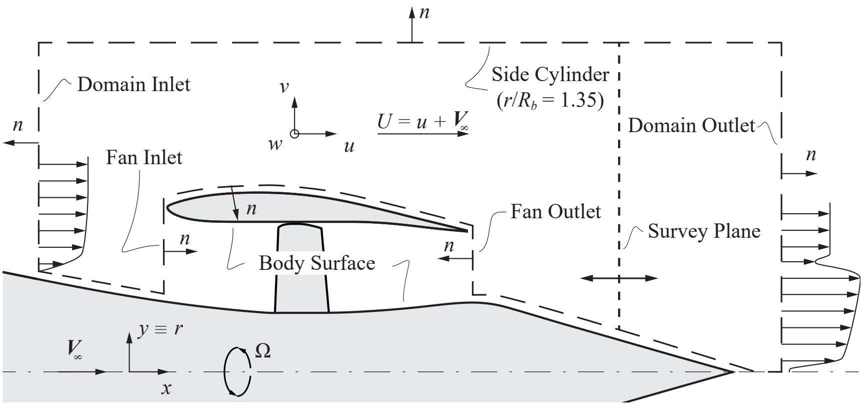

Figure 4.6: Control volume and notations defined for the pressure reconstruction and power analysis.

4.2.3. ANALYZED CASES

All the measurements were taken at symmetric inflow conditions, i.e. for a zero incidence angle. The freestream velocity, V_∞, was varied from 15 m/s to 40 m/s (corresponding to a Reynolds number based on the fuselage length, Re_{L_b}, between 1.7×10^6 and 4.7×10^6 and a freestream Mach number, M_∞, between 0.04 and 0.12) in combination with the fan angular velocity, Ω, to control the operating fan tip speed ratio. In powered conditions, the ratio between the measured net axial force and drag of the bare fuselage was used as independent parameter to characterize the operating condition.

4.2.4. PIV-BASED MOMENTUM AND POWER ANALYSIS

The Power Balance Method (see section 2.4) was applied to the PIV data obtained in the SP-FoV. Fig. 4.6 shows a sketch of the domain and notations defined for the analysis.

PRESSURE RECONSTRUCTION

The static pressure field was inferred from the PIV data by solving the Poisson equation for the pressure (see for example [81] for a review of the method). The general form of the equation is obtained by deriving the pressure gradient in space:

$$\nabla^2 p = \nabla \cdot \nabla p = \nabla \cdot \left(-\rho \frac{\partial \boldsymbol{V}}{\partial t} - \rho \boldsymbol{V} \cdot \nabla \boldsymbol{V} + \mu \nabla^2 \boldsymbol{V} \right) \tag{4.1}$$

The particular formulation used in the current study was obtained from this form by making some simplifying assumptions. First, since only phase-uncorrelated PIV data were used, the flow was assumed to be steady $\left(\frac{\partial}{\partial t} = 0\right)$. Moreover, the flow was assumed incompressible $\left(\rho = \rho_\infty, \nabla \cdot \boldsymbol{V} = 0\right)$. Lastly, the flow was assumed axisymmetric $\left(\frac{\partial}{\partial \theta} = 0\right)$. In cylindrical coordinates, $\{x, r, \theta\}$, the following Poisson equation was obtained (derived from Ref. [82]):

$$
\begin{aligned}
&\frac{\partial^2 p}{\partial x^2}+\frac{\partial^2 p}{\partial r^2}=\\
&-\rho_\infty\left\{\left(\frac{\partial u}{\partial x}\right)^2+2\frac{\partial v}{\partial x}\frac{\partial u}{\partial r}+\left(\frac{\partial v}{\partial r}\right)^2+u\frac{\partial^2 u}{\partial x^2}+v\frac{\partial^2 v}{\partial r^2}+u\frac{\partial^2 v}{\partial r\partial x}+v\frac{\partial^2 u}{\partial x\partial r}-\frac{\partial}{\partial r}\left(\frac{w^2}{r}\right)\right\}+\\
&+\mu_\infty\left\{\frac{\partial}{\partial x}\nabla^2 u+\frac{\partial}{\partial r}\left(\nabla^2 v-\frac{v}{r^2}\right)\right\}.
\end{aligned}
\tag{4.2}
$$

The equation was solved in the domain using the finite-difference method of Ref. [83]. Spatial derivatives were computed with a three-point central scheme. Dirichlet and Neumann conditions were applied at the domain boundaries. At the boundaries in the isentropic flow region, “Side Cylinder” of Fig. 4.6, placed at $r/R_b = 1.35$, the static pressure distribution was computed from the velocity by assuming $p_t = p_{t,\infty}$. At all other boundaries, “Domain Inlet”, “Domain Outlet”, “Fan Inlet”, “Fan Outlet” and “Body Surface” of Fig. 4.6, Neumann conditions were applied. On these boundaries, the static pressure gradient in the boundary-normal direction, n, was obtained from the PIV data. Finally, the total pressure field was calculated from the static pressure and velocity fields using the incompressible Bernoulli’s equation.

The inferred pressure field is affected by a stochastic uncertainty originating from the uncertainty of the PIV data which non-linearly propagates through the numerical process. The uncertainty of the pressure data was estimated by a stochastic Monte Carlo approach, analogously to Ref. [84]. The approach consisted of computing the pressure field from a number of synthetic velocity fields obtained by perturbing the measured PIV data with a pseudo-random uniform error with a magnitude equal to the uncertainty of the PIV data. A convergence statistics was reached in 10000 iterations and the maximum standard error on the C_{p_t} was equal to 0.06.

MOMENTUM AND POWER ANALYSIS

The power analysis of the flowfield followed the definitions and notations of the Power Balance Method [25]. Nevertheless, a brief description of the terms and definition used in the analysis is reported here. The power balance equation can be simplified for the current application and presented in a non-dimensional form:

$$C_{P_k} = C_{\dot{\varepsilon}} + C_\phi \tag{4.3}$$

where C_{P_k}, $C_{\dot{\varepsilon}}$ and C_ϕ are, respectively, the non-dimensional propulsor mechanical power input, total mechanical power outflow and viscous dissipation rate. The coefficients were obtained by normalizing with the factor $q_\infty V_\infty S_{\mathrm{ref}}$. Following Ref. [25], $C_{\dot{\varepsilon}}$ can be defined as:

$$C_{\dot{\varepsilon}} = \frac{1}{S_{\mathrm{ref}}}\int_0^\infty\int_0^{2\pi}\left(\frac{U}{V_\infty}C_{p_t}\right) r\,\mathrm{d}\theta\,\mathrm{d}r \tag{4.4}$$

and decomposed in:

$$C_{\dot{\varepsilon}} = C_{F_x} + C_{\dot{E}} \tag{4.5}$$

where C_{F_x} and $C_{\dot{E}}$ are, respectively, the axial momentum flux and kinetic energy deposition rate coefficients. C_{F_x} and $C_{\dot{E}}$ represent the net axial momentum and kinetic energy fluxes across the Survey Plane of Fig. 4.6.

In particular, the axial momentum flux coefficient C_{F_x}, positive for a thrust excess, was obtained following the approach of Ref. [85]:

$$C_{F_x} = \frac{1}{S_{\text{ref}}} \int_0^{\infty} \int_0^{2\pi} \left(C_{p_t} + \left(\frac{u}{V_\infty}\right)^2 - \left(\frac{v}{V_\infty}\right)^2 - \left(\frac{w}{V_\infty}\right)^2 \right) r \, \mathrm{d}\theta \, \mathrm{d}r \tag{4.6}$$

where u, v and w are the components of the perturbation velocity defined by $(U, V, W) \equiv (u + V_\infty, v, w)$.
The wake blockage effect was taken into account following Ref. [86] for the calculation of the correction ΔC_{F_x}:

$$\Delta C_{F_x} = \frac{1}{S_{\text{ref}}} \frac{u_0}{V_\infty} \int_0^{\infty} \int_0^{2\pi} \left(\frac{U^*}{V_\infty} - \frac{U}{V_\infty} \right) r \, \mathrm{d}\theta \, \mathrm{d}r \tag{4.7}$$

where u_0 is the blockage velocity, defined as:

$$\frac{u_0}{V_\infty} = \frac{1}{2S_{\text{TS}}} \int_0^{\infty} \int_0^{2\pi} \left(\frac{U^*}{V_\infty} - \frac{U}{V_\infty} \right) r \, \mathrm{d}\theta \, \mathrm{d}r \tag{4.8}$$

where S_{TS} is the test-section cross area and U^* is defined by:

$$\left(\frac{U^*}{V_\infty}\right)^2 = \left(\frac{U}{V_\infty}\right)^2 - C_{p_t} \tag{4.9}$$

Similarly, $C_{\dot{E}}$ was decomposed as:

$$C_{\dot{E}} = C_{\dot{E}_a} + C_{\dot{E}_r} + C_{\dot{E}_t} + C_{\dot{E}_p} \tag{4.10}$$

where $C_{\dot{E}_a}$, $C_{\dot{E}_r}$, $C_{\dot{E}_t}$, $C_{\dot{E}_p}$ are respectively the axial, radial and tangential kinetic energy deposition and pressure work rates:

$$C_{\dot{E}_a} = \frac{1}{S_{\text{ref}}} \int_0^{\infty} \int_0^{2\pi} \left(\frac{U}{V_\infty} \frac{\frac{1}{2}u^2}{\frac{1}{2}V_\infty^2} \right) r \, \mathrm{d}\theta \, \mathrm{d}r \tag{4.11}$$

$$C_{\dot{E}_r} = \frac{1}{S_{\text{ref}}} \int_0^{\infty} \int_0^{2\pi} \left(\frac{U}{V_\infty} \frac{\frac{1}{2}v^2}{\frac{1}{2}V_\infty^2} \right) r \, \mathrm{d}\theta \, \mathrm{d}r \tag{4.12}$$

$$C_{\dot{E}_t} = \frac{1}{S_{\text{ref}}} \int_0^{\infty} \int_0^{2\pi} \left(\frac{U}{V_\infty} \frac{\frac{1}{2}w^2}{\frac{1}{2}V_\infty^2} \right) r \, \mathrm{d}\theta \, \mathrm{d}r \tag{4.13}$$

$$C_{\dot{E}_p} = \frac{1}{S_{\text{ref}}} \int_0^{\infty} \int_0^{2\pi} \left(\frac{u}{V_\infty} C_p \right) r \, \mathrm{d}\theta \, \mathrm{d}r \tag{4.14}$$

Finally, the turbulence kinetic energy flux across the survey plane was computed as:

$$C_{\dot{E}_\kappa} = \frac{1}{S_{\text{ref}}} \int_0^{\infty} \int_0^{2\pi} \left(\frac{U}{V_\infty} \frac{\kappa}{V_\infty^2} \right) r \, \mathrm{d}\theta \, \mathrm{d}r \tag{4.15}$$

where κ is the turbulence kinetic energy. κ is computed from the PIV measurements as:

$$\kappa = \frac{1}{2}\left(\sigma_u^2 + \sigma_v^2 + \sigma_w^2 \right) \tag{4.16}$$

where σ_u, σ_v and σ_w are the standard deviations of the velocity components. Any unsteady component of the flowfield also contributes to the estimation of the standard deviation and hence to the turbulence kinetic energy.

4.3. RESULTS

The aerodynamic performance of the PFC configuration are the result of the complex interaction between the fuselage airframe and the aft-fuselage mounted fan. The pressure and velocity field induced by the fan affects the flowfield downstream and upstream of the fan itself. In order to capture the aerodynamic response of the overall configuration and the sub-system interactions, different measurement techniques were used with different objectives. Balance measurements were used to quantify the overall system performance which, in the analyzed cases, are characterized by the net axial force acting on the fuselage-fan assembly. Total pressure and PIV measurements assessed the 3-D time-averaged flowfield in the wake and around the BLI propulsor. These flowfield data served to quantify the momentum and power distribution around the fan and in the near wake.

4.3.1. CONFIGURATION PERFORMANCE

Balance measurements were performed for a range of fan operating conditions, defined by the fan tip speed ratio U_{tip}/V_∞. At each fan speed setting, the net axial force being exerted on the fuselage-fan assembly was measured. As already explained in Section 4.2.2, the net axial force of the fuselage-fan assembly was a direct output of the external balance. The net axial force coefficient is defined as $C_N = N/(q_\infty S_{\text{ref}})$, with the axial force N positive for an excess of thrust. The drag coefficient of the bare fuselage configuration, C_{D_0}, is used as reference. The ratio C_N/C_{D_0} is a measure of the net momentum excess due to the powered configuration with respect to the momentum deficit of the baseline fuselage configuration. To achieve measurements in the desired range of C_N/C_{D_0}, the freestream velocity was changed in combination with the fan shaft speed, leading to a variation of the fuselage length-based Reynolds number, Re_{L_b}, between 3.5×10^6 and 4.7×10^6. In order to minimize the effects of the changing Reynolds number, the drag coefficient of the bare fuselage were also assessed at the same freestream velocities and used to obtain the non-dimensional fraction.

Fig. 4.7 shows the fuselage-fan net axial force coefficient against the fan tip speed ratio for different freestream velocities. The plot of Fig. 4.7 shows that C_N non-linearly increased with increasing U_{tip}/V_∞. At around $U_{\text{tip}}/V_\infty = 1$, the fuselage-fan assembly produced a net force equal to that of the bare-fuselage drag resulting in $C_N/C_{D_0} = -1$. Therefore, at this condition, the net effect of the fan installation on the measured axial force was zero. The axial equilibrium condition ($C_N = 0$) was reached for $U_{\text{tip}}/V_\infty = 1.84$. For higher tip speed ratios, the net force became positive, meaning a thrust excess. The curves were measured at three different freestream velocities and Reynolds numbers and do not fall perfectly on each other, albeit being expressed in non-dimensional parameters. This is due to the effect of the Reynolds number on the airframe and fan force coefficients. In particular, an increase in the Reynolds number resulted in an upward shift of the curve, in agreement with what found in Ref. [32]. The net axial force is the integral of the pressure and shear stresses on the fuselage and propulsor surfaces. In general, the integral over the fuselage and shroud surfaces gives a negative contribution to C_N, while the integral over the fan blades gives a positive contribution. At a fixed U_{tip}/V_∞, increasing the Reynolds number produces, in absolute values, a reduction of the airframe contribution and an increase of the fan contribution. Dividing C_N by C_{D_0}, as in the plot

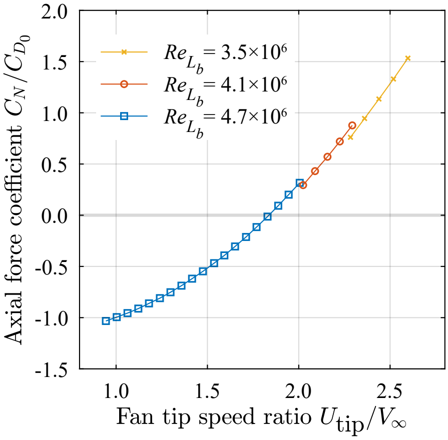

Figure 4.7: Net axial force coefficient for different fuselage-fan operating conditions. External balance measurements taken at different freestream velocities V_∞.

of Fig. 4.7, partially compensates this Reynolds number effect since it accounts for the change of the airframe contribution. On the other hand, the effect that the Reynolds number had on the fan contribution is not compensated, resulting in the upward shift of the curves in the plot of Fig. 4.7.

4.3.2. FLOWFIELD ANALYSIS IN AXIAL EQUILIBRIUM CONDITIONS

WAKE FLOWFIELD

Velocity and total pressure measurements were carried out in the WP-FoV plane as described in Sections 4.2.2 and 4.2.2. Fig. 4.8 shows the distributions of the total pressure and of the axial, transverse (sum of the tangential and radial components) and turbulence kinetic energy flux densities in the wake. Data are shown for the bare fuselage case (left subplots of Fig. 4.8) and the powered fuselage cases (central subplots of Fig. 4.8). In addition, the difference between the bare fuselage and the powered case is shown in the right subplots of Fig. 4.8. Since the fan was equipped with outlet vanes (see Fig. 4.4d), the wakes of the vanes were clearly visible even in the phase-averaged field. Because of the swirl in the propulsor slipstream, the azimuthal position of the outlet vanes wakes was a function of the axial distance between the outlet plane and the survey plane. In order to have a consistent comparison of the powered and unpowered cases, the fan slipstream was azimuthally averaged.

Fig. 4.8a (left) shows that the total pressure distribution in the wake of the bare fuselage configuration deviated from being axisymmetric because of the junction flow generating at the fuselage-fairings intersection. The interaction of the fairing pressure field and the upstream fuselage boundary layer created a pair of horseshoe vortex structures, symmetric around both the xz and xy planes. These vortices entrained high-momentum flow inside the fuselage boundary layer, producing the C_{p_t} pattern reported in the left subplot of Fig. 4.8a. The effect of the fuselage-fairing junction flow is also recognizable in the axial kinetic energy distribution shown in Fig. 4.8b (left). In the wake of the bare

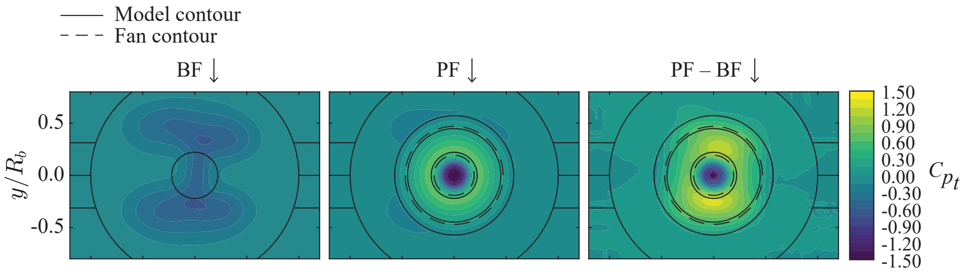

(a) Total pressure.

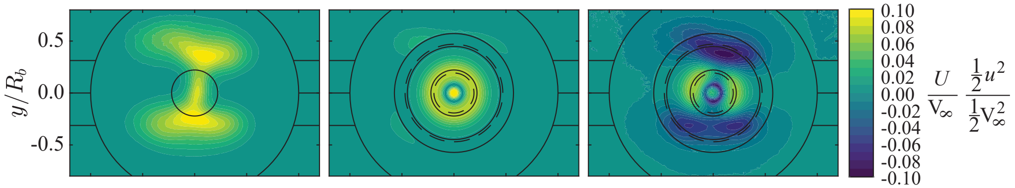

(b) Axial kinetic energy.

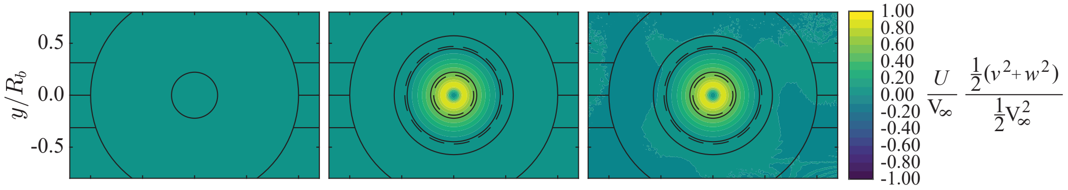

(c) Transverse kinetic energy.

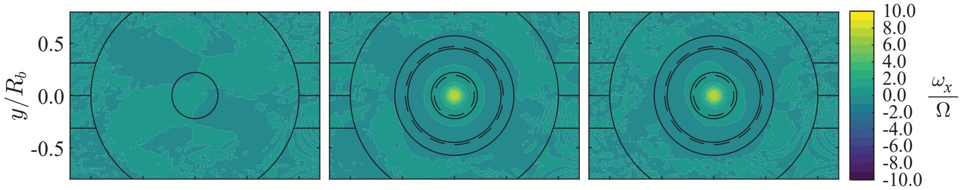

(d) Axial vorticity.

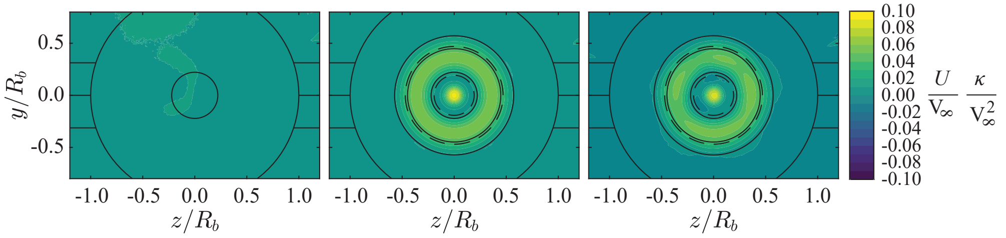

(e) Turbulent kinetic energy.

Figure 4.8: Momentum and power decomposition in the WP-FoV plane for the Bare Fuselage case (BF), Powered Fuselage case at $C_N = 0$ (PF) and their difference (PF − BF). Total pressure and PIV measurements at $Re_{L_b} = 4.7 \times 10^6$.

fuselage, the axial kinetic energy flux reached the highest values in the flow regions of low total pressure. The transverse and turbulence kinetic energy distributions, shown in left subplots of Fig. 4.8c and Fig. 4.8e respectively, are instead relatively low in the bare fuselage case.

In the powered fuselage case, the total pressure distribution (central subplot of Fig. 4.8a) was equal or higher than the freestream value in the fan slipstream. This was due to the momentum increase introduced by the fan. However, a very low total pressure value was found close to the axis, due to the onset of rotational flow around the fan hub. In fact, as Fig. 4.8d (center) shows, high axial vorticity was found in the PF case in proximity of the axis. This vortical flow also resulted in a large transverse kinetic energy (Fig. 4.8c).This hub vortex is also typically found in pusher propeller configurations [87, 88]. The onset of this vortex, characterized by a predominantly axial velocity and low pressure, is due to the blades root vorticity that merges into a single axial vortex. Because of the conservation of angular momentum, when a fluid particle moves toward the fuselage axis, its angular velocity linearly increases to keep the angular momentum constant. To compensate for the increasing centrifugal force, the centripetal pressure force, proportional to the pressure gradient in the radial direction, increases with the square of the angular velocity. As a consequence, the static pressure and the axial velocity significantly decreased toward the fuselage axis. Moreover, the associated velocity gradient enhanced the viscous losses and the viscous core of the vortical structure is clearly identifiable from Fig. 4.8c (center), where the transverse energy linearly decreased to zero from $r/R_b = 0.1$ toward the axis. The turbulence kinetic energy was also substantially increased by the fan in the powered conditions, as shown in Fig. 4.8e. In particular, the highest turbulence intensities were measured close to the axis, in coincidence of the vortical structure described above. The ensemble-average flowfields shown for the powered cases are obtained by averaging out phase-free instantaneous PIV images. Therefore, the unsteadiness of the flowfield, due to the fan blades slipstream, contributed to the standard deviation of the instantaneous velocity fields and hence affected the estimation of the turbulence statistics.

SYMMETRY PLANE FLOWFIELD

In order to visualize the flowfield around the propulsor and quantify the development of the fuselage boundary layer across the fan plane, the velocity field was measured in the horizontal symmetry plane of the model (SP-FoV PIV setup of Section 4.2.2). Fig. 4.9 shows the mean and turbulent flowfields around the fuselage aft-cone section for the BF case and the PF case in axial equilibrium condition. Phase-uncorrelated PIV measurements were taken at a freestream velocity of 20 m/s, and for the powered configuration without outlet vanes mounted. Therefore, a direct quantitative comparison with Fig. 4.8 is impossible because of the flowfield induced by the outlet vanes.

Streamlines projections for both the BF and PF cases are shown in Fig. 4.9a. Since the flow is 3-D, these do not coincide with the actual streamlines in the flow regions where swirl component was not zero. Comparing the two cases, it is possible to appreciate the key effects of the fuselage-fan on the surrounding flow. First, upstream of the fan, the boundary layer flow is directed inboard, because of the locally increased massflow rate due to the fan suction. Second, downstream of the fan, the boundary layer contracts as a consequence of the fan slipstream contraction. Further downstream, due to the onset of

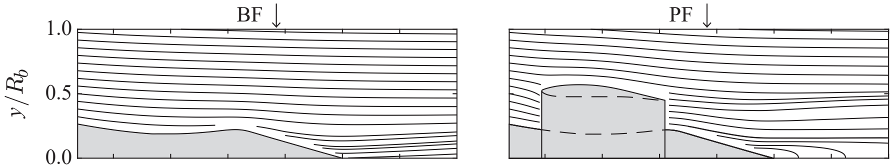

(a) Streamlines projections.

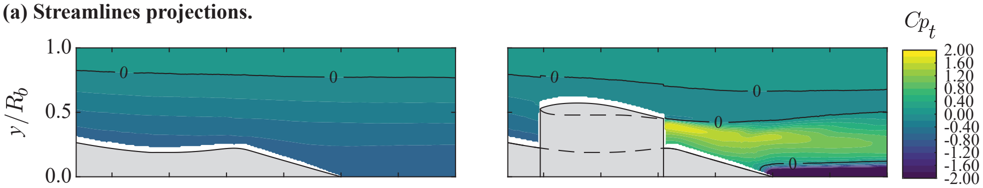

(b) Total pressure.

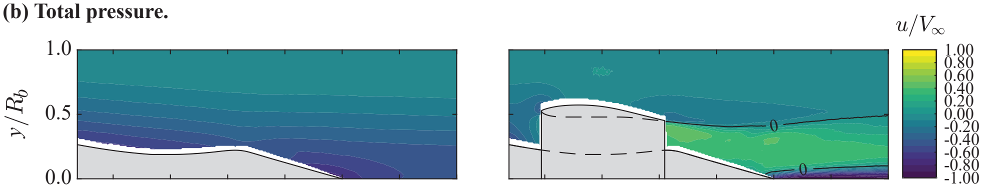

(c) Axial velocity perturbation.

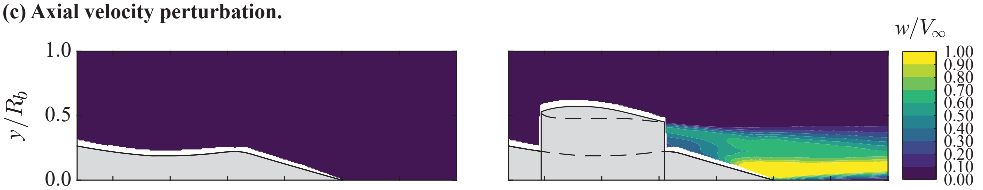

(d) Out-of-plance velocity.

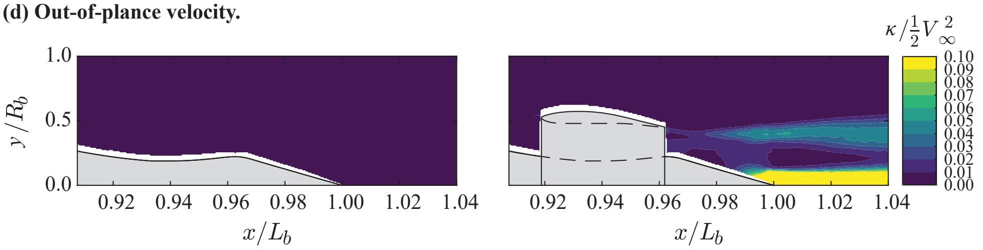

(e) Turbulent kinetic energy.

Figure 4.9: Flowfield around the fuselage-mounted propulsor. BF case (left) and PF case (right). PIV measurements in the SP-FoV plane at $V_\infty = 20\,\mathrm{m/s}$. PF case at $C_N = 0$ and without the outlet vanes.

the vortical flow structure already described in Sec 4.3.2, the fan slipstream is displaced outboard before leaving the fuselage trailing edge.

Fig. 4.9b shows the total pressure coefficient for the BF case (left subplot) and the PF case (right subplot). The total pressure field was inferred from the PIV measurements via the method discussed in Section 4.2.4. The turbulent boundary layer flow around the bare fuselage is clearly visible and characterized by a total pressure value lower than the freestream. The boundary layer physical thickness, δ_{99}, defined as the radial position at which $p_t/p_{t_\infty} = 0.99$, was estimated at $y/R_b = 0.67$ at the fan location ($x/L = 0.94$) for the BF case. The total pressure distribution for the PF case for $C_N = 0$ is shown in Fig. 4.9b (right). The contour shows that the fuselage boundary layer is larger than the fan and approximately 30% of δ_{99} is not ingested by the propulsor. Downstream of the fan, the total pressure is higher than the freestream value due to the momentum addition of the fan. In addition, the edge of the fuselage boundary layer is thinner than in the BF case and contracts more toward the fuselage trailing edge as a consequence of the local negative axial pressure gradient and slipstream contraction (see again Fig. 4.9a). At the shroud trailing edge, the viscous boundary layer over the shroud external surface mixed with the fan slipstream creating a relatively sharp mixing layer with strong total pressure and velocity gradients.

Fig. 4.9c shows the axial disturbance velocity component, $u = U - V_\infty$, for the BF case (left subplot) and the PF cases (right subplot). The effect of the BLI fan propagates upstream of the shroud, where the boundary layer flow is accelerated when compared to the unpowered case. Obviously, the slipstream of the fan also shows an increased velocity due to the imposed momentum increase. Moreover, the interaction between the shroud and the fuselage outer boundary layer flow is clearly visible. The stagnation points at the leading and trailing edges of the shroud, as well as the suction and compression around the shroud contour can be seen (see right subplots of Fig. 4.9a and Fig. 4.9c).

The out-of-plane velocity component is shown in Fig. 4.9d. The distribution of w across the shroud exit is non-uniform, and follows the blade loading distribution with the highest values found around the fan tip (see right subplot of Fig. 4.9d). As we move downstream toward the fuselage trailing edge, higher out-of-plane velocities are found, due to the slipstream contraction and the conservation of angular momentum. In addition, a strong increase of tangential velocity were measured at the trailing edge of the fuselage due to the onset of a vortex, as discussed in Sec. 4.3.2. In the PF case (right subplots of Fig. 4.9), this vortex structure was enhanced by the fact that the trailing edge of the fuselage was spinning together with the fan and hence introducing angular momentum in the flow. Moreover, the outlet vanes did not influence significantly the vortex structure. This can be confirmed by comparing qualitatively Fig. 4.8a (center) and Fig. 4.9b (right) which show the total pressure distribution for the PF case with and without outlet vanes, respectively. In both cases, a total pressure deficit of similar strength and extension was found around the fuselage axis. This could be due to the fact that the outlet vanes did not significantly alter the swirl distribution due to their design.

The hub vortex structure also features a relatively high turbulence level, as testified by Fig. 4.9e (right). Turbulence kinetic energy was also measured in the shear layer between the fan slipstream and the outer fuselage boundary layer.

To analyze the effect of the BLI fan on the local boundary layer flow, boundary layer profiles are shown for the BF and the PF at $C_N = 0$ in Fig. 4.10. The location of the survey stations is sketched in Fig. 4.10a, while Fig. 4.10b shows the streamlines projections upstream and downstream of the shroud. The plots of Fig. 4.10c confirm that the upstream effect of the BLI fan on the total pressure distribution is weak. However, a strong effect is found on the velocity field, due to the pressure field imposed by the fan. This results in an increased wall-tangential velocity, u_t, in the inboard region of the boundary layer and in the onset of a negative (i.e. inboard) normal velocity component, u_n. Downstream of the propulsor, the effect of the BLI propulsor to the local flow is much stronger, as shown in Fig. 4.10d. In particular, two key effects can be understood from the C_{p_t} profile: first, the high momentum flow ($C_{p_t} > 0$) carried by the fan slipstream entrains the boundary layer, increasing the total pressure also outside the fan slipstream itself compared to the BF case. Second, the boundary layer in the PF case becomes thinner than the BF case, due to the local slipstream contraction. In particular, at the station B, the physical boundary layer thickness, δ_{99}, decreases from $0.67R_b$ for the BF case to $0.56R_b$ for the PF case, resulting in a 15% thinner boundary layer.

POWER BALANCE ACROSS THE BLI PROPULSOR

The power balance method was applied to these flowfields in order to quantitatively assess the integral momentum and power fluxes (or deposition rates) across the propulsor location. The control volume and notations defined in Fig. 4.6 of Section 4.2.4 were used for the integral analysis of the flowfield. The momentum and power fluxes were computed on a survey plane perpendicular to the freestream velocity direction moving from the domain inlet to the domain outlet along the axial direction x (see Fig. 4.6).

Fig. 4.11 shows the variation of the integral momentum and power deposition rates along the fuselage axis for the bare fuselage (BF) and the powered fuselage (PF) cases in axial equilibrium. For the PF case, the integral values are discontinuous across the shroud location as the velocity and pressure data inside the shroud is missing. Fig. 4.11a shows the axial momentum flux coefficient C_{F_x} as a function of the axial position x/L_b, as defined by Equation 4.6 in Section 4.2.4. C_{F_x} represents the amount of axial momentum deficit (or excess) in the flow at the specific axial position, and is linked to the configuration drag (or thrust). For the BF case, C_{F_x} is always negative and is monotonically increasing in absolute value due to the viscous dissipation taking place in the fuselage boundary layer. Interestingly, C_{F_x} showed a relatively quick change in slope as we move toward the trailing edge ($x/L_b = 1$) and kept decreasing at the same rate in the near wake ($x/L_b > 1$) up to the end of the field of view. For the powered fuselage case, the momentum deficit upstream the shroud was increased by around 10% with respect to the bare fuselage case due to the detrimental interaction effects of the operating shrouded fan. Across the propulsor, the momentum flux showed a step change due to the addition of momentum in the flow by the fan. In this measured case, even though the balance measured a zero axial force, the thrust provided by the fan exceeded the fuselage momentum deficit, resulting in a momentum excess in the fan slipstream.

Fig. 4.11b shows the variation along the axis of the total mechanical energy flux $C_{\dot{\varepsilon}}$ and the kinetic energy deposition rate $C_{\dot{E}}$, obtained as the difference between $C_{\dot{\varepsilon}}$ and C_{F_x} (see Equations 4.4 to 4.10 of Section 4.2.4). $C_{\dot{\varepsilon}}$ and $C_{\dot{E}}$ varied along the fuselage axis similarly to C_{F_x} both for the bare fuselage and powered fuselage cases. For the bare fuselage

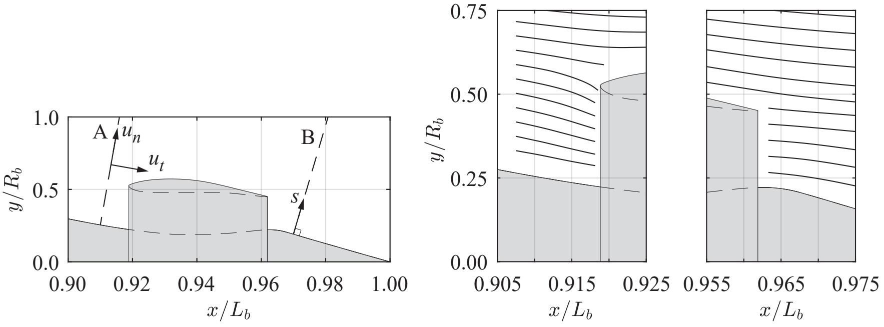

(a) Boundary layer survey stations. **(b) Streamlines projections.**

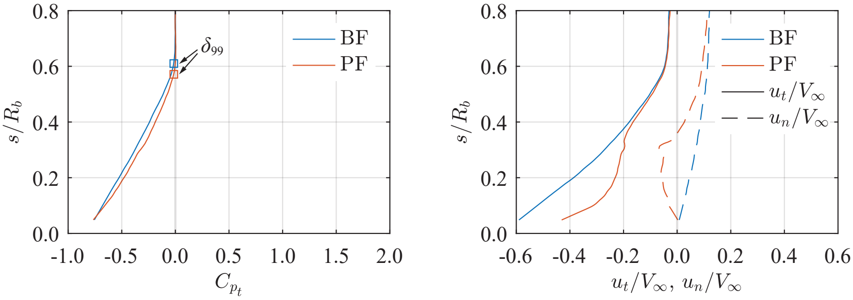

(c) Station B: x/L_b = 0.91.

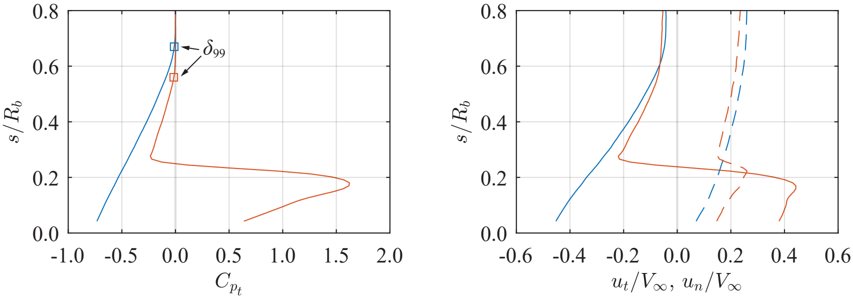

(d) Station B: x/L_b = 0.97.

Figure 4.10: Boundary layer profiles for the BF and PF cases. PIV measurements in the SP-FoV plane at $V_\infty = 20\,\mathrm{m/s}$. PF case at $C_N = 0$ and without the outlet vanes.

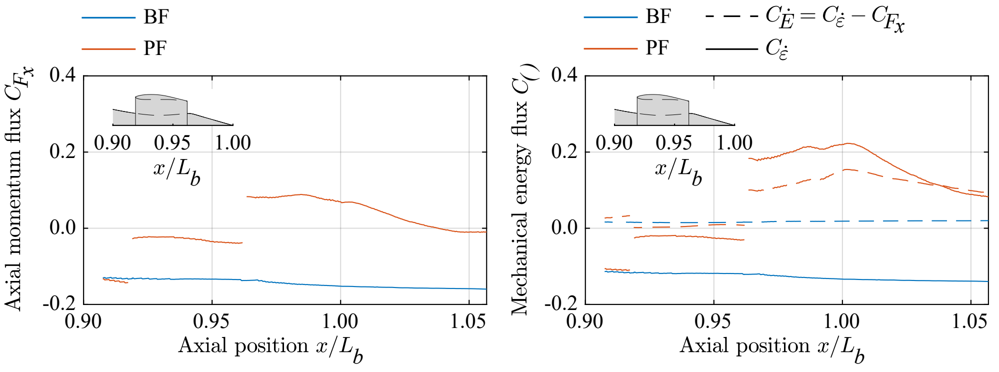

(a) Axial momentum flux.

(b) Mechanical energy flux.

Figure 4.11: Variation along the axial direction of the integral momentum and mechanical energy fluxes across the fuselage aft section. PF case taken for $C_N = 0$.

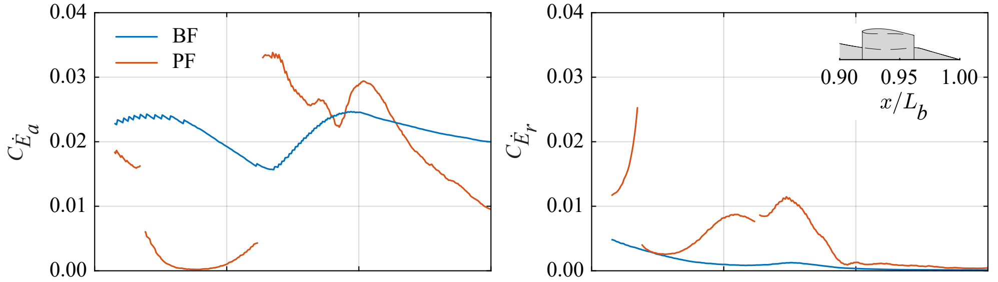

(a) Axial deposition rate.

(b) Radial deposition rate.

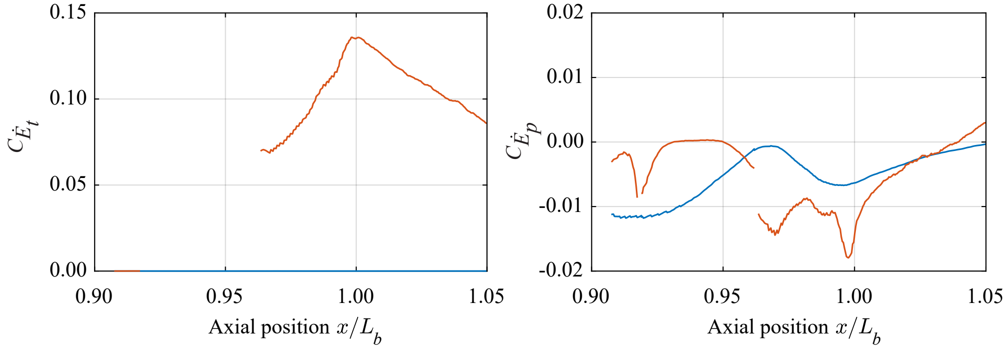

(c) Tangential deposition rate.

(d) Pressure work rate.

Figure 4.12: Integral mechanical energy flux components across the fuselage aft section. Powered measurements taken in axial equilibrium conditions ($C_N/C_{D_0} = 0$).

case, $C_{\dot{\varepsilon}}$ monotonically decreased when moving downstream, driven by C_{F_x} (see Eq. 4.5). On the other hand, $C_{\dot{E}}$ increases with x, growing from approximately 0.016 upstream the fan, to 0.019 at the fuselage trailing edge and to 0.020 at $x/L_\mathrm{b} = 1.05$. The power balance of the bare fuselage can be obtained by simplifying Eq. 4.3 to $-C_{F_x} = C_{\dot{E}} + C_{\phi}$. At the trailing edge of the fuselage ($x/L_b = 1$), $C_{\dot{E}}/-C_{F_x} = 0.13$, which means that approximately 13% of the total power losses occur in the wake of the fuselage. This value also represents the ideal power benefit of BLI for the fuselage model, achievable with an ideal BLI propulsor which entirely recovers the energy deficit in the fuselage boundary layer. Note that this benefit refers to the power needed to propel the fuselage only and needs to be scaled to the whole aircraft level if required. The value of $C_{\dot{E}}$ for the powered configuration upstream the fan was higher than for the bare fuselage case, due to the suction that the fan imposed to the upstream boundary layer fluid. Across the shrouded fan, the mechanical power flux coefficient $C_{\dot{\varepsilon}}$ experienced a jump which is linked to the mechanical power transmitted by the fan into the fluid. $C_{\dot{\varepsilon}}$ shows a slight increase immediately downstream of the shroud exit. This is thought to be due to the influence of the spinning nozzle plug, which introduced tangential momentum in the flow. This resulted in an increase of $C_{\dot{\varepsilon}}$ without adding to the axial momentum flux. This is corroborated by Fig. 4.12c. Also $C_{\dot{E}}$ showed a jump across the fan and approximately 23% of the total mechanical power introduced by the BLI fan accounted for the $C_{\dot{E}}$ component and subsequently dissipated in the wake.

$C_{\dot{E}}$ is the sum of the four different terms defined in Eq. 4.11-4.14 which are the power fluxes associated with the three velocity components and the static pressure work. Fig. 4.12 shows how each individual term varied along the fuselage axis for both the bare fuselage case and powered fuselage in axial equilibrium case. The discontinuity in the curves for the PF cases is due to the missing flowfield data inside the shroud. By comparing the curves upstream the shroud leading edge for the two cases, it can be seen that the effect of the BLI fan was to accelerate the incoming flow, producing a decrease in modulus of both $C_{\dot{E}_a}$ and $C_{\dot{E}_p}$ (Fig. 4.12a and 4.12d). At the same time, an increase of $C_{\dot{E}_r}$ (Fig. 4.12b) was measured, due to the induced radial flow component already discussed (see Fig. 4.10c). Downstream the shroud outlet, the tangential kinetic energy flux $C_{\dot{E}_t}$ (Fig. 4.12c) strongly increased in the powered case as a consequence of the tangential momentum introduced by the fan blades becoming the dominant component of $C_{\dot{E}}$. In a more realistic case at full-flight scale, this component could be effectively minimized through an optimized stator stage.

4.3.3. EFFECT OF FAN-THRUST-TO-BODY-DRAG RATIO

The previous subsection has covered the performance analysis of the PFC in cruise conditions, for which the net axial force acting on the fuselage-fan assembly was zero. To assess the effect of varying thrust settings on the aerodynamics of the overall configuration, measurements were taken at different net axial force coefficients. PIV-measurements were used to quantify the boundary-layer and near-wake flowfields around the propulsor and to infer the total pressure distribution, with the method discussed in Section 4.2.4. The axial velocity and total pressure profiles at the fan inlet ($x/L_b = 0.91$), fan outlet ($x/L_b = 0.97$) and in the fuselage near wake ($x/L_b = 1.06$) for different net axial force coefficients are shown in Fig. 4.13. A number of fan operating conditions were assessed for

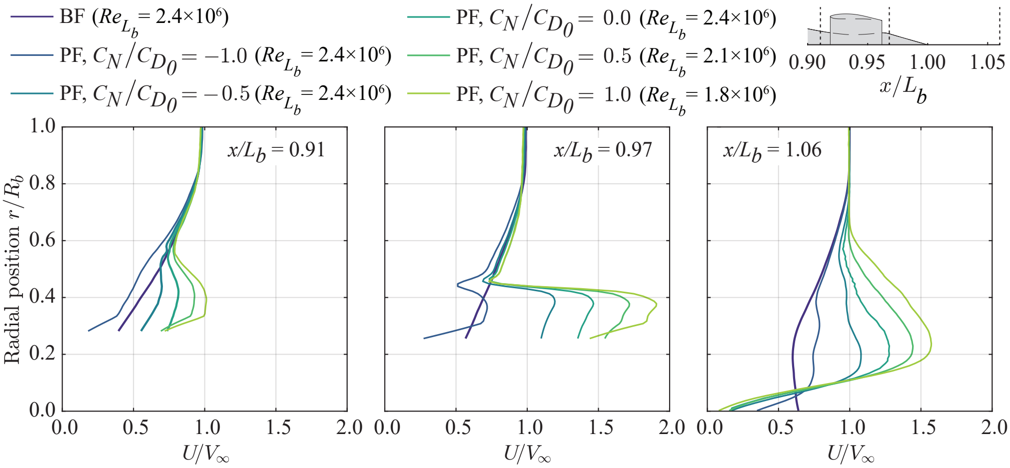

(a) Axial velocity profiles.

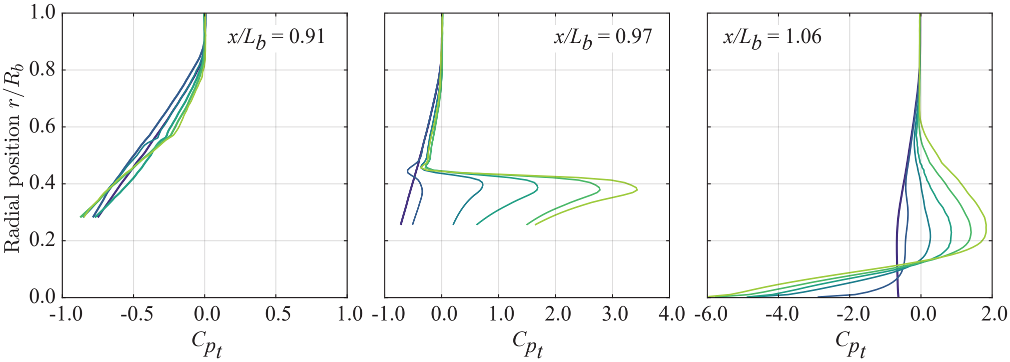

(b) Total pressure profiles.

Figure 4.13: Axial velocity and total pressure profiles for different net axial force conditions. Velocity and pressure data from the SP-FoV PIV setup.

which $-1.0 \leq C_N/C_{D_0} \leq 1.0$.

The effect of the fan on the upstream flow, is clearly visible in Fig. 4.13a (left) and 4.13b (left). Increasing the axial force produced a visible suction effect on the boundary layer resulting in an higher velocity in the lower part of the profile (left subplot of Fig.4.13a). Contrarily, the effect on the upstream total pressure profile is not significant (left subplot of Fig.4.13b). This entails that the upstream effect of the BLI fan was comparable to that of an inviscid (potential) actuator disk and the viscous interaction with the incoming boundary layer are of second order. Note that for $C_N/C_{D_0} = -1$ the fan was actually slowing down the incoming boundary layer even at a constant total pressure value. This was probably due to the fact that the shroud was operating at an off-design condition and hence spillage occurred as the massflow required by the fan was lower than the design one.

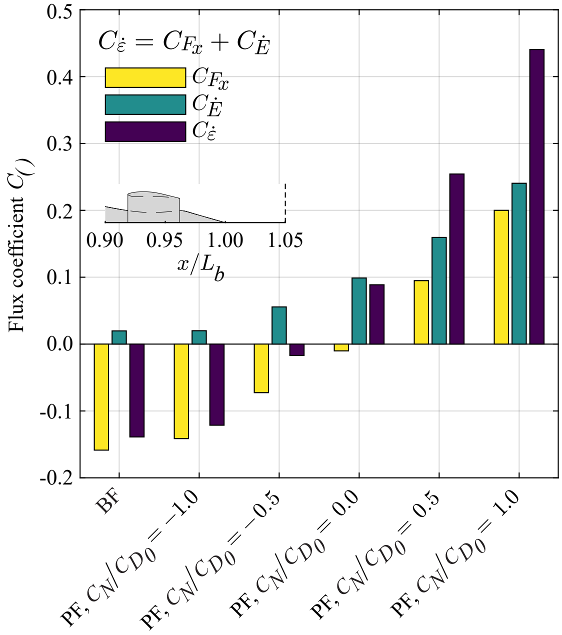

Figure 4.14: Power flux components in the near wake of the body ($x/L_b = 1.05$) for different fan settings.

Downstream the fan outlet (central subplots of Fig. 4.13a and 4.13b), the slipstream of the fan is clearly recognizable in the powered cases as the axial velocity and total pressure are both higher than in the bare fuselage case. In particular, for the $C_N/C_{D_0} = -1$ case the total pressure profile shows a slightly increased total pressure over the bare fuselage case which compensates for the shroud viscous wake, centered at around $r/R_b = 0.45$, producing a zero axial force overall.

Fig. 4.13a (right) and 4.13b (right) show the velocity and total pressure distributions in the model wake. The C_{p_t} shows a very low value at the axis for the powered cases due to the hub vortex formation described in Section 4.3.2, which increased in strength for increasing C_N. Moreover, at $C_N/C_{D_0} = -0.5$ both the average U/V_∞ and C_{p_t} were closer to the freestream values (respectively 1 and 0). This entails that $C_N/C_{D_0} = -0.5$ was the conditions, among the measured ones, for which the benefit of BLI could be maximum. This can be explained by the fact that only a part of the boundary layer was ingested by the BLI propulsor. As a consequence, only part of the momentum and kinetic energy in the boundary layer were ingested. Therefore, to compensate for the ingested deficit, the thrust produced was lower than the fuselage drag. For higher thrust conditions (i.e. for $C_N/C_{D_0} > -0.5$), a residual momentum flux was measured in the fan slipstream (right subplot of Fig. 4.13b). This means that the momentum and energy introduced by the fan into the boundary layer exceeded the ingested deficit, potentially reducing the advantage of BLI.

In order to understand the effect of the fan-thrust-to-body-drag ratio on the wake losses, the mechanical power flux $C_{\dot{\varepsilon}}$ and its two contributions C_{F_x} and $C_{\dot{E}}$ were computed in the near wake of the model. Fig. 4.14 presents the three terms for the bare fuselage and powered fuselage cases for different C_N/C_{D_0} values at $x/L_b = 1.05$. The plot shows that for the bare fuselage $C_{\dot{E}}$ was approximately equal, in modulus, to 13% of C_{F_x}, as already pointed out in Section 4.3.2. Similar values were found for the powered case for $C_N/C_{D_0} = -1.0$, as expected. Increasing the thrust setting leads to a continuous increase of the power flux in the wake. Interestingly, even though the momentum deficit was the closest to zero for $C_N/C_{D_0} = 1.0$, $C_{\dot{E}}$ was largely increased with respect to the bare fuselage, meaning that a substantial part of the energy introduced in the flowfield was still dissipated in the wake of the model. The case for $C_N/C_{D_0} = -0.5$ shows the minimum value of $C_{\dot{E}}$, suggesting that this is the condition for which the BLI benefit is maximum. However, in a more realistic configuration, where the swirl in the fan slipstream is mostly recovered, a lower $C_{\dot{E}_t}$ would be measured. As a consequence, the minimum $C_{\dot{E}}$ would be probably found at a higher C_N/C_{D_0} ratio. At larger axial forces both C_{F_x} and $C_{\dot{E}}$ increased, but at different rates. This suggests that, relatively to the total power flux $C_{\dot{\varepsilon}}$, at higher thrust settings, a smaller share of the wake energy was dissipated in the wake, while a larger share of energy was instead related to the momentum excess.

4.4. CONCLUSIONS

This chapter has presented the results of a low-speed wind-tunnel test of a Propulsive Fuselage Concept. This work represents the first experimental aerodynamic investigation concerning fuselage-BLI. The experimental setup consisted of an axisymmetric fuselage with an embedded boundary-layer-ingesting propulsor. The flowfield around the BLI fan was quantified with Particle-Image Velocimetry (PIV) measurements and used to perform a power and momentum analysis of the configuration through the Power Balance Method (PBM).

Results have shown that:

1. The BLI propulsor strongly affects the surrounding flowfield, modifying the fuselage boundary layer flow both upstream and downstream of the propulsor location. The key effects of the BLI fan on the fuselage boundary layer are:
    (a) upstream of the propulsor, an increased massflow flux in the inboard region of the boundary layer, due to the fan suction effect;
    (b) downstream of the propulsor, the boundary layer is thinner than in the bare fuselage case, due to the slipstream contraction and the momentum input in the boundary layer by the propulsor;
    (c) at the fuselage trailing edge, a strong hub vortex is induced by the swirl component, resulting in a region of very low total pressure, which increases the drag and penalizes the performance.
2. Through the application of the PBM, the distribution of momentum and mechanical energy in the boundary layer flow was quantified. For the axial equilibrium conditions, where $C_N/C_{D_0} = 0$, the effect of the fan is to increase in absolute value the axial momentum flux in the upstream boundary layer with respect to the bare

fuselage. At the same time, the kinetic energy deposition rate is increased upstream of the fan, due to the suction imposed by the fan on the fuselage boundary layer.

3. The effect of varying the fan thrust setting on the aerodynamic performance was quantified through the PBM. The analysis showed that the performance quickly diverges from the ideal wake-filling conditions when increasing the thrust setting. In fact, it was found that the mechanical energy dissipated in the downstream wake increases more than linearly with the net axial force coefficient C_N. Moreover, a larger share of the total mechanical energy is associated with the momentum addition of the BLI fan.

While the previous chapter analysed the aerodynamics of an isolated axisymmetric fuselage body, this chapter provided detailed insight into the aerodynamic interactions occurring between the fuselage and the BLI propulsor in a baseline configuration.

The study object of this chapter focused on a axisymmetric fuselage-BLI model at zero incidence, in which the interaction between the fuselage boundary layer and the BLI fan is dominating the flowfield.

In the following chapter, the aerodynamics of the PFC will be studied in a more complex configuration, where the aerodynamic performance of the aircraft is affected by additional interaction mechanisms introduced by airframe elements and non-zero incidence conditions.

5

AERODYNAMIC PERFORMANCE OF A PROPULSIVE FUSELAGE CONCEPT AIRCRAFT

5.1. INTRODUCTION

In the previous chapter, the aerodynamic performance of an axisymmetric fuselage with an aft-fuselage mounted BLI propulsor has been discussed. The chapter focused on the aerodynamic interactions between the fuselage airframe and the BLI propulsor in axial inflow conditions. The work highlighted that the propulsor has a strong effect on the fuselage boundary layer. In particular, due to the suction imposed to the fluid, higher velocity is found in the near-wall region of the boundary layer upstream of the propulsor and high momentum flow is drawn toward the fuselage wall, which affects the local boundary layer properties and physical thickness.

However, in a more realistic scenario, the flow around the fuselage aft-section is not expected to be axisymmetric, as it will result from the influences of different elements. In particular, the fuselage-mounted shrouded fan will be affected by other aerodynamic surfaces and elements of the aircraft, namely the wing and vertical tail plane. These elements will introduce total pressure and velocity distortions at the fan inlet due to viscous dissipation (i.e. boundary layers and wakes) or circulation (i.e. lift) which are a function of the flight conditions. These distortions can have an impact on propulsive efficiency, stall margin, aeromechanic and aeroacoustic performance of the fan (see, e.g., Refs. [89–93]). Moreover, the aerodynamic interaction between the BLI propulsor and the aircraft airframe can have an effect on the overall system aerodynamic performance and influence the local flowfield around the fuselage aft-cone section. For a schematic view of the

---

Contents of this chapter have been published in:
Della Corte, B., van Sluis, M., Gangoli Rao, A., and Veldhuis, L. L. M., “Aerodynamic Performance of an Aircraft with Aft-Fuselage Boundary-Layer-Ingestion Propulsion”, *Journal of Aircraft*, 2022. doi:10.2514/1.C036596.

main flow distortions and aerodynamic interaction expected in the PFC refer to Fig. 1.2 reported in Chapter 1.

In order to tailor the PFC design to minimize installation penalties and hence maximize the aero-propulsive efficiency, the main flow phenomena need to be investigated. This chapter discusses an experimental analysis of an aircraft model representative of the CENTRELINE Propulsive Fuselage Concept. The tested model featured a shrouded BLI propulsor integrated at the aft fuselage section. Differently from what discussed in the previous chapter, this test setup featured a model representing a complete aircraft configuration, which was tested in a wide range of relevant angles of incidences. Moreover, the BLI fan was tested in relative thrust conditions, representing those of the CENTRELINE full-scale aircraft. The goal of the low-speed wind-tunnel experiments was twofold. First, to assess the effect of the BLI fan on the aircraft forces in various flight conditions. Second, to characterize the aerodynamic flow around the BLI propulsor in on- and off-design conditions.

5.2. METHODS

Low-speed wind-tunnel tests were performed on a sub-scaled aircraft model equipped with a fuselage-mounted BLI shrouded fan. As a consequence of the scaling limitations, the Reynolds and Mach numbers characterizing the flow at the lab scale were lower than the expected values in typical high-subsonic cruise conditions. In particular, the wind-tunnel experiments were conducted at a wing-mean-chord-based Reynolds number, $Re_{\bar{c}}$, of 460,000 and a Mach number, M, of 0.12. As a reference, in full-scale cruise conditions $Re_{\bar{c}}$ and M would be 40,000,000 and 0.82, respectively. The Reynolds and Mach numbers scaling affects important aspects of the PFC aerodynamics, for example: the fuselage boundary layer, the BLI fan aerodynamics and efficiency, the fuselage-VTP junction flow. Due to the lower Reynolds number obtained during the experiments, delayed turbulent transition and relatively larger boundary layer thicknesses were expected compared to the full-scale flight conditions. To mitigate these effects, the transition locations were imposed on all the fixed aerodynamic surfaces (fuselage, wing, vertical tail and shroud) through tripping elements. Moreover, the BLI propulsor model was sized accordingly to the fuselage boundary layer thickness to maintain the same scaling relative to the boundary layer thickness as found in full-scale aircraft. Compressibility effects could not be simulated in the low-speed wind-tunnel used. Compressibility plays a major role in the aerodynamics of lifting surfaces (i.e. wings). However, the consequences of the low Mach number are not expected to have a strong influence on the flow around the fuselage body, since the critical Mach number of axisymmetric bodies is higher than the typical cruise Mach number (see for example Ref. [76–78]). As a consequence of the scaling limitations, quantitative results obtained at low-speed are not directly scalable to full-scale conditions. However, qualitative comparison with numerical simulations at full-scale regime performed within the CENTRELINE project (see Ref. [29] and Ref. [94]) showed that the key aerodynamic phenomena are qualitatively similar to the findings of the low-speed wind-tunnel experiments.

Furthermore, the aircraft model tested was representative of the CENTRELINE Propulsive Fuselage Concept design. However, except for some aspects (e.g. the contour of the fuselage aft-cone), the model design was simplified to avoid that configuration-specific

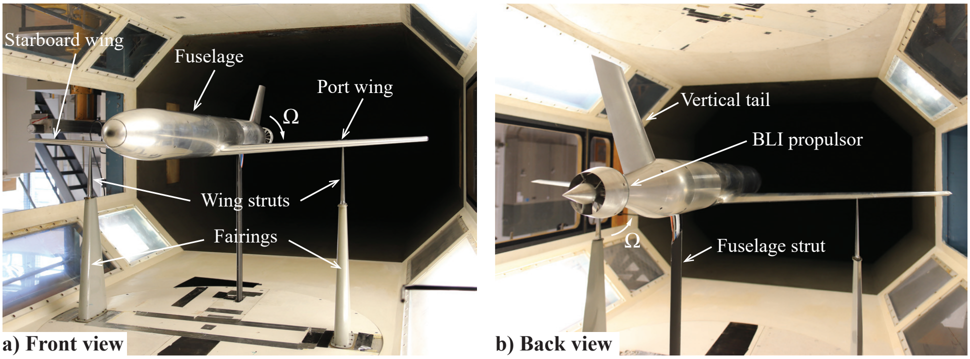

Figure 5.1: Photographs of the wind-tunnel setup assembled in the test section of the Low Turbulence Tunnel of Delft University of Technology.

design choices could affect some of the findings of this study. In particular, the aircraft model was not equipped with an horizontal tail as no significant aerodynamic interactions were expected between the horizontal tail plane and the BLI propulsor. Similarly, the aircraft trim condition was not accounted for in this study as it was not expected to alter significantly the flowfield around the fuselage aft-cone and the BLI propulsor.

Finally, since the focus of the experiment was to study the aerodynamic interaction between the aircraft and the installed BLI propulsor, and not to quantify the aircraft performance, wind-tunnel corrections were not applied and the results are based on uncorrected data.

5.2.1. WIND-TUNNEL FACILITY AND SETUP

The wind-tunnel experiments were carried out at the Low Turbulence Tunnel (LTT) of Delft University of Technology. The LTT is a closed-loop, closed test-section atmospheric wind-tunnel. The test section features and octagonal cross-section with a width of 1.80 m and height of 1.25 m. The maximum test speed that can be reached is 120 m/s with a turbulence intensity below 0.1%.

The test setup consisted of an aircraft model representative of the CENTRELINE Propulsive Fuselage Concept (PFC). Photographs of the model installed in the test section are shown in Fig. 5.1 and the main model dimensions are reported in Fig. 5.2. The reference systems and conventions used in the current study are reported in Fig. 5.3.

The aircraft model was mounted to an external six-components balance through a three-point attachment system. The support structures were hinged to the two wings and to the aft-fuselage section. The model could rotate around the wing-support hinge axis to simulate an angle of attack, α, which was controlled by vertically sliding the aft-fuselage support. In addition, the model could rotate around the vertical axis to simulate an angle of sideslip, β. The support struts rotated with the model and with a turntable embedded in the test-section wall.

The fuselage consisted of an axisymmetric body with a maximum radius, R_b, of 70 mm and a total length, L_b, of 1564 mm. The fuselage aft-cone section shape was adapted from the propulsive aft-cone of the CENTRELINE PFC aircraft. Moreover, the fuselage

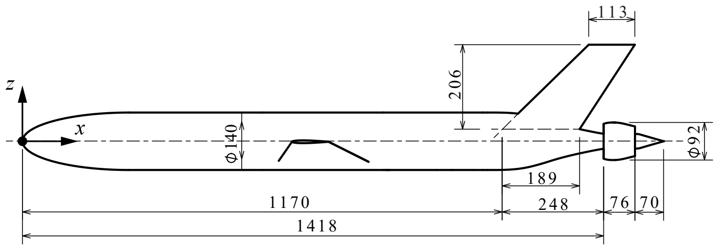

a) Lateral view

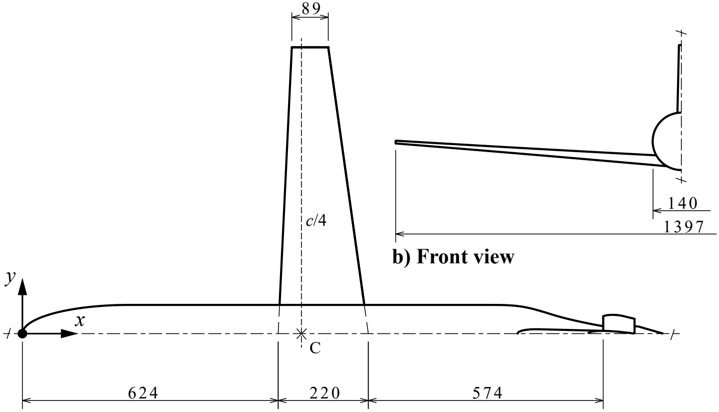

b) Front view

c) Top view

Figure 5.2: Technical views of the wind-tunnel model (dimensions in mm).

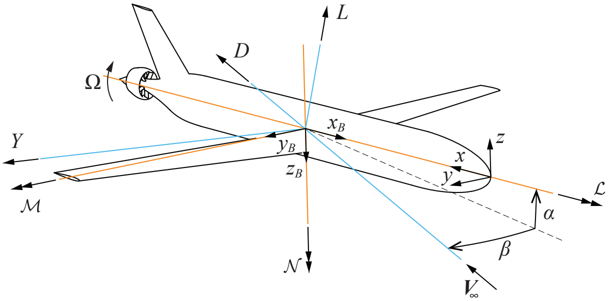

a) Aircraft attitude angles, forces and moments conventions

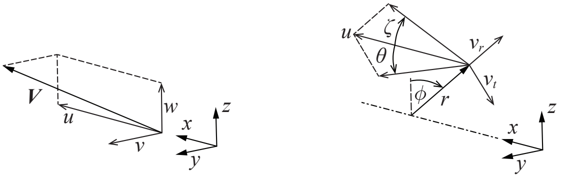

b) Cartesian velocity components c) Cylindrical velocity components

Figure 5.3: Conventions and definitions used for the aircraft forces and moments and velocity components.

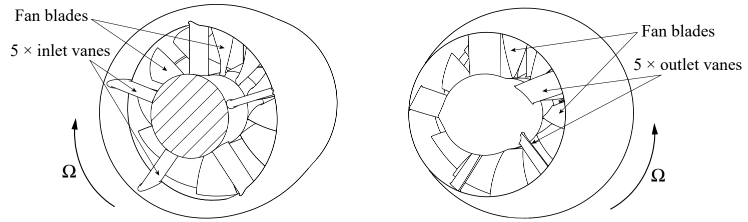

a) Isometric front view

b) Isometric back view

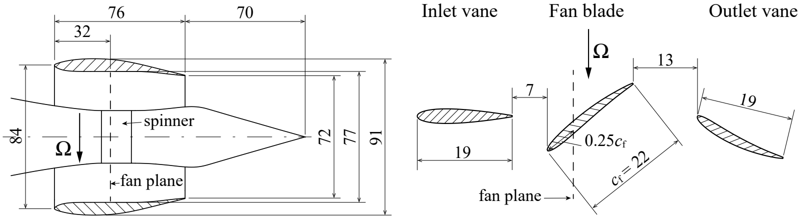

c) Section view

d) Mid-span cross-section

Figure 5.4: Details of the shrouded BLI propulsor equipping the wind-tunnel model (dimensions in mm).

aft-cone section was modular, allowing the testing of different configurations which are described in more detail in Sec. 5.2.3.

The fuselage aft-cone section was equipped with a BLI shrouded propulsor, of which technical views and details are shown in Fig. 5.4. The fan featured 12 blades with a diameter, D_f, of 75 mm, an hub-to-tip-radii ratio of 0.41 and a mid-span blade chord, c_f, of 22 mm. The fan was driven by a three-phase brushless electric motor and its rotational speed, Ω, was measured through an US Digital© optical encoder mounted on the motor shaft.

Since the fuselage boundary layer is expected to be relatively larger at the test scale when compared to the flight scale (due to the lower Reynolds number), the propulsor size was not scaled geometrically from the full scale to the wind-tunnel scale. Aerodynamic and aero-propulsive similarity between the wind-tunnel model and the full-scale aircraft were obtained by: 1) scaling the propulsor size such that the same ratio between the fan diameter and the fuselage momentum thickness at the fan location is achieved; and 2) optimizing the fan blades at the same operating conditions defined by the flow coefficient and load coefficient. The shroud geometry was also adapted from the full-scale CENTRELINE configuration to allow a tip gap of 0.75 mm, approximately corresponding to 1% of D_f. The shroud was equipped with 5 inlet and outlet vanes. The inlet vanes featured a NACA 0015 airfoil section with a rectangular planform. These vanes supported the shroud and were not optimized to de-swirl the flow. A more detailed discussion of the procedures and tools used in the fan design can be found in Ref. [95].

The unswept low wing (mean chord, $\bar{c}$, of 165 mm, and planform area, S, of 0.216 m^2) featured a cambered airfoil, an aspect ratio of 8.46, a taper ratio of 0.4 and a linear

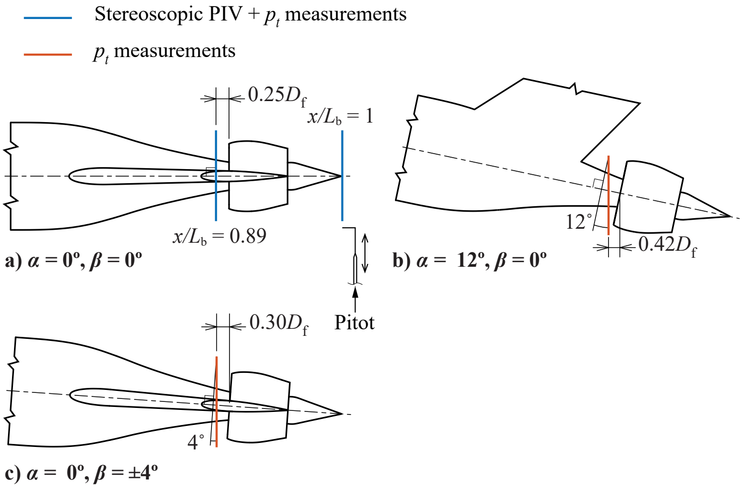

Figure 5.5: Location and orientation of the total pressure and stereoscopic PIV measurements planes.

washout of 2°. The vertical tail plane (VTP) featured a symmetric NACA 0012 airfoil, a taper ratio of 0.3 and a leading edge sweep angle of 30°.

Boundary layer transition was forced on all the surfaces through a 2.5 mm wide strips of 140 μm carborundum particles. The strips were placed on the fuselage, shroud, vertical tail and wing suction side at 5% of their respective lengths, and at 10% of the wing chord on the wing pressure side. Occurrence of transition was checked with microphone inspections of the boundary layer at all the operating conditions that were tested during the experiments.

5.2.2. MEASUREMENT TECHNIQUES

FORCE AND MOMENTS MEASUREMENTS

The aerodynamic forces and moments acting on the model were measured through the external six-components balance, to which the model was connected through the three supports. Only the model and the fuselage strut were sensed by the balance, since the wing struts were almost entirely covered by fairings bolted directly to the wind-tunnel wall (see Fig. 5.1). The balance readings were acquired for 15 s and time-averaged to filter the fluctuations due to turbulence, vibrations and other external factors. The non-dimensional force coefficients were defined using the freestream dynamic pressure, q_∞, and the wing planform area, S, as reference values. The uncertainty of the balance measurements was estimated from the deviation of repeated measurements. Tab. 5.1 reports the maximum absolute deviations from the mean measured for each force and moment coefficient for two different incidence settings.

TOTAL PRESSURE MEASUREMENTS

The total pressure distribution upstream of the fan inlet was measured with a L-shaped Pitot probe with an outer diameter of 0.6 mm. The probe was traversed in planes perpendicular to the freestream velocity direction with a variable spacing to account for the lo-

Table 5.1: Uncertainty values on the forces and moments coefficient measured through the external six-components balance.

	C_L	C_D	C_Y	$C_{\mathscr{M}}$	$C_{\mathscr{N}}$	$C_{\mathscr{L}}$
$\alpha = 0°$ $\beta = 0°$	0.0005	0.0002	0.0004	0.0009	0.0007	0.0009
$\alpha = 12°$ $\beta = 0°$	0.0025	0.0004	0.0006	0.0010	0.0007	0.0012

cal gradients. The measurements were carried out both at cruise conditions ($\alpha = \beta = 0°$) and for non-zero angles of attack or sideslip. At cruise conditions, ($\alpha = \beta = 0°$) , the total pressure distribution was measured also downstream of the fan outlet plane. For the cases under sideslip, measurements at positive and negative β were combined to obtain the complete flowfield. Fig. 5.5 shows the position and orientations of the survey planes used for the different cases.

At each probe position, after a settling time of 2 s, the pressure data were recorded through an electronic pressure scanner for a period of 5 s and averaged over this period. Simultaneously, the freestream static and total pressures were measured with a Pitot static probe mounted at the inlet of the test section and acquired through the same pressure scanner. In this way, possible fluctuations in the freestream conditions due to temperature or velocity drifts could be accounted for. The raw total pressure measurements were used to define the non-dimensional total pressure coefficient: $C_{p_t} = (p_t - p_{t\infty})/q_\infty$.

STEREOSCOPIC PARTICLE IMAGE VELOCIMETRY

Stereoscopic Particle Image Velocimetry (PIV) was employed to quantify the three velocity components in survey planes perpendicular to the freestream around the BLI propulsor for the cruise conditions ($\alpha = \beta = 0°$). The PIV planes coincided with the total pressure measurements planes which are sketched in Fig. 5.5a. The PIV system (laser, optics and cameras) were mounted on an electronic traversing system which was used to translate the measurement plane. Two LaVision© Imager sCMOS cameras (16-bit 2560 px × 2160 px) were used to record the particle images. The cameras were equipped with Nikon© AF Micro Nikkor 105 mm 1:2.8 D lenses set at an aperture of f/11 and mounted on LaVision© Scheimpflug adapter rings. A Quantel© Evergreen (double-pulse Nd:YAG, 200 mJ) laser and coated laser optics were used to generate the laser sheets with a thickness of around 2 mm. A Safex© Twin Fog smoke generator was used to seed the flow with Safex© Inside Nebelfluid. The seeding was injected downstream of the test section and spread uniformly in the entire flowfield within the wind-tunnel circuit. The image acquisition was controlled via a LaVision© Programmable Time Unit PTU X. The image pairs were recorded at a frequency of around 10 Hz and with a pulse delay of around 30 µs. For each case, a set of 500 phase-uncorrelated image pairs were acquired. The processing of the raw images was carried out in LaVision© Davis 8.4 using an iterative multi-pass correlation algorithm with a decreasing interrogation window size (from 96 px × 96 px for the first pass to 32 px × 32 px for the last pass, with an overlap factor of 50%), leading to a final vector field resolution of 0.25 mm. The uncertainty of the resulting velocity

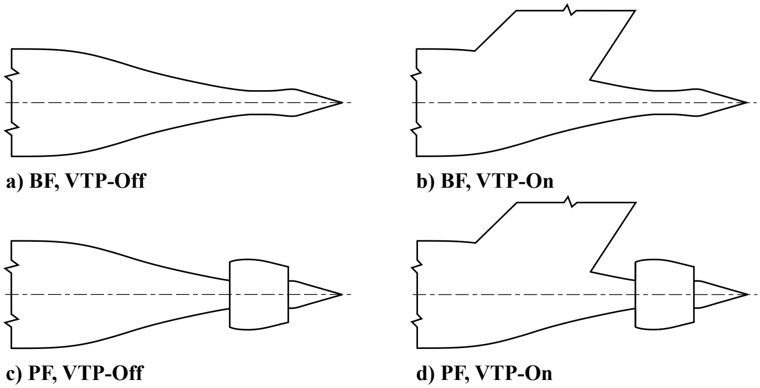

Figure 5.6: Geometrical configurations tested in the wind-tunnel experiments.

field was estimated directly at the correlation phase, using a statistical analysis of the correlation function implemented in LaVision© Davis 8.4 (see Ref.[63]). The uncertainty value resulted in around $0.010V_\infty$ for the velocity components and around $0.015V_\infty$ for the velocity magnitude.

5.2.3. INVESTIGATED CASES

GEOMETRIC CONFIGURATION

The modularity of the model allowed for the testing of four different geometric configurations, which are sketched in Fig. 5.6. In particular, the two main configurations were: a) the bare fuselage (BF), obtained by removing the BLI propulsor; b) the powered fuselage (PF), obtained by equipping the fuselage with the shrouded fan. For each of these configurations, the vertical tail plane could be installed (VTP-On) and disassembled (VTP-Off).

FLOW AND OPERATING CONDITIONS

All the measurements were taken at a freestream velocity, V_∞, of 40 m/s, corresponding to a freestream Reynolds number based on the wing mean chord, $Re_{\bar{c}}$, of around 460,000 and a Mach number of 0.12. At this freestream velocity, the freestream turbulence level is lower than 0.03% of V_∞ [79]. The angle of attack, α, was varied between $-6°$ and $12°$, while the angle of sideslip, β, was varied between $-8°$ and $8°$. Balance measurements were carried out in several conditions, including cases in which both α and β were varied together. Contrarily, other measurements were carried out in conditions obtained by varying one of the angles while the other was kept equal to zero. In addition, for the powered fuselage cases, the fan tip speed ratio, $U_{\mathrm{tip}}/V_\infty = \frac{1}{2}\Omega D_{\mathrm{f}}/V_\infty$, was varied by controlling the fan rotational speed, Ω.

5.2.4. MOMENTUM AND ENERGY ANALYSIS

The momentum and energy components in the flowfield were analyzed through the Power Balance Method [25] based on the total pressure and stereoscopic PIV measurements. The momentum and energy flow rates across the survey planes were evaluated through the following definitions:

$$F_x = \iint \left[(p_t - p_{t\infty}) + \frac{1}{2}(u - V_\infty)^2 - \frac{1}{2}(v^2 + w^2) \right] \mathrm{d}S \tag{5.1}$$

$$\dot{E}_a = \iint \frac{1}{2}\rho u (u - V_\infty)^2 \mathrm{d}S \tag{5.2}$$

$$\dot{E}_v = \iint \frac{1}{2}\rho u (v^2 + w^2) \mathrm{d}S \tag{5.3}$$

$$\dot{E}_p = \iint (p - p_\infty)(u - V_\infty) \mathrm{d}S \tag{5.4}$$

where: F_x is the axial momentum flow rate, $\dot{E}_a$ is the axial kinetic energy flow rate, $\dot{E}_v$ is the transverse kinetic energy flow rate, $\dot{E}_p$ is the pressure work rate; and where: u, v and w are the Cartesian velocity components, ρ is the flow density, p_t is the total pressure and p is the static pressure.

The integrals were carried out over a circular survey plane, S, perpendicular to the freestream velocity direction. The integration domain extended up to $r = 0.8R_\mathrm{b}$, to capture entirely the propulsor slipstream, the fuselage wake and the fuselage-VTP junction flow. The momentum flow rate, F_x, is defined positive when corresponding to a momentum deficit and hence to a force component in the drag direction. In selected cases, to ease the interpretation of the results, F_a is defined as $F_a = -F_x$, and hence positive for a momentum excess and a force component in the thrust direction. The velocity components, u, v and w, were directly measured through the stereoscopic PIV measurements, while the total pressure, p_t, was obtained from the Pitot measurements. The effect of the probe incidence angle on the total pressure readings was corrected using the velocity data. For each probe position, the corresponding inflow angle was evaluated from the velocity field and used to correct the Pitot measurement through the probe calibration curve. The calibration curve was measured by placing the probe in the freestream flow and by tilting it with respect to the freestream velocity direction. Throughout the present analysis, the flow was assumed to be incompressible and hence $\rho = \rho_\infty$. The static pressure, p, was computed from the stereoscopic PIV and Pitot data through the incompressible Bernoulli's equation.

5.3. RESULTS

The aerodynamic performance of the Propulsive Fuselage Concept, resulting from the complex aerodynamic interactions occurring between the BLI propulsor and the airframe was investigated through several measurement techniques. In this section, the main findings from the experimental study are presented and discussed. First, the effect of the BLI propulsor on the overall aircraft forces and moments is discussed. Subsequently, the flowfield around the BLI propulsor is investigated in detail. Finally, the distribution of the momentum and power components in the flowfield is presented. The results discussed in this section are focused on the aerodynamics of the powered fuselage (PF) configuration, while the performance of the bare fuselage (BF) configuration is discussed in the Appendix B.

5.3.1. EFFECT OF BLI PROPULSOR ON AERODYNAMIC FORCES AND MOMENTS

The effect of the BLI propulsor on the overall aircraft aerodynamic forces and moments was quantified in different operating conditions through the six-components external balance. Fig. 5.7 presents the aerodynamic force and moment coefficients induced by the BLI propulsor as a function of the fan tip speed ratio, U_{tip}/V_∞. The propulsor-induced components were obtained by subtracting the values measured for the bare fuselage (BF) case from those measured for the powered fuselage (PF) case ($\Delta C_{()} = C_{()}^{\text{PF}} - C_{()}^{\text{BF}}$). These $\Delta C_{()}$ components account for the effects of the fan and of the shroud. The results of the balance measurements for the BF configuration are presented in Fig. B.1 of the Appendix B.

Fig. 5.7a reports the propulsor-induced lift, drag and pitching moment coefficients, respectively ΔC_L, ΔC_D, and $\Delta C_{\mathscr{M}}$, at $\beta = 0°$ and $\alpha = 0°$ and $12°$. The measurements show that:

1. C_L is not affected by the propulsor installation and operating condition at $\alpha = 0°$. At $\alpha = 12°$, C_L slightly increases ($\Delta C_L \leq 0.01 C_L^{\text{BF}}$) due to the lift produced by the shroud and the component of the fan thrust in the lift direction.

2. C_D changes significantly due to the propulsive unit installation. At $\alpha = 0°$, the added drag due to the shrouded fan was compensated by the propulsor at around $U_{\text{tip}}/V_\infty = 1$, at which $C_D^{\text{BF}} = C_D^{\text{PF}}$. The addition of the VTP contributes to the drag increase but it is not significantly influenced by the fan installation and settings. A consistent behavior is found at $\alpha = 12°$, although higher drag is measured relatively to the respective BF case at a given U_{tip}/V_∞. This is due to the higher drag produced by the shroud and to the composition of the thrust in the lift and drag directions.

3. $C_{\mathscr{M}}$ is un-affected by the propulsor installation and setting at $\alpha = 0°$. However, at $\alpha = 12°$, the fan installation introduces a nose-down contribution to $C_{\mathscr{M}}$, due to the lift produced by the shroud contour and to the onset of an in-plane force component on the fan. The nose-down effect increases in magnitude for increasing U_{tip}/V_∞, suggesting that the fan in-plane force and the shroud lift increase at higher fan thrust settings.

Fig. 5.7b reports the propulsor-induced side force, yawing and rolling moment coefficients, respectively ΔC_Y, $\Delta C_{\mathscr{N}}$, and $\Delta C_{\mathscr{L}}$, at $\alpha = 0°$ and $\beta = 0°$ and $4°$. The measurements show that:

1. ΔC_Y is small at $\beta = 0°$ due to the symmetric flow conditions and the effect of the fan is negligible. However, at $\beta = 4°$, C_Y slightly decreased (increased in magnitude) for increasing U_{tip}/V_∞, due to an increase in magnitude of the side force produced by the shroud and of the in-plane fan force. Comparing the VTP-Off and VTP-On data, it can be seen that the presence of the tail affected the side force produced by the propulsor unit which resulted in a change in slope of the ΔC_Y curve.

2. $\Delta C_{\mathscr{N}}$ shows a behavior which is consistent with that of ΔC_Y. $\Delta C_{\mathscr{N}}$ is small at $\beta = 0°$ and is not affected by the fan, due to the symmetric flow conditions. At $\beta = 4°$,

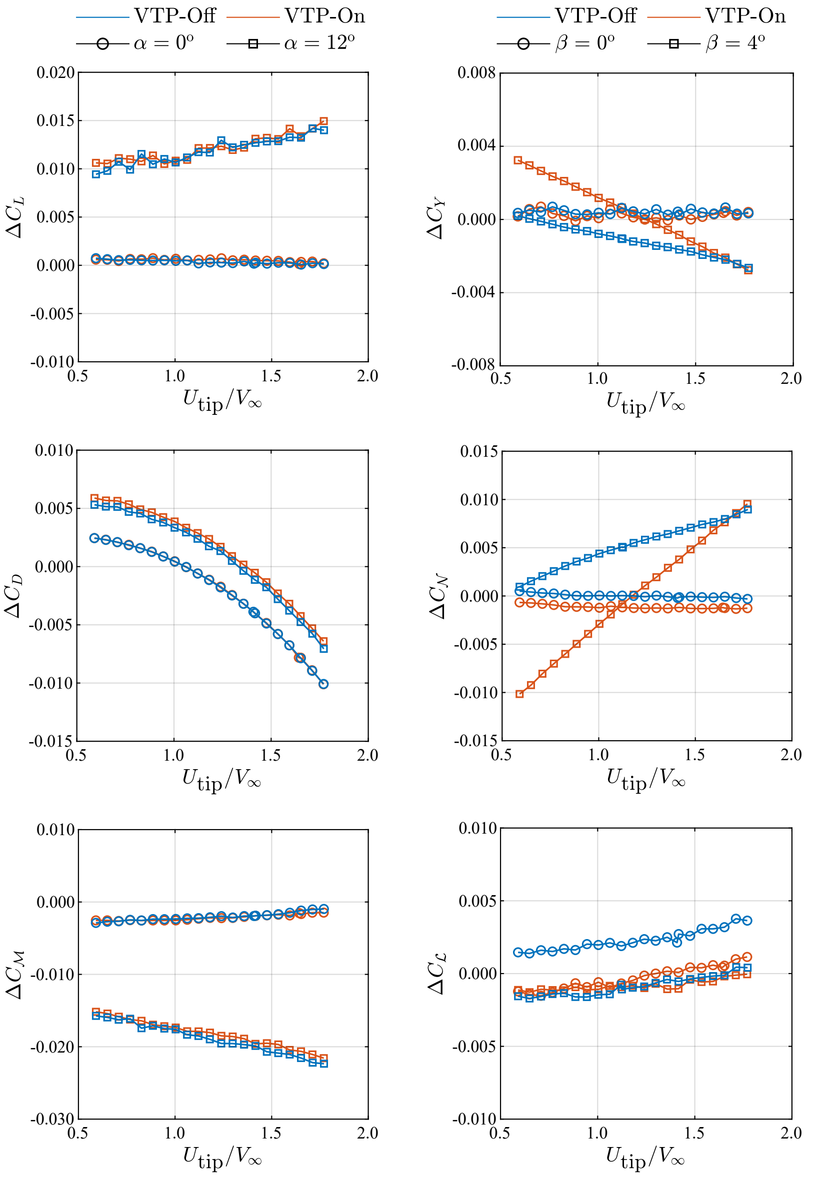

a) Longitudinal equilibrium ($\beta = 0^o$) **b) Lateral-directional equilibrium ($\alpha = 0^o$)**

Figure 5.7: Effect of the BLI propulsor on the aerodynamic forces and moments coefficients. Balance measurements taken at $Re_{\bar{c}} = 460,000$.

the onset of the side force on the propulsor introduces a positive yawing moment contribution which increases with U_{tip}/V_∞. As noted for ΔC_Y, the interaction with the VTP results in an increased slope of the curve in the VTP-On case.

3. The effect of the fan installation and setting on $C_{\mathscr{L}}$ is negligible both at $\beta = 0°$ and $\beta = 4°$. The small increase seen in $\Delta C_{\mathscr{L}}$ at $\beta = 0°$ for increasing U_{tip}/V_∞ might be due to the increasing torque induced by the fan on the outlet vanes.

5.3.2. DISTORTIONS OF THE BLI PROPULSOR INFLOW FIELD

Fig. 5.8 shows the total pressure coefficient, C_{p_t}, measured upstream of the shroud inlet for the powered fuselage (PF) case at various incidence conditions. In the PF cases the propulsor was operated at $U_{\text{tip}}/V_\infty = 1.7$. Moreover, for the cruise conditions ($\alpha = \beta = 0°$), both VTP-On and VTP-Off cases are shown. Fig. 5.8a and 5.8b show that in cruise conditions the fuselage boundary layer introduces total pressure gradients in the radial direction. In particular, at the survey plane location, the boundary layer thickness is approximately $0.65R_\text{b}$. In both VTP-Off and VTP-On cases, the bottom sector of the plot ($|\phi| > 120°$) is affected by the influence of the fuselage support strut (region A). The vertical tail plane introduces a non-uniform p_t distribution (region B) which is due to two sources: the viscous wake of the tail, introducing a narrow and relatively strong p_t deficit (approximately for $-5° < \phi < 5°$), and the junction flow, introducing a wide and relatively weak p_t deficit close to the fuselage wall (approximately for $-30° < \phi < 30°$).

The inflow total pressure was measured at $\alpha = 12°$ and $\beta = 0°$ to simulate conditions representative of take-off or top-of-climb maneuvers. Fig. 5.8c shows the p_t distribution for the PF, VTP-On case. The increased incidence angle results in the onset of a cross-flow around the fuselage section (see for example Ref. [48, 80]). This cross-flow displaces the lower p_t flow farther from the fuselage on the leeward side (region C), while higher p_t flow is entrained on the windward side (region D). The VTP causes a p_t deficit due to its viscous wake similarly to the $\alpha = 0°$ case (region E). However, the junction flow distortion is not clearly visible anymore close to the fuselage contour. This could be a consequence of the cross-flow component that displaces the horseshoe vortex further from the surface.

Fig. 5.8d reports the fan-inflow total pressure for $\alpha = 0°$ and $\beta = 4°$ for the PF, VTP-On case. Similarly to the case at $\alpha = 12°$, due to the cross-flow component around the fuselage contour, the low momentum fluid is displaced on the leeward side (region F) while higher p_t flow is entrained on the windward side (region G). Moreover, the vertical tail produces a strong asymmetric distortion which is enhanced by the fact that the tail is producing lift under the sideslip β. In particular, a low p_t region is found on the leeward side (corresponding to the suction side of the vertical tail) in proximity of the fuselage body (region H), presumably due to trailing edge separation. In fact, inside the fuselage boundary layer, the effective incidence angle of the tail sections are most likely higher than the sideslip angle, due to the lower axial velocity component. On the windward side (corresponding to the pressure side of the vertical tail), the p_t distribution typical of an horseshoe vortex can be identified, as a result of the junction flow developing at the tail-fuselage intersection (region I). Consequently, strong pressure gradients are found in the azimuthal direction around $\phi = 0°$.

The total pressure distribution at the fan inlet found in cruise conditions, displayed

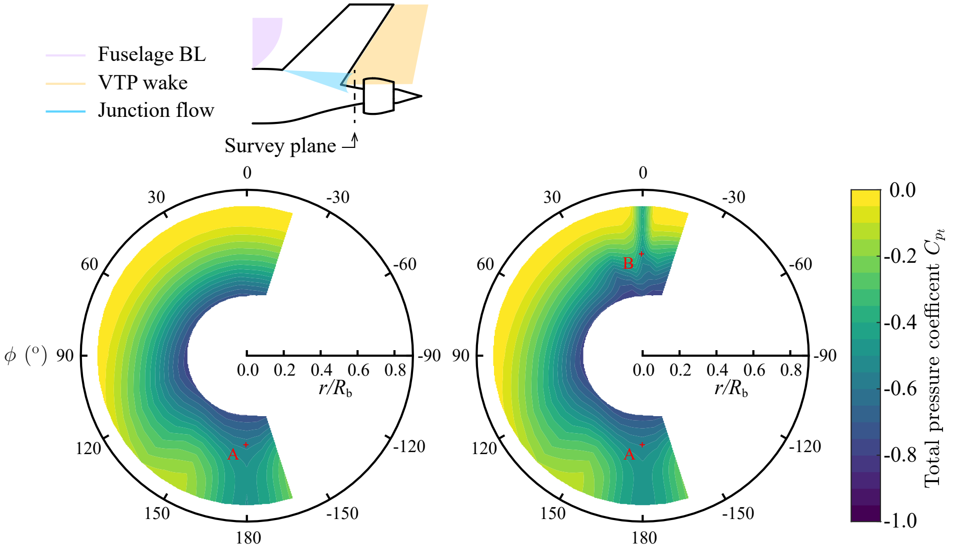

a) $\alpha = 0°$, $\beta = 0°$ (PF, VTP-Off)

b) $\alpha = 0°$, $\beta = 0°$ (PF, VTP-On)

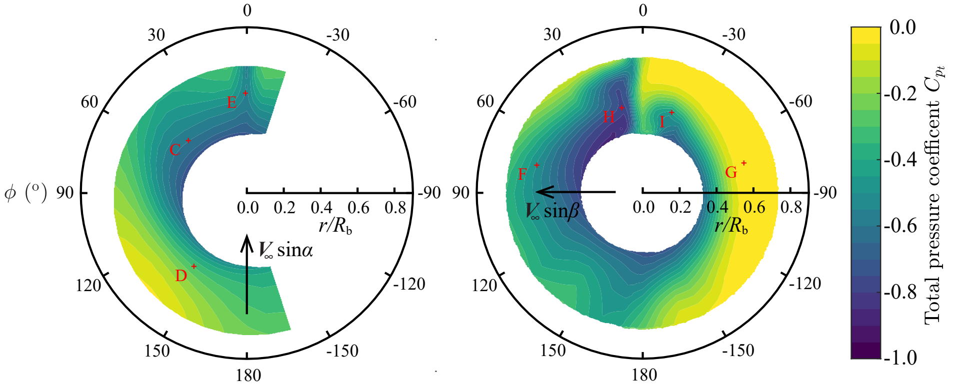

c) $\alpha = 12°$, $\beta = 0°$ (PF, VTP-On)

d) $\alpha = 0°$, $\beta = \pm 4°$ (PF, VTP-On)

Figure 5.8: Total pressure distributions upstream of the BLI propulsor for the powered fuselage (PF) case at various incidence angles (back view). Arrows indicate the direction of the crossflow component. Total pressure measurements taken at $Re_{\bar{c}} = 460{,}000$ and $U_{\text{tip}}/V_\infty = 1.7$.

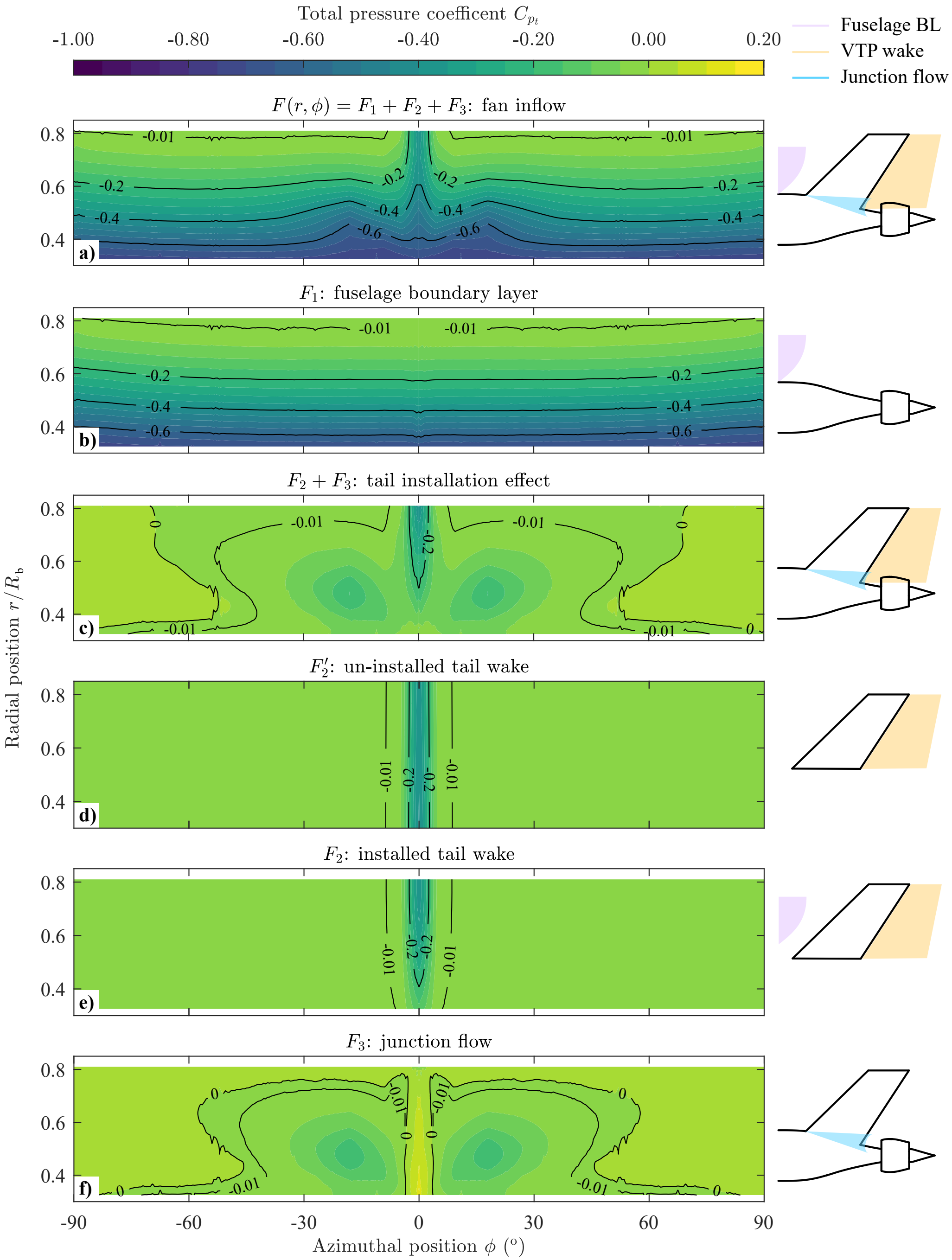

Figure 5.9: Fundamental components of the fan inflow total pressure distribution in cruise conditions. Total pressure measurements taken at $\alpha = 0° = \beta = 0°$, $U_{\text{tip}}/V_\infty = 1.7$ and $Re_{\bar{c}} = 460,000$.

in Fig. 5.8b, was decomposed in the three basic components associated to the fundamental aerodynamic phenomena that cause them, namely: the fuselage boundary layer, the VTP wake and the junction flow. The results of the decomposition are reported in Fig. 5.9. Note that the total pressure measurements were done only for $0° \leq \phi \leq 180°$ and then mirrored for visualization purposes. Moreover, the distortions induced by each of these distortion components were summarized through the standard distortion parameters DC(60), CDI and RDI, and are gathered in Tab. 5.2. The parameters were defined as (see Ref. [96]):

$$\mathrm{DC}(60) = \frac{p_t^{\mathrm{avg}} - p_{t,60°}^{\mathrm{avg}}}{p_t^{\mathrm{avg}}} \tag{5.5}$$

$$\mathrm{CDI} = \max_r \left(\frac{p_t^{\mathrm{avg}}(r) - p_t^{\mathrm{min}}(r)}{p_t^{\mathrm{avg}}} \right) \tag{5.6}$$

$$\mathrm{RDI} = \max \left(\frac{p_t^{\mathrm{avg}} - p_t^{\mathrm{avg}}(r_{\mathrm{min}})}{p_t^{\mathrm{avg}}}, \frac{p_t^{\mathrm{avg}} - p_t^{\mathrm{avg}}(r_{\mathrm{max}})}{p_t^{\mathrm{avg}}} \right) \tag{5.7}$$

where: p_t^{avg} is the average total pressure value in the survey plane (360°), $p_{t,60°}^{\mathrm{avg}}$ is the minimum average total pressure value in a sector of 60°, $p_t^{\mathrm{avg}}(r)$ is the average total pressure value at the radial position r, and $p_t^{\mathrm{min}}(r)$ is the minimum total pressure value at the radial position r.

The momentum distribution, C_{p_t}, shown in Fig. 5.9a, is primarily the result of the flow around the fuselage, vertical tail and their mutual interaction and is a function of both r and ϕ, i.e. $C_{p_t} = F(r, \phi)$.

F_1, shown in Fig. 5.9b, represents the momentum deficit due to the fuselage boundary layer and it was directly measured on the VTP Off configuration. Ideally, for an axisymmetric fuselage at zero incidence, and neglecting the effect of the wings, F_1 would be a function of r and constant with ϕ. In practice, due to the lifting wings and the interference of the fuselage support strut, the measured F_1 deviates from an axisymmetric condition.

Furthermore, the total pressure distribution component due to the tail installation was isolated by subtracting the VTP-On and VTP-Off cases and it is reported in Fig. 5.9c. This component can be further decomposed in two parts: F_2, representing the viscous wake of the VTP, and F_3, representing the effect of the tail-fuselage junction flow. To obtain F_2, firstly the un-installed tail wake, F_2', reported in Fig. 5.9d, was estimated. F_2' represents the momentum deficit distribution in the wake of the VTP operating in uniform freestream flow (hence without the effect of the fuselage boundary layer). F_2' was estimated by assuming a C_{p_t} profile equal in shape to the profile that was measured outside of the fuselage boundary layer ($r/R_{\mathrm{b}} = 0.795$). At each radial position r, this C_{p_t} profile was scaled proportionally to the local VTP chord length. This is valid in the assumption that the section drag scales linearly with the section chord length. Subsequently, the installed tail wake, F_2, reported in Fig. 5.9e, was obtained by scaling F_2' with the local total pressure ratio, $p_t/p_{t\infty}$, in order to take into account the non-uniform dynamic pressure impinging on the different VTP sections. This is valid in the assumption that radial

Table 5.2: Inlet distortion metrics for the fundamental components of the fan inflow total pressure distribution in cruise conditions (F: fan inflow; F_1: fuselage boundary layer; F_2: installed tail wake; F_3: junction flow). Total pressure measurements taken at $\alpha = 0° = \beta = 0°$, $U_{\text{tip}}/V_\infty = 1.7$ and $Re_{\bar{c}} = 460,000$.

	F	F_1	F_2	F_3
DC(60)	0.06	0.03	0.02	0.04
CDI	0.85	0.10	0.39	0.20
RDI	0.66	0.63	0.01	0.01

static pressure gradients can be neglected in the fuselage boundary layer. F_2 results in a p_t deficit concentrated around the center of the VTP ($-5° < \phi < 5°$) and non-linearly decreasing in intensity toward the fuselage wall. Finally, F_3, reported in Fig. 5.9f, was obtained as complementary of F_2 to the total tail installation effect. F_3 is strongly two-dimensional and characterized by a low total pressure region coincident with the core of the horse-shoe vortex.

The decomposition of C_{p_t} clearly shows that the total momentum deficit characterizing the BLI fan inflow can be obtained as a combination of elementary components associated with well-defined physical sources of momentum deficit. Comparing the different elements, it can be concluded that the lowest p_t values are induced by the fuselage boundary layer (Fig. 5.9b). However, since this deficit is approximately axisymmetric, it does not induce non-uniform disk loads and the design of the BLI propulsor can be adapted to sustain the distortion with minor performance penalties (see for example Ref. [42]). On the contrary, the inlet distortions induced by the tail installation will induce non-uniform disk loads and hence potentially affect the aero-acoustic and aero-mechanical performance of the BLI fan [91, 92]. This qualitative analysis is supported by the distortion parameters reported in Tab. 5.2. In fact, it can be observed that the momentum deficit due to the fuselage boundary layer, F_1, contributes with the highest RDI coefficient, while the VPT wake, F_2, is characterized by the highest CDI coefficient. Overall, the DC(60) values measured are relatively low due to the fact that the axisymmetric component of the inlet distortions (F_1) is dominant and the strongest non-axisymmetric component of the distortions (F_2) is concentrated in a narrow sector.

Stereoscopic PIV measurements were carried out in a plane perpendicular to the freestream direction at $x/L_b = 0.89$ to quantify the velocity field at the shroud inlet in cruise conditions (see Sec. 5.2.2). Fig. 5.10 reports the three velocity components, u, v, and w, together with the swirl angle, θ, and the axial vorticity component, ω_x, for the BF, VTP-On configuration.

Fig. 5.10b displays the axial velocity contour which, similarly to the C_{p_t} in Fig. 5.8b, is characterized by the fuselage boundary layer, VTP wake (region A) and junction flow (region B). The VTP influences the fan inflow field with in-plane velocity components, which can be easily visualized in Fig. 5.10a. In fact, in the VPT wake, the lateral velocity component, v, is directed toward the center of the wake itself (Fig. 5.10c) due to the wake contraction. Moreover, a positive vertical (spanwise) velocity component, w, is found (Fig. 5.10d). This vertical flow, directed from the root to the tip of the tail, is due to the onset of a crossflow component in the tail boundary layer induced by the leading edge

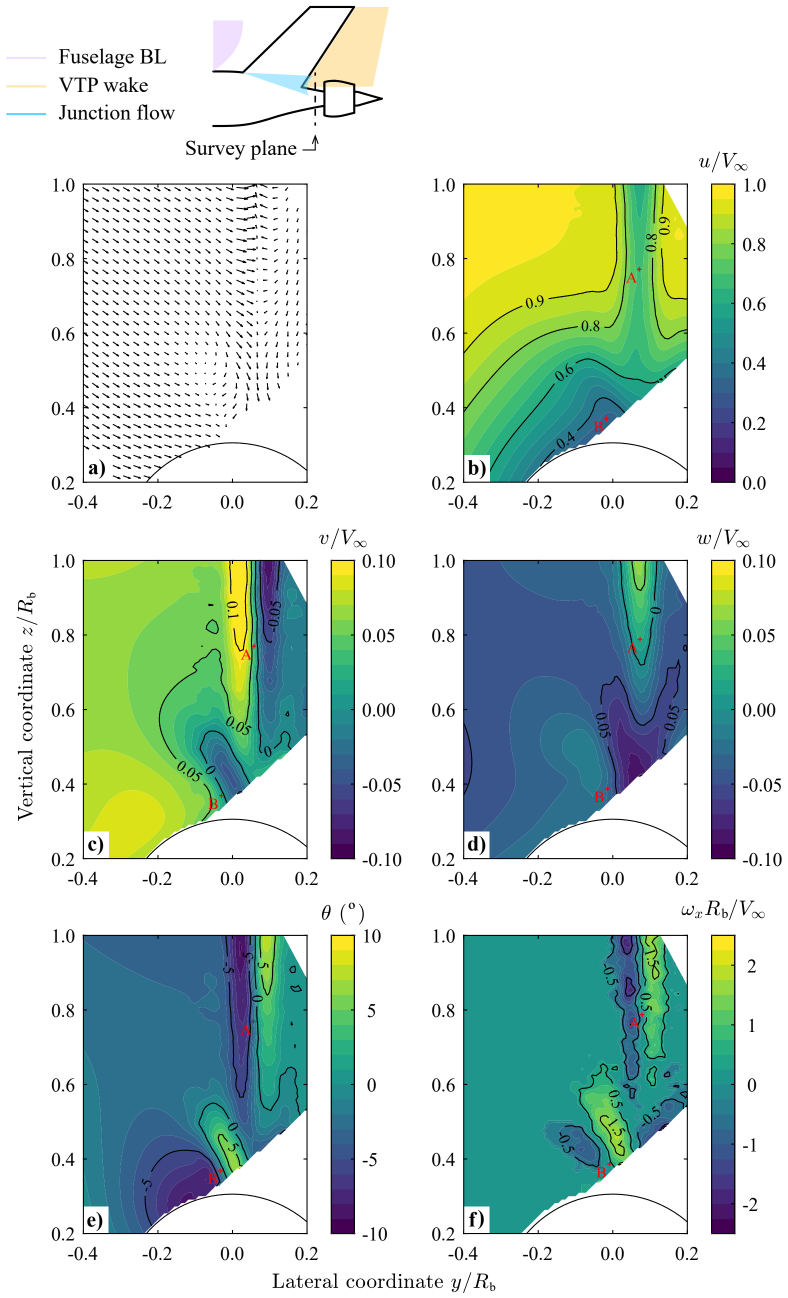

Figure 5.10: Flowfield at $x/L_b = 0.89$ for the BF, VTP-On configuration (back view). Stereoscopic PIV measurements for $\alpha = 0° = \beta = 0°$ and $Re_{\bar{c}} = 460,000$.

sweep. These v and w distributions have two direct consequences on the fan inflow. First, downstream of the tail plane, a velocity tangent to the fan plane is induced, which is co-rotating with the blades on the approaching-blade side (in this case left-hand side) and counter-rotating on the retreating-blade side (in this case right-hand case). This results in a swirl angle, θ, displayed in Fig. 5.10e, peaking at around $\pm 8^\circ$ in the VPT wake. Second, the vertical crossflow in the VTP boundary layer introduces streamwise vorticity ω_x that is transported downstream and ingested by the fan (Fig. 5.10f).

5.3.3. FLOWFIELD DOWNSTREAM OF THE BLI PROPULSOR

The flowfield downstream of the BLI propulsor was quantified through total pressure and stereoscopic PIV measurements on a survey plane perpendicular to the freestream velocity direction located at the fuselage trailing edge (plane at $x/L_\mathrm{b} = 1$ of Fig. 5.5). The measurements were carried out at $\alpha = \beta = 0^\circ$ and at $U_\mathrm{tip}/V_\infty = 1.7$. The distributions of total pressure, p_t, axial velocity velocity, u, tangential velocity, v_t, and axial vorticity, ω_x, are reported in Fig. 5.11.

The fan slipstream clearly shows a total pressure and axial velocity higher than the freestream (Fig. 5.11a and Fig. 5.11b, respectively). The low total pressure and velocity region around the fuselage axis is due to the onset of a vortical structure around the fuselage hub. This structure, induced by the fan slipstream, was analyzed in detail in a previous related work [97]. Furthermore, C_{p_t} and u show a non-axisymmetric distribution over the entire slipstream annulus. In particular, the wakes of the outlet vanes (see Fig. 5.12) are visible as they are characterized by a relatively lower total pressure and axial velocity.

Moreover, the outer region of the slipstream is affected by the presence of streamwise vortices (Fig. 5.11d) which induce the structures labeled as A and B in Fig. 5.11. These vortices are thought to be due to the interactions between the shroud-vanes junction flow and the fan slipstream, as sketched in Fig. 5.12. The horseshoe vortex generated at the intersection between the outlet and inlet vanes and the shroud results in five pairs of counter-rotating vortices, corresponding to the vortices A and B respectively. These vortices are convected downstream in the fan slipstream, hence following an helical trajectory. The viscous interaction with the swirling flow in the fan slipstream results in an enhanced dissipation of the co-rotating ($+\Gamma$) filament while keeping the counter-rotating filament ($-\Gamma$) stable. It must be noted that, though consistent with the experimental observations, no experimental data are available to directly validate the proposed phenomena. A more detailed investigation of the flowfield is required through dedicated measurements of numerical analysis, possibly with time-resolved flow data.

Finally, the tangential velocity component, v_t (Fig. 5.11c), has a uniform distribution in the center of the fan slipstream and strongly increases toward the hub region due to the presence of the hub vortex.

5.3.4. FLOW MOMENTUM AND POWER ANALYSIS

The total pressure and velocity data were combined to estimate the main momentum and power fluxes across a survey plane perpendicular to the flow and positioned at $x/L_\mathrm{b} = 0.89$ and at $x/L_\mathrm{b} = 1$ for the BF and PF configurations. The terminology, main equations and procedures used are discussed in Sec. 4.2.4. Fig. 5.13 reports the distribu-

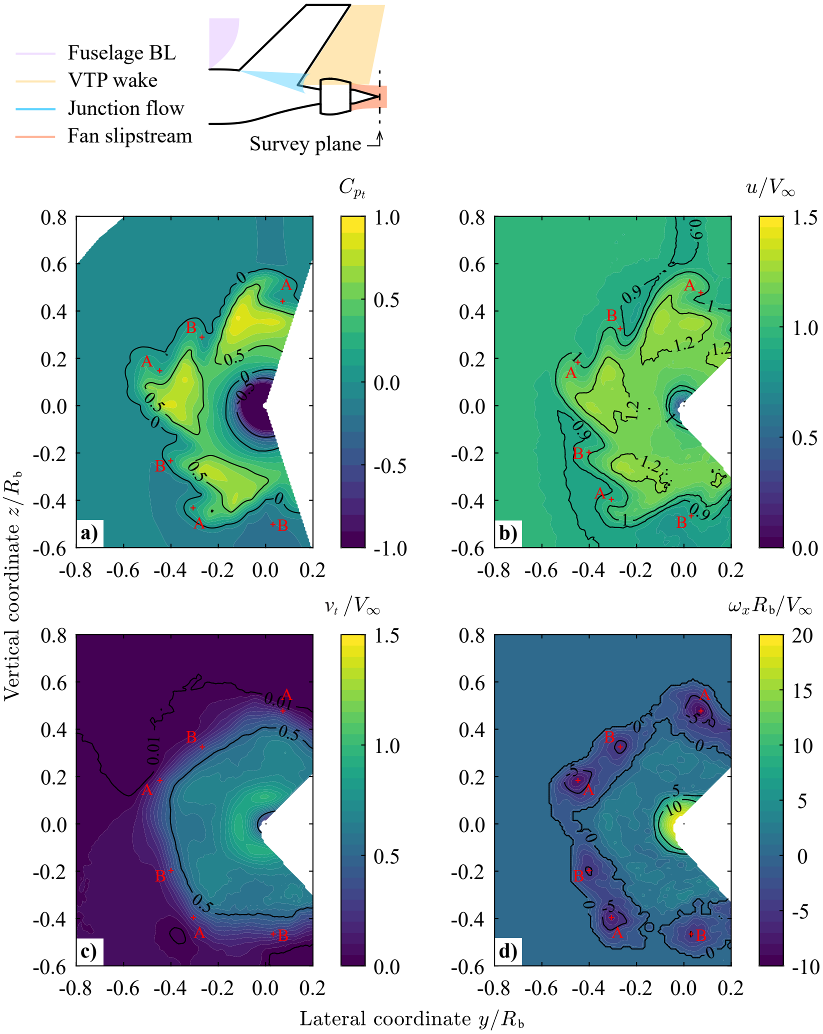

Figure 5.11: Flowfield at $x/L_b = 1$ for the PF, VTP-On configuration (back view). Total pressure and stereoscopic PIV measurements for $\alpha = 0^\circ = \beta = 0^\circ$, $U_{\text{tip}}/V_\infty = 1.7$ and $Re_{\bar{c}} = 460,000$.

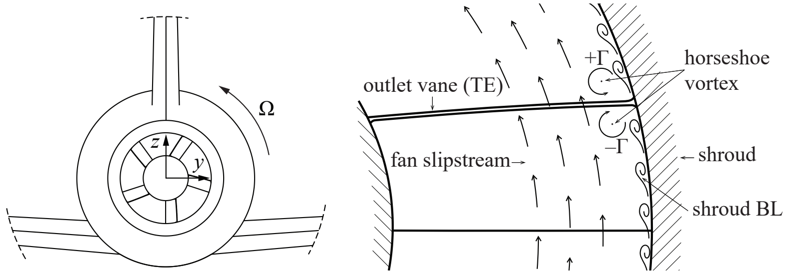

Figure 5.12: Schematic of the flow interactions between the fan slipstream and the viscous flow around the vane and shroud surfaces.

tion of the momentum and power flux densities in the survey planes. The fluxes, dF_a, $d\dot{E}_a$, $d\dot{E}_v$, and $d\dot{E}_p$, represent the amount of momentum or power transported through the survey plane per unit area and their surface integral is equal to the respective flow rates, F_x, $\dot{E}_a$, $\dot{E}_v$, $\dot{E}_p$, defined in Sec. 4.2.4. The momentum and power flux densities were expressed as ratio to D_0 and $D_0 V_\infty$, respectively, where D_0 is the measured drag of the BF, VTP-On case at $\alpha = \beta = 0°$. Therefore, the momentum and power terms were related to a reference drag and drag power associated to the baseline aircraft configuration. In particular, in the calculation of D_0 the drag of the fuselage strut was estimated through a 2-D viscous flow solver (`XFOIL`, Ref. [98]) and subtracted from the balance measurements.

Fig.5.13a shows the momentum flux density, $dF_a = -dF_x$, which is positive for a local momentum excess and negative for a local momentum deficit. Clearly, for the BF cases, dF_a shows a momentum deficit in the fuselage boundary layer and in the wake of the VTP on both survey planes. For the PF configuration, a momentum excess is found in the fan slipstream while a strong momentum deficit is measured around the fuselage axis due to the onset of the vortical flow already discussed. Similarly, the axial kinetic energy flux density, $d\dot{E}_a$ in Fig. 5.13b, shows that for the BF case the kinetic energy flux is concentrated in the regions of momentum deficit (i.e. the fuselage boundary layer and the VTP wake). However, for the PF case, $d\dot{E}_a$ shows relatively low values thanks to the axial velocity induced by the BLI fan. Contrarily, as shown in Fig. 5.13c, the transverse kinetic energy flux density, $d\dot{E}_v$, is relatively low for the BF cases. For the PF case, the swirl velocity induced by the fan resulted in a strong $d\dot{E}_v$, which reaches the maximum values in the vortical flow region around the fuselage axis. Finally, the pressure work flux, $d\dot{E}_p$ in Fig. 5.13d, shows that for the BF case the flow is expanded in the fuselage boundary layer at $x/L_\text{b} = 0.89$ and that the static pressure recovers substantially already at $x/L_\text{b} = 1$. For the PF case, the static pressure slightly exceeds the freestream value in the fan slipstream while very low pressure is found the vortical structure around the fuselage axis.

Fig. 5.14 reports the momentum and energy flow rates obtained as surface integrals of the flux densities discussed above. As already discussed, the momentum and power terms are expressed in terms of D_0 and $D_0 V_\infty$. It can be seen that for the BF case at $x/L_\text{b} = 0.89$ a momentum flow rate equal to approximately 16% of the total aircraft drag was measured in the survey plane. Moreover, F_x increased to almost 20% of D_0 at $x/L_\text{b} = 1$. This suggests that a substantial share of momentum in the fuselage boundary layer

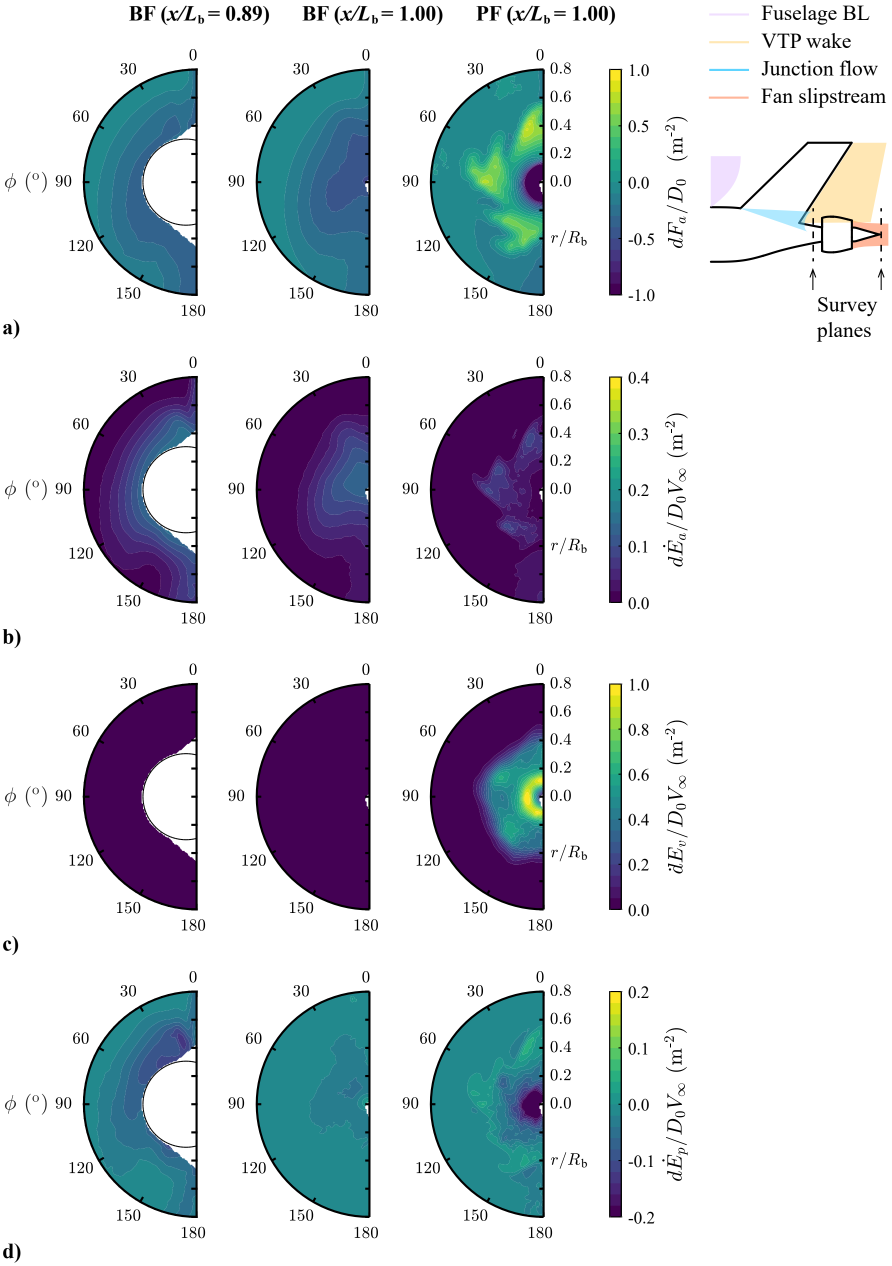

Figure 5.13: Distributions of the momentum and energy flux densities at x/L_b = 0.89 and x/L_b = 1.00 for the BF, VTP-On and PF, VTP-On cases (back view). Total pressure and stereoscopic PIV measurements for $\alpha = 0° = \beta = 0°$, $U_{tip}/V_\infty = 1.7$ (PF case) and $Re_{\bar{c}} = 460,000$.

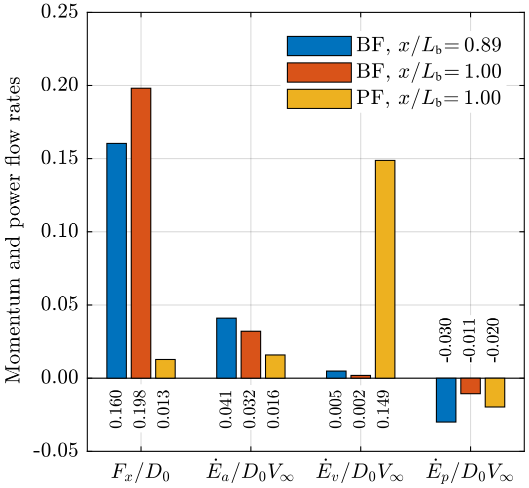

Figure 5.14: Integral momentum and energy flow rates at $x/L_b = 0.89$ and $x/L_b = 1.00$ for different fuselage configurations. Measurements for $\alpha = 0° = \beta = 0°$.

(around 20-25%), associated to the fuselage body drag, is dissipated in the flow around the contracting aft-cone of the fuselage body. This shows very good consistency with the results of a related study focused on the study of the same fuselage geometry in a 2-D axisymmetric setup [97].

The kinetic energy flow rate, $\dot{E}_a$, shows an opposite variation when moving from $x/L_b = 0.89$ to $x/L_b = 1$ for the BF case, resulting in around 25% lower flow rate at the trailing edge. This is due to the contributions to $\dot{E}_a$ found in the wakes of the VTP and of the fuselage support strut which are clearly visible at $x/L_b = 0.89$ and are much weaker at $x/L_b = 1$. In fact, the results of a previous related work (Ref. [97]) have shown that, for the same fuselage geometry without the VTP and the fuselage strut, $\dot{E}_a$, has a similar value at $x/L_b = 0.89$ and $x/L_b = 1$. For the PF case, the value of $\dot{E}_a$ was effectively reduced of around 50% at $x/L_b = 1$ compared to the BF case. The analysis of $\dot{E}_a$ shows that: first, around 3-4% of the total aircraft drag power, D_0V_∞, is transported and dissipated in the wake of the aircraft; this values represent the ideal power benefit that could be achieved with a so-called ideal BLI propulsor (see Ref. [25]). Moreover, the acceleration imposed by the BLI fan on the low-momentum fuselage boundary layer effectively reduces $\dot{E}_a$ and hence the wake dissipation.

The transverse kinetic energy flow rate, $\dot{E}_v$, shows very small values for the BF cases, due to the relatively small in-plane velocity components. On the contrary, $\dot{E}_v$ is the dominant factor for the PF case, due to the relatively strong swirl component in the fan slipstream. This component can be mitigated with an accurate design of the outlet vanes to recover the swirl velocity induced by the fan stage. Finally, the pressure work rate, $\dot{E}_p$, shows a negative value for the BF cases, due to the fact that the flow accelerates (decreasing pressure) due to the fuselage curvature. The expanded flow then undergoes a compression (increasing pressure) around the contracting aft-cone toward the trailing edge and the associated pressure recovery results in a decreasing (in magnitude) pressure work rate at $x/L_\mathrm{b} = 1$. The decrease in $\dot{E}_p$ for the PF case due to the BLI fan is due to the low static pressure found in the core of the vortical flow around the fuselage axis (see again Fig. 5.13d).

5.4. CONCLUSIONS

This chapter has presented an experimental analysis of an aircraft featuring a fuselage-mounted boundary-layer ingesting propulsor representative of the CENTRELINE Propulsive Fuselage Concept. The wind-tunnel tests were carried out in the low-speed wind-tunnel facilities of Delft University of Technology. The measurements were performed at a mean-chord-based Reynolds number of 460,000 and a Mach number of 0.12. As a reference, in full-scale cruise conditions the Reynolds and Mach numbers would be 40,000,000 and 0.82, respectively.
The goals of the experiment were:

1. To study the effect of the fuselage-mounted BLI propulsor on the overall-aircraft aerodynamic forces and moments of a complete aircraft configuration under realistic angles of incidence and relative thrust conditions.
2. To characterize the flowfield around the BLI propulsor and the aerodynamic interactions occurring between the propulsor and the airframe.

The analysis of the experimental data shows that:

1. In symmetric conditions ($\alpha = \beta = 0°$ and $U_\mathrm{tip}/V_\infty = 1.7$), the effect of the BLI propulsor on the aircraft forces and moments are mostly limited to the thrust–drag equilibrium. However, at incidence, the BLI propulsor showed a non-negligible effect on both longitudinal and lateral-directional equilibrium.
2. In symmetric conditions, the fuselage boundary layer represents the strongest distortion to the fan inflow while the influence of the wing lift and downwash is secondary. The vertical tail plane (VTP) introduces a total pressure deficit which can be decomposed in two contributions: the VTP viscous wake, with a restricted azimuthal extension ($-5° < \phi < 5°$), and the horseshoe vortex structure that develops at the fuselage-tail junction. The VTP wake induces in-plane velocity components, associated with the wake contraction and spanwise crossflow, which create non-negligible swirl at the BLI propulsor inlet.
3. In off-design conditions ($\alpha, \beta \neq 0°$), the crossflow component around the fuselage contour introduces a non-axisymmetric distortion characterized by low total pressure on the leeward side and high total pressure on the windward side. At $\beta = 4°$, the vertical tail strongly affects the inflow field as it produces lift under the sideslip. The associated total pressure distortion is characterized by sharp gradients in the azimuthal and radial directions.
4. The BLI propulsor strongly alters the flow around the fuselage aft-section. The flowfield is characterized by regions of relatively high momentum (fan slipstream) and low momentum (hub vortex).

5. An axial momentum flow rate equal to 16% and 20% of the total aircraft drag was estimated at $x/L = 0.89$ and $x/L = 1$, respectively, which represent the drag force associated to the fuselage body and VTP root section. Moreover, the axial kinetic energy flow rate, $\dot{E}_a$, varied from 3% to 4% of the aircraft drag power, $D_0 V_\infty$, across the same planes. This indicates that a power saving of around 3-4% could be achieved through an ideal BLI propulsor.

6. The axial momentum and kinetic energy flow rates at the fuselage trailing edge are substantially reduced by the BLI propulsor, suggesting that the acceleration induced on the boundary layer flow by the BLI propulsor effectively decreases $\dot{E}_a$ and hence the dissipation occurring in the aircraft wake. However, in the investigated setup, only 50% of the available axial kinetic energy flow rate was recovered by the BLI fan.

The previous chapters have discussed the aerodynamics of a fuselage-BLI configuration in several operating conditions and with an increasing grade of geometrical complexity. The discussion was based exclusively on experimental data gathered through *ad hoc* wind-tunnel campaigns held at the low speed facilities of TU Delft. These experiments provided valuable insights in the aerodynamics of such configuration, identifying the flow phenomena that drive the flowfield topology and the aircraft performance. However, the quantitative analysis carried out based on the experimental data are only valid for the tested model and at the test conditions.

Generalization to different shapes and conditions is not trivial, if possible at all. More specifically, this means that what found in the previous chapters has to be justified and put into perspective if one wants to take some conclusions to drive the design of a full-scale commercial aircraft.

Although giving a detailed estimation of full-aircraft performance with BLI lies outside of the focus of the current thesis, the next chapter will provide some insights into the effects of the main aerodynamic scaling parameters.

6

AERODYNAMIC SCALING EFFECTS ON AN AXISYMMETRIC PFC

6.1. INTRODUCTION

MOTIVATION

In Chapters 3-5, the aerodynamics of axisymmetric bodies has been studied both in a clean configuration (Chapter 3) and with a BLI propulsor integrated at the aft-section of the fuselage (Chapters 4 and 5). These aerodynamic investigations were based on results of low-subsonic, sub-scale wind-tunnel experiments. The operating conditions at which these studies were performed substantially differ from those typical of a passenger aircraft in flight or, in particular, of the CENTRELINE Propulsive Fuselage Concept (see e.g. Ref. [29]). Consequently, the results obtained from the experiments and the conclusions drawn from their results are inherently valid at the conditions at which the experiments were carried out. However, the ultimate goal of the presented research work is to improve the understanding that we have of BLI configurations *at real flight conditions*.

In order to do so, it is paramount to understand how the sub-scaling affects the experimental results both from a qualitative and quantitative perspective. In fact, a better understanding of the effects of the sub-scaling allows a higher confidence in the validity of the results extrapolated to full-scale and contributes in bridging the gap between the laboratory model and the actual case study.

Within the CENTRELINE project, numerical studies focused on the design and analysis of the BLI fan at flight conditions (Ref. [51]), and have been validated against low-speed experiments (Ref. [42]). These previous works provide detailed insight into the aerodynamics of BLI-ingesting fans and into the scaling effects on their performance, of which compressibility is a dominant factor. Moreover, numerical studies at full-scale flight conditions have been performed to investigate and design the overall aircraft aerodynamics (Ref. [94]). Although providing insights into the aerodynamic performance of the CENTRELINE aircraft in both cruise and off-design conditions, the scaling effects on the wind-tunnel experiments were not investigated in details.

In this chapter, the effects of scaling from full-scale flight conditions to wind-tunnel scale on the aerodynamic performance of the fuselage-BLI configuration are investigated through a numerical study. The aim of this work is to understand how the dominant physical mechanisms of BLI are simulated at the wind-tunnel scale and, consequently, how effective low-speed sub-scale testing is to study the aerodynamics of such configurations both qualitatively and quantitatively.

FOCUS

The goal of this study is quite broad since aerodynamic scaling concerns different elements of the aircraft (i.e. wings, fuselage, propulsors) in different and complex ways. However, the focus of this analysis is to characterize the physical mechanisms that play a key role in the fuselage-BLI aerodynamics. Other aspects, albeit equally important to the overall aerodynamic performance of the aircraft system, are not considered in this study. In particular, only the fuselage and BLI propulsor were investigated. Other airframe elements, such as wing and tail surface, were removed from the study. In fact, the effects of scaling on these elements is not related to the specific configuration and can be studied separately. Moreover, the BLI propulsor is simulated through an actuator volume model, equivalent to the model implemented in the related numerical work of Ref. [94]. This approach was chosen since the main focus is on the effects of the BLI propulsor on the surrounding flow and its interactions with the fuselage and not on the details of the flow around the propulsor blades. Furthermore, the effects of aerodynamic scaling on the BLI fan design and aerodynamic performance is already discussed in great details by previous work (see again Ref. [42, 51]).

ASSUMPTIONS

Through the scaling process from the wind-tunnel to full-scale flight conditions, both the geometry and the operating conditions were modified. To narrow the scope of this study, some assumptions on the geometry scaling and operating conditions were made.

First, the geometry of the fuselage and nacelle contours were linearly scaled to match the size of the wind-tunnel model and the size of the full-scale CENTRELINE aircraft. The atmospheric and flow conditions were selected to match the typical conditions encountered at both the two scales considered. In particular, at both scales, the simulations were carried out at conditions for which the dominant aerodynamic scaling parameters, the Reynolds and Mach numbers, were representative of the wind-tunnel and real-flight conditions.

As already mentioned in Chapter 4, the propulsor height of the wind-tunnel model is scaled proportionally to the local boundary-layer momentum thickness. This scaling principle is aimed at ensuring that through the scaling process, the relative size of the propulsor and ingested boundary layer is maintained constant, rather than the relative size between the propulsor and the fuselage body. Moreover, at each scale considered, the thrust of the propulsor is set equal to the drag of the isolated fuselage in the respective scale and conditions. This is to ensure that the momentum addition of the propulsor is scaled with the momentum deficit (i.e. drag) produced by the fuselage body.

More details on the geometry, operating conditions and scaling procedure, together with the details of the numerical setup are given in the following section.

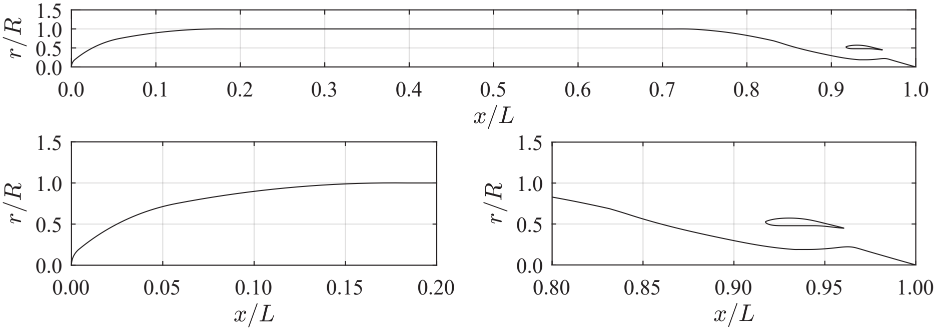

Figure 6.1: Fuselage geometry (WT scale) tested in the numerical analysis.

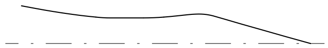

a) Bare Fuselage (BF)

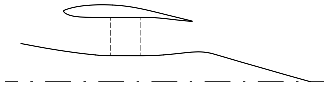

b) Powered Fuselage (PF)

Figure 6.2: Definition of the geometric configurations tested in the numerical analysis.

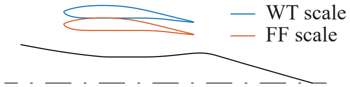

Figure 6.3: Comparison of the PF geometries at the two scales considered in the numerical analysis.

6.2. METHODS

6.2.1. STUDY CASES

To study the effects of Reynolds and Mach number scaling on the aerodynamics of BLI, numerical simulations were carried out on an axisymmetric fuselage body with BLI propulsion at two different scales: 1) The *wind-tunnel scale* (WT scale), representative of the physical size and operating conditions of the wind-tunnel experiments discussed in the previous Chapters 3-5; 2) The *full-scale flight scale* (FF scale), representative of the conditions typical of a long-range commercial aircraft in transonic cruise.

GEOMETRIC CONFIGURATIONS

The axisymmetric fuselage body analyzed in this study coincided with the geometry tested in the wind-tunnel campaign discussed in Chapter 4 and 5, in which the fuselage contour was scaled down from the CENTRELINE Propulsive Fuselage Concept (see e.g. [29, 74]). The fuselage aft-cone features an integrated boundary-layer ingesting shrouded propulsor. The fuselage geometry (at wind-tunnel scale) is shown in Figure 6.1. During the simulations, two different geometric configurations were tested: the *bare-fuselage* (BF) configuration, consisting of the fuselage body without the BLI propulsor, and the *powered-fuselage* (PF) configuration, consisting of the fuselage body with the BLI propulsor. The two configurations are sketched in Figure 6.2.

During the process of scaling down the fuselage geometry from the FF conditions to the WT conditions, the relative size between the propulsor and the fuselage was con-

Table 6.1: Operating conditions defined for the numerical simulations.

	WT scale	FF scale
Scaling parameters		
Re_L	4.8e6	4.1e8
M	0.12	0.82
Geometric parameters		
L (m)	1.776	67.60
R (m)	0.080	3.045
h_f/R	0.287	0.204
Operating conditions		
h (m)	0	9144 (FL300)
ρ (kg/m^3)	1.225	0.363
T (K)	288.15	288.80
p_atm (Pa)	101325	23842
V_∞ (m/s)	40.0	248.5

trolled to maintain aerodynamic similarities between the two scales. In fact, due to the Reynolds and Mach number differences, the relative size between the boundary layer and the fuselage body was expected to be different at the two scales considered. Therefore, the propulsor height, h_f , was scaled with respect to the momentum thickness, θ^*, at the propulsor plane of the BF configuration. In particular, the propulsor was scaled such that $\left.\frac{h_\mathrm{f}}{\theta^*}\right|_\mathrm{FF} = \left.\frac{h_\mathrm{f}}{\theta^*}\right|_\mathrm{WT} = 2.90$.

Figure 6.3 compares the propulsor sizes at WT and FF conditions, while the main geometrical properties of the fuselage at both WT scale and FF scale are summarized in Table 6.1.

OPERATING CONDITIONS

The WT cases were simulated at conditions that were typically encountered during the low-speed wind-tunnel testings: atmospheric conditions at sea level and a freestream Mach number, M_∞, of 0.12. The FF cases were simulated at the conditions of transonic cruise phase of the CENTRELINE configuration: atmospheric conditions at FL300+10K and at $M_\infty = 0.82$. The Reynolds number based on the fuselage length, Re_L, was equal to 4.8×10^6 and 4.1×10^8 for the WT and FF, respectively. The main properties defining the atmospheric and operating conditions are summarized in table 6.1.

6.2.2. COMPUTATIONAL SETUP

The numerical simulations were carried out using the ANSYS commercial CFD package. 2-D axisymmetric Reynolds Averaged Navier-Stokes (RANS) equations were solved with ANSYS Fluent, while the geometry and grid were created using ICEM CFD.

In both the WT and FF scale simulations, air was modeled as an ideal gas and the air viscosity was modeled using Sutherland's law. Turbulence was modeled using the Spalart-Allmaras model in the strain-vorticity formulation.

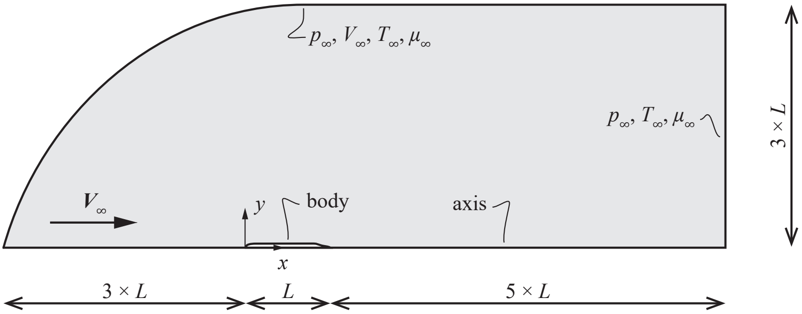

a) Fluid domain

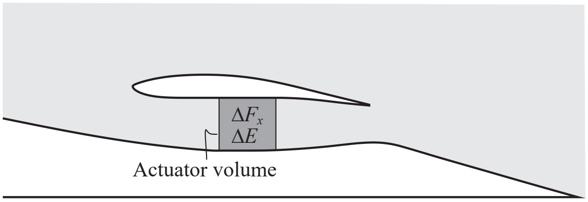

b) Actuator volume

Figure 6.4: Computational domain and boundary conditions used in the 2D-axisymmetric RANS simulations.

DOMAIN, BOUNDARY CONDITIONS AND SPATIAL DISCRETIZATION

The flow was simulated in a bullet-shaped domain as shown in Fig. 6.4a. The domain had an extension of 3 and 5 body lengths upstream and downstream of the fuselage body, respectively, while measuring $3L$ in the radial direction. Thanks to the condition of symmetry around the axis, a planar domain was used covering only the top part of the flowfield.

The boundary conditions were tailored to each case. For the low-subsonic cases at WT scale, velocity inlet conditions were used on the upstream and top boundaries, defining the values of static pressure, static temperature and velocity components. For the high-subsonic cases at FF scale, pressure farfield conditions were used, defining the values of static pressure, static temperature, Mach number and flow direction. In both cases, pressure outlet were used on the downstream boundary, defining the values of static pressure and static temperature. In all simulations, the freestream turbulent viscosity ratio was set to 3 in order to achieve fully turbulent boundary layers. [64]

The fluid domain was discretized using a structured mesh with quadrilateral elements. The fuselage and shroud contours was meshed with 600 and 400 elements, respectively, non-uniformly spaced along the longitudinal direction. The first layer height was tailored for the WT and FF scale simulations and fixed on all the no-slip walls to achieve a $y^+ < 1$ condition. The final grid size ranged between 400000 and 600000 elements for the BF and PF configurations, respectively. The grid resolution was based on the results of the mesh convergence studies of previous related works (see Refs. [94, 99, 100]).

PROPULSOR MODEL

In the numerical simulations of the fuselage in PF configuration, the effect of the propulsor on the flowfield was simulated with an Actuator Volume model, similar to what used in the numerical studies carried out in the CENTRELINE project (Ref. [94]). In particular, momentum and energy volumetric density sources, ΔF_x and ΔE, respectively, are defined for the grid cells contained in the volume enclosing the rotor blades, as shown in Fig. 6.4b. The momentum source was chosen to obtain the required resulting thrust equal to the drag of the fuselage in the BF conditions. The momentum source distribution was constant, representing a constant blade loading distribution. Moreover, only axial momentum sources were defined. As a consequence, the actuator volume produces only an axial force (thrust) while the tangential force component and the associated swirl velocity are ignored. Finally, the energy source was imposed to the work exerted by the actuator volume on the fluid per unit volume, $U\Delta F_x$, where U is the local axial velocity component.

During the simulations, the momentum source of the AV was set such to obtain a thrust component equal to the drag of the BF configuration.

SOLVER SETTING

Reynolds Averaged Navier-Stokes (RANS) equations were solved using ANSYS Fluent. A pressure-based, coupled solver was used with a pseudo-transient formulation. Gradients were computed with a Green-Gauss node based scheme, while second-order upwind discretization schemes were used for all the equations. Simulations were run for 20000 iterations, during which all the scaled, normalized residuals reached convergence at values between 10^{-8} and 10^{-10} and stayed constant for at least 5000 iterations.

6.3. RESULTS

6.3.1. THRUST–DRAG BOOK-KEEPING AND INPUT POWER ANALYSIS

To understand the effects of scaling on the aerodynamic performance of the bare fuselage (BF) and powered fuselage (PF) configurations, first the axial forces (drag and thrust) and required propulsive power are compared at WT and FF scales. Together with the drag coefficient, $C_D = D/\frac{1}{2}\rho V_\infty^2 \pi R^2$, both the pressure drag and viscous drag components, C_{D_p} and C_{D_v}, were extracted from the simulations results. Moreover, the thrust and input power supplied by the actuator volume (AV) were non-dimensionalized as $C_T = T/\frac{1}{2}\rho V_\infty^2 \pi R^2$ and $C_{P_K} = P_K/\frac{1}{2}\rho V_\infty^3 \pi R^2$. The values of these coefficients at WT scale and FF scale are reported in Tab. 6.2.

For the BF configuration, increasing the scaling approximately halves the fuselage C_D. This effect is predominantly associated to the increase in Reynolds number (see, for example, Ref. [60]). However, the scaling does not significantly affect the relative contributions of the pressure and viscous drag components. In fact, at both the WT and FF scales, the viscous drag term represents approximately 95% of the total drag.

For the PF configuration, the fuselage–shroud interaction plays an important role for the resulting total drag. Tab. 6.2 shows that for the PF configuration the pressure drag term of the fuselage, C_{D_p}, is negative at both WT and FF scales, resulting in a forward force contribution. This effect is due to the interaction between the pressure fields of the fuselage and of the shroud in presence of the actuator volume. As a result of the pressure

Table 6.2: Detail of the thrust, drag and power coefficients resulting from the CFD simulations at WT and FF scales and for the BF and PF configurations.

	Coefficient	WT scale		FF scale	
		BF	PF	BF	PF
Fuselage	C_{D_p}	0.0065	-0.0140	0.0049	-0.0213
	C_{D_v}	0.1258	0.1248	0.0642	0.0635
	C_D	0.1323	0.1108	0.0691	0.0422
Shroud	C_{D_p}	-	0.0236	-	0.0280
	C_{D_v}	-	0.0064	-	0.0025
	C_D	-	0.0301	-	0.0305
Propulsor	C_T	-	0.1323	-	0.0691
	C_{P_K}	-	0.1008	-	0.0402
Net	$\sum C_D - C_T$	0.1323	0.0086	0.0691	0.0036

distribution induced by the shroud and actuator disk on the fuselage surface, a forward force contribution is produced. Similarly, the shroud is subjected to an increased pressure drag. As a result, the overall pressure drag of the fuselage-shroud system is positive (contrary to the direction of flight). This interaction and its effects are enhanced by the increase in scaling as a consequence of the increased Mach number that amplifies the pressure gradients.

Moreover, in the PF configuration the actuator volume exerts a thrust equal to the fuselage drag in the BF configuration, as detailed in Sec. 6.2. This resulted in a positive overall net force (i.e. drag) for the entire system (i.e. fuselage, shroud and AV). This residual drag is due to the shroud drag and interaction effects and it is approximately 5% of the bare fuselage drag at both WT and FF scales. As already discussed, the drag coefficient of the BF configuration, C_D, decreases by almost 50% when going from the WT to the FF scale. As a consequence, relatively less thrust is exerted by the BLI propulsor. This results in an increase of the thrust-to-power coefficient ratio (C_T/C_{P_K}) of around 30% at FF scale.

6.3.2. EFFECTS OF SCALING ON THE BF CONFIGURATION PERFORMANCE

FLOWFIELD ANALYSIS

The effects of geometric and aerodynamic scaling on the bare fuselage (BF configuration of Fig. 6.2) were studied by comparing CFD simulations of the BF fuselage carried out at WT and FF scales.

Fig. 6.5 reports the Mach number field around the BF fuselage configuration at WT and FF scales. For both scales, the Mach number field clearly shows the stagnation at the leading edge and subsequent expansion around the nose section, the compression around the aft section, and the growth of the boundary layer along the body surface. Qualitatively, the increase of the Mach number, M_∞, and of the Reynolds number, Re_L, does not introduce substantial changes to the flowfield. In particular, the flowfield is fully subsonic (i.e. $M < 1$ everywhere) also at the FF scale conditions. As a consequence,

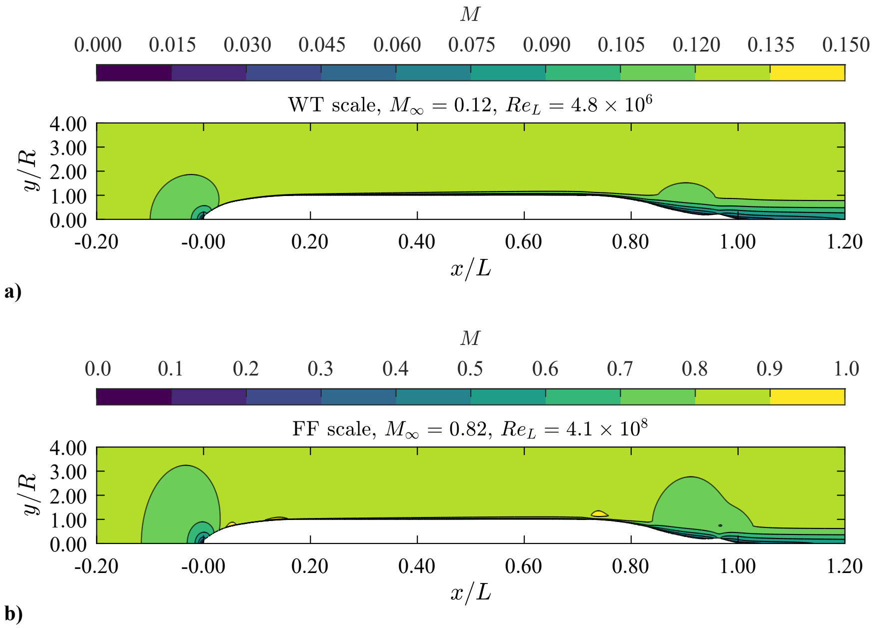

Figure 6.5: Mach number field for the BF configuration at WT and FF scales.

no strong compressibility effects (i.e. region of supersonic flows and shock-waves) are found. Furthermore, the effects of the increased M_∞ and Re_L can be appreciated on both the potential and viscous regions of the flowfield. In particular, the pressure gradients are enhanced, primarily due to the increase of the Mach number. On the other hand, the boundary layer and wake flows are relatively thinner as a consequence the higher Reynolds number and reduced viscous effects.

The effects of the Mach and Reynolds numbers on the potential and viscous flowfields can be done by comparing the surface pressure and skin friction coefficients for both the WT and FF scales, reported in Fig. 6.6. In particular, Fig. 6.6a confirms that the scaling mainly enhances uniformly the C_p across the entire body surface. Moreover, this variation is partially captured by a Mach-number based non-linear correction following from the linear-perturbation theory for axisymmetric bodies [101]. The correction, similarly to the well-known Prandtl-Glauert transformation for 2D flows, is applied to the WT scale results to scale them to the FF scale conditions. The differences between the corrected data and the FF scale can be ascribed to the fact that the correction is valid within the linearized small-perturbation theory with the assumption of inviscid flow. Both assumptions are not satisfied in the examined flow cases. Furthermore, Fig. 6.6b reports the skin friction coefficient, C_f, on the fuselage surface. The plot shows that C_f uniformly decreases along the entire fuselage surface when going from the WT to the FF scale. This variation is primarily induced by the Reynolds number increase. This is confirmed by the good agreement between the FF scale and the corrected WT scale results showed in Fig. 6.6b. The correction of the C_f at WT scale followed from the estimation

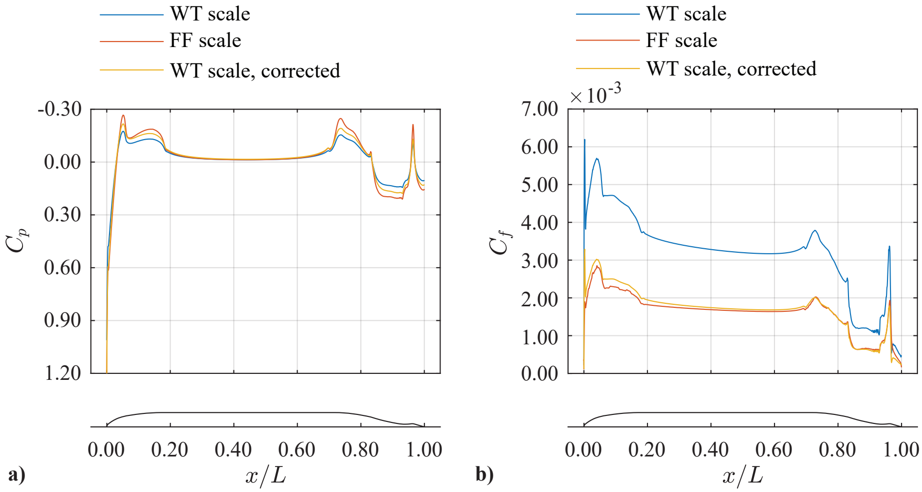

Figure 6.6: Pressure and skin friction coefficients on the fuselage body wall for the WT and FF scales.

of the skin friction over a turbulent flat plate [69].

The analysis of the Mach number field and of the surface pressure and shear forces distribution shows that the scaling quantitatively affects the flow around the fuselage but does not alter it substantially. Moreover, the changes in the surface flow can be reasonably well-explained with correction following from simplified models (i.e. linearized, small-perturbation models and flat-plate solutions).

BOUNDARY LAYER ANALYSIS

In this subsection, a more detailed analysis of the scaling effects on the fuselage boundary layer is presented. Particular attention is given to the development of the boundary layer around the aft-cone of the fuselage. Figure 6.7 reports the total pressure field around the aft section of the BF at both WT and FF scales. The contour of total pressure, p_t, clearly highlights the effect of the aerodynamic scaling on the fuselage boundary layer. In fact, the boundary layer, characterized by $p_t/p_{t\infty} < 1$, is relatively thinner in the FF case, as expected, due to the effects of the Reynolds and Mach numbers.

To analyze the difference in the boundary layer flow more quantitatively, the boundary layer integral parameters were computed as a function of the axial position. In particular, the boundary layer edge, δ_{99}, was defined as the radial position at which $p_t/p_{t,\infty} = 0.99$. At each x position, the displacement thickness, δ^*, momentum thickness, θ^*, and shape factor, H, were computed using the standard definitions of compressible planar

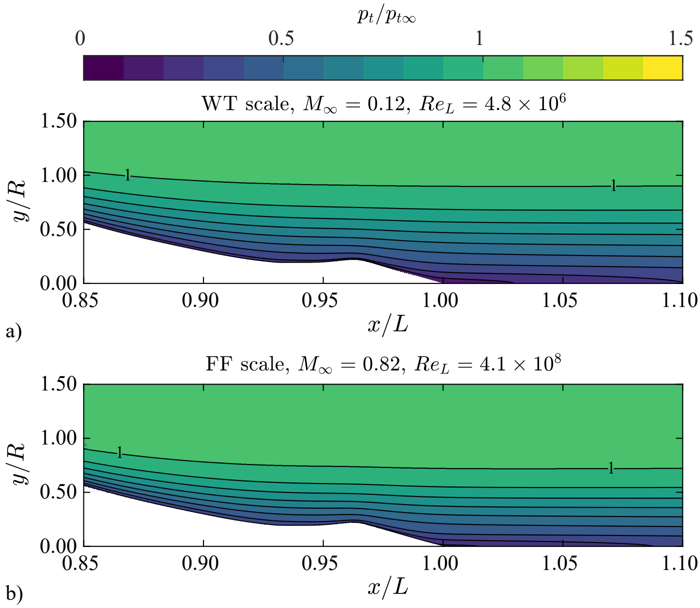

Figure 6.7: Total pressure field around the aft-cone section of the BF configuration at WT and FF scales.

thin boundary layers:

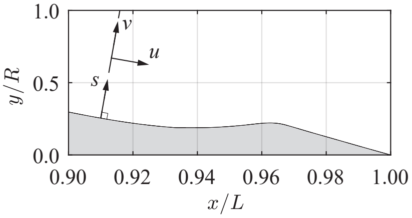

Figure 6.8: Reference system defined for the boundary layer analysis.

$$\begin{aligned} \delta^* &= \int_0^{\delta_{99}} \left(1 - \frac{\rho u}{\rho_e u_e}\right) \mathrm{d}s \\ \theta^* &= \int_0^{\delta_{99}} \frac{\rho u}{\rho_e u_e}\left(1 - \frac{\rho u}{\rho_e u_e}\right) \mathrm{d}s \\ H &= \delta^*/\theta^* \end{aligned} \tag{6.1}$$

where u is the wall-tangent velocity component, ρ is the local flow density and s the wall-normal coordinate. In the equations, the subscript e indicates values evaluated at the boundary layer edge.

Fig. 6.9a confirms that the physical thickness of the boundary layer uniformly decreases along the fuselage body when moving from the WT scale to the FF scale. In particular, the decrease of the boundary layer thickness is around 20% at the trailing edge of the fuselage. In addition to the thinning of the boundary layer, the integral properties of the velocity profile are also affected by the aerodynamic scaling. Figures 6.9b and 6.9c report the variation of the displacement thickness and momentum thickness along the fuselage body. In the plots, δ^* and θ^* are expressed as ratio of the body radius, R, and of the local boundary layer thickness, δ_{99}. δ^* and θ^* both decrease along the entire

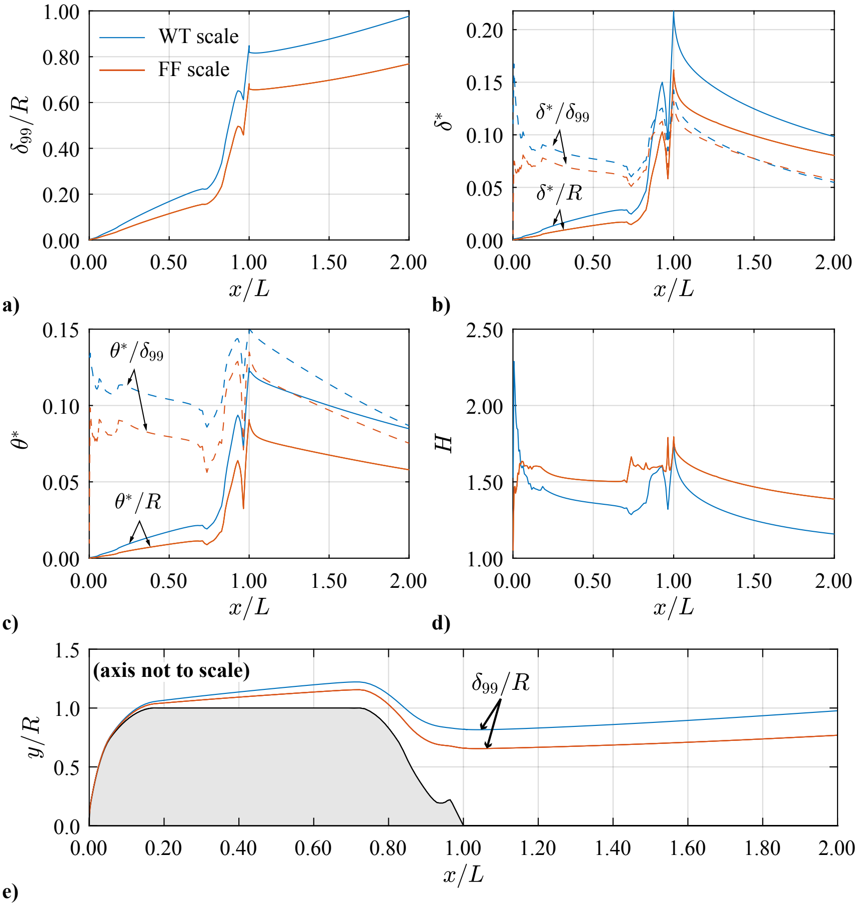

Figure 6.9: Boundary layer parameters for the BF configuration at WT and FF scales.

fuselage body when going from the WT to the FF scale. This is a consequence of the relatively lower skin friction found at FF scale (see again Fig. 6.6b) which leads to a lower mass and momentum deficit through the boundary layer and hence lower δ^* and θ^* values. However, the shape factor, H, increases as a consequence of the increasing scale. The increase in shape factor is due to increase in Mach number, M, and the associated compressibility effects on the boundary layer.The evolution of H along the axial position remains qualitatively unchanged. The effects of the aerodynamic scaling on the integral characteristics of the boundary layer are aligned with the results reported in Ref. [58].

Fig. 6.10 reports the normalized total pressure and velocity components distribution in the fuselage boundary layer on the cylindrical section ($x/L = 0.60$ in Fig 6.10a) and on the aft-cone section ($x/L = 0.94$ in Fig 6.10b). In the right-hand plots, both the tangential velocity, u, and the wall-normal velocity, v, are plotted as a fraction of the boundary-layer-edge velocity, u_e. The boundary layer profiles confirm that both the momentum and velocity deficits decreases when moving from the WT to the FF scale. However, the

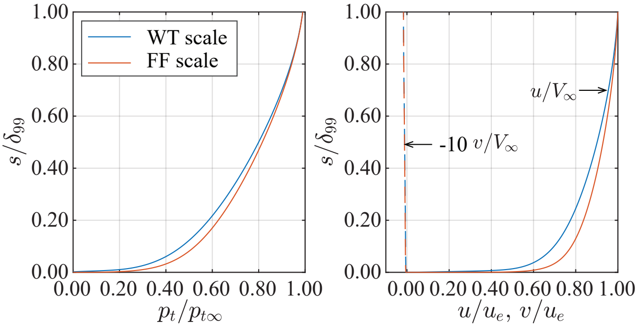

a) *x/L* = 0.60

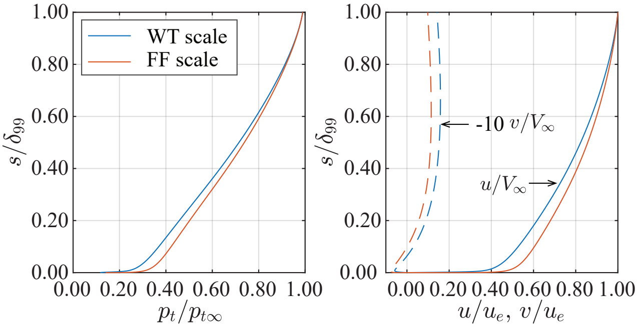

b) *x/L* = 0.94

Figure 6.10: Total pressure and velocity components in the boundary layer of the BF configuration at WT and FF scales.

shape of the normalized boundary layer profiles remain similar through the scaling process. This also confirms that the increase in the shape factor, H, is a consequence of compressibility and does not reflect a change in the actual velocity profile shape.

6.3.3. EFFECTS ON SCALING ON THE PF CONFIGURATION PERFORMANCE

In the previous section, the effects of scaling on the aerodynamic performance of the bare fuselage configuration (BF) were discussed. In this section, the scaling effects on the powered fuselage configuration (PF) are analyzed.

Fig. 6.11 reports the total pressure flowfield around the aft-cone section of the PF configuration at both WT and FF scales. In both flowfields, the boundary layer around the fuselage aft-section is clearly visible and characterized by $p_t/p_{t\infty} < 1$. In particular, the boundary layer is larger than the BLI propulsor and approximately half of the boundary layer flow is ingested by the propulsor. Moreover, in the slipstream of the BLI propulsor (simulated through the actuator volume model), $p_t/p_{t\infty} > 1$ due to the momentum added by the propulsor to the flow.

The effect of the aerodynamic scaling that can be appreciated by comparing the two flowfields reported in Fig. 6.11 is twofold: first, the boundary layer becomes thinner due to the increased Reynolds number, similarly to what found for the BF configuration (see

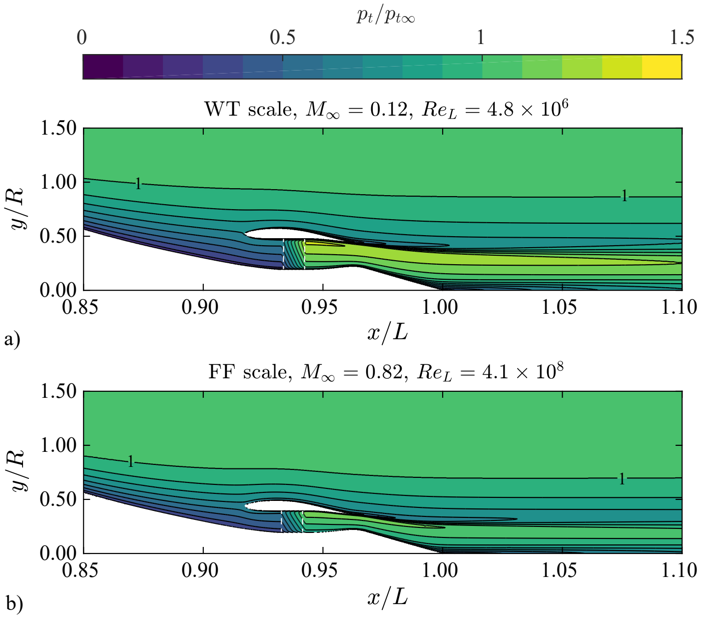

Figure 6.11: Total pressure field around the aft-cone section of the PF configuration at WT and FF scales.

again Fig. 6.7). However, since the propulsor radius was scaled according to the local boundary layer momentum thickness, as detailed in Sec. 6.2, the relative size between the boundary layer and the propulsor is unchanged. Second, the total pressure jump caused by the propulsor is relatively higher at the WT scale. In fact, since the thrust exerted by the propulsor was set equal to the drag of the BF configuration at the same scale, the momentum addition at the AV is proportional to the momentum deficit found in the boundary layer. However, the decrease of the fuselage drag coefficient at FF scale resulted in a lower disk loading necessary to overcome the fuselage drag and hence in a lower momentum increase across the AV.

The Mach number distribution around the fuselage aft-section at WT and FF scales is shown in Fig. 6.12. At both WT and FF conditions, the flowfield is characterized by the expansion around the nacelle leap and throughout the duct toward the nozzle exit section. At the FF scale the pressure gradients are enhanced as a consequence of the increased M_∞. However, the flowfield is still fully subsonic (i.e. $M < 1$ everywhere). Note that since the propulsor is modeled as an actuator volume, this analysis does not consider the flow around the fan blades which is typically transonic at the FF regime (see Ref. [51]). Moreover, transonic flow is expected around the nacelle leap and nozzle exit section in off-cruise operating conditions at the FF scale (see Ref. [94]).

Compressibility effects, even though confined to the subsonic regime (i.e. not related to the presence of shockwaves), has strong effects on the flowfield induced by the propulsor and on its interactions with fuselage. Fig. 6.13 reports the flow development throughout the BLI propulsor along the midspan section of the duct for the WT and FF conditions. Fig. 6.13 confirms that, at both WT and FF conditions, the AV produces an

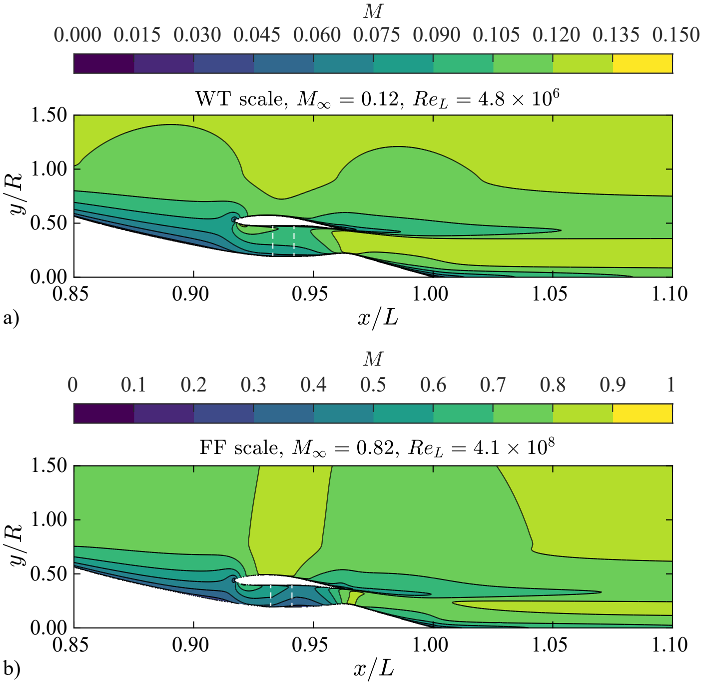

Figure 6.12: Mach number field around the aft-cone section of the PF configuration at WT and FF scales.

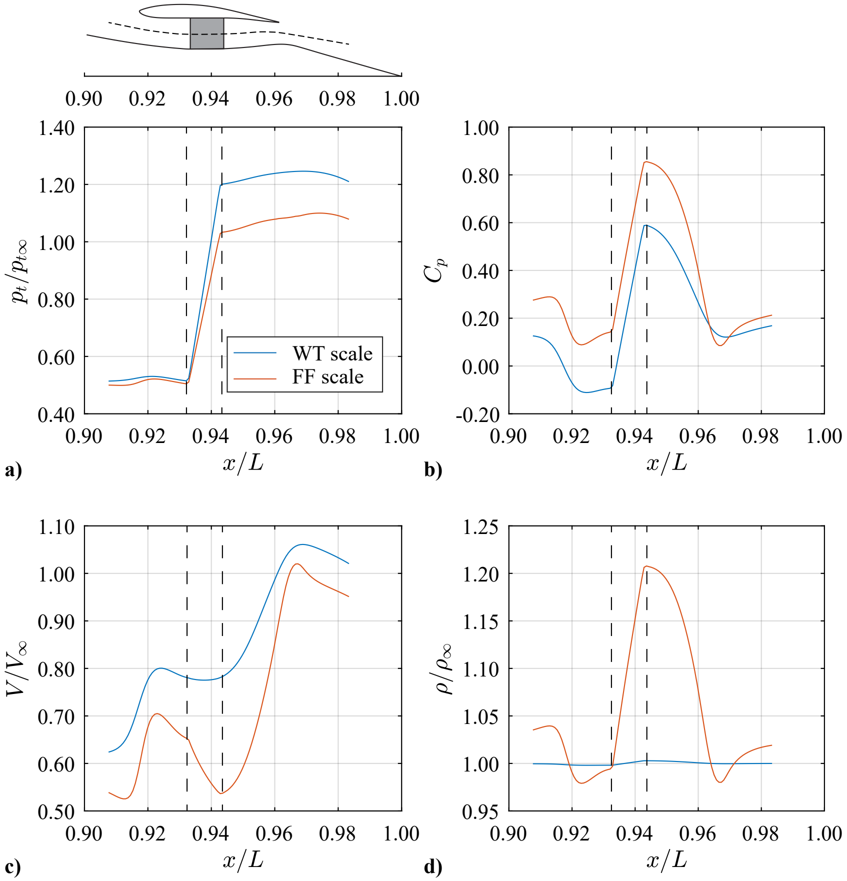

Figure 6.13: Flow development across the BLI propulsor along its midspan section (represented with the dashed contour in the top sketch).

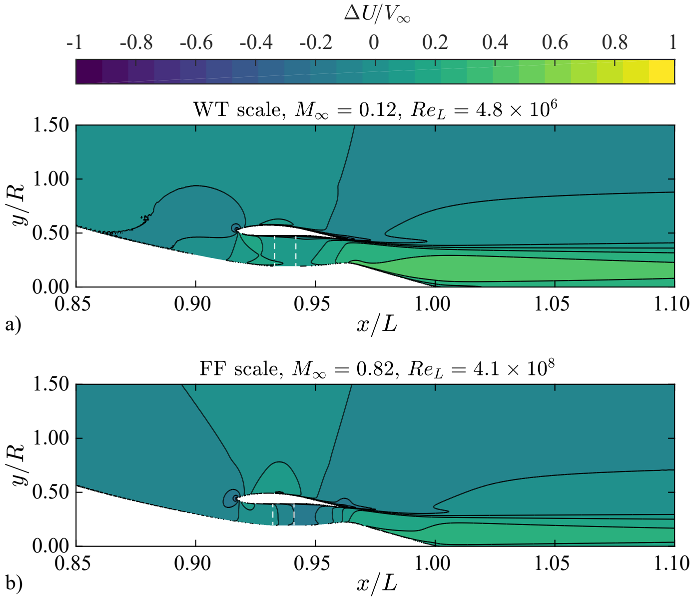

Figure 6.14: Propulsor-induced axial velocity field around the aft-cone section of the PF configuration at WT and FF scales.

increase in both total and static pressure (fig. 6.13a and fig. 6.13b, respectively). However, as already mentioned above, the pressure increase was larger at WT due to the relatively higher body drag and hence required thrust. On the other hand, while at WT conditions the velocity remains nearly constant through the AV, at FF conditions the velocity reduces through the AV (see fig. 6.13c). At the same time, the density increases (fig. 6.13d), such that ρV remains constant and continuity is satisfied. This behaviour is in line with what expected from the compressible actuator disk theory (see for example Ref. [102, 103]).

To further understand the compressibility effects on the fuselage-propulsor interactions, Fig. 6.14 presents the axial velocity component induced by the BLI propulsor, ΔU, at both WT and FF conditions. This velocity is defined as the difference between the PF and BF flowfields: $\Delta U = U^{\text{PF}} - U^{\text{BF}}$ and represents the change in the flowfield due to the BLI propulsor with respect to the bare fuselage configuration.

Comparing the effects of the BLI propulsor at WT and FF conditions (fig. 6.14a and fig. 6.14b, respectively), clarify the effects of compressibility on the fuselage-propulsor interaction. First, as already discussed above, due to the increased M_∞, the velocity gradients are enhanced. This mainly affects the flowfield around the shroud section. In particular, the influence of the compression toward the stagnation point and the subsequent expansion around the shroud inlet leap is strengthened at FF conditions compared to the WT conditions. Moreover, also as a consequence of the decrease in velocity through the AV, the expansion downstream of the AV toward the duct nozzle is stronger at FF conditions (see again fig. 6.13d).

The changes in the flowfield around the BLI propulsor induced by compressibility

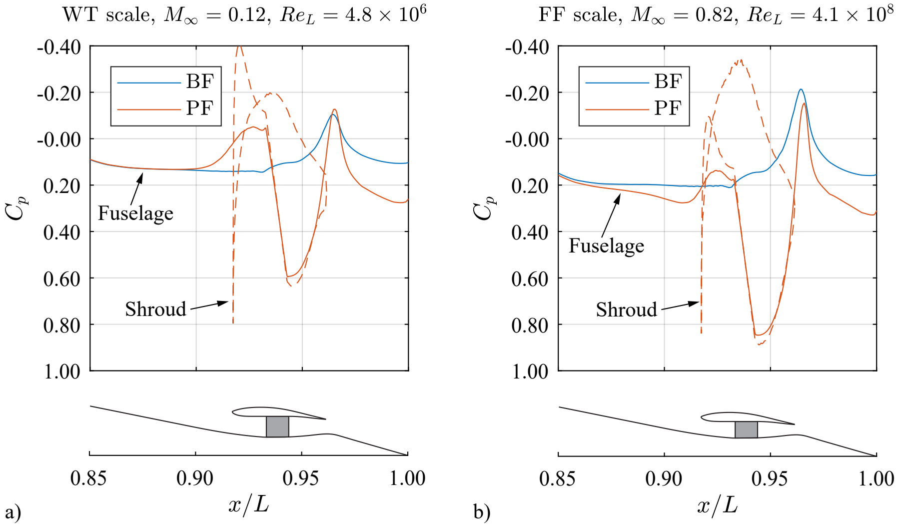

Figure 6.15: Propulsor-induced axial velocity field around the aft-cone section of the PF configuration at WT and FF scales.

also reflect onto the pressure distribution on the fuselage and shroud contours. The C_p distributions along the axial direction on the fuselage and shroud surfaces are reported in Fig. 6.15. The effects of compressibility on the C_p distribution is twofold. First, at FF an adverse pressure gradient is induced on the fuselage ($0.85 < x/L < 91$) as a consequence of the pressure increase around the stagnation point on the shroud leap. Second, the C_p on the fuselage aft-cone downstream of the AV ($x/L > 0.95$) is higher at FF scale than WT scale. Both these effects contribute to the decrease in the fuselage pressure drag component, C_{D_p}, already discussed in Section 6.3.1 (see Tab. 6.2).

6.4. COMPARISON AGAINST EXPERIMENTAL RESULTS

As already discussed in the Section 6.1, the objective of this numerical study is to investigate how the aerodynamic performance of a sub-scaled system (i.e. the wind-tunnel model at low-speed conditions) differ from those of the reference, full-scale system (i.e. the full-scale CENTRELINE aircraft). In order to define the scope of this study and to simplify the studied problem, a number of assumptions were made regarding, in particular, the BLI propulsor modeling. Within the CFD simulations, the BLI propulsor was simulated through an Actuator Volume model, with a constant disk loading distribution and zero induced swirl. In order to highlight the effects that this modeling choice has on the resulting flowfield, the numerical and experimental results at WT scale are compared. The comparison also allows to identify those flow phenomena that were measured in the experiments but not captured by the numerical simulations due to the simplified propulsor model employed. Moreover, even though a complete CFD validation is out of the scope of this section, comparing the experimental and numerical results provides a useful insight on the capability of the (simplified) CFD model in predicting the flowfield.

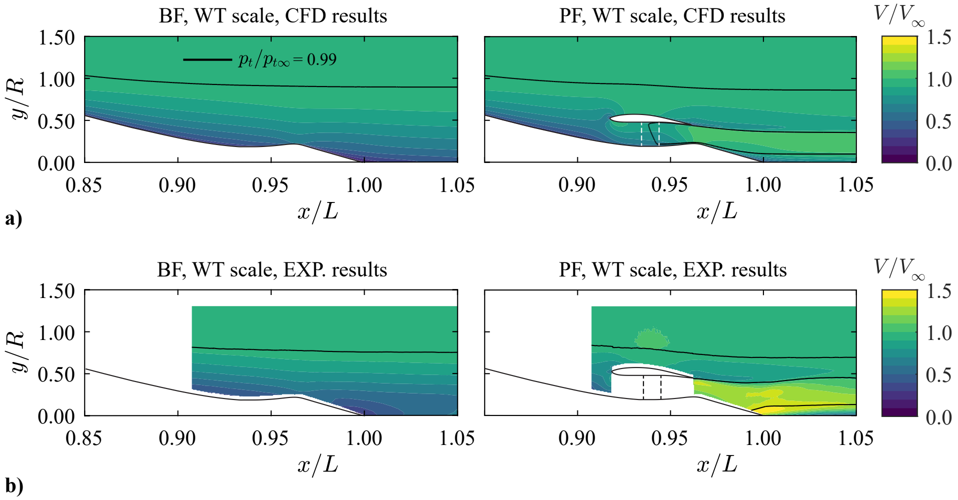

Figure 6.16: Velocity field around the aft-cone section of the BF and PF configurations at WT scale. Comparison of numerical and experimental results.

The reference experimental data set is obtained from the fuselage-BLI investigation discussed in Chapter 4. Even though the model setup was not fully axisymmetric due to the presence of the two fairings (see again e.g. fig. 4.1), the results of this experiments are the closest to replicate axisymmetric flow conditions around the fuselage aft-cone. Moreover, for the PF configuration, the fan settings for which $C_N/C_{D,0} = -0.5$ is chosen as reference, as this is the conditions that is closest to the thrust setting simulated in the CFD analysis through the AV model.

Fig. 6.16 reports the velocity field around the fuselage aft-section for the BF and PF configurations at WT conditions obtained from the numerical (Fig. 6.16a) and experimental (Fig. 6.16b) analysis. For the BF configuration (left-hand contours of Fig. 6.16), the numerical and experimental flowfields are in good agreement. The boundary layer development along the fuselage aft-cone is well captured, even though the boundary layer thickness is over-predicted by the CFD simulations. In the contours, the boundary layer edge is defined as the point at which $p_t/p_{t\infty} = 0.99$ and it is represented with a thick black line. It must be noted though that a small discrepancy in the total pressure distribution can result in a substantial variation in the definition of the boundary layer edge. For the PF configuration, the comparison between the CFD and experimental data compares well for the regions of the flow upstream of the nacelle and outside the fan slipstream. Within the fan slipstream and downstream of the fan, the results of the numerical and experimental analysis show stronger differences. This is mainly due to the simplifications introduced in the propulsor modeling. First, the thrust exerted by the AV model is different that what obtained during the experiment. In fact, during the experiment the fan thrust setting was relatively higher than what simulated in the CFD analysis. This results in a higher momentum addition in the flow and hence in an higher total pressure in the fan slipstream in the experimental results. Second, the loading distribution simulated through the AV model is constant unlike the disk loading distribu-

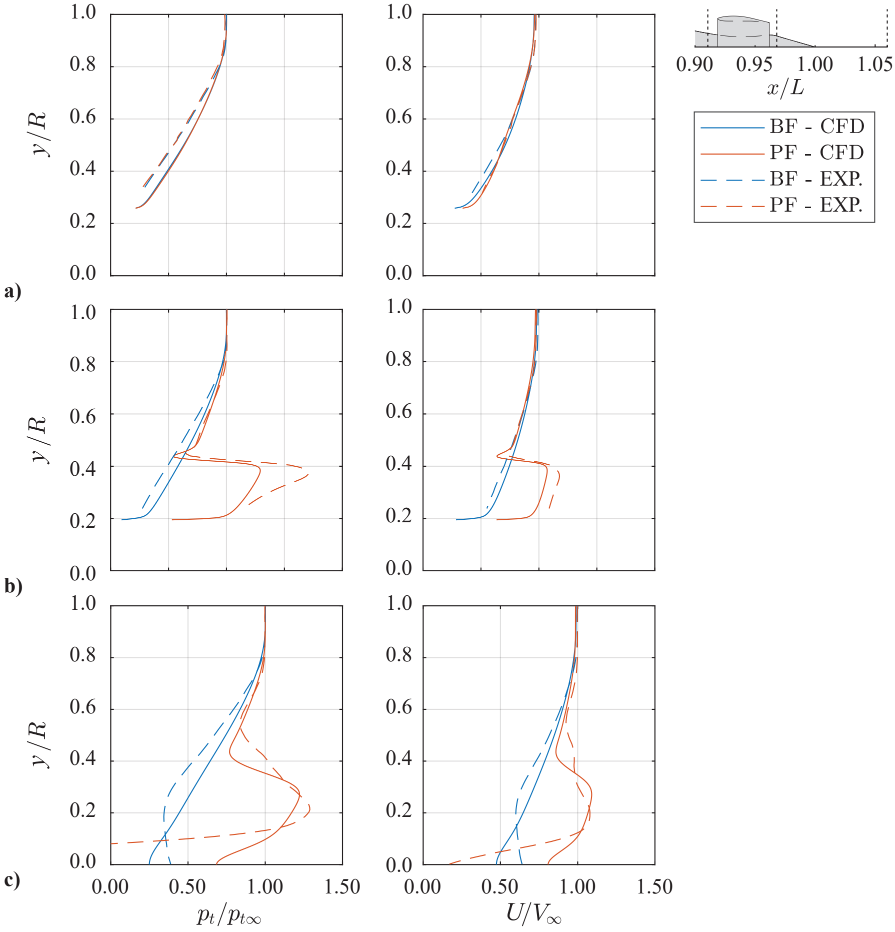

Figure 6.17: Total pressure and axial velocity profiles around the aft-cone section of the BF and PF configurations at WT scale. Comparison of numerical and experimental results.

tion of the fan model used in the experiments. In the experimental results, this results in higher p_t values toward the outboard region of the propulsor slipstream, which is not replicated in the CFD results. Finally, the AV model employed in the CFD simulations, unlike the real propulsor model, does not introduce tangential momentum and hence does not introduce swirl velocity components. As a consequence, the flow development around the fuselage nozzle plug measured during the experiment was not well captured by the CFD simulations. In particular, the vortical flow structure developing around the nozzle plug which, as discussed in Chapter 4, strongly affects the slipstream development and the resulting fuselage axial force, is not found in the numerical results.

These considerations can be confirmed in a more quantitative fashion by comparing the total pressure and axial velocity profiles upstream and downstream of the BLI propulsor from the experimental and numerical results, which are reported in Fig. 6.17.

Upstream of the BLI propulsor (Fig. 6.17a), the boundary layer profile obtained through the CFD simulations is in good agreement with the experimental results. However, the CFD results show an overestimated p_t value in the boundary layer which can be due to the numerical turbulence modeling and to the experimental approach used to infer the total pressure distribution from the velocity data (see Chapter 4). Immediately downstream of the nozzle exit (Fig. 6.17b), the CFD model captures well the variations of total pressure and velocity induced by the fan outside of the fan slipstreams ($y/R > 0.4$) for the PF configurations. However, inside the propulsor slipstream ($y/R < 0.4$), the total pressure and velocity distributions measured in the experiments are not matched in the CFD analysis because of the different blade loading simulated through the AV model. Finally, downstream of the fuselage trailing edge (Fig. 6.17c), the numerical and experimental data show stronger differences. First, for both the BF and PF configurations the total pressure and velocity profiles show the effects of a higher viscous diffusion, which is not well reproduced by the CFD simulation. Moreover, the low total pressure and velocity values found close to the wake center ($y/R < 0.2$) for the PF configuration, resulting from the onset of a strong vortical structure induced by the fan-induced swirl, is not reproduced by the CFD model. This is due to the simplifying assumptions used in the AV model definition which does not introduce any swirl in the flow.

6.5. CONCLUSIONS

This chapter presented the results of a numerical study aimed at investigating the effects of scaling on sub-scale low-speed wind-tunnel experiments. RANS-based CFD simulations were performed of the fuselage-BLI configuration tested in the wind-tunnel experiments reported in Chapters 4 and 5 in axisymmetric flow conditions. The simulations were carried out at two scales: the wind-tunnel (WT) scale, replicating the geometrical scale and typical operating conditions obtained in the wind-tunnel experiments; and the full-scale flight (FF) scale, replicating the geometrical scale and typical operating conditions representative of the full-scale CENTRELINE Propulsive Fuselage Concept. At each scales, both bare fuselage (BF) and the powered fuselage (PF) configurations were studied. the This study allows a better understanding on how the aerodynamic scaling, and in particular the variation of the freestream Reynolds and Mach numbers, affected the aerodynamics of the configuration. In particular, it was found that:

1. The change in Reynolds and Mach number has important effects on the flowfield around the BF configuration. However, the flowfield is subsonic everywhere and hence compressibility effects are confined to the subsonic regime. Moreover, the effects of increasing Reynolds and Mach numbers on the surface pressure and friction distribution can effectively be explained and corrected through conventional scaling methods.

2. The boundary layer thickness decreases at FF scales mainly due to the increased Reynolds number. However, the evolution of the boundary layer properties along the fuselage surface, together with the boundary layer profile shape, remains qualitatively similar.

3. For the PF configuration, the effects of the increasing Reynolds number are essen-

tially similar to what found for the BF configuration. However, as a consequence of the lower fuselage drag coefficient, C_D, the thrust coefficient of the BLI propulsor, C_T, was also lower at the FF scale. This reduces the detrimental aerodynamic interaction effects and results in a thrust-to-power coefficient ratio, C_T/C_P, around 30% higher at the FF scale.

4. The compressibility effects on the PF configuration are limited to the subsonic domain and no supersonic flow is found around the fuselage aft-section and around the propulsor shroud. However, because of the increased freestream Mach number, the potential flow interactions occurring between the fuselage and the shroud are enhanced at FF scale. This produces, on one hand, an adverse pressure gradient on the fuselage contour upstream of the BLI propulsor, and, on the other hand, a decrease of the fuselage pressure drag component.

7

CONCLUSION & RECOMMENDATIONS

To ensure sustainability of civil aviation, CO_2 emissions of the future aircraft generations need to be drastically decreased. In order to reduce fuel consumption, novel aircraft architectures featuring unconventional airframe–propulsion integration technologies are being studied. In these configurations, the propulsive devices are mounted in close proximity of the airframe or integrated with it, and the airframe–propulsor aerodynamic interactions are exploited to improve the aircraft efficiency. Among these technologies, Boundary Layer Ingestion (BLI) has raised interest due to the expected power consumption benefit. In BLI, the engine is directly mounted onto the airframe and operates onto the boundary layer flow that develops on the airframe surfaces. By accelerating the low-momentum fluid in the boundary layer to produce the required thrust, less energy is dissipated in the aircraft wake and hence the flight can be sustained with a lower power consumption when compared to a conventional aircraft configuration.

This thesis has investigated the aerodynamic interactions occurring in boundary layer ingestion between the airframe and the integrated propulsor. The thesis has focused on a specific BLI aircraft configuration, the so-called Propulsive Fuselage Concept (PFC), a tube-and-wing aircraft with a BLI engine integrated on the aft-fuselage section. The PFC is the most promising BLI configuration and has been extensively investigated in the EU-funded CENTRELINE project, within which this research was carried out.

To characterize the aerodynamics of the PFC, comprehensive wind-tunnel experiments have been performed. The results of these experimental studies are presented in Chapters 3 to 5. The experimental work has shed light on the fundamental aero-propulsive interaction mechanisms and their effect on the resulting system performance. The knowledge built through these experiments provides a positive contribution to the literature and an extensive data set that can be used for the validation and tailoring of numerical models. The experiments have been integrated through a numerical study investigating the effects of the Reynolds and Mach numbers scaling on the experimental findings (Chapter 6).

7.1. CONCLUSIONS

In this section, the key findings and conclusions of this research work are summarized with reference to the research questions formulated in Chapter 1.
To define the goal of this study, the following research question was formulated:

> *What are the key aerodynamic interaction effects in boundary layer ingestion and how do they impact the overall system aerodynamic performance?*

The research question was divided into three main sub-questions. In this section, the key findings of this research are summarized with respect to each of the three sub-questions.

1. What are the fundamental flow mechanisms that drive the aerodynamic interaction occurring between the propulsor and the airframe?

Regarding this sub-question, the following conclusions can be drawn from the presented research:

1. The BLI propulsor has strong upstream and downstream effects on the airflow around the fuselage. These effects are associated with the potential pressure and velocity field induced by the propulsor. Upstream of the propulsor plane, the favourable pressure gradient and increased axial velocity alter the boundary layer profile, resulting in an enhanced massflow close to the fuselage surface. Downstream of the propulsor, the fuselage boundary layer thickness decreases by around 15% following the propulsor slipstream contraction. Moreover, the tangential momentum in the slipstream produces a vortical structure around the fuselage trailing edge cone with detrimental effects on the fuselage parasite drag.

2. The inflow of the BLI propulsor is a superposition of the distortions induced by different airframe elements. In cruise conditions ($\alpha = \beta = 0°$), the fuselage boundary layer and the vertical tail plane wake represent the strongest source of inlet distortions. In these conditions, the effect of the BLI propulsor on the aircraft forces and moments are mostly limited to the thrust-drag equilibrium.

3. The momentum and mechanical energy fluxes across the propulsor plane were quantified through the power balance method. The analysis shows that the BLI propulsor decreases the upstream momentum flux, indicating an increased momentum dissipation and fuselage drag. The mechanical energy flux is also increased upstream of the propulsor plane, as a consequence of the suction effect. For the aircraft model considered in this study, a momentum deficit of around 15% of the total aircraft drag, D_0, was contained in the fuselage boundary layer at the propulsor inlet plane. However, only 3-4% of the total aircraft drag power, $D_0 V_\infty$, was measured at the same plane. This indicates that a power saving of less than 3-4% could be, ideally, associated to the “wake-filling” effect of BLI. In particular, in the experiments discussed in this thesis, the propulsor was able to recover only up to around 50% of the available axial kinetic energy.

2. What are the effects of the operating conditions (i.e. thrust setting and aircraft incidence) on the local flow phenomena and overall aerodynamic performance?

Regarding this sub-question, the following conclusions can be drawn from the presented research:

1. The aerodynamics of the fuselage-BLI configuration has been shown to be strongly sensitive to the thrust setting of the BLI propulsor. When increasing the thrust setting, the aerodynamic performance quickly diverges from the ideal wake-filling conditions, as the mechanical energy dissipated in the propulsor slipstream increases more than linearly with the net axial force. This is due to the decreased efficiency at higher disk loading conditions which are not compensated by the BLI benefit. Moreover, the upstream and downstream effects of the fan become stronger at higher thrust settings, inducing detrimental drag contributions which negatively offset the BLI advantages.
2. In presence of a non-zero angle of attack, the crossflow component around the fuselage contour plays a major role in the resulting flow at the BLI propulsor inlet, resulting in strong azimuthal distortions. Moreover, in presence of a sideslip angle, the vertical tail strongly affects the inflow field as it produces lift under the sideslip. The associated total pressure distortion is characterized by sharp gradients in the azimuthal and radial directions. In these conditions, the BLI propulsor showed a non-negligible effect on both the longitudinal and lateral-directional forces and moments.

3. What are the effects of Reynolds and Mach number scaling on the main flow phenomena?

Regarding this sub-question, the following conclusions can be drawn from the presented research:

1. The Reynolds and Mach numbers scaling introduces significant effects on the BLI-fuselage aerodynamic performance. At the FF scale the viscous effects were relative weaker than at WT scale, resulting in a lower fuselage C_D and a lower boundary layer thickness. Moreover, for the considered test case, the flowfield remained subsonic everywhere at the FF scale. Consequently, no flow phenomena related to the formation of shockwaves were found at the FF scale.
2. It was shown that the effects of the Reynolds and Mach numbers scaling could be taken into account through the use of simple analytical models stemming from the turbulent flat plate and compressible potential flow solutions. Moreover, it was shown that by scaling appropriately the propulsor size and thrust setting the effects of the aerodynamic scaling on the resulting flowfield could be limited. More importantly, the underlying interaction mechanisms occurring between the fuselage and the BLI propulsor that were identified at the WT scale were confirmed to have similar effects also at the FF scale.

The following table summarizes the main contributions that this thesis has provided to the knowledge around boundary layer ingestion:

Knowledge before this thesis	**Knowledge after this thesis**
Limited experimental proof of BLI in an integrated PFC configuration.	Detailed wind tunnel data and analysis on BLI for an integrated PFC aircraft, revealing key aerodynamic interaction mechanisms.
Limited examples of the experimental applications of novel flow analysis techniques in BLI configurations.	Experimental flowfield data fed the application of the power balance method to estimate the BLI aero-propulsive performance.
Uncertainty on how thrust setting and flight conditions affect BLI performance.	Quantified the effects of thrust, angle of attack, and sideslip on inlet distortion and system performance.
Aerodynamic scaling effects from wind tunnel to full-scale conditions not well established.	The fundamental interaction mechanisms are preserved across the scaling as demonstrated through numerical simulations.

7.2. RECOMMENDATIONS

The aerodynamic interactions in BLI discussed in this thesis could be further investigated through future research. In this section, some recommendations based on the experience developed during this research work are given to steer and aid future studies in the topic of boundary layer ingestion.

1. This thesis has focused on the study of time-averaged flow physics and aerodynamic performance. Thorough studies should be performed on possible unsteady aerodynamic phenomena occurring in BLI. Unsteady phenomena are expected, for example, in configurations in which the presence of non-axisymmetric distortions in the inflow to the BLI propulsor induce unsteady blade loadings on the propulsor. Moreover, the disturbance introduced by a rotating blade immersed in a viscous boundary layer, could induce unsteady effects on the boundary layer itself. Furthermore, the aero-acoustics of BLI was not investigated during the presented research. It is expected that the operation of a propulsor into a turbulent boundary layer will affect the generated aerodynamic noise. In particular, the relatively high turbulence at the propulsor inlet can represent a noise source and alter the ratio between the intensity of tonal and broadband noise produced by the BLI propulsor.

2. The design of the wind-tunnel model employed during the experimental activities of this research has been adapted from the results of the CENTRELINE project. Within the project, the design of propulsive fuselage aircraft and, namely, of the geometry of the aft-fuselage section and BLI propulsor, was obtained through simplified numerical simulations. In future, it is recommended to investigate experimentally the effects of the main design parameters (e.g. propulsor height and location, unshrouded propulsor etc.) on the system performance. Furthermore, the relation between the boundary layer conditions and the power consumption benefit should be studied. In fact, aspects like transition location and/or surface roughness, have an influence of resulting boundary layer thickness and hence on the design and performance of the BLI propulsor.

3. Even though the main effects of Reynolds and Mach numbers scaling was partially assessed during this research, it is envisioned that a better quantitative assessment of the aero-propulsive benefit expected from BLI should be obtained through experimental investigations at larger scales and/or transonic conditions.

4. Given the strong interactions between the airframe and the propulsor, their design should be optimized through a coupled, high-fidelity numerical model. In fact, the presence of the inflow boundary layer affects the optimum blade loading distribution and hence the propulsor shape. On the other hand, it was shown also by the presented work that the propulsor has a strong effect on the upstream boundary layer profile and pressure distribution. This affects the performance of the airframe (in the case of this thesis, the fuselage) and, in turns, the optimum airframe and propulsor design.

A

MODEL SUPPORT DESIGN FOR THE AXISYMMETRIC BLI SETUP

A.1. INTRODUCTION

The aerodynamic interaction taking place between a wind-tunnel model and the support structure can have a large influence on the flowfield and hence on the resulting measurements. The disturbances introduced in the flowfield by the model support can be divided into two categories: 1) far-field effects, mainly due to inviscid interactions (e.g. induced velocity components), and 2) near-field effects, mainly due to viscid interactions between the support and the boundary layer of the model [104]. Junction flow is one example of the near-field interaction effects. Junction flow appears when an obstacle is immersed in the boundary layer flowing along a wall [105]. As a consequence of the adverse pressure field induced by the obstacle, flow reversal occurs on the wall from which the obstacle is protruding [106]. The onset of flow reversal leads to the formation of an horseshoe vortex structure and corner separation [107, 108]. One way of mitigating the junction flow is by reducing the induced pressure gradient through the employment of a leading-edge fillet. The performance and the design of LE fillets have been vastly assessed in literature, also through CFD-based methods [109, 110]. Van Oudheusden *et al.* [111] proposed a design procedure based on the combination of a panel method for the solution of the potential flow and an integral method for the solution of the approaching boundary layer on the attachment line.

This chapter discusses the wind-tunnel model–support interference encountered in the development of a test rig for the study of boundary layer ingestion (BLI) at Delft University of Technology. The work, performed under the EC-funded Horizon 2020 CENTRELINE project [49], is aimed at a detailed aerodynamic study of the “Propulsive Fuse-

---

Contents of this chapter have been published in:
Della Corte, B., Perpignan, A. A. V., van Sluis, M., and Gangoli Rao, A., “Experimental and Computational Analysis of Model–Support Interference in Low-Speed Wind-Tunnel Testing of Fuselage-Boundary-Layer Ingestion”, *9th EASN International Conference on “Innovation in Aviation & Space”*, Paper No. 02020, 2019. doi:10.1051/matecconf/201930402020.

lage Concept" (PFC). The concept features a boundary–layer ingesting fan integrated at the aft fuselage section. The goal of the experiments is that of analysing the configuration through momentum- and energy-based approaches. In particular, the scope of the work is to isolate the effects of BLI from other integration effects (e.g. inflow distortions due to the wings). Therefore, an idealized aircraft model featuring an axysimmetric fuselage was utilized in the experiments. The fuselage model was connected to the external balance through a support beam, which was covered with a wing-shaped fairing. Numerical and experimental analysis have been carried out to design the fairing with the goal of mitigating the flow distortions introduced by the support structure setup.

A.2. METHODOLOGY

A.2.1. EXPERIMENTAL SETUP

The experimental campaigns were carried out in the Low-Turbulence Wind-Tunnel (LTT) facilities of Delft University of Technology. This closed-circuit wind-tunnel features a closed test section with an 1.25 m × 1.80 m octagonal cross-section. The tunnel is driven by a 525 kW electric fan and is capable of a maximum test speed of around 120 m/s. The free-stream turbulence level is reported to be between 0.015 % at 20 m/s and 0.07 % at 75 m/s.

A sketch of the setup is presented in Figure A.1. The model used in the experiments consisted of an axisymmetric body representative of an aircraft fuselage. The fuselage featured a maximum radius $R = 80\,\text{mm}$ and a length $L = 1776\,\text{mm}$. Turbulent boundary-layer flow was ensured with a zig-zag transition strip at 5% of the fuselage lentgth from the nose. The fuselage model was centered with the test section and connected to the external balance through a vertical support beam. A wing-shaped fairing was mounted around the support beam and bolted directly to the wind-tunnel ceiling.

Two different fairing configurations, referred to as 'baseline' and 'optimized', were tested as sketched in Figures A.1b and A.1c. In both cases the fairings featured a NACA 66_4-021 airfoil section and a rectangular planform with a chord $c = 236\,\text{mm}$. In the baseline configuration of Figure A.1b, a single fairing without any fillet and a flat tip was implemented. A gap of around 1.5 mm was left between the fuselage and the fairing tip. On the contrary, the optimized configuration featured an elliptical leading-edge blending at the fuselage, as shown in Figure A.1c. The tip of the fairing featured a curved surface with a curvature radius equal to the fuselage radius. The elliptical leading-edge fillet was obtained by following the design proposed by van Oudheusden *et al.* [111, 112] To minimize the distortions induced in the flowfield by the presence of the fairing, a second setup was obtained by mirroring the upper fairing around the horizontal plane and placed on the bottom part of the setup. All measurements were taken at zero-incidence conditions and at freestream velocity, V_∞, equal to 20 m/s and 40 m/s.

Different measurement techniques were performed to quantify the airflow around the fuselage and the fairing surfaces. As already mentioned, an external six-component balance was used to measure the aerodynamic forces and moments acting on the fuselage surface. In addition, total pressure measurements were carried out in the wake of the model by means of a rake of 44 total-pressure probes. The scanned plane was orthogonal to the freestream velocity direction and placed at a distance from the trailing

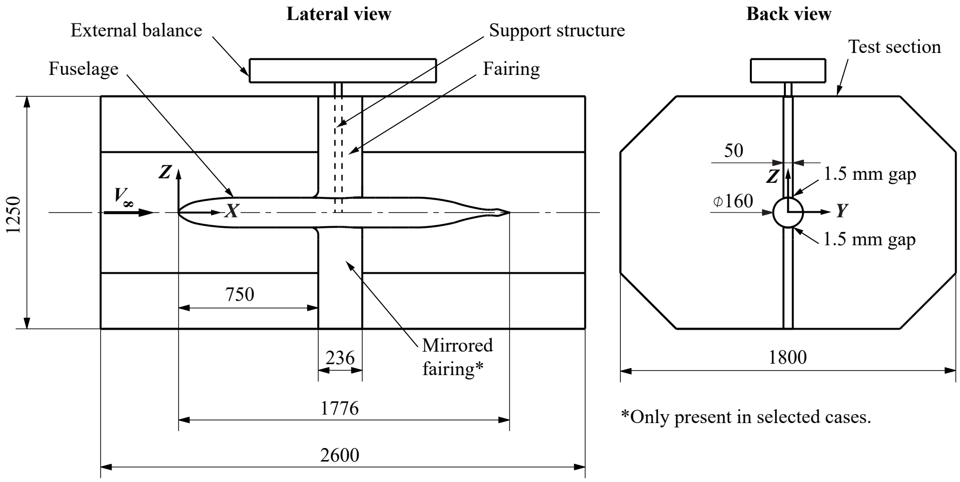

(a) Wind-tunnel model installed in the test section.

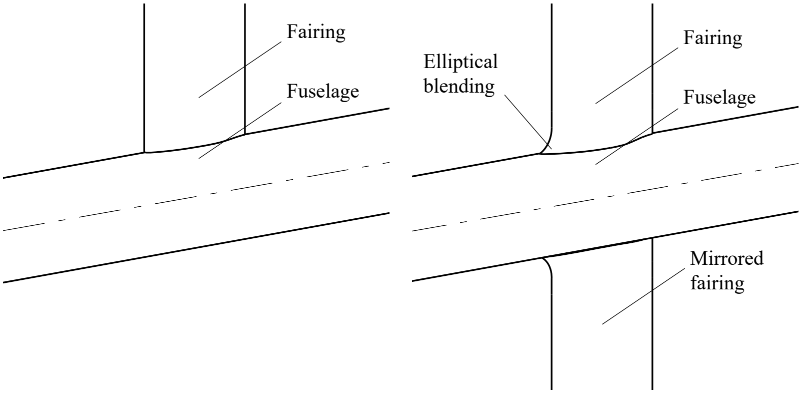

(b) Baseline configuration.

(c) Optimized configuration.

Figure A.1: Experimental setup and different tested configurations. Dimensions in millimeters.

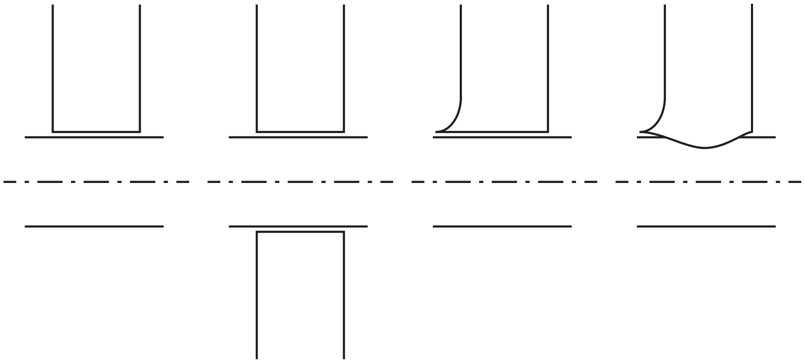

(a) baseline (b) baseline, mirrored (c) elliptical LE (d) elliptical LE, curved tip

Figure A.2: Comparison of the different fairing design iterations.

edge of the fuselage varying from $X_{TE} = 1R$ to $X_{TE} = 2R$. The probes were non-evenly distributed with a minimum lateral spacing of 3 mm (equal to 3.75 % of R) at the center of the rake. The rake was traversed in the vertical (spanwise) direction with a spacing of 0.5 mm (0.625 % of R) at the fuselage center and gradually increasing at larger Z positions. At each vertical position, measurements were taken with an electronic pressure scanner at 5 Hz for a period of 10 s and time-averaged to obtain the single data point.

A.2.2. NUMERICAL SETUP

In order to find a better option capable of reducing the interference of model support on the flow field, Computational Fluid Dynamics (CFD) simulations were carried out to investigate the performance of different fairing designs. As shown in Figure A.2, in addition to the baseline (a), three new configurations were tested utilizing CFD, which featured a dummy fairing placed on the opposite side of the model (b), a fairing equipped with a leading edge insert (c), and a curved fairing tip following the model curvature (d). The CFD simulations were performed utilizing ANSYS Fluent. Computational meshes were unstructured and composed of tetrahedral elements with prism layers along the walls of the fuselage and fairing. The prism layers were composed of 20 layers with the total height sufficiently covering the boundary layers and the initial height in accordance with the adopted near-wall treatment (y^+ in the order of 1). Three different turbulence models were employed: Spalart-Allmaras [64], κ-ω SST [65], and an ω-based Reynolds Stress model [113]. Second order discretization was employed for all simulations. The SIMPLE pressure-velocity coupling scheme was adopted. Velocity was imposed to the inlet boundary (40 m/s) along with 5% turbulence intensity and a turbulent viscosity ratio of 10. The outlet of the domain was modelled by imposing a zero gauge pressure. A symmetry boundary condition was applied to all simulations with respect to the plane cutting through the centreline of the fuselage and fairing. The case with a mirrored fairing had another symmetry plane so that one fourth of the domain was simulated. The mesh independence study was conducted by refining the element sizes on the surface

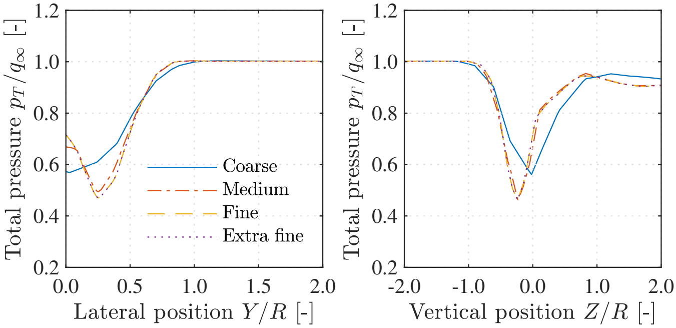

Figure A.3: Grid sensitivity

of the fuselage and fairing, as well as the elements in the surroundings of the fuselage, the fairing and their wakes. The prism layer settings were maintained for all meshes. Four different mesh sizes were tested ('Coarse', 'Medium', 'Fine', and 'Extra fine') with approximately 7, 13, 15 and 17 million elements, respectively. The dependency of the numerical solution with respect to the mesh size was evaluated by comparing the total pressure profiles at the wake measurement plane for the different meshes, as shown in Fig. A.3. The fine mesh with 15 million elements was considered to be the best compromise between accuracy and computational time.

A.3. RESULTS

A.3.1. CFD ANALYSIS

The comparison between the three different turbulence models (Figures A.4 and A.5) show that they have similar performance. The near-wall total pressure and velocity profiles (Figure A.4) show minor differences between the models. Additionally, the total pressure profiles at the measurement plane (Figure A.5) show that all three models deviate from the experimental values on a similar fashion. Based on these results, the study of alternative configurations was performed utilizing the Spalart-Allmaras model, since its computational cost is lower.

The comparison between the four different configurations is shown on Figure A.6. Some conclusions could be drawn from analysing these results: i) having a mirrored fairing (configuration b) decreases the intensity of the distortion and, obviously, creates another symmetry plane, ii) modifying the fairing LE (configuration c) provides only marginal improvement with respect to the baseline, and iii) having the fairing to follow the fuselage geometry on its tip reduces the distortion both in intensity as well as in its area. Therefore, these results led to the decision of adopting the optimized configuration (Figure A.1), as it combines the benefits of having the mirrored fairing with the smoothed fairing and fuselage connection.

A.3.2. EXPERIMENTAL RESULTS

The baseline and optimized configurations sketched in Figures A.1b and A.1c were tested in a wind-tunnel campaign. The results of the measurements are reported in Figure A.7,

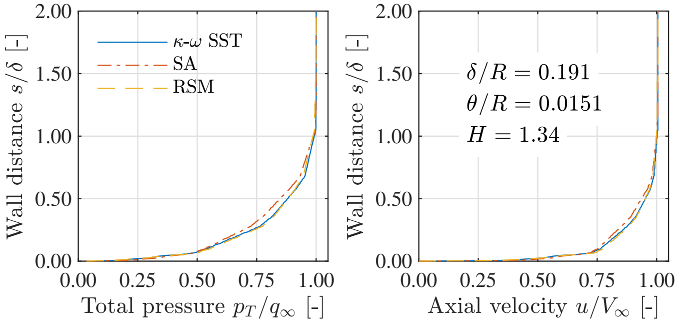

Figure A.4: Total pressure and axial velocity profiles in the fuselage boundary layer measured 0.5c upstream of the fairing leading edge.

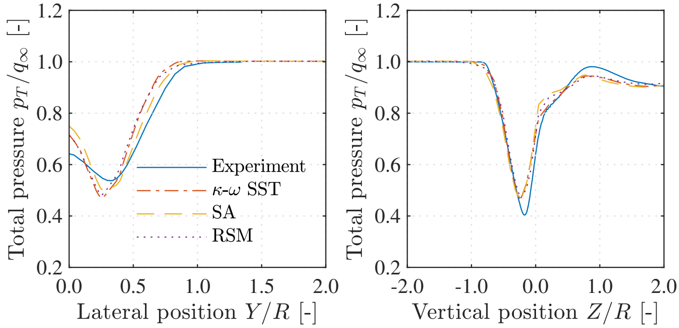

Figure A.5: Total pressure profiles along the vertical and lateral radial directions measured in the wake of the model.

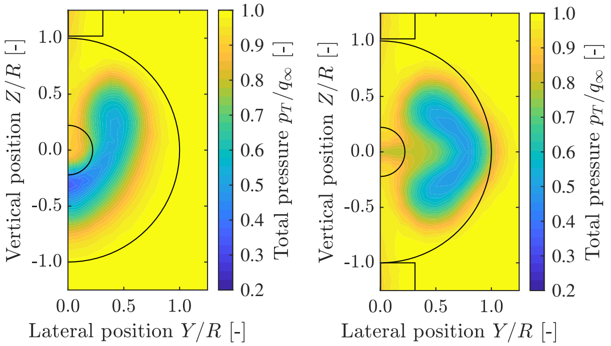

(a) Baseline.

(b) Baseline, mirrored.

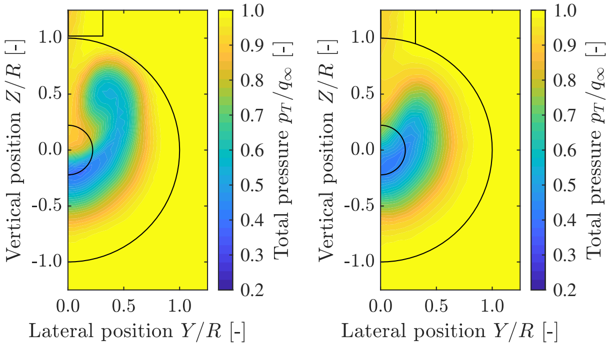

(c) Elliptical LE.

(d) Elliptical LE, curved tip.

Figure A.6: Total pressure distribution at $X_{TE} = 1.875R$ (CFD results).

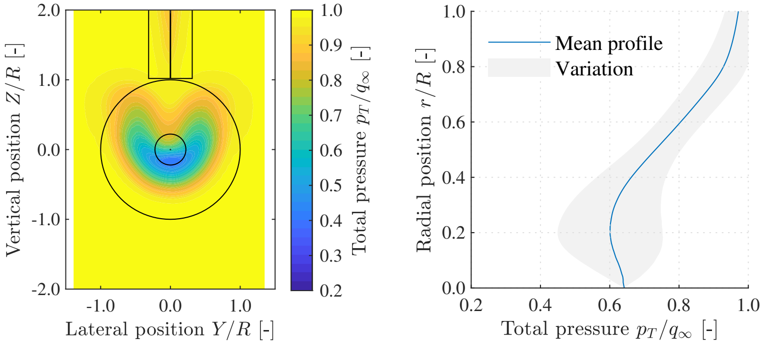

(a) Baseline configuration, wake contour.

(b) Baseline configuration, mean profile.

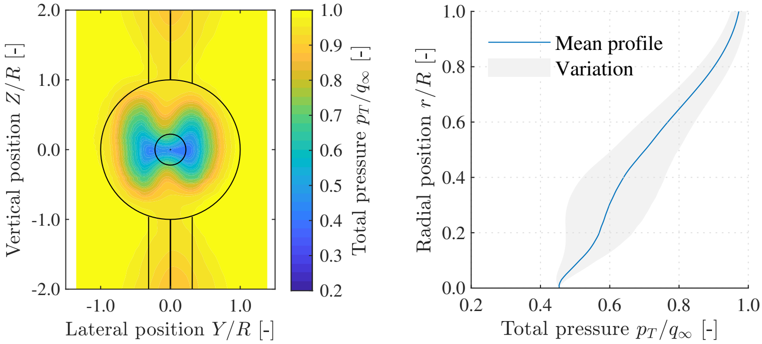

(c) Optimized configuration, wake contour.

(d) Optimized configuration, mean profile.

Figure A.7: Total pressure distribution in the wake of the model (experimental results).

in terms of wake total-pressure ratio distributions.

Similarly to what obtained by the CFD analysis, the p_T contour for the baseline configuration (Fig A.7a) shows a strongly asymmetric distribution around the horizontal plane ($Z/L = 0$). In particular, on the upper side ($Z/L > 0$) it is evident the effect of the horseshoe vortex which entrains high-momentum flow inside the fuselage boundary layer. It is also confirmed that the vortex produces a vertical displacement of the fuselage wake toward the bottom. In fact, the minimum total pressure is not found at the location of the trailing edge but slightly below. The plot of Figure A.7b displays the mean radial p_T profile and its standard deviation obtained by averaging out the profiles at various azimuth angles. The mean profile features a double curvature due to the vortex-induced entrainment. The maximum variation is equal to $0.15q_\infty$.

In addition, due to the implementation of the mirrored fairing on the bottom of the setup (see Fig. A.1), also the horizontal plane is a symmetry plane. This condition has a direct effect on the flow development in the wake of the model, as the downward displacement of the wake measured for the baseline configuration is now completely avoided. As a result, the center of the wake (i.e. the location of the minimum total pressure) remains on the fuselage axis. The interaction with the vortex also shows improvements over the baseline configuration. Due to the addition of the leading-edge fillet, the pressure gradient acting on the boundary layer at the wing-junction location is reduced. Consequently, the strength of the vortex forming at the fairing leading edge is lower and the wake contour shows a less pronounced footprint when compared to the baseline configuration. The mean radial profile shown in Figure A.7d displays a maximum variation of $0.12q_\infty$, meaning a reduction of 20% over the baseline configuration.

B

PERFORMANCE OF THE BASELINE UNPOWERED AIRCRAFT CONFIGURATION

This section provides a brief analysis of the aerodynamic performance of the PFC aircraft studied in chapter 5 in the bare fuselage (BF) configuration. External balance measurements were taken to investigate the aerodynamic forces and moments acting on the overall configuration at various operating conditions. Fig. B.1 shows the coefficients for varying incidence angle (Fig. B.1a) and sideslip angle (Fig. B.1a). The coefficients presented here take into account the forces and moments acting on the entire aircraft model, the fuselage support strut and the exposed section of the wing struts.
Fig. B.1a shows that:

1. C_L increases linearly for $\alpha < 8°$, after which a non-linear behavior is found, probably due to the onset of flow separation on the wings. The tail installation have no meaningful effect on C_L.

2. C_D shows the expected quadratic trend against α, centered around the zero-lift angle. The tail installation increases the C_D with a bias that decreases with α. It must be noted that the aft-cone shape of the BF configuration was obviously not optimized for unpowered (i.e. propulsor-off) conditions. As a consequence, the fuselage aerodynamic performance in the BF configuration is penalized when compared to a conventional aft-cone design. However, the drag penalty due to the BF aft-cone design with respect to a conventional aft-cone shape was quantified to be less than 1%.[95]

Contents of this chapter have been published in:
Della Corte, B., van Sluis, M., Gangoli Rao, A., and Veldhuis, L. L. M., "Aerodynamic Performance of an Aircraft with Aft-Fuselage Boundary-Layer-Ingestion Propulsion", *Journal of Aircraft*, 2022. doi:10.2514/1.C036596.

3. $C_{\mathcal{M}}$ linearly increases for $\alpha < 8°$, similarly to C_L. The tail installation has a negligible effect on $C_{\mathcal{M}}$.

Fig. B.1b shows that:

1. C_Y non-linearly increases in modulus with β. Similarly, the VTP contribution linearly increases with β.
2. $C_{\mathcal{N}}$ linearly increases with β. The contribution of the VTP also linaerly increases with β, due to the side-force produced by the VTP.
3. $C_{\mathcal{L}}$ non-linearly increases with β. The contribution of the VTP reduces $C_{\mathcal{L}}$, due to the side-force on the VTP.

To identify the main surface flow features at different operating conditions, the surface flow on the fuselage aft-cone and vertical tail was visualized with a fluorescent oil flow visualization. Fig. B.2 shows the surface flow for the BF configuration in cruise conditions ($\alpha = \beta = 0°$). The film oil pattern highlights the formation of a separation line on the fuselage surface in proximity of the tail leading edge, which is linked to the onset of an horseshoe vortex. The vortex structure bends around the tail leading edge and flows alongside the tail root, leading to corner flow separation downstream. Moreover, the oil pattern on the vertical tail shows that the shear-lines curve outboard toward the trailing edge. This is probably due to the onset of crossflow caused by the streamlines curvature typical of swept wings.

Fig. B.3 reports the total pressure distribution at the trailing edge of the fuselage of the BF configuration in cruise conditions. The fuselage boundary layer presents a distribution which is largely axisymmetric. The wakes of the VTP and of the fuselage-support strut are clearly visibly on the top and bottom sectors, respectively. At this location, the fuselage boundary layer edge is equal to approximately $r/R_\mathrm{b} = 0.7$.

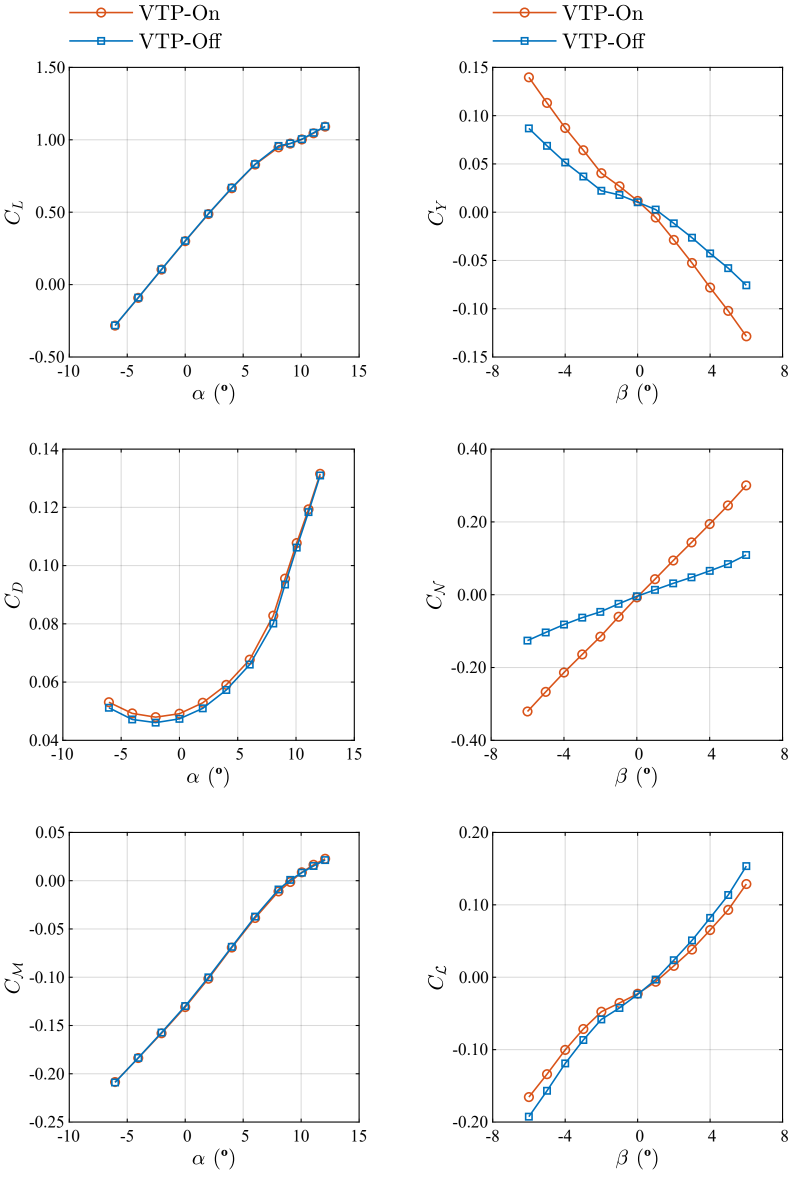

a) Longitudinal equilibrium ($\beta = 0°$) **b) Lateral-directional equilibrium ($\alpha = 0°$)**

Figure B.1: Aerodynamic forces and moments coefficients on the Bare Fuselage configuration. Balance measurements taken at $Re_{\bar{c}} = 460,000$.

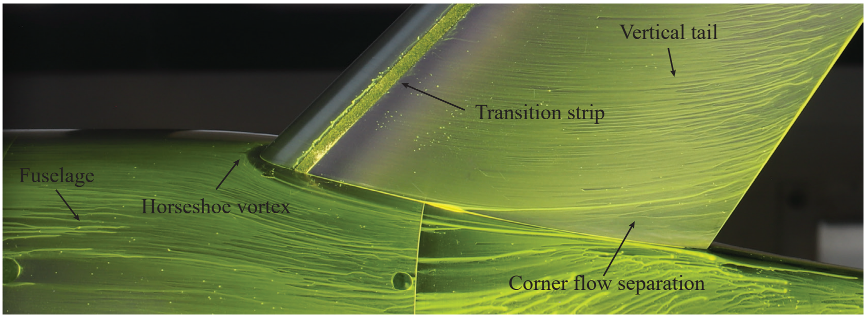

Figure B.2: Surface flow at the fuselage-tail intersection for the Bare Fuselage configuration in cruise conditions. Oil-flow measurements taken at $\alpha = 0° = \beta = 0°$ and $Re_{\bar{c}} = 460,000$.

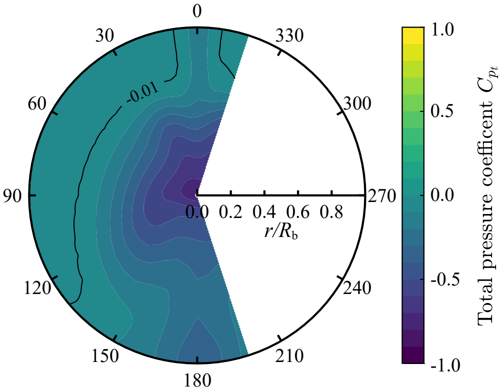

Figure B.3: Total pressure distribution at $x/L = 1$ for the BF, VTP-On case (back view). Total pressure measurements at $\alpha = 0° = \beta = 0°$ and $Re_{\bar{c}} = 460,000$.

C

MODEL-SCALE FAN DESIGN

The fan that equipped the wind-tunnel model used in Chapters 4 and 5 was specifically designed to be representative of the full-scale CENTRELINE PFC design. Here, a brief description of the design procedure and assumptions is given. More details are available in Ref. [97].

Firstly, the propulsor size was scaled down such that the ratio between the rotor blade height and the local boundary layer momentum thickness (θ^*) was held constant. The expected boundary layer profiles for the full- and model-scale PFC aircraft were obtained through axisymmetric RANS simulations, similar to those carried out in Chapter 6. The boundary layer profiles, together with the physical and momentum thicknesses heights are showed in Fig. C.1. Due to the scaling effects, the boundary layer is relatively thicker in model-scale conditions with an increase of relative momentum thickness of around 30%. As a result, the fan-to-fuselage-diameter ratio is 22% higher at model scale than at full scale.

The nacelle geometry was scaled in the radial direction to comply with the enlarged fan diameter, while the chord and axial position of the nacelle profile was kept as in the full-scale design.

Having established the fan diameter, the fan geometry was designed to match the operating conditions and performance metrics of the full-scale CENTRELINE design (see Ref. [28, 29]). In particular:

1. Flow coefficient: $\phi = \dot{m}/\rho S_d U_{\text{mid}} = 0.68$
2. Load coefficient: $\psi = \Delta h_0 / U_{\text{mid}}^2 = 0.44$

where $\dot{m}$ is the mass flow through the fan, U_{mid} is the blade velocity at the mid-span location and Δh_0 is the specific stagnation enthalpy rise across the fan disk.

The design followed an iterative approach in the effort to capture the fan upstream effects on the fuselage. A schematics of the process is presented in Fig. C.2.

After an initial guess on the pressure jump based on the input geometry and operating conditions, a RANS simulation of the wind-tunnel fuselage with the shrouded fan is

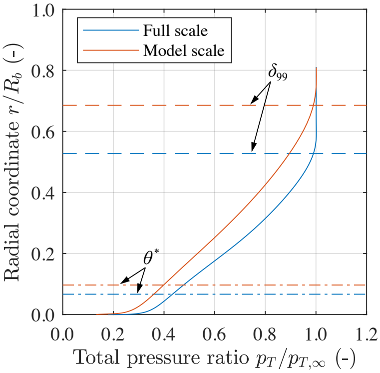

Figure C.1: Fuselage boundary layer profile at the fan face.

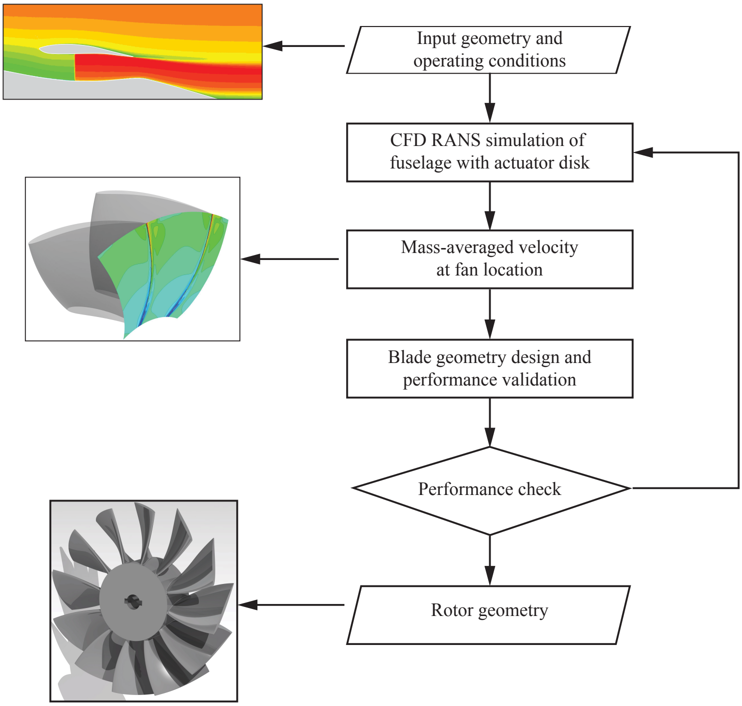

Figure C.2: Fuselage fan design procedure.

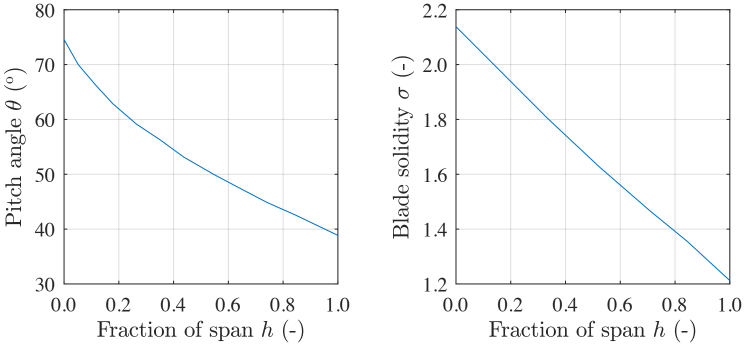

Figure C.3: Fan blade geometrical characteristics.

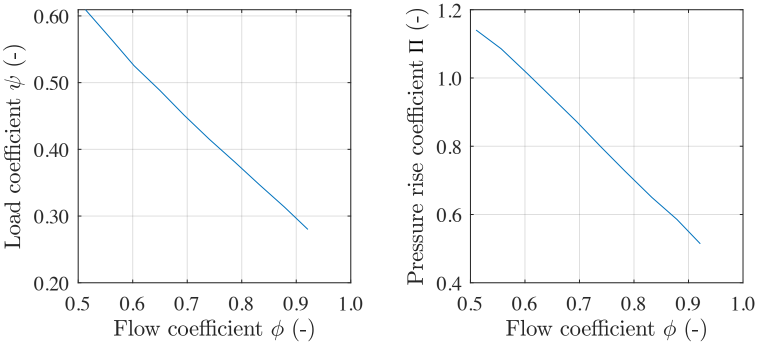

Figure C.4: Fan isolated performance.

performed. The fan is simulated through an actuator disk model with uniform pressure jump. The velocity profile at the fan plane are then mass-averaged. The averaged mass-flow is used to obtain a preliminary blade planform geometry based on a low-fidelity design tool (Ref. [114]). The fan design is validated through RANS for a single blade sector (axisymmetric conditions). The process is iterated until the performance metrics obtained via CFD are satisfactorily matching the objective.

The resulting fan blade geometry is summarized in Fig. C.3. The pitch angle (θ) and blade solidity ($\sigma = 2\pi r / n_b c$) are reported against the non-dimensional span height h.

Finally, the main performance metrics obtained from CFD are reported in Fig. C.4. The load coefficient ψ and the pressure rise coefficient ($\Pi = \Delta p_t / \rho U_{\text{mid}}^2$) are plotted against the flow coefficient ϕ.

REFERENCES

[1] ICAO, *Traffic growth and airline profitability were highlights of air transport in 2016,* `https://www.icao.int/Newsroom/Pages/traffic-growth-and-airline-profitability-were-highlights-of-air-transport-in-2016.aspx` (2017), accessed: 24/06/2021.

[2] International Civil Aviation Organization (ICAO), *Annual report of the council 2017,* (2017), accessed: 2024-11-23.

[3] IATA, *2036 forecast reveals air passengers will nearly double to 7.8 billion,* `http://www.iata.org/pressroom/pr/Pages/2017-10-24-01.aspx` (2017), accessed: 24/06/2021.

[4] International Air Transport Association (IATA), *20-year air passenger forecast,* (2017), accessed: 2024-11-23.

[5] Airbus, *Global market forecast 2022-2041,* (2022), accessed: 2024-11-23.

[6] International Air Transport Association (IATA), *Air passenger numbers in the wake of covid-19,* (2021), accessed: 2024-11-23.

[7] ICAO, *Effects of novel coronavirus (covid-19) on civil aviation: Economic impact analysis,* (2022).

[8] Boeing, *Commercial market outlook 2023-2042,* (2023), accessed: 2024-11-23.

[9] EC, *Reducing emissions from aviation,* `https://ec.europa.eu/clima/policies/transport/aviation_en` (2021), accessed: 24/06/2021.

[10] B. Graver, D. Rutherford, and S. Zheng, *CO_2 Emissions from Commercial Aviation*, Tech. Rep. (The International Council of Clean Transportation, 2020).

[11] B. Graver, D. Zhang, and D. Rutherford, *Co2 emissions from commercial aviation: 2013, 2018, and 2019,* (2020), accessed: 2024-11-23.

[12] ACARE, *Flightpath 2050,* European Commission (2011).

[13] ACARE, *Strategic research and innovation agenda,* European Commission (2011).

[14] I. C. on Clean Transportation, *Mitigating international aviation emissions: Risks and opportunities for alternative jet fuels,* (2020), accessed: 2024-11-23.

[15] M. Hornung, A. T. Isikveren, M. Cole, and A. Sizmann, *Ce-Liner - Case Study for eMobility in Air Transportation,* in *AIAA Aviation Forum* (2013).

[16] A. T. Isikveren, A. Seitz, J. Bijewitz, A. Mirzoyan, A. Isyanov, R. Grenon, O. Atinault, J.-L. Godard, and S. Stückl, *Distributed propulsion and ultra-high by-pass rotor study at aircraft level,* The Aeronautical Journal **119**, 1327–1376 (2015).

[17] R. Froude, *A description of a method of investigation of screw-propeller efficiency,* Transactions of the Institution of Naval Architects (1883).

[18] A. Betz, *Introduction to the Theory of Flow Machines* (Pergamon, 1966) pp. 215–217.

[19] W. Durand, *Aerodynamic theory: A general review of progress,* Julius Springer (1935).

[20] G. Wislicenus, *Hydrodynamics and propulsion of submerged bodies,* journal of the American Rocket Society (1960).

[21] P. A. Cerreta, *Wind-tunnel investigation of the drag of a proposed boundary-layer-controlled airship,* Tech. Rep. (Washington DC, David Taylor Aerodynamics Lab, 1957).

[22] S. Miley and E. von Lavante, *Propeller propulsion integration—state of technology survey,* NASA CR-3882 (1985).

[23] B. Moffitt, P. Bowles, J. Joo, B.-Y. Min, and B. Wake, *Analysis and Testing of BLI Pusher Propeller for High Speed Aircraft,* in *AHS International* (2017) pp. 1–27.

[24] L. H. Smith, *Wake ingestion propulsion benefit,* Journal of Propulsion and Power **9**, 74 (1993).

[25] M. Drela, *Power balance in aerodynamic flows,* AIAA Journal **47**, 1761 (2009).

[26] P. Lv, A. Gangoli Rao, D. Ragni, and L. Veldhuis, *Performance analysis of wake and boundary-layer ingestion for aircraft design,* Journal of Aircraft **53**, 1517 (2016).

[27] H.-J. Steiner, A. Seitz, K. Wieczorek, K. Plötner, A. T. Isikveren, and M. Hornung, *Multi-disciplinary design and feasibility study of distributed propulsion systems,* in *28th International Congress of the Aeronautical Sciences* (2012).

[28] A. Castillo Pardo and C. Hall, *Aerodynamics of boundary layer ingesting fuselage fans,* in *24th ISABE Conference* (2019).

[29] A. Seitz, A. Habermann, F. Peter, F. Troeltsch, A. Castillo Pardo, B. Della Corte, M. van Sluis, Z. Goraj, M. Kowalski, X. Zhao, T. Gronstedt, J. Bijewitz, and G. Wortmann, *Proof of concept study for fuselage boundary layer ingesting propulsion,* Aerospace **8** (2021), https://doi.org/10.3390/aerospace8010016.

[30] J. Welstead and J. L. Felder, *Conceptual design of a single-aisle turboelectric commercial transport with fuselage boundary layer ingestion,* in *54th AIAA Aerospace Sciences Meeting* (2016).

[31] M. Drela, *Development of the d8 transport configuration,* in *29th AIAA Applied Aerodynamics Conference* (2011).

[32] A. Uranga, M. Drela, E. Greitzer, N. Titchener, M. Lieu, N. Siu, A. Huang, G. M. Gatlin, and J. Hannon, *Preliminary experimental assessment of the boundary layer ingestion benefit for the d8 aircraft,* in *52nd Aerospace Sciences Meeting* (2014).

[33] A. Uranga, M. Drela, E. M. Greitzer, D. K. Hall, N. A. Titchener, M. K. Lieu, N. M. Siu, C. Casses, A. C. Huang, G. M. Gatlin, *et al.*, *Boundary layer ingestion benefit of the d8 transport aircraft,* AIAA Journal **55**, 3693 (2017).

[34] L. Wiart, O. Atinault, J.-C. Boniface, and R. Barrier, *Aeropropulsive performance analysis of the nova configurations,* in *30th Congress of the International Council of the Aeronautical Sciences* (2016).

[35] K. R. Antcliff and F. M. Capristan, *Conceptual design of the parallel electric-gas architecture with synergistic utilization scheme (pegasus) concept,* in *18th AIAA/ISSMO multidisciplinary analysis and optimization conference* (2017).

[36] K. A. Brown, J. L. Fleming, M. Langford, W. Ng, K. Schwartz, and C. Combs, *Development of a ducted propulsor for bli electric regional aircraft-part i: Aerodynamic design and analysis,* in *AIAA Propulsion and Energy 2019 Forum* (2019).

[37] K. Schwartz, R. Burdisso, B. Witcher, K. A. Brown, J. L. Fleming, and C. Combs, *Development of a ducted propulsor for bli electric regional aircraft-part ii: Aeroacoustic analysis,* in *AIAA Propulsion and Energy 2019 Forum* (2019).

[38] E. Gunn and C. Hall, *Aerodynamics of boundary layer ingesting fans,* in *ASME Turbo Expo 2014: Turbine Technical Conference and Exposition* (American Society of Mechanical Engineers, 2014).

[39] P. D. Bravo-Mosquera, H. D. Cerón-Muñoz, and F. M. Catalano, *Potential propulsive and aerodynamic benefits of a new aircraft concept: a low-speed experimental study,* Aerospace **10**, 651 (2023).

[40] P. Lv, D. Ragni, T. Hartuc, L. Veldhuis, and A. Gangoli Rao, *Experimental investigation of the flow mechanisms associated with a wake-ingesting propulsor,* AIAA Journal **55**, 1332 (2017).

[41] O. Atinault, G. Carrier, R. Grenon, C. Verbecke, and P. Viscat, *Numerical and experimental aerodynamic investigations of boundary layer ingestion for improving propulsion efficiency of future air transport,* in *31st AIAA Applied Aerodynamics Conference* (2013).

[42] A. Castillo Pardo and C. A. Hall, *Aerodynamics of Boundary Layer Ingesting Fuselage Fans,* ASME Journal of Turbomachinery **143**, 1 (2021).

[43] T. Lengyel-Kampmann, J. Karboujian, K. Koc, R. Schnell, and P. Winkelmann, *Experimental investigation on a lightweight, efficient, counter-rotating fan with and without boundary layer ingestion,* CEAS Aeronautical Journal **15**, 207 (2024).

[44] D. Barara, M. v. Sluis, and T. Sinnige, *Impact of installation effects on optimal propeller design: Application to a boundary-layer-ingesting propeller,* in *AIAA AVIATION FORUM AND ASCEND 2024* (2024) p. 3522.

[45] V. Patel, A. Nakayama, and R. Damian, *Measurements in the thick axisymmetric turbulent boundary layer near the tail of a body of revolution,* Journal of Fluid Mechanics **63**, 345 (1974).

[46] T. Sarkar, P. Sayer, and S. Fraser, *Flow simulation past axisymmetric bodies using four different turbulence models,* Applied Mathematical Modelling **21**, 783 (1997).

[47] Z. Xiao, Y. Zhang, J. Huang, H. Chen, and S. Fu, *Prediction of separation flows around a 6: 1 prolate spheroid using rans/les hybrid approaches,* Acta Mechanica Sinica **23**, 369 (2007).

[48] C. J. Chesnakas, D. Taylor, and R. L. Simpson, *Detailed investigation of the three-dimensional separation about a 6: 1 prolate spheroid,* AIAA journal **35**, 990 (1997).

[49] A. Seitz, F. Peter, J. Bijewitz, A. Habermann, Z. Goraj, M. Kowalski, A. Castillo Pardo, F. Meller, R. Merkler, S. Samuelsson, B. Della Corte, M. van Sluis, G. Wortmann, and M. Dietz, *Concept validation study for fuselage wake-filling propulsion integration,* in *31st Congress of the International Council of the Aeronautical Sciences* (2018).

[50] A. Castillo Pardo and C. A. Hall, *Effects of sideslip direction on a rear fuselage boundary layer ingesting fan,* Journal of Turbomachinery **144**, 121012 (2022).

[51] A. Castillo Pardo and C. A. Hall, *Design of a transonic boundary layer ingesting fuselage fan,* in *Proceedings of Global Power and Propulsion Society* (2020).

[52] A. L. Habermann, J. Bijewitz, A. Seitz, and M. Hornung, *Performance bookkeeping for aircraft configurations with fuselage wake-filling propulsion integration,* CEAS Aeronautical Journal **11**, 529 (2019).

[53] A. Plas, D. Crichton, M. Sargeant, T. Hynes, E. Greitzer, C. Hall, and V. Madani, *Performance of a boundary layer ingesting (bli) propulsion system,* in *45th AIAA Aerospace Sciences Meeting and Exhibit* (2017).

[54] S. THURSTON and M. S. EVANBAR, *Efficiency of a propulsor on a body of revolution-inducting boundary-layer fluid.* Journal of Aircraft **3**, 270 (1966).

[55] P. Baskaran, B. Della Corte, M. van Sluis, and A. Gangoli Rao, *Aeropropulsive performance analysis of axisymmetric fuselage bodies for boundary-layer ingestion applications,* AIAA Journal **60**, 1592 (2022).

[56] V. C. Patel, *On the equations of a thick axisymmetric turbulent boundary layer,* Tech. Rep. (Institute of Hydraulic Research, University of Iowa, 1973).

[57] ESDU, *Geometrical characteristics of typical bodies,* IHS ESDU **Item. 77028** (1977).

[58] ESDU, *The influence of body geometry and flow conditions on axisymmetric boundary layers at subcritical Mach numbers,* IHS ESDU **Item n. 79020** (1979).

[59] D. F. Myring, *A theoretical study of body drag in subcritical axisymmetric flow,* The Aeronautical Quarterly **27**, 186 (1976).

[60] ESDU, *Profile drag of axisymmetric bodies at zero incidence for subcritical Mach numbers,* IHS ESDU **Item n. 78019** (1978).

[61] F. Scarano and M. L. Riethmuller, *Iterative multigrid approach in piv image processing with discrete window offset,* Experiments in Fluids **26**, 513 (1999).

[62] B. Wieneke and K. Pfeiffer, *Adaptive PIV with variable interrogation window size and shape,* in *15th International Symposium on Applications of Laser Techniques to Fluid Mechanics (Lisbon, Portugal, 5–8 July)* (2010).

[63] B. Wieneke, *Piv uncertainty quantification from correlation statistics,* Measurement Science and Technology **26** (2015), 10.1088/0957-0233/26/7/074002.

[64] P. Spalart and S. Allmaras, *A one-equation turbulence model for aerodynamic flows,* in *30th Aerospace Sciences Meeting and Exhibit* (1992) pp. 439–462.

[65] F. R. Menter, *Two-equation eddy-viscosity turbulence models for engineering applications,* AIAA journal **32**, 1598 (1994).

[66] J. B. Barlow, W. H. Rae, and A. Pope, *Low-speed wind tunnel testing* (John wiley & sons, 1999).

[67] V. Patel and S. Kim, *Topology of laminar flow on a spheroid at incidence,* Computers & fluids **23**, 939 (1994).

[68] K. Wang, H. Zhou, C. Hu, and S. Harrington, *Three-dimensional separated flow structure over prolate spheroids,* Proceedings of the Royal Society of London. A. Mathematical and Physical Sciences **429**, 73 (1990).

[69] H. Schlichting and K. Gersten, *Boundary-layer theory* (Springer, 2016).

[70] C. A. Hall, E. Schwartz, and J. I. Hileman, *Assessment of technologies for the silent aircraft initiative,* Journal of Propulsion and Power **25**, 1153 (2009).

[71] G. K. Kenway and C. C. Kiris, *Aerodynamic shape optimization of the starc-abl concept for minimal inlet distortion,* in *AIAA/ASCE/AHS/ASC Structures, Structural Dynamics, and Materials Conference* (2018).

[72] B. T. Blumenthal, A. A. Elmiligui, K. A. Geiselhart, R. L. Campbell, M. D. Maughmer, and S. Schmitz, *Computational investigation of a boundary-layer-ingestion propulsion system,* Journal of Aircraft **55**, 1141 (2018).

[73] J. S. Gray, C. A. Mader, G. K. W. Kenway, and J. R. R. A. Martins, *Modeling boundary layer ingestion using a coupled aeropropulsive analysis,* Journal of Aircraft **55**, 1191 (2018).

[74] A. Seitz, A. L. Habermann, and M. van Sluis, *Optimality considerations for propulsive fuselage power savings,* Proceedings of the Institution of Mechanical Engineers, Part G: Journal of Aerospace Engineering (2020), 10.1177/0954410020916319.

[75] L. L. Kob, J. J. Doherty, D. M. Birch, and J. Robson, *Experimental and computational investigation for in-line boundary layer ingestion,* in *AIAA Aviation* (2019).

[76] ESDU, *A Method for Estimating Drag-Rise Mach Number at Zero Incidence of Smooth or Bumpy Non-Ducted Axisymmetric Bodies Without or With Fins*, Tech. Rep. 74013 (IHS ESDU, 1974).

[77] B. Drew and A. Jenn, *Pressure drag calculations on axisymmetric bodies of arbitrary moldline,* in *28th Aerospace Sciences Meeting* (1990).

[78] J. W. Purvis and J. E. Burkhalter, *Prediction of critical mach number for store configurations,* AIAA Journal **17**, 1170 (1979).

[79] J. Serpieri, *Cross-Flow Instability: Flow Diagnostics and Control of Swept Wing Boundary Layers*, Ph.D. thesis, Delft University of Technology (2018).

[80] B. Della Corte, A. A. Perpignan, M. van Sluis, and A. G. Rao, *Experimental and computational analysis of model–support interference in low-speed wind-tunnel testing of fuselage-boundary-layer ingestion,* in *9th EASN International Conference* (2019).

[81] B. Van Oudheusden, *Piv-based pressure measurement,* Measurement Science and Technology **24** (2013), 10.1088/0957-0233/24/3/032001.

[82] F. White, *Viscous Fluid Flow* (McGraw-Hill, 2006).

[83] D. Ragni, B. Van Oudheusden, and F. Scarano, *3d pressure imaging of an aircraft propeller blade-tip flow by phase-locked stereoscopic piv,* Experiments in fluids **52**, 463 (2012).

[84] T. Sinnige, B. D. Corte, R. De Vries, F. Avallone, R. Merino-Martínez, D. Ragni, G. Eitelberg, and L. L. Veldhuis, *Alleviation of propeller-slipstream-induced unsteady pylon loading by a flow-permeable leading edge,* Journal of Aircraft **56**, 1214 (2019).

[85] G. Brune, *Quantitative low-speed wake surveys,* Journal of Aircraft **31**, 249 (1994).

[86] E. Maskell, *Progress Towards a Method for the Measurement of the Components of the Drag of a Wing of Finite Span*, Tech. Rep. 72232 (RAE, 1972).

[87] M.-H. Wang, *Hub Effects in Propeller Design and Analysis*, Ph.D. thesis, Massachusetts Institute of Technology (1985).

[88] Q. R. Wald, *The aerodynamics of propellers,* Elsevier Progress in Aerospace Sciences **42**, 85 (2006).

[89] E. J. Gunn and C. A. Hall, *Non-axisymmetric stator design for boundary layer ingesting fans,* ASME Turbo Expo (2017), 10.1115/GT2017-63082.

[90] D. K. Hall, E. M. Greitzer, and C. S. Tan, *Analysis of fan stage design attributes for boundary layer ingestion,* ASME Turbo Expo (2016), 10.1115/GT2016-57808.

[91] H. Mårtensson, *Harmonic forcing from distortion in a boundary layer ingesting fan,* Aerospace **8**, 1 (2021).

[92] F. Petrosino, M. Barbarino, and M. Staggat, *Aeroacoustics assessment of an hybrid aircraft configuration with rear-mounted boundary layer ingested engine,* Applied Sciences **11** (2021), 10.3390/app11072936.

[93] G. Romani, Q. Ye, F. Avallone, D. Ragni, and D. Casalino, *Numerical analysis of fan noise for the nova boundary-layer ingestion configuration,* Aerospace Science and Technology **96** (2020), 10.1016/j.ast.2019.105532.

[94] M. van Sluis, B. Della Corte, and A. Gangoli Rao, *Final PFC Aircraft Aerodynamic Design and Analysis* (CENTRELINE Public Deliverable D3.03, 2021).

[95] B. Della Corte, M. van Sluis, and A. Gangoli Rao, *Results of Overall Configuration Wind Tunnel Testing* (CENTRELINE Public Deliverable D3.02, 2021).

[96] N. C. Bissinger and T. Breuer, *Encyclopedia of Aerospace Engineering* (John Wiley & Sons, 2010).

[97] B. Della Corte, M. van Sluis, and A. Gangoli Rao, *Results of Overall Configuration Wind Tunnel Testing* (CENTRELINE Public Deliverable D3.02, 2021).

[98] M. Drela, *Xfoil: An analysis and design system for low reynolds number airfoils,* in *Low Reynolds Number Aerodynamics*, edited by T. J. Mueller (Springer-Verlag, 1989) pp. 1–12.

[99] B. Della Corte, L. Orsini, M. van Sluis, A. Gangoli Rao, and L. L. M. Veldhuis, *Experimental investigation of the flow past an axisymmetric body at low speed,* in *Proceedings of the 24th International Society of Air Breathing Engines Conference* (2019).

[100] P. Baskaran, B. Della Corte, M. van Sluis, and A. Gangoli Rao, *Aeropropulsive performance analysis of axisymmetric fuselage bodies for boundary-layer ingestion applications,* AIAA Journal **60**, 1592 (2022).

[101] E. Reissner, *On Compressibility Corrections for Subsonic Flow Over Bodies of Revolution*, Tech. Rep. 1815 (NACA, 1949).

[102] J. B. Delano and J. L. Crigler, *Compressible-Flow Solutions for the Actuator Disk*, Tech. Rep. L53AO7 (NACA, 1953).

[103] A. W. Vogeley, *Axial-Momentum Theory for Propellers in Compressible Flow*, Tech. Rep. 2164 (NACA, 1951).

[104] B. J. C. Horsten, *Low-Speed Model Support Interference-Elements of an Expert System*, Ph.D. thesis, Delft University of Technology (2011).

[105] R. L. Simpson, *Junction flows,* Annual Review of Fluid Mechanics **33**, 415 (2001).

[106] J. L. Fleming, R. Simpson, J. Cowling, and W. Devenport, *An experimental study of a turbulent wing-body junction and wake flow,* Experiments in fluids **14**, 366 (1993).

[107] F. Gand, S. Deck, V. Brunet, and P. Sagaut, *Flow dynamics past a simplified wing body junction,* Physics of Fluids **22**, 115111 (2010).

[108] F. Gand, V. Brunet, and S. Deck, *Experimental and numerical investigation of a wing-body junction flow,* AIAA journal **50**, 2711 (2012).

[109] B. C. Hinson and K. A. Hoffmann, *Parametric exploration of wing–body junction flow using computational fluid dynamics,* Journal of Aircraft **52**, 1492 (2015).

[110] B. E. Green and J. L. Whitesides, *Method for designing leading-edge fillets to eliminate flow separation,* Journal of Aircraft **40**, 282 (2003).

[111] B. W. Van Oudheusden, C. B. Steenaert, and L. M. Boermans, *Attachment-line approach for design of a wing-body leading-edge fairing,* Journal of Aircraft **41**, 238 (2004).

[112] Z. Belligoli, A. J. Koers, R. P. Dwight, and G. Eitelberg, *Using an anti-fairing to reduce drag at wing/body junctions,* AIAA Journal **57**, 1468 (2018).

[113] D. C. Wilcox *et al.*, *Turbulence modeling for CFD*, Vol. 2 (La Canada, 1998).

[114] S. Ng, *Development of a design and sizing tool for conceptual turbofan engines*, Master's thesis, Delft University of Technology (2020).

LIST OF PUBLICATIONS

JOURNAL PAPERS

6. **Della Corte, B.**, van Sluis, M., Gangoli Rao, A., and Veldhuis, L. L. M., “Aerodynamic Performance of an Aircraft with Aft-Fuselage Boundary-Layer-Ingestion Propulsion”, *Journal of Aircraft*, 2022. doi:10.2514/1.C036596.

5. Baskaran, P., **Della Corte, B.**, van Sluis, M., and Gangoli Rao, A., “Aeropropulsive Performance Analysis of Axisymmetric Fuselage Bodies for Boundary-Layer Ingestion Applications”, *AIAA Journal*, Vol. 60, No., 3, 2022. doi:10.2514/1.J060362.

4. **Della Corte, B.**, van Sluis, M., Gangoli Rao, A., and Veldhuis, L. L. M., “Power Balance Analysis Experiments on an Axisymmetric Fuselage with an Integrated Boundary-Layer-Ingesting Fan”, *AIAA Journal*, Vol. 59, No. 12, 2021. doi:10.2514/1.C036596.

3. Seitz, A., Habermann, A. L., Peter, F., Troeltsch, F., Castillo Pardo, A., **Della Corte, B.**, van Sluis, M., Goraj, Z., Kowalski, M., Zhao, X., Grönstedt, T., Bijewitz, J., and Wortmann, G., “Proof of Concept Study for Fuselage Boundary Layer Ingesting Propulsion”, *Aerospace*, Vol. 8, No. 16, 2021. doi:10.3390/aerospace8010016.

2. Sinnige, T., **Della Corte, B.**, de Vries, R., Avallone, F., Merino-Martínez, R., Ragni, D., Eitelberg, G., and Veldhuis, L. L. M., “Alleviation of Propeller-Slipstream-Induced Unsteady Pylon Loading by a Flow-Permeable Leading Edge”, *Journal of Aircraft*, Vol. 56, No. 3, 2019. doi:10.2514/1.C035250.

1. Sinnige, T., de Vries, R., **Della Corte, B.**, Avallone, F., Ragni, D., Eitelberg, G., and Veldhuis, L. L. M., “Unsteady Pylon Loading Caused by Propeller-Slipstream Impingement for Tip-Mounted Propellers”, *Journal of Aircraft*, Vol. 55, No. 4, 2018. doi:10.2514/1.C034696.

CONFERENCE PAPERS

9. Sinnige, T., and **Della Corte, B.**, "Aerodynamic Performance of a Tip-Mounted Propeller-Wing System at Positive and Negative Thrust", *AIAA Aviation Forum*, AIAA paper 2024-3520, 2024. doi: 10.2514/6.2024-3520.

8. Margalida, G., **Della Corte, B.**, Sinnige, T., Knepper, K., Soemarwoto, B., and Nahuis, R., "Low Fidelity Multidisciplinary Methodology for Efficient and Quiet Propeller Design", *30th AIAA/CEAS Aeroacoustics Conference*, AIAA paper 2024-3317, 2024. doi: 10.2514/6.2024-3317.

7. van Sluis, M., **Della Corte, B.**, and Gangoli Rao, A., "Aerodynamic Design Space Exploration of a Fuselage Boundary Layer Ingesting Aircraft", *AIAA Aviation Forum*, AIAA paper 2023-4069, 2023. doi: 10.2514/6.2023-4069.

6. **Della Corte, B.**, van Sluis, M., Gangoli Rao, A., and Veldhuis, L. L. M., “Aerodynamic Performance of an Aircraft with Aft-Fuselage Boundary-Layer-Ingestion Propulsion”, *AIAA Aviation 2021 Forum*, AIAA Paper 2021-2467, 2021. doi:10.2514/6.2021-2467.

5. **Della Corte, B.**, Orsini, L., van Sluis, M., Gangoli Rao, A., and Veldhuis, L. L. M., “Experimental Investigation of the Flow Past and Axisymetric Body at Low Speed”, *24th International Society of Air Breathing Engines Conference*, ISABE Paper 2019-24151, 2019.

4. **Della Corte, B.**, Perpignan, A. A. V., van Sluis, M., and Gangoli Rao, A., “Experimental and Computational Analysis of Model–Support Interference in Low-Speed Wind-Tunnel Testing of Fuselage-Boundary-Layer Ingestion”, *9th EASN International Conference on “Innovation in Aviation & Space”*, Paper No. 02020, 2019. doi:10.1051/matecconf/201930402020.

3. Seitz, A., Peter, F., Bijewitz, J., Habermann, A. L., Goraj, Z., Kowalski, M., Castillo Pardo, A., Meller, F., Merkler, R., Samuelsson, S., **Della Corte, B.**, van Sluis, M., Wortmann, G., and Dietz, M., “Concept Validation Study for Fuselage Wake-Filling Propulsion Integration”, *31st Congress of the International Council of the Aeronautical Sciences*, 2018.

2. de Vries, R., Sinnige, T., **Della Corte, B.**, Avallone, F., Ragni, D., Eitelberg, G., and Veldhuis, L. L. M., “Tractor Propeller-Pylon Interaction, Part I: Characterization of Unsteady Pylon Loading”, *55th AIAA Aerospace Sciences Meeting*, AIAA Paper 2017:1175, 2017. doi:10.2514/6.2017-1175.

1. **Della Corte, B.**, Sinnige, T., de Vries, R., Avallone, F., Ragni, D., Eitelberg, G., and Veldhuis, L. L. M., “Tractor Propeller-Pylon Interaction, Part II: Mitigation of Unsteady Pylon Loading by Application of Leading-Edge Porosity”, *55th AIAA Aerospace Sciences Meeting*, AIAA Paper 2017:1176, 2017. doi:10.2514/6.2017-1176.

PROJECT DELIVERABLES

3. **Della Corte, B.**, “Results of the Overall Configuration Wind Tunnel Testing”, CENTRELINE Public Deliverable D3.2, 2021.

2. van Sluis, M., and **Della Corte, B.**, “Final PFC Aircraft Aerodynamic Design and Performance”, CENTRELINE Public Deliverable D3.2, 2021.

1. **Della Corte, B.**, and van Sluis, M., “Specification of Wind-Tunnel Model Design and Test Campaign Plan”, CENTRELINE Public Deliverable D3.1, 2018.

CURRICULUM VITÆ

Biagio DELLA CORTE

21-05-1992	Born in Naples, Italy

RESEARCH & WORK EXPERIENCE

2024–today	Aerodynamic Testing Technology Engineer Airbus Defence & Space, Manching, Germany
2021–2023	Researcher Delft University of Technology, Delft, The Netherlands
2017–2021	Ph.D. Candidate Delft University of Technology, Delft, The Netherlands

EDUCATION

2014–2017	MSc in Aerospace Engineering University of Naples “Federico II”, Naples, Italy
2011–2014	MSc in Aerospace Engineering University of Naples “Federico II”, Naples, Italy

ACKNOWLEDGEMENTS

Acknowledgements are available in the printed version of this thesis.

Caminante, no hay camino,
se hace camino al andar.

Antonio Machado